Author:
Okeme, Ilemona C

Title:
Opportunities and challenges for rare earth element and actinide recovery from coal and coal fly ash

Opportunities and challenges for rare earth element and actinide recovery from coal and coal fly ash.

Ilemona Cornelius Okeme

A dissertation submitted to the University of Bristol in accordance with the requirements for award of the degree of DOCTOR OF PHILOSOPHY in the Faculty of Science.

Interface Analysis Centre

School of Physics

May 2021

57,324 words

In loving memory of my late parents (Arch. & Mrs. Anthony Okeme) and the members of my immediate family, who are my sure pillars.

Commit your actions to the Lord, and your plans will succeed.

Proverbs 16:3

Author’s declaration

I declare that the work in this dissertation was carried out in accordance with the requirements of the University's Regulations and Code of Practice for Research Degree Programmes and that it has not been submitted for any other academic award. Except where indicated by specific reference in the text, the work is the candidate's own work. Work done in collaboration with, or with the assistance of, others, is indicated as such. Any views expressed in the dissertation are those of the author.

SIGNED: ..... DATE: .....

Abstract

Coal fly ash is an industrially useful by-product of coal combustion, with millions of tonnes held in repositories globally. This fine and cheaply-available waste material, is proven to sometimes be enriched in valuable elements/compounds, such as rare earth element (REE) minerals and actinides, alongside heavy toxic elements such as Cr, Pb, As and Cd, making coal fly ash both a potential unconventional source of valuable minerals and a hazardous material depending on the elemental trace chemistry of the parent coal body. The importance of REE and actinides for use in advanced electronics technologies and the nuclear industry, alongside concerns over geopolitics and instability in the global supply market, means there is now a renewed incentive for countries to secure native sources of economically-sustainable rare earth elements through research and development efforts. Unconventional sources of REE, such as coal fly ash, represent a potentially interesting value proposition, especially for developing countries.

The work presented in this thesis provides a study of rare earth elements and actinides in Nigerian simulant coal fly ash from the perspective of resource recovery and environmental protection. A suite of advanced analytical laboratory techniques and novel synchrotron radiation techniques, alongside micromanipulation methods, were used in this study to understand the amounts and mineralogical association of REE and actinides in 3 different Nigerian coal deposits.

Bulk and micro mineralogical analyses were first performed on the simulant coal fly ash using x-ray diffraction and scanning electron microscopy / with energy dispersive x-ray fluorescence and spectroscopy used for elemental analysis. It was observed that the Nigerian simulant coal fly ash samples were less complex in mineralogy than conventional rare earth ores (with quartz, mullite, haematite and cristobalite as the major mineral phases), composed of discrete micron-scale particles of rare earth mineral monazite ($[Ce,La,Nd,Th]PO_4$), xenotime (YPO_4) and zircon ($ZrSiO_4$), alongside uraninite (UO_2) and thorite ($ThSiO_4$). Subsequent bulk elemental analysis performed using inductively-coupled plasma mass spectrometry, showed the simulant coal fly ash to be enriched in the rare earth elements, being more enriched in the higher-valued critical rare earth elements Nd, Eu, Tb, Dy, Y and Er, compared to conventional rare earth ores. Sequential extraction analysis of the simulant fly ash materials showed significant recoverability of rare earth elements in the acid-soluble fraction using cheap and environmentally-friendly ethanoic acid; the toxic heavy metals Cd and As were also significantly recovered in the acid-soluble fraction.

Synchrotron radiation analysis of individual micro-particles of monazite and uraninite using micro-x-ray fluorescence mapping, micro-x-ray fluorescence tomography, micro-x-ray absorption near edge spectroscopy and micro-x-ray diffraction showed a zonation pattern in the monazite particles, with the rims rich in the rare earth elements, and the core rich in U and Th but depleted in the rare earth elements. In the uraninite particles, U was homogeneously-distributed, existing in the chemically reduced IV oxidation state.

Gamma-ray spectrometry analysis of the bulk coal and simulant coal fly ash was also performed using a high-purity Ge gamma-ray detector. Compared to World mean levels, the radioactivity and associated hazard associated with the parent coal samples were insignificantly-low. However, the equivalent activity concentration and radiological hazard levels associated with the simulant coal fly ashes were significantly-high, above United

Nations Scientific Committee on the Effects of Atomic Radiation (UNSCEAR) World mean and recommended levels.

The results from this study are valuable for the development of customised methods for rare earth element and actinide recovery from Nigerian coal fly ash and coal fly ash in repositories globally, including the derivation of methodologies for general management and recycling of coal fly ash to extract best economic value. If Nigerian coal is substantially consumed by power generating processes over the coming decades, the REE content of the amassed residual fly ash materials presents a potentially exciting economic prospect for the country. Regardless of REE exploitation, the high residual metal, REE and actinide content of the fly ashes dictates that they should be responsibly managed to prevent environmental or human harm.

Acknowledgements

Firstly, my profound gratitude goes to God Almighty, whose unconditional love and blessings made this academic journey possible. How can I repay the Lord for his goodness to me?

I would like to thank Professor Thomas Scott, my primary supervisor, for his support, guidance and mentorship; you are too kind-hearted! My gratitude also goes to Dr Keith Hallam, my secondary supervisor, for lending listening ears to my many enquiries and support with thesis writing. I, no doubt, learnt from you how to give attention to seemingly insignificant tiny details!

Special thanks to all the staff and PhD students at the Interface Analysis Centre (IAC), for their support, in particular:

- Dr Peter Martin and Dr Christopher Jones, for the many times they helped me with experimental techniques, procedures and data analysis; Dr Peter Martin, with your help, my research article writing capability has improved greatly.
- Dr Adel Turke and Dr Peter Heard, for their help with the operation of microanalysis techniques.
- my superb colleagues Macarena Leal Olloqui, Ian Ang ('my gamma spec buddy'), Fahed Aloufi, Erin Holland, Gareth Griffiths, Haris Paraskevoulakos, Antonis Banos, Siqi He, Dean Connor and Jacek Wasik, for their support and encouragement. And also to Dr Ross Springell for his friendship and 'hard tackles' during 5-a-side games.

Thanks are likewise extended to all my friends (outside of the IAC), in both the UK and abroad, who were supportive during this PhD.

I am also appreciative of: Dangote Cement plc, Nigeria, for their permission and assistance with sample collection; Dr Rich Crane (Camborne School of Mines, University of Exeter, UK), for his generous assistance with running ICP-MS analysis of my samples; Dr Yukihiko Satou (Collaborative Laboratories for Advanced Decommissioning Science, Japan), for his help with autoradiography analysis.

How can I forget the prayers, love and support of my parents (of blessed memory) and my siblings? You guys have been my pillars and I am forever grateful.

My unalloyed gratitude goes to Professor Martins Emeje, my God-sent benefactor and 'friend'. Without you, this journey will not have started in the first place; thank you for the love and kindness you have shown me and my family. Get ready to redeem the many promises you made to me at the beginning of this PhD journey! My special thanks also go to Dr Ochala Isaiah, who has also been a long-time mentor and father-figure; thank you for your prayers, moral support and advice. To my colleagues at Kogi State University, I say thank you for your support.

And last, but definitely not least, to the most important persons in my life: my wonderful wife, Helen (Onemi), and my adorable son and bundle of joy, Ojomideju Winner (Deju). You guys are my jewels of inestimable worth; I cannot be more grateful.

Publications and conference presentations

Journal Publications – Available in Prints

1. **Ilemona C. Okeme**, Peter G. Martin, Christopher Jones, Richard A. Crane, Theophilus I. Ojonimi, Konstantin Ignatyev, Dave Megson-Smith, Thomas B. Scott. An advanced analytical assessment of rare earth element concentration, distribution, speciation, crystallography and solid-state chemistry in fly ash. *Spectrochimica Acta Part B: Atomic Spectroscopy*, 2020.
2. **Ilemona C. Okeme**, Thomas B. Scott, Peter G. Martin, Yukihiko Satou, Theophilus I. Ojonimi, Moromoke O. Olaluwoye. Assessment of the mode of occurrence and radiological impact of radionuclides in Nigerian coal and resultant post-combustion coal ash using scanning electron microscopy and gamma-ray spectroscopy. *Minerals*, 10 (2020) 241p.
3. **Ilemona C. Okeme**, Peter G. Martin, Thomas B. Scott. Characterisation of radioactive particles in coal fly ash using electron microscopy and synchrotron-based techniques. Accepted conference paper: *the European Nuclear Young Generation Forum (ENYGF), Tarragona, Spain, 2021.*

Journal/Conference Publications – In Preparation

1. **Ilemona C. Okeme**, Peter G. Martin, Christopher Jones, Rich A. Crane, William Mark Nash, Theophilus I. Ojonimi, Konstantin Ignatyev, Isaiah Ochala, Thomas B. Scott. Distribution and leaching behaviour of rare earth elements and toxic heavy metals in coal and coal fly ash. *Hydrometallurgy.*

Conference Presentations

1. **I.C. Okeme**, T.B. Scott and K.R. Hallam. Characterisation of radioactive particles in coal ash using electron microscopy and synchrotron-based techniques. Radiation Applications conference, Belgrade, Serbia. 16th - 19th September 2019.
2. **I.C. Okeme**, T.B. Scott and K.R. Hallam. Micro and bulk analysis of radioactive particles in coal and coal ash. Co-ordinating Group for Environmental Radioactivity conference, University of Bristol, UK. 24th - 26th April 2019.

Contents

List of figures

List of tables

Abbreviations

$Bqkg^{-1}$	Becquerel per kilogram
CCPs	Coal Combustion Products
CCS	Carbon Capture and Storage
EXAFS	Extended X-ray Absorption Fine Structure
FGD	Flue Gas Desulphurisation
g/cc	gram per cubic centimeter
$gkWh^{-1}$	gram per kilowatt hour
Gt	gigatonne
ha	hectare
HELE	High Efficiency Low Emission
HPGe	High-Purity Germanium
IAEA	International Atomic Energy Agency
ICP-MS	Inductively Coupled Plasma Mass Spectrometry
$mgkg^{-1}$	milligram per kilogram
Mt	megaton
MW	megawatt
MWe	megawatt electric
NIST	National Institute of Standards and Technology
NORM	Naturally Occurring Radioactive Material
OD	Odagbo
ODA	Odagbo Ash
ODC	Odagbo Coal

OECD	Organisation for Economic Co-operation and Development
OK	Okaba
OKA	Okaba Ash
OKC	Okaba Coal
OM	Omelewu
OMA	Omelewu Ash
OMC	Omelewu Coal
REE	Rare Earth Element
SCFA	Simulant Coal Fly Ash
sCMOS	scientific Complementary Metal-Oxide-Semiconductor
SEM-EDS	Scanning Electron Microscopy-Energy Dispersive Spectroscopy
TENORM	Technologically Enhanced Naturally Occurring Radioactive Material
UNSCEAR	United Nations Scientific Committee on the Effects of Atomic Radiation
USA	United States of America
XANES	X-ray Absorption Near Edge Spectroscopy
XAS	X-ray Absorption Spectroscopy
XRD	X-ray Diffraction
XRF	X-ray Fluorescence
Wt%	Weight percent

Chapter 1

Introduction

Rapid technological development and population growth over the past century has led to a global race for critical and strategic minerals and metals, vital for further economic and technological growth. These critical minerals and metals include (but are not limited to) titanium, germanium, nickel, tungsten, zirconium, lithium, cobalt and titanium, plus the 'in-demand' rare earth elements (REEs) [1]. Whilst REEs were not considered strategically important 20 or 30 years ago, the demand for REEs has grown exponentially over the past two decades due to their broad range of applications in advanced technologies [1].

REEs, referred to as the 'vitamins' of modern materials [2], consist of the fourteen naturally occurring and chemically similar lanthanides, plus yttrium and scandium [3]. Owing to their particularly unique and exceptional ductile, magnetic, conductive and optical properties, REEs are of vital industrial importance, with applications within the automotive, green technology, electronics and defence sectors [4,5]. As shown in Table 1.1, these elements, in their metallic, oxide or alloy forms, are used in the production of hybrid batteries and motors (both domestic and automotive), catalytic converters, strong permanent magnets (for use within wind turbine electrical generators), energy efficient fluorescent lamps, hard disk drives, smart phones, flat-screen televisions and computers, lasers, optical fibres, glass-polishing powders, etc. [5]. These elements came into the limelight when their respective prices skyrocketed more than ten-fold in the year 2010 owing to the major producer, China, slashing export quotas by 40% [6]. Due to the natural radioactive content (U, Th and their decay products) of

most REE minerals and the acidic and basic reagents required for REE extraction, the separation of one REE from another is typically considered to be environmentally polluting and expensive [7]. In China, it is estimated that the process of refining one tonne of REEs generates close to 75 m^3 of acidic waste water and 1 tonne of radioactive waste residue [8]; which, if poorly controlled/regulated, have cumulative environmental and epidemiological effects (such as cancers of the pancreas and lungs, and leukaemia).

Currently, over 75% of REE production, about half of the known reserves and the majority of REE metallurgical technologies occur, or are located in China [10,11]. While there is a projected surge in demand over the coming decades for use in high-tech devices, growing concerns over sustainability, supply stability, geopolitics and trade policies, processing technologies and resource weaponisation [5,12], have resulted in not only a near-total market monopoly by China but also instabilities in the global REE supply market. Arising out of such a combination of factors, there is now a renewed stimulus for countries to secure economically sustainable REE supplies through research and development efforts; focused on improving REE recoveries, recycling and alternate sources. Amongst these, there are a growing number of 'unconventional sources' of REE, such as coal and coal waste products (e.g. coal mine waste, coal fly ash, acid mine drainage and mine tailings).

Table 1.1: Selected uses of REEs. From [9].

Element	**Selected applications**
Scandium (Sc)	Super alloys, ultra-light aerospace components, X-ray tubes, baseball bats, lights, semiconductors
Yttrium (Y)	Ceramics, metal alloys, rechargeable batteries, television phosphors, high-temperature superconductors
Lanthanum (La)	Batteries, optical glass, camera lenses, petroleum refining catalysts
Cerium (Ce)	Catalysts, metal alloys, radiation shielding, water purifiers
Praseodymium (Pr)	Magnets, lasers, pigments, cryogenic refrigerants
Neodymium (Nd)	High-strength permanent magnets, lasers, infrared filters, hard disc drives
Samarium (Sm)	High-temperature magnets, nuclear reactor control rods and shielding, lasers, microwave filters
Europium (Eu)	Liquid crystal displays, fluorescent lighting, red and blue phosphors
Gadolinium (Gd)	Magnetic resonance imaging contrast agent, memory chips, nuclear reactor shielding, compact discs
Terbium (Tb)	Green phosphors, lasers, fluorescent lamps, optical computer memories
Dysprosium (Dy)	Permanent magnets, lasers, catalysts, nuclear reactor control rod
Holmium (Ho)	Lasers, neutron poison in nuclear reactors, catalysts, magnets
Erbium (Er)	Infrared lasers, vanadium alloys, infrared absorbing glasses, optical fibres
Thulium (Tm)	Portable X-ray machines, microwave ovens
Ytterbium (Yb)	Infrared lasers, chemical reducing agent, rechargeable batteries, fibre optics
Lutetium (Lu)	Positron emission tomography scan detectors, superconductors, high refractive index glass, X-ray phosphors

Coal fly ash, a fine by-product of the coal combustion process [13,14], has emerged in recent years as a highly-viable target for REE recovery [15]. Post combustion, micron-sized REE-bearing mineral particles (including monazite, xenotime and zircon) in the precursor coal become concentrated in the resultant ash; this is the result of the elimination of carbon during combustion, and the REE-bearing mineral particles possessing volatilisation temperatures considerably greater than those at which the coal is burnt [16]. Nonetheless, in most cases, the concentrations of REEs in these resources are several orders of magnitude lower than those of REE ores [17], making the extraction of REEs from these materials challenging and requiring the optimisation and/or development of extraction methods specifically targeted for REEs contained within coal fly ash. This is not to say that REE extraction from coal fly ash is always unviable.

The recovery of REEs from coal fly ash, rather than traditional REE-containing ores, has several notable advantages [15]. It is a cheap and readily-available post-combustion by-product enriched in inorganic REE minerals such as phosphates, (by a factor of six to ten relative to precursor coal) dependent upon the geological origin of the feedstock - a consequence of the phosphates' high melting, boiling and thermal decomposition temperatures [18-20]. Furthermore, coal fly ash does not require extensive excavation, unlike the mining of REE ores, which necessitates significant capital investment and yields significant environmental destruction; with REE mining generating large volumes of waste rock rich in radionuclides. In addition, coal fly ash is an inorganic fine powder, therefore, making it ideal for chemical processing through eliminating the need for costly and energy intensive crushing and grinding [21]. Lastly, REE recovery from coal fly ash greatly reduces the huge operating costs involved in the surveillance and maintenance of coal fly ash storage ponds - as the volume of coal fly ash wastes increases, so does the demand for new storage ponds and operating costs.

With billions of tonnes of coal fly ash already stored in repositories globally, and millions produced annually (especially in the USA, China, India, developing and underdeveloped countries), studies to underpin the optimisation and/or development of new methodologies of the existing and future REE extraction methodologies from this major untapped resource are hence urgently required. For example, following currently deteriorating USA-China trading activities that have been exacerbated in recent years, the USA Senate reintroduced the "REE Advanced Coal Technologies Act", initiating research into the characterisation of coal fly ash and the development of technologies capable of extracting REEs from coal and coal by-products [22]. The USA Department of Energy has consequently funded a number of research projects on the feasibility of rare earth recovery from coal and coal fly ash with focus on the characterisation of USA coal and coal fly ash materials, aimed at providing vital information for the development of custom recovery methods [23].

As formerly alluded to, an inherent issue that is associated with coal fly ash is the significantly-elevated level of naturally-occurring radioactive material (NORM), otherwise referred to as technologically-enhanced NORM (TENORM) [24]. These radio- and chemo-toxic NORMs (^{238}U and ^{232}Th, plus their decay products, alongside ^{40}K) occur as µm-sized particulates and constitute a commensurate human health and environmental hazard [25], making coal fly ash disposal a major global concern. Within radiation protection and radioecology studies on the human and environmental hazards associated with NORM have been largely associated with bulk radiological characteristics - traditionally based on average bulk specific activity concentrations of the radionuclides [26-29]. This does not account for inter particle heterogeneities, leading to significantly biased inventories and risk assessments [30]. The physical and chemical forms of NORM (at the micro- and nano-scales) are of utmost importance in establishing links between the source terms and the deposition, fate, transport,

bioavailability and health risks of these NORMs [31,32]. From the point of view of resource recovery, coal fly ash with significantly high concentrations of uranium (≥100 $mg.kg^{-1}$) could also serve as a cheap unconventional source of uranium, alongside REEs. For example, studies have shown that some coal mines across China are anomalously rich in uranium (Table 1.2), making coal fly ash materials from these 'uraniferous' coal mines viable sources of uranium accessible for recovery. Sparton Resources Inc., a Canadian company, after successfully producing yellowcake (U_3O_8) from a uranium-rich Chinese coal fly ash (averaging some 0.4 pounds (~180 g) of U_30_8 per tonne of ash) in 2007, signed an agreement with China, South Africa and six countries in Central Europe on a three-phase programme to test the viability and possible commercialisation of uranium extraction from waste coal ash [33].

Table 1.2: Range and mean concentrations of uranium and coal rank of uranium-rich coals in China. Modified from [34].

Coalfield / Province	**Range / Mean ($mgkg^{-1}$)**	**Coal rank**
Yanshan coalfield / Yunnan	167-167 / 167	Low volatile bituminous
Yanshan coalfield / Yunnan	111-178 / 153	Semi-anthracite
Guiding coalfield / Guizhou	192-264 / 229	High-to-low volatile bituminous
Guiding coalfield / Guizhou	67.9-288 / 200	Bituminous
Heshan coalfield / Guangxi	10.2-176 / 73.8	Low volatile bituminous
Heshan coalfield / Guangxi	12.0-326 / 69.0	Low volatile bituminous
Heshan coalfield / Guangxi	10.2-176 / 73.8	Low volatile bituminous
Sawabuqi Mine / Xinjiang	210-520 / 365	Lignite
Yili coalfield / Xinjiang	1.76-7207 / 320	High volatile bituminous coal
Yili coalfield / Xinjiang	6.89-724 / 147	Lignite

Advanced non-destructive characterisation studies on coal fly ash samples are extremely useful methods to derive unique information (at the micro- and sub-micro scale) on REEs and radionuclides, such as the most dominant REE-bearing phases in coal fly ash, element oxidation states, crystallographic structure alterations, speciation and distribution within REE and radioactive mineral particles. Such information is essential for the optimisation and/or development of methods for REE recovery from coal fly ash, environmental protection strategies and remediation for unplanned releases of coal fly ash [35,36].

1.1 The place of coal in the global energy mix

Despite the growing importance and drive towards low carbon energy sources (i.e. geothermal, wind and solar and nuclear energy [37]), and the falling reliance on coal by most of Organisation for Economic Co-operation and Development (OECD) member countries, coal remains a major, cheap and abundant energy source, mostly used for electricity generation (and steel manufacture) [37,38]. As shown in Figure 1.1, the share of coal in the global energy mix for the year 2018 stands at 27%, with coal also accounting for nearly 40% of the world's electricity generation [37]. Worldwide coal capacity increased annually between 2000 and 2019, and there are currently 80 countries using coal-fired electricity generating power plants, with over 13 more countries planning to build such facilities in the near-future [39]. Table 1.3 shows the top 10 global producers of coal and their consumption rank.

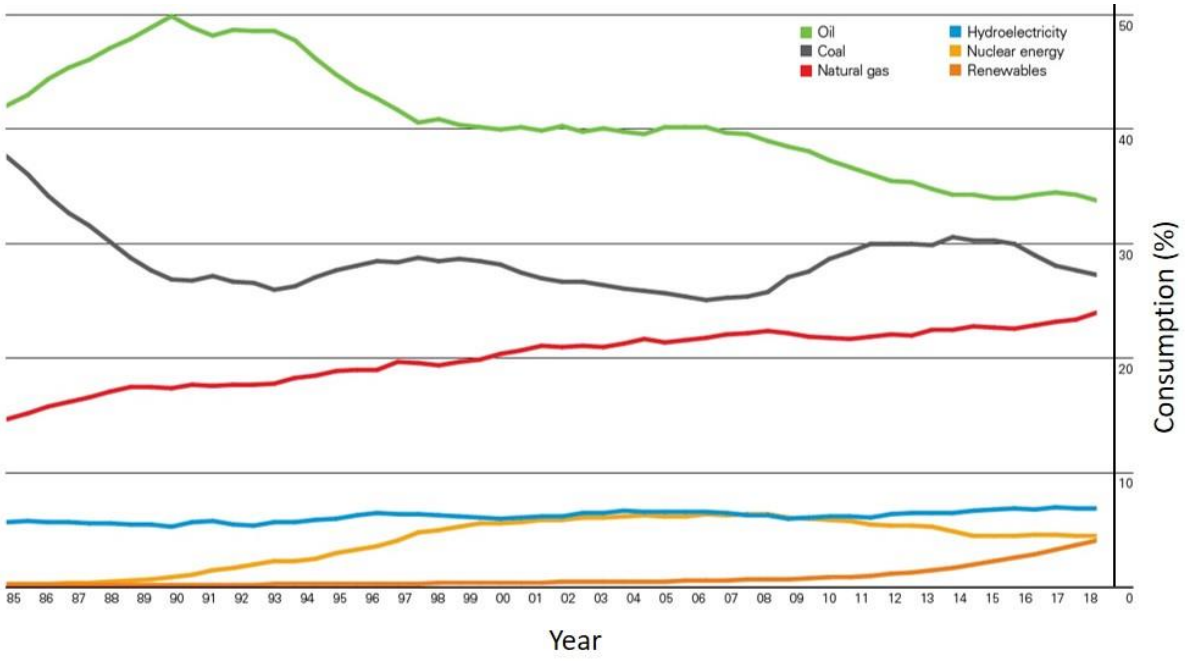

Figure 1.1: Shares of global primary energy consumption by fuel (%). Modified from [37].

Table 1.3: Top 10 coal producers and their coal consumption rank. From [40].

Country	**Coal production (million tonnes)**	**Coal consumption rank**
China	3,523.20	1
India	716.0	2
USA	702.3	3
Australia	481.3	10
Indonesia	461.0	12
Russia	411.2	5
South Africa	252.3	7
Germany	175.1	4
Poland	127.1	10
Kazakhstan	111.1	13

A rapidly growing global energy demand with increasing large-scale deployment of clean coal/decarbonisation technologies (high-efficiency low-emission (HELE) coal-fired power plant and carbon capture and storage (CCS) technologies) [41-43] could see continued use of coal for the foreseeable future by reducing emission of pollutants and CO_2. HELE coal-fired power plants (with operational thermal efficiencies between 40% and 45%) burn coal more efficiently [44], reducing global average carbon dioxide (CO_2) emissions by about 670 gkWh-1 [45]. HELE technologies have the further benefits of also significantly reducing emissions of pollutants (such as nitrogen oxides, sulphur dioxide and particulate matter), improving air quality and reducing pollutant-related health concerns globally [42]. CCS, which involves the capture, storage and/or recycling of CO_2 from fuel combustion or industrial processes, reduces CO_2 emissions by 90%, to less than 100 gkWh-1 [45]. Between 2017 and 2020, CCS gained further momentum through funding from governments and international organisations; currently, a total of 19 large-scale CCS facilities are in operation globally, an

additional 32 are at various advanced stages of development, with a further 39 pilot and demonstration scale CCS facilities on-going globally [43]. The integration of these decarbonisation technologies has been identified as key to meeting the 2015 Paris Agreement Energy and Climate goals of limiting future temperature increases to “well below 2°C” [46], while ensuring sustained affordable energy for economic development and poverty reduction [42]. Both HELE and CCS technologies are resultantly being deployed (on a large-scale) globally across America, Europe, Asia and also in parts of Africa [43,44]. But these technologies are more expensive and as yet have not received more than token interest in the developing world.

Despite climate pressures and international treaties promoting actions in energy reforms, many countries are still largely dependent on coal-fired power plants, with a significant number of new plants also in the pipeline (as shown in Table 1.4) – the majority of which are located predominantly across Asia and the developing countries, spurred on by funding arising from the Chinese national government [47,48]. Consequently, due to the continued global coal fly ash production (in addition to the billions of tonnes already present in surface impoundments across the globe), there is a pressing and urgent need for its beneficial utilisation and/or management. Achieving best possible value for this waste material or at least responsible management, should be an important goal for coal burning countries.

Table 1.4: Status of global coal-fired electricity-generating power plant distribution. From [49].

Status	Number of plants	Continent concentrated
Operational	6,549	Asia, America, Europe
Mothballed	73	Europe
Under construction	367	Asia
Permitted	215	Asia
Pre-permit	256	Asia, Europe, Africa
Announced	217	Asia, Europe, Africa
Shelved	475	Asia, Europe, Africa

1.2 Nigeria's electrical power challenges

Nigeria, with a population of about 200 million people [50], is the largest economy in sub-Saharan Africa – but physical limitations in the power generation and distribution sector constrain economic growth. Nigeria is fortunate to be endowed with large oil, gas, hydro, coal and solar resources, and the potential to generate 12,522 MW of electric power from its existing power plant infrastructure [51,52]. However, due to critical infrastructure and operational challenges in the transmission subsector, it currently generates only around 4,000 MWe, which is grossly insufficient for the nation's needs and below the national peak demand of about 26,000 MWe [53]. Currently, Nigeria generates its electricity only from gas-fired and hydroelectric power plants; with the country's first and only coal-fired power plant (Oji River station, built in 1956) now dilapidated and abandoned since 2004 [54].

To address this deficiency in the country's power output, the Nigerian government is at an advanced stage of planning to construct two coal-fired electricity-generating power plants (with capacities of 1,200 MWe and 2,400 MWe) in Itobe, Kogi State [55-58], to diversify

electricity generation. The project has almost completed financial close and execution of the construction agreement. These power stations are to be fed with coal from the native Okaba, Odagbo and Omelewu coal deposits (all in the 225,000 ha Kogi coal mining district) [59,60]. Currently, these coal deposits are commercially mined for coal briquette production and as an energy source for regional cement production [61,62].

Nigeria has known coal reserves of approximately 639 Mt, plus additional estimated reserves of approximately 2.75 Gt, with over eleven major coal deposits distributed across the northern, north central and eastern regions of the country [60,63]. This resource equates to a substantial amount of future electricity for Nigeria's national grid, but given the potential presence of REE at significant levels, they may also serve as a significant unconventional source of REE, but also a source of naturally occurring radioactive material (NORM).

1.3 Aims and objectives of the study

The primary aim of this study was to gain enhanced understanding of the distribution, speciation, crystallography and solid-state chemistry of REE and actinides in Nigerian simulant coal fly ash. This study has examined Nigerian coal and simulant coal fly ash as a country-specific case study from the perspective of resource recovery and environmental protection. The results obtained will be essential for underpinning a fundamental understanding of the optimisation and/or development of high-efficiency, environmentally friendly and cost-effective REE recovery methods requiring the use of less-aggressive dilute mineral acids (at lower temperatures and in less time) than conventional processes. A deeper understanding of the mineral form, species and structure of actinides in coal fly ash is also crucial for the development of cost-effective waste management and environmental protection methodologies. This study, which is not only valuable for the Nigerian government, is also

valuable for the global scientific community, through elucidating opportunities for more cost effective REE recovery from coal fly ash and subsequent waste management. The PhD has the following objectives:

- Perform bulk and micro characterisation of rare earth minerals and toxic heavy metals in simulant coal fly ash samples, thereby understanding the economic viability and the implications for REE extraction from coal fly ash.
- Determine mass concentrations and fractional distribution of REEs and toxic heavy metals present in coal ash.
- Perform economic valuation of REE content of simulant coal fly ash and the viability of their extraction.
- Determine the form, size and morphology of rare earth minerals present in simulant coal fly ash.
- Perform single REE particle lift-out from within bulk simulant coal fly ash using in-situ micro-manipulation, and analysis to determine the distribution, speciation, crystallography and solid-state chemistry of REEs in the lift-out particles.
- Perform bulk and micro characterisation of radioactive particles in simulant coal fly ash samples, thereby understanding the human and environmental impact of radionuclides released during coal burning.
- Determine activity concentrations and radiological parameters (absorbed dose; effective dose; radium equivalent) from ^{226}Ra and ^{228}Ra via their gamma (γ)-emitting radiogenic daughters.

- Generate isotopic ratio fingerprints (^{226}Ra:^{228}Ra) from the activity concentrations of ^{226}Ra and ^{228}Ra, to trace provenance in the case of a coal fly ash spill accident during transport or storage.
- Undertake single particle micro-manipulation and analysis to determine size, morphology, distribution and oxidation state of radionuclides in the particles.
- Evaluate the risks and benefits associated with the coal fly ash material once it is being produced 'at scale' by powerplant operation. This will include an evaluation of the human and environmental impact of the bulk simulant coal fly ash and the constituent 'heavy' microparticles observed.

1.4 Outline of the thesis

In addition to this introductory chapter, this thesis also contains the following:

Chapter 2: Literature Review

This chapter will review literature on the formation and characteristics of coal and coal types, alongside the generation, physical and chemical properties, management, environmental impact and beneficiation of coal combustion by-products. The geology, geochemistry, sources, mining and processing challenges of REE mineral ores, alongside NORM sources and exposure pathways are also reviewed. Finally, this chapter contains a review of the basics of nuclear decay and equilibrium, alongside a detailed review of previous studies on REEs and NORM in coal fly ash.

Chapter 3: Research Materials and Methods

The geologic setting of sampling sites, sampling protocol, analytical procedures and experimental methods used in this study to address the research objectives are herein presented. This chapter also provides a detailed outline of the procedures used for simulant coal fly ash generation. Lastly, the laboratory- and synchrotron-based characterisation techniques that were used during this study are presented.

Chapter 4: Elemental Composition and Mineralogical Analysis of simulant coal Fly Ash

Results of the lab-based X-ray fluorescence (XRF), powder X-ray diffraction (XRD) and scanning electron microscopy/energy dispersive spectroscopy (SEM-EDS) analysis of the bulk simulant coal fly ash are presented and discussed. The results of major and trace toxic metals,

major and micro REE and actinide mineral phases in simulant coal fly ash are discussed to understand their mode of occurrence and morphology, and implications on REE-bearing minerals beneficiation and REE recovery, recycling and the environment. These results enable the comparison between the simulant coal fly ash and coal fly ash derived from a typical coal-fired power plant.

Chapter 5: Bulk Characterisation of REEs and toxic heavy metals in Simulant coal Fly Ash

The results of acid digestion, sequential extraction and subsequent inductively-coupled plasma mass spectrometry (ICP-MS) analysis of simulant coal fly ash and coal samples are presented and discussed. The mass concentration of REEs and selected toxic heavy metals in the simulant coal fly ash samples, the associated phases and the implications for economic viability of REEs recovery and the environment are hence discussed. The results will also inform the best methods applicable to further preconcentrate the REE particles prior to any chemical (acid/alkali) extraction. The results are also compared to those reported in previous studies and significant findings are highlighted.

Chapter 6: Synchrotron speciation analysis of rare earth containing microparticles in Simulant Coal Fly Ash

In this chapter, in-situ lift-out procedure for individual REE-containing microparticles, alongside the results of analysis performed on the REE-containing microparticles using synchrotron based techniques (μ-XRF; micro-x-ray absorption near edge spectroscopy (μ-XANES); μ-XRD; μ-XRF tomography) are presented and findings discussed. These analyses are aimed at determining the speciation, distribution pattern, crystallography and solid-state

chemistry of REE mineral particles, which will deepen the present understanding of transformations of REE-bearing mineral particles during coal combustion, thereby informing the best beneficiation method(s) for REE minerals in coal fly ash and pave the way for the development or optimisation of existing extraction methods. The effect of ashing temperature on the structure of the rare earth mineral particles is also investigated and results presented.

Chapter 7: Bulk and particulate radiological analysis of coal and simulant coal fly ash

The results of gamma spectrometric analysis of coal and simulant coal fly ash samples are presented and discussed. The results of specific activity and radiological parameters (absorbed dose; effective dose; radium equivalent; excess lifetime cancer risk) determined for radium 226 (^{226}Ra) and radium 228 (^{2288}a) via their gamma-emitting radiogenic daughters are discussed from the perspective of human and environmental impact of coal fly ash waste management and its recycling within industrial uses. Isotopic ratio fingerprints from the activity concentrations of ^{226}Ra and ^{228}Ra are determined to trace their provenance in the case of a coal ash spill accident during the materials transportation or storage.

Also, in this chapter, the results of analysis performed on isolated individual radioactive microparticles using synchrotron-based techniques (μ-XRF and μ-XANES) are presented and discussed. These analyses are aimed at determining the distribution and chemical speciation of U in the radioactive microparticles. The evaluation of human and environmental impact of the radioactive particles observed is also performed.

Chapter 8: Final Conclusions and Future Work

The salient findings and conclusions of each results chapter, alongside implications for REE recovery from coal fly ash in repositories globally are summarised. The knowledge and experience acquired from this study are utilised to make appropriate recommendations for future work.

1.5 References

[1] British Geological Survey. Critical raw materials. https://www.bgs.ac.uk/mineralsuk/statistics/criticalRawMaterials.html (2017) (accessed 30 July 2020)

[2] Science History Institute. Industrial vitamins. https://www.sciencehistory.org/distillations/ (2016) (accessed 20 July 2020)

[3] British Geological Survey. Mineral profiles-Rare earth elements. https://www.bgs.ac.uk/mineralsuk/statistics/mineralProfiles.html (2011) (accessed 18 July 2019)

[4] Xiaoyue D, Graedel T. E. Global in-use stocks of the rare earth elements: A first estimate. Environmental Science and Technology, 45 (2011) 4096-4101.

[5] BBC. Are rare earth minerals China's trump card in its trade war with the US? https://www.bbc.com/news/amp/world-asia-48366074 (2019) (accessed 30 May 2019)

[6] Eggert R., Wadia C., Anderson C., Bauer D., Fields F., Meinert L., Taylor P. Rare earths: Market disruption, innovation, and global supply chains. Annual Review of Environment and Resources, 41 (2016) 199-222

[7] Ganguli R., Cook D. Rare earths: A review of the landscape. MRS Energy and Sustainability, 5 (2018)

[8] Massachusetts Institute of Technology. Environmental costs of refineries. http://web.mit.edu/12.000/www/m2016/finalwebsite/problems/refining.html (2016) (accessed 20 July 2020)

[9] United States Geological Survey. Potential uses of rare earth elements found in marine minerals. https://www.usgs.gov/media/images/potential-uses-rare-earth-elements-found-marine-minerals (accessed 20 July 2020)

[10] McLellan B., Corder G., Ali S. Sustainability of rare earths: An overview of the state of knowledge. Minerals, 3 (2013) 304-317

[11] United States Geological Survey. Mineral commodity summaries. https://www.usgs.gov/centers/nmic/mineral-commodity-summaries (2019) (accessed 2 July 2019)

[12] De Medeiros C. A., Trebat N. M. Transforming natural resources into industrial advantage: The case of China's rare earths industry. Brazilian Journal of Political Economy, 37 (2017) 504-526

[13] American Coal Ash Association. Fly ash. https://www.acaa-usa.org/aboutcoalash/whatareccps/flyash.aspx (2020) (accessed 10 April 2020)

[14] United States Environmental Protection Agency. Coal ash basics. https://www.epa.gov/coalash/coal-ash-basics (2020) (accessed 10 April 2020)

[15] Taggart R. K., Hower J. C., Dwyer G. S., Hsu-Kim H. Trends in the rare earth element content of U.S.-based coal combustion fly ashes. Environmental Science and Technology, 50 (2016) 5919-5926

[16] Stuckman M. Y., Lopano C. L., Granite E. J. Distribution and speciation of rare earth elements in coal combustion by-products via synchrotron microscopy and spectroscopy. International Journal of Coal Geology, 195 (2018) 125-138

[17] Huang Z., Fan M., Tian H. Coal and coal by products: A large and developable unconventional resource for critical materials – Rare earth elements. Journal of Rare Earths, 36 (2018) 337-338

[18] Mardon S. M., Hower J. C. Impact of coal properties on coal combustion by-product quality: examples from a Kentucky power plant. International Journal of Coal Geology, 59 (2004) 153-169

[19] Kolker A., Scott C., Hower J. C., Vazquez J. A., Lopano C. L., Dai S. Distribution of rare earth elements in coal combustion fly ash, determined by SHRIMP-RG ion microprobe. International Journal of Coal Geology, 184 (2017) 1-10

[20] Hower J. C., Dai S., Seredin V. V., Zhao L., Kostova I. J., Silva L. F. O., Mardon S. M., Gurdal G. A note on the occurrence of yttrium and rare earth elements in coal combustion products. Coal Combustion and Gasification Products, 5 (2013) 39-47

[21] Jordens A., Cheng Y. P., Waters K. E.. A review of the beneficiation of rare earth element bearing minerals. Minerals Engineering, 41 (2013) 97-114

[22] US Senate Committee on Energy and Natural Resources. Manchin, Capito & Murkowski reintroduce Rare Earth Element Advanced Coal Technologies Act. https://www.energy.senate.gov/public/index.cfm/democratic-news?ID=7CDC8217-FF79-41BD-B821-7CCC79019B2B (2019) (accessed 6 May 2019)

[23] National Energy Technology Laboratory. Feasibility of recovering rare earth elements from coal and fly ash. https://edx.netl.doe.gov/ree/ (accessed 25 July 2020)

[24] World Nuclear Association. Naturally Occurring Radioactive Materials (NORM). https://www.world-nuclear.org/information-library/safety-and-security/radiation-and-health/naturally-occurring-radioactive-materials-norm.aspx (2020) (accessed 10 April 2020)

[25] Kanazawa Y., Kamitani M. Rare earth minerals and resources in the world. Journal of Alloys and Compounds, 408-412 (2006) 1339-1343

[26] Isinkaye O. M., Jibiri N. N., Olomide A. A. Radiological health assessment of natural radioactivity in the vicinity of Obajana cement factory, North Central Nigeria. Journal of Medical Physics, 40 (2015) 52-59

[27] Santawamaitre, T., Malain, D., Al-Sulaiti H. A., Matthews M., Bradley D. A., Regan P. H. Study of natural radioactivity in riverbank soils along the Chao Phraya river basin in Thailand. Nuclear Instruments and Methods in Physics Research Section A, 652 (2011) 920-924

[28] Lauer N. E., Hower J. C., Hsu-Kim H., Taggart R. K, Vengosh A. Naturally occurring radioactive materials in coals and coal combustion residuals in the United States. Environmental Science and Technology, 49 (2015) 11227-11233

[29] Karangelos D. J., Petropoulos N. P., Anagnostakis M. J., Hinis E. P., Simopoulos S. E. Radiological characteristics and investigation of the radioactive equilibrium in the ashes produced in lignite-fired power plants. Journal of Environmental Radioactivity, 77 (2004) 233-246

[30] International Atomic Energy Agency. Radioactive particles in the environment: Sources, particle characteristics and analytical techniques. IAEA-TECDOC-1663 Vienna (2011), p. 2

[31] McGuire C., Dale P., Copplestone D., Wilson C., Tyler A. Characterising radium-226 particles from legacy contamination to support radiation dose assessments. Journal of Environmental Radioactivity, 212 (2020) 106-127

[32] Salbu B., Kashparov V., Lind O. C., Garcia-Tenorio R., Johansen M. P., Child D. P., Roos P., Sancho C. Challenges associated with the behaviour of radioactive particles in the environment. Journal of Environmental Radioactivity, 186 (2018) 101-115

[33] World Nuclear News. Sparton produces first yellowcake from Chinese coal ash. https://www.world-nuclear-news.org/explorationNuclearFuel/Sparton_produces_first_yellowcake_from_Chinese_coal_ash-161007.shtml (2007) (accessed 25 July 2020)

[34] Chen J., Chen P., Yao D., Huang W., Tang S., Wang K., Liu W., Hu Y., Zhang B., Sha J. Abundance, distribution, and modes of occurrence of uranium in Chinese coals. Minerals, 7 (2017)

[35] Cheisson T., Schelter E. J.. Rare earth elements: Mendeleev's bane, modern marvels. Science, 363 (2019) 489-493

[36] Salbu B., Skipperud L. Speciation of radionuclides in the environment. Journal of Environmental Radioactivity, 100 (2009) 281-282

[37] British Petroleum. Statistical review of world energy. https://www.bp.com/content/dam/bp/business-sites/en/global/corporate/pdfs/energy-economics/statistical-review/bp-stats-review-2019-full-report.pdf (2020) (accessed 27 March 2020)

[38] Franus W., Wiatros-Motyka, M.M., Wdowin M. Coal fly ash as a resource for rare earth elements. Environmental Science and Pollution Reserch, 22 (2015) 9464-9474

[39] CarbonBrief. Global coal power. https://www.carbonbrief.org/mapped-worlds-coal-power-plants (2020) (accessed 26 March 2020)

[40] World Atlas. The Top 10 Coal Producers Worldwide. https://www.worldatlas.com/articles/the-top-10-coal-producers-worldwide.html (2020) (accessed 26 April 2020)

[41] Drax Group. 5 projects proving carbon capture is a reality. https://www.drax.com/technology/5-projects-proving-carbon-capture-is-a-reality/ (2020) (accessed 26 March 2020)

[42] International Energy Agency Clean Coal Centre. Could high-efficiency, low-emissions (HELE) technology revive U.S. coal power? https://www.iea-coal.org/could-high-efficiency-low-emissions-hele-technology-revive-u-s-coal-power/ (2020) (accessed 26 March 2020)

[43] Global CCS Institute. Global status of CCS. https://www.globalccsinstitute.com/wp-content/uploads/2019/12/GCC_GLOBAL_STATUS_REPORT_2019.pdf (2019) (accessed 27 July 2020)

[44] World Coal Association. Explaining high efficiency low emissions coal. https://www.worldcoal.org/explaining-high-efficiency-low-emissions-coal (2016) (accessed 27 July 2020)

[45] International Energy Agency. Technology roadmap: High-efficiency, low-emissions coal-fired power generation. https://webstore.iea.org/download/direct/503 (2012) (accessed 27 July 2020)

[46] United Nations Framework Convention on Climate Change. Paris Agreement. https://unfccc.int/process-and-meetings/the-paris-agreement/the-paris-agreement, (accessed 27 July 2020)

[47] Shearer C., Myllyvirta L., Yu A., Aitken G., Mathew-Shah N., Dallos G., Nace T. Boom and bust 2020: Tracking the global coal plant pipeline. https://endcoal.org/wp-

content/uploads/2020/03/BoomAndBust_2020_English.pdf (2020) (accessed 27 March 2020)

[48] International Energy Agency. Coal 2019: Analysis and forecasts to 2024. https://www.iea.org/reports/coal-2019 (2020) (accessed 27 March 2020)

[49] End coal. Global coal plant tracker. https://endcoal.org/tracker/ (accessed 27 July 2020)

[50] The World Bank. Population-Nigeria. https://data.worldbank.org/indicator/SP.POP.TOTL?locations=NG (2018) (accessed 7 June 2020)

[51] USAID. Nigeria-power Africa fact sheet. https://www.usaid.gov/powerafrica/nigeria (2020) (accessed 28 March 2020)

[52] Nigerian Electricity Regulatory Commission. Transmission. https://nerc.gov.ng/index.php/home/nesi/404-transmission (2020) (accessed 28 March 2020)

[53] Daily Trust. Investigation: Despite 36 mining licences, 10,000MW coal for power capacity idle. https://www.dailytrust.com.ng/investigation-despite-36-mining-licences-10000mw-coal-for-power-capacity-idle.html (2019) (accessed 28 March 2020)

[54] Eziukwu, E. N. Nigerian coal power stations: Their future in the light of global warming. (Master's thesis, North-West University, South Africa). https://pdfs.semanticscholar.org/cb30/50fcbe95af53f38bd53006e9ee450774ad95.pdf (2008) (accessed 9 June 2020)

[55] GEM Wiki. Kogi Power Station. https://www.gem.wiki/Kogi_power_station., (accessed 5 June 2018)

[56] Energy Mix Report. Power China, Kogi partner on 3000Mw coal, hydro power projects. https://www.energymixreport.com/powerchina-kogi-partner-3000mw-coal-hydro-power-projects/ (2018) (accessed 29 March 2020)

[57] African Development Bank Group. Power transmission line for zuma coal-fired power plant: environmental and social impact assessment executive summary https://www.afdb.org/fileadmin/uploads/afdb/Documents/Environmental-and-Social-Assessments/Nigeria_%E2%80%93_Power_transmission_line_for_Zuma_coal-fired_power_plant_%E2%80%93_ESIA_Summary.pdf, (accessed 29 March 2020)

[58] Enviro News Nigeria. Nigeria committed to building coal-fired electricity by 2020, says minister. https://www.environewsnigeria.com/nigeria-committed-to-building-coal-fired-electricity-by-2020-says-minister/ (2019) (accessed 29 March 2020)

[59] Onoduku U. S. Geochemical evaluation of Okaba (Odagbo) coal deposit, Anambra Basin, Nigeria. Research Journal of Science & IT Management, 3 (2014)

[60] Ministry of Solid Minerals Development, Federal Republic of Nigeria. Feasibility study: Nigerian coal resource development. https://electricityinnigeria.com/sites/default/files/Nigeria%20Coal%20Feasibility%20Study%20-%20USTDA.pdf (2016) (accessed 18 March 2019)

[61] Energy Mix Report. ETA-ZUMA launches coal briquette production plant-Kogi state. www.energymixreport.com/eta-zuma-launches-coal-briquette-production-plant-kogi/ (2018) (accessed 7 June 2018)

[62] Alli F. Cement manufacturers cut power cost with investments in coal. www.vanguardngr.com/2017/11/cement-manufacturers-cut-power-cost-coal-investments/ (2017) (accessed 8 June 2018)

[63] International Energy Agency Clean Coal Centre. Nigeria: The magic of smokeless coal. https://www.iea-coal.org/nigeria-the-magic-of-smokeless-coal/ (2019) (accessed 30 March 2020).

Chapter 2

Literature Review

2.1 Coal and coal combustion by-products

2.1.1 Coal

Coal is a combustible, organic sedimentary rock predominantly made up of carbon, hydrogen and oxygen. It is formed from accumulated and preserved decaying organic debris (peat) typically of terrestrial or estuarine origin, buried in swampy wetlands; burial under anoxic conditions with subsequent lithification at tremendous pressure and temperature induce the transformation of the peat physically and chemically into coal over geologic time periods [1]. Most major coal measures were laid down several million years ago during the Carboniferous period (~360 – 300 million years ago), when land masses were located at paleolatitudes that constituted warmer and wetter environmental conditions compared to those of today [2]. Coal is found consolidated into strata/bands (i.e. coal seams of varying thickness) between other sedimentary rock strata, covering regions referred to as coal basins. The thickness and location of a coal seam and the spatial extent of a coal basin vary significantly and depend upon the amount of peat that was initially deposited [3]. The quality of a coal deposit is determined by the types of vegetation from which the coal originated, the depths of burial, the temperatures and pressures at those depths, and the length of time the coal has been forming in the deposit [4].

Coal types and uses

According to the degree of physical and chemical transformations of the original plant material, coal is typically classified into three major types: lignite coal; bituminous coal; anthracite. As these transformations progress over millions of years, the moisture content and volatile matter content decrease while the fixed carbon content and calorific value increases, as shown schematically in Figure 2.1.

When peat is buried at increasing depths, compaction and heating results in loss of water and volatiles, and increase in fixed carbon content. This transformation of peat first gives rise to lignite. Lignite is the lowest rank (or grade) of coal; being soft and brownish-black in composition - with the highest moisture and the lowest fixed carbon content of between 25% and 35% [5]. With continued burial, and progressively increasing pressure and temperature, this low-quality lignite is physically and chemically transformed into the sub-bituminous form of coal, bituminous coal and eventually, anthracitic coal, respectively - with increasing quality, carbon content and hardness (Figure 2.1). While sub-bituminous coal (the stage between lignite coal and bituminous coal) has a fixed carbon content of between 35% and 45%, bituminous and anthracite coals have fixed carbon contents of between 45% and 86% and 86% and 97%, respectively [5]. Generally anthracite is the most highly prized for burning, achieving the highest burns temperatures.

Coal is largely used for power generation, cement, iron and steel manufacture, as well as heating homes (Figure 2.1). Coal and coal by-products are also used in industries such as chemical and pharmaceutical; where in by-products, e.g. ammonia gas, tars, and residues produced when coal is heated, can be used in the manufacture of plastics and synthetic rubbers (such as rayon and nylon). Medicines (such as aspirin), solvents, ammonia salt, nitric

acid, fertilisers and chemicals (such as naphthalene, phenol and benzene) can also be produced from coal by-products [6]. Coal and coal by-products are also vital components in the production of specialist products, such as activated carbon, carbon fibre and silicon metal [3,6].

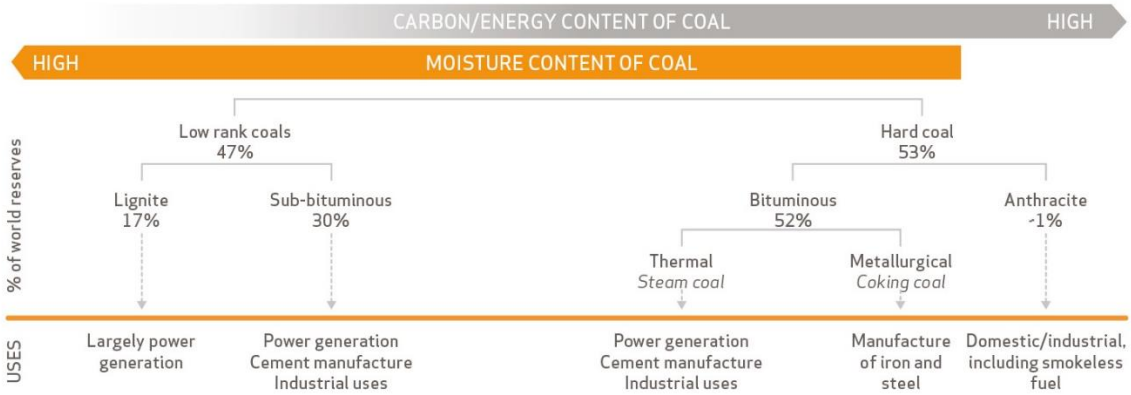

Figure 2.1: Types of coal and major uses. From [4].

Coal composition

Coal, being a heterogeneous material, is made up of both organic and inorganic constituents of various physical properties and chemical forms [1,3]. The inorganic constituents in coal are all elements excluding the main organic constituents (C, H, O, N and S) that exist in mineral form (referred to as mineral matter) and/or organically bound [7,8]. The concentrations of these elements vary non-uniformly within coal seams and between coalfields [9]; this variation in elemental concentrations depends on factors such as physical and chemical changes in sediment, depositional environment and geologic condition of the coal basin, type of source rock and intra-seam partings, and influence of marine water and hydrothermal fluids on organic matter [10-12].

Occurring mainly as discrete crystalline mineral particles and/or encapsulated within the coal organic matter [13], mineral matter in coal is of both intrinsic and extrinsic origin. While

intrinsic mineral matter (e.g. framboidal pyrite and marcasite) is formed in place (authigenic), extrinsic mineral matter (e.g. quartz and monazite) is ascribed to detrital sources, transported by water or wind as suspended particulates from catchments, deposited in the coal basin and subsequently incorporated into the coal during coal formation (coalification) [14,15].

Mineral matter in coal is classified into five components [7]:

(i) Clay minerals (aluminosilicates); mostly kaolinite ($Al_2Si_2O_5(OH)_4$), illite ($K_{1-1.5}Al_4(Si_{0.57}Al_{1-1.5}O_{20})(OH)_4$), montmorillonite $(Al,Mg)_2Si_4O_{10}(OH)_2$ and mixed illite-montmorillonites.

(ii) Carbonate minerals; mainly calcite ($CaCO_3$), siderite ($FeCO_3$), dolomite ($CaCO_3{\cdot}MgCO_3$) and other variously-mixed carbonates of Ca, Fe, Mg and Mn.

(iii) Sulphides and disulphides; mostly pyrite, FeS_2 (cubic), and markasite, FeS_2 (orthorhombic).

(iv) Silica; the majority of which occurs as quartz (SiO_2).

(v) Sulphates; mostly present as hydrated iron sulphates and mixed Na, K, Fe sulphates.

Table 2.1 shows the general species of minerals found in coal, and include quartz, pyrite, clays and carbonates [3]. Coals with high contents of mineral matter such as apatite ($Ca_5(PO_4)_3(F,Cl,OH)$), xenotime (YPO_4), monazite $(Ce,La,Nd,Th)PO_4$, rutile (TiO_2), zircon ($ZrSiO_4$) and uraninite (UO_2) are hence potential unconventional sources of REE and are therefore the subject of this study.

Table 2.1: Selected minerals identified in coals. Modified from [8].

Mineral group	Minerals
Sulphide	Pyrite**, marcasite**, galena*, sphalerite*, melnikovite*
Oxide	Quartz**, chalcedony*, haematite*, *cristobalite, uraninite, ilmenite, corundum, spinel, chromite, magnetite, hetaerolite, anatase, rutile, brookite, cassiterite, columbite*
Hydroxide	Limonite**, bauxite**, *goethite*
Silicate	Kaolinite***, illite**, sericite**, montmorillonite**, mixed-layer clay minerals**, dickite*, halloysite*, chlorite*, ferrihalloysite*, muscovite*, hydromuscovite*, feldspar*, zircon*, *leucite, zeolite, coffinite, allanite*
Carbonate	Calcite***, siderite***, dolomite**, ankerite**, *magnesite, rhodochrosite, aragonite*
Phosphate	Apatite*, phosphotite*, *xenotime, monazite, svanbergite, berlinite*
Sulphate	Barite*, gypsum*, *anhydrite*

*** - abundant; ** - common; * - rare; italics - seldom seen.

Despite the predominance of C, H and O as the primary components of the various ranks of coal, it is the inorganic constituents that together have the most economic, environmental and human health impacts. Information on the mode of occurrence and concentration of these elements in coal (and consequently, in the combustion by-products) is vital in the evaluation of the potential of coal and its by-products for resource recovery (rare earths and metallics) and the negative environmental and health impacts resulting from coal and coal by-products post-combustion [16].

Several elements in coal are known to be carcinogenic and/or toxic, causing oxidative deterioration of biological micro- and macro-molecules and are, therefore, dangerous to biological species (plants and animals) and the environment [17]. The United States of America National Research Council (NRC) [18], grouped these elements (occurring in trace amounts) into four main classes:

(i) Major concern: arsenic (As); boron (B); cadmium (Cd); lead (Pb); mercury (Hg);

molybdenum (Mo); selenium (Se).

(ii) Moderate concern: chromium (Cr); vanadium (V); copper (Cu); zinc (Zn); nickel (Ni); fluorine (F).

(iii) Minor concern: barium (Ba); strontium (Sr); sodium (Na); manganese (Mn); cobalt (Co); antimony (Sb); lithium (Li); chlorine (Cl); bromine (Br); germanium (Ge).

(iv) Radioactive elements: uranium (U); thorium (Th); their decay products; radium (Ra), polonium (Po) and radon (Rn).

Studies have shown that the toxic heavy metals (Cd, Pb, As and Cr) alongside the radioactive elements (U and Th, and their decay products), may be associated with both the mineral and organic matter fractions within coal [19]. Due to the removal of the organic matter fraction during the coal combustion process, these elements can become concentrated and partitioned into the coal combustion products (CCPs), such as fly ash and bottom ash.

2.2 General characteristics of coal combustion by-products

CCPs, also referred to as coal ash, are by-products of coal combustion process in coal-fired power plants [20]. Following combustion, the mineral (inorganic) matter (with radioactive and toxic trace elements) present in the precursor coal become oxidised and concentrated in the CCPs. CCPs therefore represent the bulk mineral matter remaining after carbon, oxygen, sulphur and water are driven-off during the combustion process [21]. The main mineral phases and major elements commonly found in CCPs, include; quartz (both amorphous and crystalline), mullite, aluminosilicates, haematite, magnetite, oxides of Ca, Mg, S and K [22,23]. The concentrations and modes of occurrence of these major elements and the toxic trace elements (such as As, Cd, Cr and Hg) in CCPs depend on the rank and composition of the

precursor coal, mode of occurrence of such elements in the precursor coal, physicochemical properties of the elements and combustion temperature [24].

Coal combustion by-products include fly ash, bottom ash, boiler slag, and flue gas desulphurisation gypsum [20,25]:

(i) **Fly ash** is the major component (more than 80%) of the waste material produced from the combustion of coal. It constitutes a very fine, powdery and glassy material composed mostly of silica, produced from the burning of finely pulverised coal in the plants furnace. The shape of fly ash particles depends on the type of coal plant, combustion temperature and minerals found in the precursor coal. Such fly ash consists of a range of spherical and irregularly shaped particles of different sizes; ranging from <1 μm to >200 μm, formed from the various physical and chemical reactions that occur during the coal combustion process. Owing to the cementitious and pozzolanic properties of fly ash, it has found widespread industrial use as a raw material in concrete and cement production [20].

(ii) **Bottom ash** is composed of agglomerated, coarse and angular ash particles, that are too large to be carried up into the smokestacks, and consequently falls to the bottom of the coal furnace. This is the most dense fraction of the mineral component of the coal.

(iii) **Boiler slag** is composed of molten bottom ash from slag tap and cyclone type furnaces that turns into pellets with a smooth glassy appearance after it is quenched with water. The common applications of bottom ash and boiler slag include filler material in asphalt and embankments and as raw materials in concrete products.

(iv) **Flue gas desulpurisation (FGD) material** results from the process of sulphur oxide removal from power plant flue gas streams to form gypsum ($CaSO_4$). During the FGD process, the flue gas is sprayed with limestone ($CaCO_3$) which reacts with the sulphur oxide to produce gypsum, which is subsequently captured using an electrostatic precipitator. The applications of gypsum include use as raw material within plasterboard, filler material for structural applications, soil amendment and in cement and concrete products [20].

Out of the millions of tonnes of CCPs generated annually around the world (as detailed in Figure 2.2), only about 30% is recycled into the aforementioned products and materials, with the remainder held in ash ponds or alternatively disposed of in landfill sites [26].

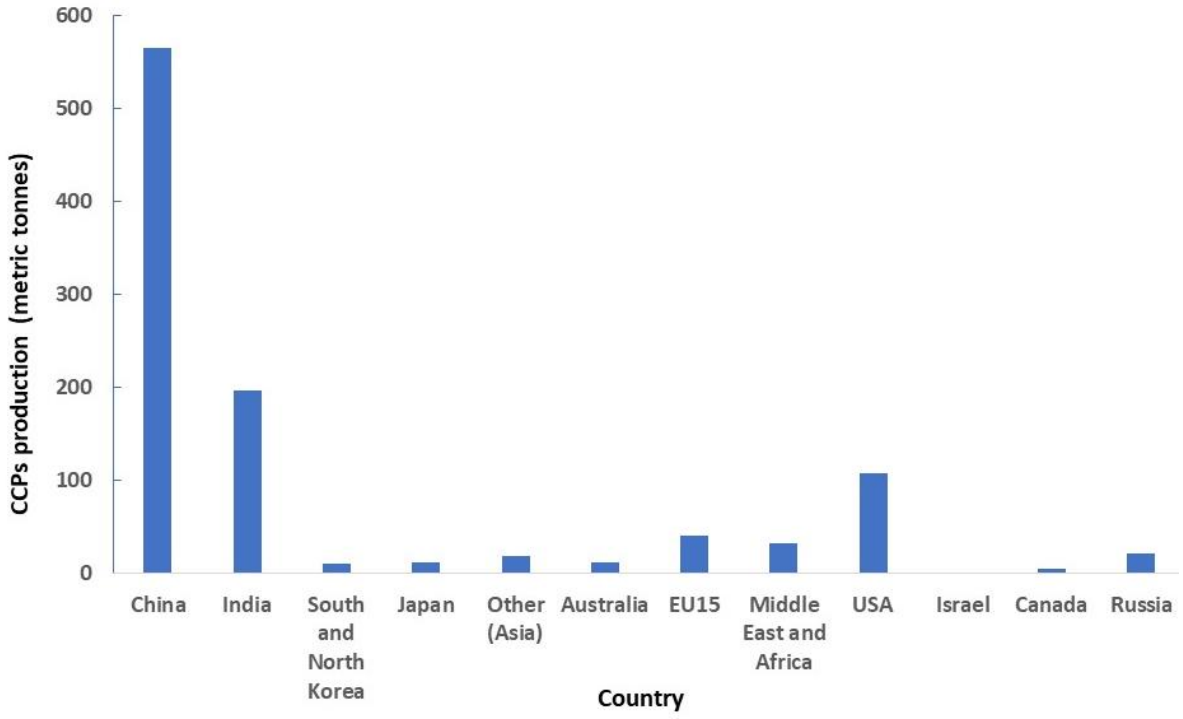

Figure 2.2: 2016 annual production of CCPs in selected countries. Modified from [27].

Figure 2.3 presents a simplified schematic of the operation of a coal-fired thermal power plant and, consequently, how CCPs are generated. All coal-fired thermal plants deliver the simplistic

transfer of energy; the chemical energy held within the coal is transformed into thermal energy during combustion, with the thermal energy further turned into mechanical energy by the heating of water into steam - using the pressure of the steam to spin a turbine, and transform the mechanical energy into electrical energy for distribution. To generate electricity from coal in a coal-fired thermal plant, lumps of mined coal are delivered to the plant site. These lumps of coal are delivered by a conveyor belt to the crusher/pulveriser for size-reduction into fine dust (~75 μm) before being introduced into the furnace to increase combustion efficiency [28]. This pulverised coal is mixed with air and injected into the boiler/furnace, where it is then combusted at temperatures between 800°C and 1,700°C, depending on the type of coal plant and coal rank [28]. To produce steam, millions of litres of purified and demineralised water are pumped under pressure through tubes inside the boiler; with the intense heat from the burning coal transforming the water in the boiler tubes into steam, which consequently spins the turbine blades to generate electricity. The combustion process produces flue gas composed of O_2, N_2, CO_2, oxides of sulphur and nitrogen, as well as fly ash, bottom ash, boiler slag and flue gas desulphurisation gypsum (produced during the process of sulphur oxide removal from flue gas using a limestone slurry). While the heavy and coarse bottom ash falls to the bottom of the furnace, the light fly ash suspended in the flue gas is removed using the electrostatic precipitator. CCPs are usually collected and stored in dry or wet form in repositories called ash ponds – engineered surface impoundments, lined with low permeability barriers (e.g. clays or geopolymer liners).

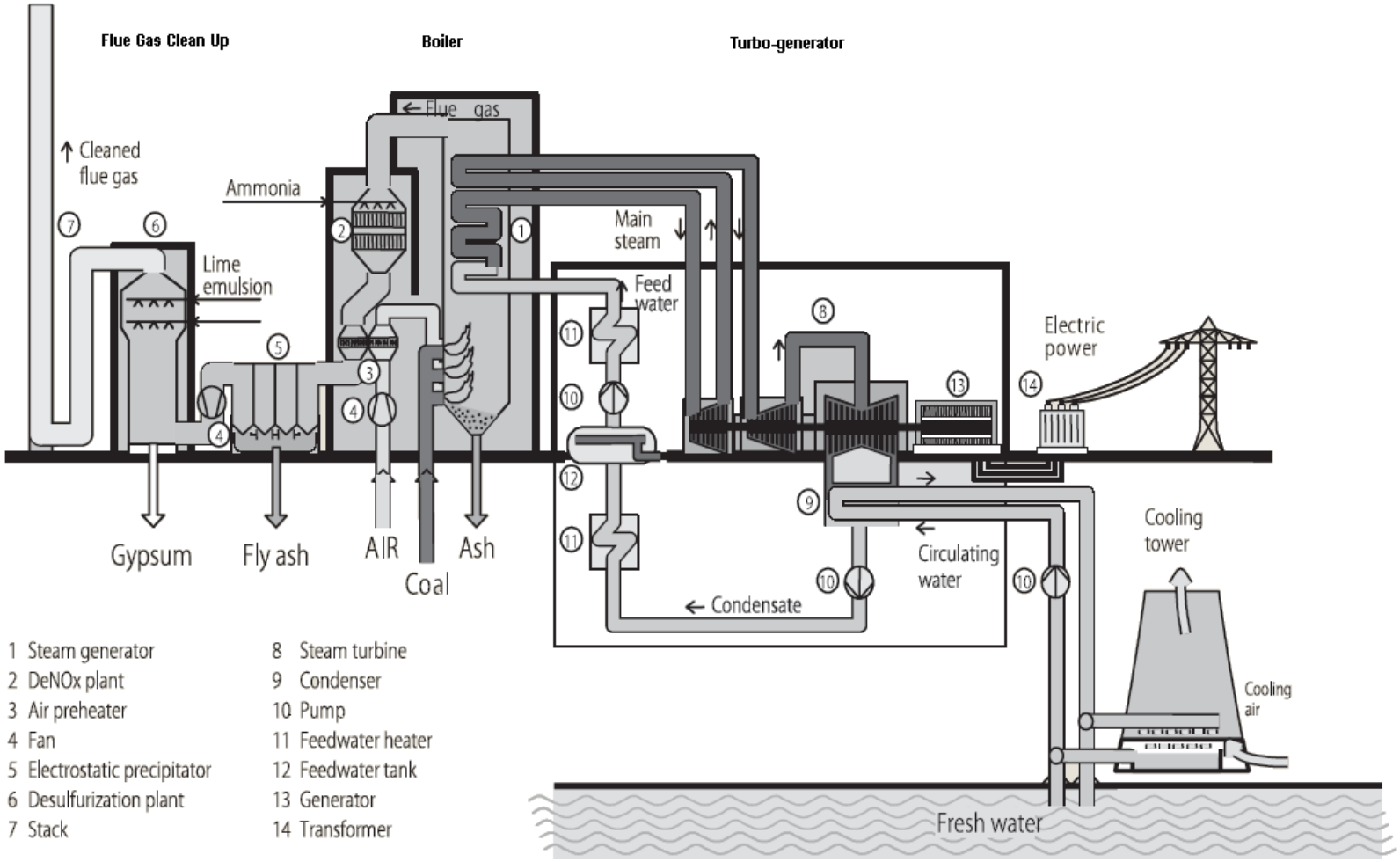

Figure 2.3: A schematic diagram of the operation of a coal-fired power plant [29].

2.2.1 Partitioning of trace elements in CCPs

During combustion of coal, the non-volatilised trace elements become partitioned into the CCP fractions. The degree of partitioning of the trace elements between the bottom ash and fly ash depends primarily on their geochemical association, volatility, coal combustion temperature and fly ash particle size [7,30]. Based on these factors, the classification as shown in Figure 2.4 follows. **Group 1 elements** (often associated with the mineral matter) are the least volatile and are concentrated in the coarse residues, such as the bottom ash, although they may be equally distributed between bottom ash and fly ash as discrete micro mineral particles [31,32]. **Group 2 elements** are predominantly concentrated within the very fine fly ash particulate, compared with the coarser bottom ash. These elements volatilise during combustion and then become adsorbed on the surfaces of fine particles [31]. The most volatile elements (Cd, Zn, Se, As, Sb, W, Mo, Ga, Pb, V) exhibit the highest particle size dependence. Dependent on particle size is due to the greater surface-area-to-volume ratio of the fine particles [33,34]. **Group 3 elements** (including Cl, Hg and Se) are the most volatile, but show little-to-no tendency to condense from the vapour phase and are almost exclusively emitted from the plants smokestack into the air [35,36].

CCPs and their associated chemo- and radio-toxic elements, such as Cd, As, Cr, Pb, U and Th (and their decay products, such as Ra and Rn), pose potentially serious environmental and human health hazards. The toxic, metal-laden micro-particles, that constitute the CCPs can pose a hazard to humans or animals when (re)suspended and inhaled, to be deposited in the lungs, resulting in internal exposure and potentially leading to respiratory illnesses such as lungs cancer [17]. Indirectly, the leaching of these toxic elements by water during disposal or utilisation in different environmental conditions could contaminate water bodies and damage

aquatic animals and plants [37,38]. When exposed to acid rain during storage or disposal, coal fly ash becomes highly acidic, consequently leading to increased leaching rate of its radionuclide and toxic heavy metal contents; drinking water polluted with toxic metals and radionuclides at concentrations above specified safety limit can equally be dangerous for humans and animals, causing chronic health issues, including kidney failure, nerve damage and even cancer [17]. Shown in Figure 2.5 is a source-pathway-receptor diagram for radionuclides and toxic heavy metals transfer from coal fly ash to humans.

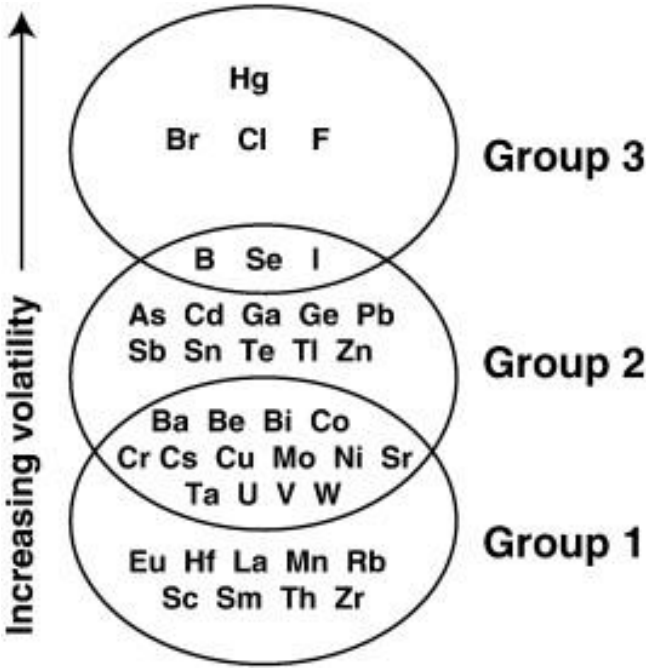

Figure 2.4: Classification of trace elements by their volatilisation behaviour during the combustion process [31].

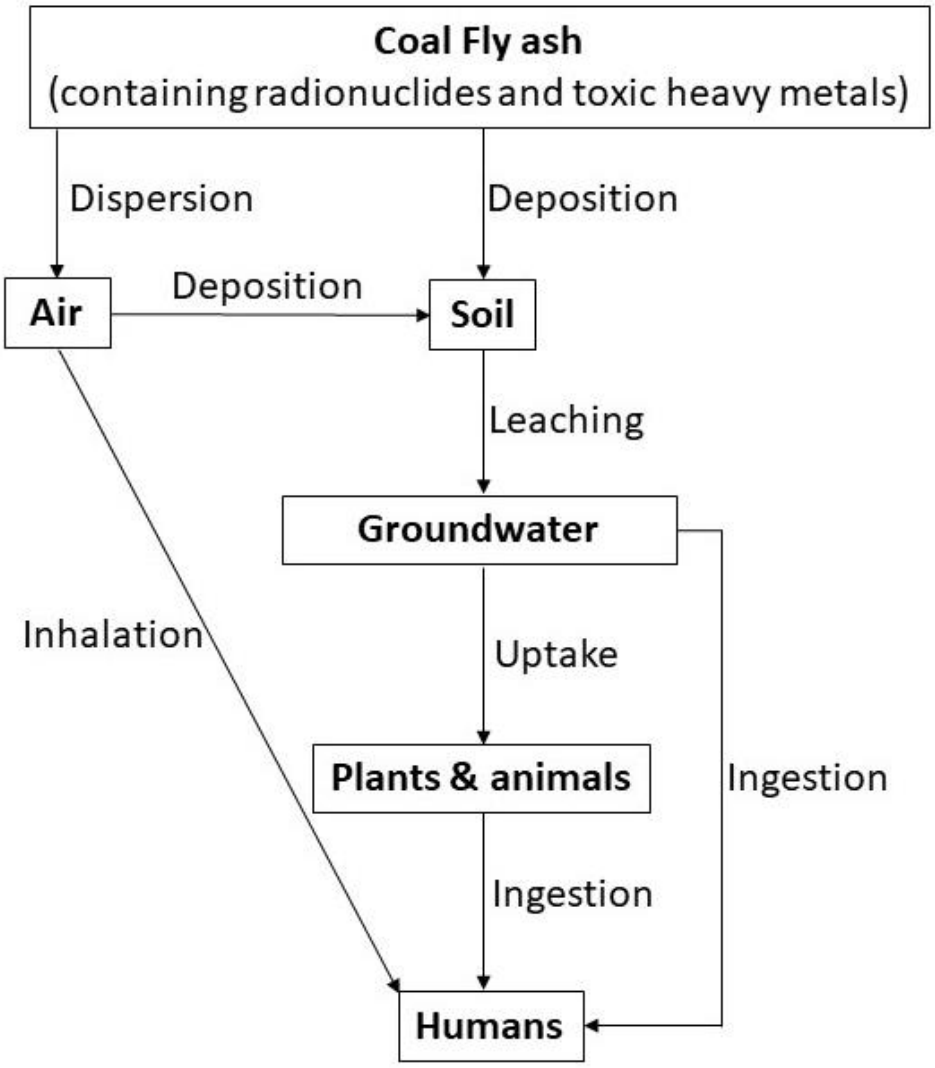

Figure 2.5: Source-pathway-receptor diagram for radionuclides and heavy metals transfer from coal fly ash to humans.

2.3 Rare earth elements

REE consist of a series of chemically-similar elements; the fourteen naturally occurring lanthanides, plus Y and Sc (Table 2.2) [39]. The lanthanides are the series of elements with atomic numbers 57 through 71, all of which, except promethium, occur in nature. Based on their electronic configurations, these elements are further subdivided into the light REE (LREE) (La to Gd) and the heavy REE (HREE) (Tb to Lu, plus Sc and Y) [40]. Owing to their unique

chemical and physical properties, REE are of fundamental industrial importance, with applications including automobiles, green energy, electronics and defence [41,42]; the production of fighter jets, hypersonic missiles, electric cars, satellites, smartphones, lasers and radiation-hardened electronics is dependent on this group of elements [42].

Despite the discovery of REE between 1787 and 1941, it was not until the 1960s that large-scale production of purified rare earths supported identification of newer properties and uses in a variety of important commercial applications [43]. Between 1965 and 1980, the Mountain Pass mine in California (USA) generated most of the global supply of REE. However, in the late 1990s the operation filed for bankruptcy due to its inability to finance compliance with stricter environmental protection laws concerning radioactive, toxic heavy metals as well as acidic mine tailings and processing wastes. Also, the matter was compounded by cheaper imports arising from China [44]. From the mid-1980's to 2010, mines in China progressively supplied a greater share of the global demand due to availability of cheap labour and lack of stringent environmental regulations [45]. Currently, more than 75% of REE production and nearly half of the known reserves (Table 2.3), alongside the majority of REE metallurgical refining and separations, occur (or are located) in China [42].

Table 2.2: Selected properties of REE. Modified from [39,46,47].

Element	**Symbol**	**Atomic number**	**Atomic weight**	**Density ($g.cm^{-3}$)**	**Melting point (°C)**	**Upper Continental Crust abundance ($mg.kg^{-1}$)**
Scandium	Sc	21	44.95	2.989	1541	13.6
Yttrium	Y	39	88.90	4.469	1522	22
Lanthanum	La	57	138.90	6.146	918	30
Cerium	Ce	58	140.11	8.160	798	64
Praseodymium	Pr	59	140.90	6.773	931	7.1
Neodymium	Nd	60	144.24	7.008	1021	26
Promethium	Pm	61	145.00	7.264	1042	N/A
Samarium	Sm	62	150.36	7.520	1074	4.5
Europium	Eu	63	151.96	5.244	822	0.88
Gadolinium	Gd	64	157.25	7.901	1313	3.8
Terbium	Tb	65	158.92	8.230	1356	0.64
Dysprosium	Dy	66	162.50	8.551	1412	3.5
Holmium	Ho	67	164.93	8.795	1474	0.8
Erbium	Er	68	167.26	9.066	1529	2.3
Thulium	Tm	69	168.93	9.321	1545	0.33
Ytterbium	Yb	70	173.04	6.966	819	2.2
Lutetium	Lu	71	174.97	9.841	1663	0.32

Table 2.3: Rare earth element global production and estimated reserves (tonnes) [48].

Country	Mine production		Reserves
	2018	2019	
United States	18,000	26,000	1,400,000
Australia	21,000	21,000	3,300,000
Brazil	1,100	1,000	22,000,000
Burma (Myanmar)	19,00	22,000	Not applicable
Burundi	630	600	Not applicable
Canada	—	—	830,000
China	120,000	132,000	44,000,000
Greenland	—	—	1,500,000
India	2,900	3,000	6,900,000
Madagascar	2,000	2,000	Not applicable
Russia	2,700	2,700	12,000,000
South Africa	—	—	790,000
Tanzania	—	—	890,000
Thailand	1,000	1,800	Not applicable
Vietnam	920	900	22,000,000
Other countries	60	—	310,000
World total (rounded)	190,000	210,000	120,000,000

Chemically, all REE are found in +3 oxidation state in natural surface environments with decreasing atomic radii across the series [43]. Some of the REEs also occur in the +2 and +4 states, with this being of considerable importance in rare earth extraction and separations, as REEs in +2 and +4 states can be easily extracted from the other REEs [49]. The unusual and steady decrease in the ionic radii with increasing atomic number among the lanthanides (termed “lanthanide contraction”) is due to the imperfect shielding of one 4f-electron by another in the same sub-shell, as the 4f shell is filled [43]. This imbues REE with unique and

useful chemical and physical properties, such as their magnetic and/or optical properties [50]. The chemical similarities of REE means that they occur interchangeably in geologic deposits and behave as a single chemical entity, making it difficult and time-consuming to separate them from their ores and from one another [43]. Their use in final products is, therefore, dependent upon their efficient extraction and separation from the host minerals [51,52].

2.4 REE minerals and deposits

The rare earths are moderately-abundant elements in the Earth's crust that occur in many minerals [39]. However, REE (excluding the radioactive promethium, which never occurs naturally) are rarely found in easily-exploitable high-grade deposits; when compared against their total average crustal abundance (typically 160 $mg.kg^{-1}$ to 205 $mg.kg^{-1}$ [53]), their mass fraction within minerals and ores is relatively low [39]. The relative abundance of REE varies considerably; this is due to the Oddo-Harkins effect which states that REE with even atomic numbers have greater abundance than their odd-numbered neighbours.

There are over 200 known minerals containing significant quantities of REE (most abundant detailed in Table 2.4); with these minerals typically occurring as carbonates, oxides, phosphates and silicides. Even though there are many rare earth minerals, only bastnaesite ($[Ce,La]CO_3F$), monazite ($[Ce,La,Nd,Th]PO_4$), xenotime (YPO_4) and ion-adsorption clays are mined commercially for REE production [54,55]. Monazite and bastnaesite are typically exploited for LREE minerals, and xenotime and ion-adsorption clays for the HREE [54,55]. These REE minerals are common accessory minerals of uranium and thorium deposits (with varying concentrations), and are, therefore, invariably radioactive, constituting a commensurate human health and environmental hazard [55]. Globally, the economic or potentially economic REE deposits occur primarily in the following geologic settings [50]:

(i) Carbonatites.

(ii) Peralkaline igneous systems.

(iii) Magmatic magnetite-haematite bodies.

(iv) Iron oxide-copper-gold deposits.

(v) Xenotime-monazite accumulations in mafic gneiss.

(vi) Ion-absorption clay deposits.

(vii) Monazite-xenotime-bearing placer deposits.

The world's largest rare earth deposits, Bayan Obo in China and Mountain Pass in the USA, are both examples of carbonatite deposits [50]. Rare earth minerals in most of the deposits, however, are such that they can be recovered only as co-products or by-products of other minerals; an example is the Bayan Obo iron-REE-niobium deposit [50].

Table 2.4: Selected rare earth minerals. Modified from [39,51].

Mineral	**Formula**	**Approximate rare earth oxide (wt%)**
Aeschyniye-(Ce)	$(Ce,Ca,Fe,Th)(Ti,Nb,)_2(O,OH)_6$	32
Allanite-(Ce)	$(Ce,Ca,Y)_2(Al,Fe^{3+})_3(SiO_4)_3OH$	38
Apatite	$Ca_5(PO_4)_3(F,Cl,OH)$	19
Bastnasite-(Ce)	$(Ce,La,)(CO_3)F$	75
Branerrite	$(U,Ca,Y,Ce)(Ti,Fe)_2O_6$	9
Euxenite-(Y)	$Y.Ca.Ce,U,Th)(Nb,Ta,Ti)_2O_6$	24
Fergusonite-(Ce)	$(Ce,La,Nd)NbO_4$	53
Gadolinite-(Ce)	$(Ce,La,Nd,Y)_2Fe^{2+}Be_2SiO_2O_{10}$	60
Loparite	$(Ce,La,Na,Ca,Sr)(Ti,Nb)O_3$	30
Monazite-(Ce)	$(Ce,La,Nd,Th)PO_4$	65
Parisite-(Ce)	$Ca(Ce,La)_2(CO_3)_3F_2$	61
Xenotime	YPO_4	61
Zircon	$(Zr,REE)SiO_4$	<5

2.5 Coal fly ash as an unconventional source of REE

Increasing demand for REE, alongside growing concerns over sustainability as well as resource "weaponization" and monopolisation by China [51,33], have together resulted in a renewed interest in fly ash (among other unconventional sources such as acid mine drainage and mine tailings) in recent years as a highly-viable target for REE recovery [22]. Post-combustion, µm-sized REE-bearing mineral particles (mostly monazite, xenotime and zircon) in the precursor coal are concentrated in the resultant fly ash; this is a result of the elimination of carbon during combustion – with the REE-bearing mineral particles possessing volatilisation temperatures considerably greater than those at which the coal is burnt remaining [56]. For evaluation of coals and fly ash as REE raw materials, REE are divided into critical (Nd, Eu, Tb, Dy, Y, Er), uncritical (La, Pr, Sm, Gd) and excessive (Ce, Ho, Tm, Yb, Lu) groups [57]. This classification is based on the Kingsnorth forecasts of the relationship between demand and supply of individual REE in recent years in relation to the extensive application of REEs, China's monopoly of rare earth reserves and production and rare earth production and operation planning outside China [58]. The average REE content of world coals is estimated to be 68.5 $mg.kg^{-1}$, about 2.5 times lower than that in the lithologies of the upper continental crust, with the average REE content of the world's fly ashes (404 $mg.kg^{-1}$) approximately three times higher than that in the Upper Continental Crust. Such concentrations, therefore, make some fly ash economically viable for REE recovery [57].

The recovery of REE from fly ash, rather than traditional REE-containing ores, has several notable advantages [22]. Firstly, fly ash is a cheap and readily-available post-combustion by-product (or waste) enriched in inorganic REE minerals, such as phosphates, by a factor of six to ten relative to the precursor coal, depending on the geological origin of the feedstock - a

consequence of the phosphates' high melting, boiling and thermal decomposition temperatures [59,60]. Certain coals and fly ash have elevated concentrations of HREE - which are most limited in supply, rank high in criticality and price, and are projected to further increase in demand through the century - making them potentially lucrative targets for REE recovery, despite their low composite REE concentrations [22,51,52,54]. Furthermore, fly ash does not require extensive excavation, unlike the mining of REE containing ores, which requires significant capital investment and often results in considerable environmental disruption – with REE mining generating large volumes of waste rock that is enriched in radionuclides. In addition, coal fly ash is an inorganic fine powder, therefore making it ideal for chemical processing due to its very high surface area, therefore eliminating the need for costly and energy-intensive crushing and grinding [61]. Finally, REE recovery from fly ash greatly reduces the substantial operating costs involved in the surveillance and maintenance of fly ash storage ponds - as the volume of fly ash wastes increases, so does the demand for new storage ponds and operational/disposal costs. Hence, reduction of the waste volume and/or reducing its chemical reactivity for leaching and acid water generation is highly desirable.

Nonetheless, in most cases the concentrations of REE in these resources are several orders of magnitude lower than those of REE ores [62], making the extraction of REE from these alternative source materials difficult to justify unless at high concentrations. Other challenges common to and associated with recovery of REE from fly ash, rich or low in REE content, is the development of customised, environmentally friendly and financially advantageous extraction technologies/methods. These extraction technologies are directly dependent on the types of REE-bearing minerals and physicochemical transformations of the material post-combustion), and radionuclide and toxic heavy metal content of the bulk fly ash [63,64].

Radionuclides and heavy metals in fly ash present a great environmental toll for extracting and separating out rare earths, as these elements are highly-regulated, increasing the cost of production and waste disposal in most countries (where industry is well regulated).

Though promising, none of the laboratory-scale methods developed or studied for REE extraction from fly ash are yet to be proven as economically viable for commercialisation due to having limited efficiency and/or the high costs involved [63-71]. Just as in conventional REE recovery from ores, REE recovery from fly ash involves a series of beneficiation steps (to further concentrate REE minerals) followed by total acid dissolution/treatment at high temperature to break the strong chemical bonds in the structure of REE minerals [52,55,72]. These processes are costly as they require large amounts of energy and quantities of acids/reagents. Therefore, further research into the physicochemical and crystallographic transformations of REE-bearing mineral phases in fly ash during coal combustion is vital for understanding the processing properties of each REE-bearing mineral in fly ash. This would inform the best way to cost-effectively tune the cracking and leaching conditions to attack the matrix of the mineral assemblage in an environmentally friendly process.

Previous independent and government-funded studies in recent years have demonstrated the occurrence and distribution of REE in coal deposits and their respective residual ash [22,56-59,62,73,74]. Seredin et al [74] used inductively-coupled plasma mass spectrometry (ICP-MS) to characterise coal samples from Russia's Pavlovka deposit and found REE concentrations up to 1290 $mg.kg^{-1}$, with REE in the resulting ash having a mass fraction (wt%) of 1%. Two further ICP-MS studies of ash samples from a power plant burning coal from the Kentucky Fire Clay bed (a lithology rich in volcanic ash) observed REE contents of 1200 to 1670 $mg.kg^{-1}$ [33,75]. Recent surveys published by the United States Department of Energy

indicated total REE contents (not including Sc) of 41 to 1286 $mg.kg^{-1}$ in U.S. fly ash [22,56]. Additional studies on fly ash using scanning electron microscopy (SEM) coupled with energy dispersive (X-ray) spectroscopy (EDS), have shown the main REE-bearing phases retained in fly ash to be phosphate minerals (monazite and xenotime), zircon ($ZrSiO_4$), bastnaesite, Ce-Nd-bearing carbonates and organically-associated lanthanides [59,60,62]. These studies reported REE-bearing minerals occurring both as discrete particles and encapsulated in glassy fly ash material.

Mengling et al [76], applied synchrotron techniques of micro-x-ray fluorescence (μ-XRF) and micro-x-ray absorption near edge structure (μ-XANES) to bulk fly ash samples, using Ce as a proxy for LREE; the results revealed the mixed oxidation state of Ce (with Ce(III) being the dominant species present) and co-location amongst the LREE. However, the results suffered interference from elements in the surrounding bulk sample. Currently, other synchrotron radiation techniques, e.g. μ-XRF tomography and micro-x-ray diffraction (μ-XRD), which could reveal structural and crystallographic transformations within REE-bearing mineral particles in fly ash, vital for the optimisation and/or development of recovery method, have not yet been exploited in previous studies on REE-bearing minerals in fly ash.

Therefore, studies employing such enhanced synchrotron radiation techniques and in addition, micro-manipulation methods (for particle lift-out prior to analysis) represent a powerful means to derive unique and high quality information on REE. Information on REE such as oxidation state (at the micron scale), distribution within REE minerals and alterations to crystallographic structure, is vital for combined elucidation of geochemical and thermal changes in REE minerals within residual fly ash following combustion of precursor coal.

2.6 Radioactivity and radioactive decay

The stability of the nucleus of an atom is determined by the ratio of neutrons to protons and by the atomic mass number (A) [77]. For light nuclei (atomic number ≤ 20), the ideal stability condition is a neutron:proton ratio that equals or is slightly greater than one; for heavy nuclei (atomic number ≥ 83), the ideal stability condition is a ratio of 1.5:1 [78]. Departure from these ratios results in nuclear instability. Unstable nuclei seek stability by undergoing intra-nuclear transformations which shift the neutron:proton ratio towards a more stable configuration [78].

Radioactivity is the spontaneous transformation of unstable atomic nuclei (termed "parent nuclei") into more stable configurations (referred to as "daughter" nuclei) [79]. This process is independent of the effects of physical and chemical conditions [80], with the energy associated with the transformation of one (unstable) nucleus into another (stable) nucleus released via the emission of nuclear particles and/or electromagnetic radiation such as alpha and beta particles, and gamma radiation [81].

The activity of a radioactive source otherwise called the intensity of the radioactivity, is the number of disintegrations per second in unit of Becquerel, Bq [82]. The probability per unit time for the decay of a given nucleus is a constant termed the decay constant, λ. The rate of radioactive decay in relation to the activity (A) can be expressed by the fundamental law of radioactive decay:

$$\mathbf{A} = \frac{-dN}{dt} = \lambda \mathbf{N} \qquad (2.1)$$

where A is the activity of an isotropic source, equal to the number, dN, of radioactive nuclei decaying in a given time, dt, and proportional to the number, N, of radioactive nuclei present

at time, t. The value λ is termed the decay constant, with the negative sign indicating that the number of radioactive nuclei decreases with increasing time.

The solution of Equation 2.1 results to the exponential laws of radioactive decay, expressed as:

$$\boldsymbol{N_t = N_0 e^{-\lambda t}} \tag{2.2a}$$

$$\boldsymbol{A_t = A_0 e^{-\lambda t}} \tag{2.2b}$$

where N_0 is the initial number of nuclei present at time t = 0 and A_0 is the activity at time t= 0. The number of nuclei, (N_t) decreases exponentially with time (t).

The rate of radioactive decay can be characterised in terms of a specific time frame, known as the half-life. The half-life ($t_{\frac{1}{2}}$) is the time required for one-half of a certain number of active nuclei to disintegrate. The decay constant relates to the half-life via [83]:

$$\boldsymbol{\lambda = \frac{0.693}{T_{\frac{1}{2}}}} \tag{2.3}$$

The decay constant is also expressed in terms of the mean lifetime, τ, defined as the average time a radioactive nucleus is likely to survive before it decays. The expression between the decay constant and the mean lifetime is:

$$\boldsymbol{\tau = \frac{1}{\lambda}} \tag{2.4}$$

Hence, the mean lifetime can be written in terms of the half-life:

$$\boldsymbol{\tau = \frac{t_{\frac{1}{2}}}{0.693}} \tag{2.5}$$

The half-life and mean lifetime for radionuclides can range from fractions of seconds to billions of years [84].

In some cases, the decay of an unstable nucleus occurs via several modes; this type of disintegration is termed 'branching' and the relative probability of the modes of decay can be defined by the branching ratios [84]. For example, ^{40}K decays either to ^{40}Ar (12%) via electron capture and positron emission, or to ^{40}Ca (88%) by emission of a negative beta particle.

2.7 Radioactive decay processes

The simplest radioactive decay is one were a radioactive parent nuclide decays (with a distinctive decay constant) to a stable daughter nuclide. One example is the decay of ^{40}K. However, another common decay series can take place when the decay of a parent radionuclide leads to the formation of an unstable daughter product. Thus, a series (or chain) of radioactive decays (termed "radioactive series") results until a stable nuclide is eventually reached [83]. Examples are the ^{238}U and ^{232}Th decay series (Figure 2.6, section 2.10.1).

For chains of radioactive decay, there are two main limiting conditions[79]:

(i) Secular equilibrium.

(ii) Transient equilibrium.

2.8 Radioactive equilibrium

'Radioactive equilibrium' is the term used to describe the state when the members of the radioactive series decay at the same rate as they are produced [85]. The two predominant cases of the state of equilibrium can be explained as below.

2.8.1 Secular equilibrium

Secular equilibrium is a steady-state condition in which the half-life of the parent is very much greater than that of the daughter, such that there is very slow decay of the parent over the time interval of interest. When secular equilibrium is established (usually within seven daughter half-lives), the activity of the daughter becomes equal to that of its parent with time, and the formation rate and the decay rate of every radioactive daughter ($\lambda_D N_D$) equals the decay rate of its parent ($\lambda_P N_P$):

$$\boldsymbol{\lambda_P N_P = \lambda_D N_D} \tag{2.6}$$

where λ_P and N_P represent the decay constant and number of nuclei of the parent while λ_D and N_D represent the decay constant and number of nuclei of the daughter. Secular equilibrium can be disturbed when one of the intermediary daughters escapes from the system (e.g. sample container where its parents are confined – such as radon gas escaping from a soil sample within a container).

2.8.2 Transient equilibrium

Transient equilibrium is a state which the parent half-life is longer-lived than that of the daughter, but not significantly longer, with the concentration of parent nuclei significantly decreasing with time. In transient equilibrium, the parent nuclide decays and the daughter nuclide builds up, but both nuclide concentrations decrease as the concentration of parent nuclei decreases. The transient equilibrium equation is given as:

$$\frac{\boldsymbol{N_D}}{\boldsymbol{N_p}} = \frac{\boldsymbol{\lambda \mathrm{p}}}{\boldsymbol{\lambda_D - \lambda \mathrm{p}}} \tag{2.7}$$

Since $\lambda \mathrm{p}$ is not negligible for intransient equilibrium, the activity of the daughter is not equal

to that of the parent and the term $\frac{\lambda p}{\lambda_D - \lambda p}$ in Equation 2.7 becomes greater than unity. The time at which equilibrium between the parent and daughter nuclides will be established depends on the magnitudes of their half-lives; the shorter the half-life of the daughter compared with the parent, then the faster the state of equilibrium will be reached [86].

2.9 Types of radioactive decay

Excess energy arising from the transformation of unstable nuclei into more stable configurations (or other radioactive species with lower mass – such as neutrons, antineutrinos) results in the emission of nuclear radiation. The three main kinds of radiation given off by radioactive substances are alpha, beta and gamma.

2.9.1 Alpha decay

Alpha particles are made up of two protons and two neutrons, represented by the nucleus of the He-4 isotope (^4_2He), symbolised α. During radioactive decay, many heavy unstable nuclei - both naturally-occurring radionuclides of atomic number >82 and artificially-produced transuranic elements (Z > 92), emit alpha particles as decay products. The decay of heavy nuclei favours alpha particles emission rather than other light particles given that alphas have a very stable structure; therefore, a large positive 'Q-value' energy - the characteristic energy liberated in the radioactive decay, can be released. Emission of alpha particle from a nucleus leads to reduction in both atomic number (Z) by two units, and mass number (A) by four units, on the resultant nucleus:

$$\mathbf{^A_ZX \rightarrow {}^{A-4}_{Z-2}X + {}^4_2He + Q} \quad (2.8)$$

Alpha particles are slightly deflected by magnetic and electric fields, and have very low

penetrating power, but high ionising potential. They can hence be stopped by paper. In general, the energy ranges of alpha particles emitted from radioactive decay are between 1 MeV and 10.5 MeV [86].

2.9.2 Beta decay

A beta particle (β) originates from an unstable nucleus rich in neutrons and protons. The beta particle is a fundamental charged particle with the same mass as an electron. Beta decay processes can occur by the emission of negative or positive beta particles, or by the competing process of (inner atomic) electron capture. Beta decay process changes the atomic number (Z) of a nucleus by one unit, while mass number (A) remains constant.

$$\begin{aligned} &{}_{Z+1}^{A}X \rightarrow {}_{Z}^{A}Y + e^{-} + \bar{\upsilon} && \textbf{(}\beta^{-}\textbf{ decay)} \\ &{}_{Z-1}^{A}X \rightarrow {}_{Z}^{A}Y + e^{+} + \nu && \textbf{(}\beta^{+}\textbf{ decay)} \\ &e^{-} + {}_{Z}^{A}X \rightarrow {}_{Z-1}^{A}Y + \nu && \textbf{(electron capture)} \end{aligned} \qquad (2.9)$$

2.9.3 Gamma decay

Gamma radiation (or photon) is electromagnetic and has no electrical charge and has the highest energy on the electromagnetic spectrum. The origin of gamma-rays can be correlated with decays from nuclear excited states which may have been populated following alpha and/or beta decay processes. The excited nuclei can release some of its energy via the transition to a lower and more-stable energy state by means of gamma-ray emission, with the atomic number and mass number of the nuclide resulting from the decay process remaining unchanged. Typically, gamma-ray energies span a range of 0.1 MeV to 10 MeV; gamma-rays can be stopped by lead blocks or thick concrete walls.

2.10 Environmental sources of radioactivity

Humans are exposed to environmental ionising radiation from several sources. The sources of radioactivity in the environment can be classified into two main categories [87]:

(i) Natural.

(ii) Anthropogenic.

2.10.1 Natural sources

Naturally occurring radioactive material (NORM) which gives rise to radiation exposure for human surroundings is comprised of isotopes which occur individually (^{40}K) or which are components of the three main radioactive decay series (^{238}U, ^{235}U, ^{232}Th). These radionuclides can be categorised into two types: primordial and cosmogenic, in relation to their origin.

Primordial radionuclides

The radionuclides which are of terrestrial origin and have been on Earth since its formation are known as primordial radionuclides. These radionuclides have very long decay half-lives, comparable to the age of the earth. They are ubiquitous in the Earth's crust and are, consequently, assumed to represent a primordial inventory. Examples of primordial radionuclides are ^{238}U, ^{232}Th and their decay products (Figure 2.6), alongside ^{40}K. Industries known to have primordial NORM issues include coal (mining, combustion), oil and gas (production), mineral sands (rare earth minerals, titanium, zirconium) and fertilisers (phosphate); due to further concentration of NORM during such industrial processes, the term technologically enhanced NORM (TENORM) is also used [88].

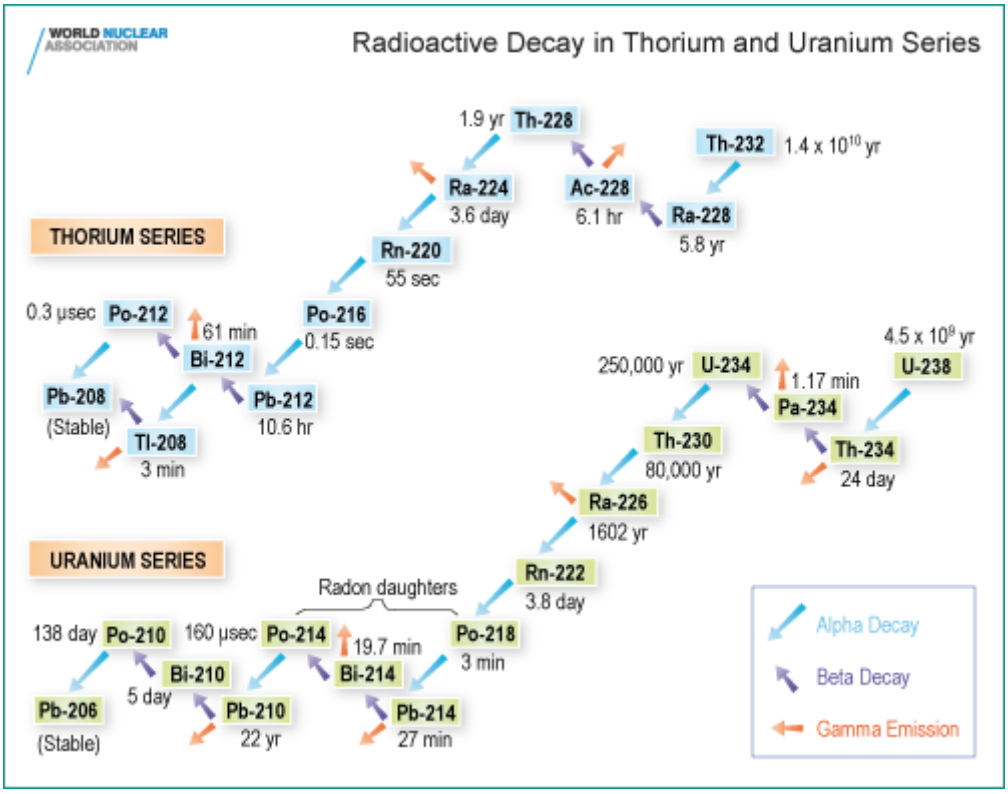

Figure 2.6: Radioactive decay in Th and U series [88].

Cosmogenic radionuclides

Most of the important cosmogenic radionuclides are generated continuously by the interaction of high energy nucleons (released from cosmic radiation) with target nuclei (such as Ar, O and N gases) in the Earth's upper atmosphere. These interactions lead to a variety of spallation or neutron capture reactions. Spallation and charge exchange result in lighter or the same mass radionuclides being created compared with the target atom. By contrast, neutron capture products are radionuclides which are one mass unit heavier than the original stable 'target' nuclide.

A large number of cosmic-ray-produced radionuclides exist, with such cosmogenic radionuclides possessing half-lives ranging from minutes to millions of years; however, only four are responsible for a significant measurable dose of radiation to humans. From a

radiation health aspect, the main cosmogenic radionuclides are tritium (^{3}H), beryllium-7 (^{7}Be), carbon-14 (^{14}C) and sodium-22 (^{22}Na). The most significant cosmogenic radionuclide is ^{14}C – a beta emitter, which can be taken up by plants and enter the food chain, becoming a source internal radiation exposure to humans.

2.10.2 Anthropogenic sources

Detectable quantities of man-made radionuclides are widely distributed in the atmosphere, particularly as a result of nuclear weapons testing (the biggest source) and nuclear reactor accidents (e.g Chernobyl (1986) and Fukushima (2011)). A significant radionuclide produced from nuclear reactor accidents is ^{137}Cs, with a half-life of 30.7 years. This nuclide has been globally-dispersed and deposited through rain and dry deposition on terrestrial surfaces. It can be taken up by plants and, subsequently, be incorporated into foodstuffs. However, the environmental levels of released radionuclides are slowly declining. Other sources (e.g. ^{131}I) may be released from nuclear power fuel reprocessing (such as at the Sellafield reprocessing plant).

2.11 NORM in coal and CCPs

Naturally occurring radionuclide concentrations in coal and associated CCPs can occur at levels well above typical background levels albeit dependent upon the origin of the precursor coal. In some deposits the content of NORM is sufficient to raise potential human health and environmental impact concerns [89]. This can result from potential prolonged external and internal exposure to gamma and alpha radiation emitted by these radioactive and chemo-toxic species (U, Th, Ra and their associated decay products). These exposures result from the release of coal dust and coal ash into the environment due to emissions from mines

and smoke stacks, direct disposal to landfills, discharges into rivers, and through their use as raw material in the construction of residential dwellings [89,90]. The NORM commonly found in coal consists of primordial ^{238}U and ^{232}Th alongside their decay products, in addition to a component of ^{40}K [89]. This, in addition to uranium minerals of detrital origin, is due to coal measures, when deeply buried under layers of other strata, serving as "traps" for circulating hydrothermal fluids [91,92]. Coal horizons provide chemically reducing zones (that is, negative redox potential, E_h) and hence, act as excellent redox filters for groundwaters carrying metals and uranium. As a result of thorium oxide being highly insoluble, thorium rarely circulates through the natural environment.

The modes of occurrence, distribution and concentration of radionuclides in coal vary significantly across regions and coal fields due to factors including geologic conditions of a coal basin, organic matter, type of source rocks/intra-seam non-coal partings and influence of marine water and hydrothermal fluids [91,93]. This resultantly determines the degree of concentration of these radionuclides in the associated coal-derived ash. Fly ash contains elevated levels of TENORM, compared to the feed coal [89], as a result of:

(i) The elimination of carbon during combustion.

(ii) The radionuclide-bearing minerals (uraninite, monazite, xenotime, zircon) possessing volatilisation temperatures considerably greater than that at which the coal is burnt.

One study has shown that radionuclide concentrations are strongly coal rank dependent, with the concentration being highest in low-rank deposits such as lignite and sub-bituminous coals [89]; this is due to the low rank coals having higher organic matter content – effective at adsorbing NORMs and other metals during coalification. Additional studies have also shown

that typical NORM concentrations in coal ash range from three to ten times the concentration in the precursor coal [89,94,95].

Within radiation protection and radioecology, studies on the human and environmental hazards associated with NORM have largely been through bulk radiological characteristics, traditionally based on average bulk specific activity concentrations of the radionuclides determined using gamma spectroscopy [89,94,96,97]. This, however, does not account for inter-particle heterogeneities, leading to significantly biased inventories and risk assessments [98]. The physical and chemical forms of NORM (at the micro- and nano-scales) are of utmost importance in establishing links between the source terms and the deposition, fate, transport, bioavailability and health risks [99,100]. To capture the fate, transport and health risks associated with these radionuclides which are functions of their mode of occurrence, distribution, species, particle size and morphology [101], there exists the need to complement these techniques (e.g. ICP-MS, and gamma-ray spectroscopy) with sub-micron spatial resolution microanalytical techniques, such as SEM-EDS and synchrotron radiation techniques (e.g. μ-XRF, μ-XANES, μ-XRF tomography and μ-XRD).

Several studies on U, Th and their decay products in coal and CCPs using gamma spectroscopy have been carried out [89,95,102-107]; however, studies on Nigerian coal and coal fly ash using SEM-EDS and synchrotron techniques are lacking. Arbuzov et al [92], in their study on the modes of occurrence of uranium and thorium in coals, peats (and ash) of Northern Asia (using SEM-EDS), reported uranium and thorium as being associated with both the organic and mineral matter (with particle size range of 1.5 μm to 3 μm). A similar study by Parzentny et al [108] reported uranium and thorium to be concentrated in simple phosphates (monazite) and Al-Si glass, as well as in the magnetic and non-magnetic fractions of the fly ash.

Previous studies have determined the mode of occurrence and valences of selected trace elements in coal and ash via μ-XANES [109,110]. However, few studies have focused on U μ-XANES speciation analysis in coal fly ash. Sun et al [111], in their study on U speciation in raw (untreated) coal fly ash as well as coal fly ash treated with ferrous solution ($FeSO_4$), reported that while uranium existed in mixed oxidation states of +5 and +6 in the untreated coal fly ash, it existed largely (~90%) in the +4 state in the treated ash, an indication of the resultant uranium reduction, by Fe^{2+}, in the ferrous solution. Both μ-XRD and μ-XRF tomography, which provide vital information on crystallographic structure and radionuclide distribution within a particle, have not previously been used for the study of NORM in fly ash. This thesis will seek to address these gaps in the experimental literature.

2.12 Summary

Coal is composed of both organic and inorganic (mineral) components; following combustion, the inorganic mineral component (made up of radionuclides, REEs and toxic heavy metals) become concentrated in the CCPs. The concentrations of REEs, radionuclides and toxic heavy metals in coal fly ash vary according to the rank and composition of the precursor coal and mode of occurrence of such elements in the precursor coal. Although a promising unconventional source of REEs, coal fly ash is also potentially detrimental to the environment due to its radionuclide and toxic heavy metal contents. Analytical techniques such as ICP-MS, gamma-ray spectroscopy, SEM-EDS and synchrotron radiation μ-XRF, μ-XANES, μ-XRF tomography and μ-XRD provide vital information about the forms of occurrence, physicochemical properties, concentration, distribution and chemical speciation of these elements. This information is vital for the recovery of the REEs, understanding of the human and environmental hazards associated with the radionuclides and toxic heavy metals, and inform the best way to manage coal fly ash waste. In the next chapter, these analytical techniques are presented and discussed.

2.13 References

[1] Dee E., Chris K. Geoscience: understanding geological processes. London: Hodder and Stoughton (1999).

[2] Cunningham, B.W., Woodworth, B.S. Environmental science: a global concern (6th edition). New York: McGraw-Hill (2001).

[3] British Geological Survey. Coal. https://www.bgs.ac.uk/downloads/start.cfm?id=1404 (2010) (accessed 17 August 2020).

[4] World Coal Association. Coal. https://www.worldcoal.org/coal (2020) (accessed 19 August 2020).

[5] U.S. Energy Information Administration. Coal explained. https://www.eia.gov/energyexplained/coal/ (2019) (accessed 19 August 2020).

[6] World Coal Association. Uses of coal. https://www.worldcoal.org/coal/uses-coal (2020) (accessed 19 August 2020).

[7] Rađenović A. Inorganic constituents in coal. Chemistry in Industry: Journal of Chemists and Chemical Engineers, 55 (2006) 65-71.

[8] Xiuyi T. Mineral matter in coal; In Coal, Oil Shale, Natural Bitumen, Heavy Oil and Peat, Volume 1. Eolss Publishers (2009) 166-177.

[9] Gurdal G. Abundances and modes of occurrence of trace elements in the Can coals (Miocene) Canakkale-Turkey. International Journal of Coal Geology, 87 (2011) 157-173.

[10] Belkin H.E., Tewalt S.J., Hower J.C., Stucker J.D., O'Keefe J.M.K. (2009). Geochemistry and petrology of selected coal samples from Sumatra, Kalimantan, Sulawesi, and Papua, Indonesia. International Journal of Coal Geology, 77 (2009) 260-268.

[11] Dai S., Ren D., Chou C.L., Finkelman R.B., Seredin VV, Zhou Y. Geochemistry of trace elements in Chinese coals: a review of abundances, genetic types, impacts on human health, and industrial utilization. International Journal of Coal Geology, 94 (2012) 3-21.

[12] Hower J.C., Ruppert L.F., Eble C. F. Lateral variation in geochemistry, petrology, and palynology in the Elswick coal bed, Pike County, Kentucky. International Journal of Coal Geology, 69 (2007) 165-178.

[13] Dai S., Hower J.C., Finkelman R.B., Graham I.T., French D., Ward C. R., Eskenazy G., Wei Q., Zhao L. Organic associations of non-mineral elements in coal: a review. International Journal of Coal Geology, 218 (2020) 103347.

[14] Juniper L., Schumacher G. Advances in pulverized fuel technology: understanding coal comminution, combustion and ash deposition. The Coal Handbook: Towards Cleaner Production, Woodhead Publishing (2013) 312-352.

[15] Britannica. Coal types. https://www.britannica.com/science/coal-fossil-fuel/Coal-types (2020) (accessed 23 August 2020).

[16] Renton J.J. Mineral matter in coal. Coal Structure. New York: Academic Press (1982) 283-326.

[17] Jaishankar M., Tseten T., Anbalagan N., Mathew B.B., Beeregowda K.N. Toxicity, mechanism and health effects of some heavy metals. Interdisciplinary Toxicology, 7 (2014) 60-72.

[18] Coal Trading Blog. Significance of trace elements in coal: an overview. http://bestcoaltrading.blogspot.com/2011/11/significance-of-trace-elements-in-coal.html (2011) (accessed 24 August 2020).

[19] Querol X., Fernandez T.J.L., Lopez S.A. Trace elements in coal and their behavior during combustion in a large station. Fuel, 74 (1995) 331-343.

[20] World Coal Association. Coal combustion products. https://www.worldcoal.org/coal/uses-coal/coal-combustion-products (2020) (accessed 25 August 2020).

[21] Muthu R.D.K., Anand R. Production of biofuel from biomass downdraft gasification and its applications. Advanced Biofuels. Cambridge: Elsevier (2019) 129-151.

[22] National Energy Technology Laboratory, U.S. Department of Energy. Characterization of Rare Earth Element Minerals in Coal Utilization By-products.

https://edx.netl.doe.gov/dataset/characterization-of-rare-earth-element-minerals-in-coal-utilization-byproducts (2017) (accessed 8 May 2019).

[23] Vassilev S.V., Menendez R., Alvarez D., Diaz-Somoano M., Martinez-Tarazona M.R. Phase-mineral and chemical composition of coal fly ashes as a basis for their multicomponent utilisation. Characterisation of feed coals and fly ashes. Fuel, 82 (2003) 1793-1811.

[24] Vejahati F., Xu Z.H., Gupta R. Trace elements in coal: associations with coal and minerals and their behavior during coal utilization - a review. Fuel, 89 (2010) 904-911.

[25] American Coal Ash Association. What are coal combustion products? https://www.acaa-usa.org/what-are-ccps.aspx (2019) (accessed 24 August 2020).

[26] Haynes, R.J. Reclamation and revegetation of fly ash disposal sites - challenges and research needs. Journal of Environmental Management, 90 (2009) 43-53.

[27] Coaltrans conferences. Global aspects on coal combustion products. https://www.coaltrans.com/insights/article/global-aspects-on-coal-combustion-products (2019) (accessed 28 August 2020).

[28] International Energy Agency. Pulverised coal combustion (PCC). https://www.iea-coal.org/pulverised-coal-combustion-pcc/ (2018) (accessed 28 August 2020).

[29] Audai Hussein Al-Abbas, Jamal Naser. Oxy–fuel combustion in the lab–scale and large–scale fuel– fired furnaces for thermal power generations. Rasul M. (Ed.), Thermal Power Plants - Advanced Applications, IntechOpen (2013).

[30] Swanson S.M., Engle M.A, Ruppert L.F., Affolter R.H., Jones K.B. Partitioning of selected trace elements in coal combustion products from two coal-burning power plants in the United States. International Journal of Coal Geology, 113 (2013) 116-126.

[31] Clarke L.B., Sloss L.L. Trace elements - emissions from coal combustion and gasification. London: IEA Coal Research (1992).

[32] Xu M., Yan R., Zheng C., Qiao Y., Han J., Sheng C. Status of trace element emission in a coal combustion process: a review. Fuel Processing Technology, 85 (2003) 215-237.

[33] Hower J.C., Trimble A.S., Eble C.F., Palmer C., Kolker A. Characterization of fly ash from low-sulfur and high-sulfur coal sources: partitioning of carbon and trace elements with particle size. Energy Sources, 21 (1999) 511-525.

[34] Wilcox J., Rupp E., Ying S.C., Lim D.H., Negreira A.S., Kirchofer A., Feng F., K. Lee K. Mercury adsorption and oxidation in coal combustion and gasification processes. International Journal of Coal Geology, 90-91 (2012) 4-20.

[35] Meij R. Trace element behavior in coal-fired power plants. Fuel Processing Technology, 39 (1994) 199-217.

[36] Ratafia-Brown J.A., Manfredo L.M., Hoffmann J.W., Ramezan M. Stiegel, G.J. An environmental assessment of IGCC power systems. 19th Annual Pittsburgh Coal Conference, Pittsburgh, September 23-27 (2002).

[37] Finkelman R.B., Orem W., Castranova V., Tatu C.A., Belkin H.E., Zheng B., Lerch H.E., Maharaj S. V., Bates A. L. Health impacts of coal and coal use: possible solutions. International Journal of Coal Geology, 50 (2002) 425-443.

[38] Kim A., Kazonich G., Dahlberg M. Relative solubility of cations in class F fly ash, Environmental Science and Technology, 37 (2003) 4507-4511.

[39] British Geological Survey. Rare earth elements. https://www.bgs.ac.uk/downloads/start.cfm?id=1638 (2011) (accessed 18 July 2019).

[40] Asian Metals. Rare earth minerals and classification. http://metalpedia.asianmetal.com/metal/rare_earth/mineral.shtml (accessed 6 July 2019).

[41] Du X., Graedel T.E. Global in-use stocks of the rare earth elements: a first estimate. Environmental Science and Technology, 45 (2011) 4096-4101.

[42] British Broadcasting Corporation. Are rare earth minerals China's trump card in its trade war with the US? https://www.bbc.com/news/amp/world-asia-48366074 (2019) (accessed 30 May 2019).

[43] Gupta C.K., Krishnamurthy N. Extractive metallurgy of rare earths. London: Boca Raton (2005).

[44] Humphries, M. Rare earth elements: the global supply chain. Washington, DC: Congressional Research Service (2013).

[45] Lin J.Y. Demystifying the Chinese economy. Cambridge: Cambridge University Press (2011).

[46] Taylor S.R., McLennan S.M. The continental crust: its composition and evolution. Oxford: Blackwell (1985).

[47] Taylor S.R., McLennan S.M. The geochemical evolution of the continental crust. Reviews of Geophysics, 33 (1995) 241-265.

[48] United States Geological Survey. Rare earths statistics and information. https://pubs.usgs.gov/periodicals/mcs2020/mcs2020-rare-earths.pdf (2020) (accessed 5 September 2020).

[49] Li K., Chen J., Zou D. Extraction and recovery of cerium from rare earth ore by solvent extraction. IntechOpen Chapter 2 (2018) 6-21.

[50] United States Geological Survey. Rare-earth elements. https://pubs.usgs.gov/pp/1802/o/pp1802o.pdf (2017) (accessed 30 August 2020).

[51] Weng Z.H., Jowitt S.M., Mudd G.M., Haque N. Assessing rare earth element mineral deposit types and links to environmental impacts. Transactions of the Institute of Mining and Metallurgy, Section B., 122 (2013) 83-96.

[52] Jordens A., Cheng Y.P., Waters K.E. A review of the beneficiation of rare earth element bearing minerals. Minerals Engineering, 41 (2013) 97-114.

[53] Wedepohl K.H. The composition of the continental crust. Geochimica et Cosmochimica Acta, 59 (1995) 1217-1232.

[54] Taggart R.K., Hower J.C., Dwyer G.S., Hsu-Kim H. Trends in the rare earth element content of U.S.-based coal combustion fly ashes. Environmental Science and Technology, 50 (2016) 5919-5926.

[55] Kanazawa Y., Kamitani M. Rare earth minerals and resources in the world. Journal of Alloys and Compounds, 408-412 (2006) 1339-1343.

[56] National Energy Technology Laboratory, U.S. Department of Energy. Rare earth element, 2019 project portfolio. https://netl.doe.gov/sites/default/files/2019-04/2019-REE-Project-Portfolio.pdf (2019) (accessed 2 July 2019).

[57] Seredin V., Dai S. Coal deposits as potential alternative sources for lanthanides and yttrium. International Journal of Coal Geology, 94 (2012) 67-93.

[58] Kingsnorth D.J. An overview of the rare earths market. Industrial Minerals Company of Australia (IMCOA). Informa Rare Earths Conference (2010).

[59] Hower J.C., Eble C.F., Dai S., Belkin H.E. Distribution of rare earth elements in eastern Kentucky coals: indicators of multiple modes of enrichment? International Journal of Coal Geology, 160-161 (2016) 73-81.

[60] Montross S., Circe A.V., Falcon A., Poston J., Mark M. Characterization of rare earth element minerals in coal utilization by-products and associated clay deposits from Appalachian Basin coal resources. 34th International Pittsburgh Coal Conference, Pittsburgh (2017).

[61] Smith J.V., Rivers M.L. Synchrotron x-ray microanalysis; microprobe techniques in the earth sciences. Boston: Springer US (1995) 163-233.

[62] Hood M.M., Targgart R.K., Smith R.C., Hsu-Kim H., Henke K.R., Graham U., Groppo J.G., Unrine J.M., Hower J.C. Rare earth element distribution in fly ash derived from the Fire Clay coal, Kentucky. Coal Combustion and Gasification Products, 9 (2017) 22-33.

[63] Yang X., Rathmell A., Preda D.V., Joshi P.B., Bollas G.M. Process Design and economics of a novel process for the extraction of rare earth elements from coal ash. Paper Presented at AIChE Annual Meeting (744b), November 13-18, San Francisco, CA (2016). https://www.aiche.org/conferences/aiche-annual-meeting/2016/proceeding/paper/744b-process-design-and-economics-novel-process-extraction-rare-earth-elements-coal-ash (accessed May 4, 2017).

[64] Mondal S., Ghar A., Satpati A.K., Sinharoy P., Singh D.K., Sharma J.N., Sreenivas T., Kain V. Recovery of rare earth elements from coal fly ash using TEHDGA impregnated resin. Hydrometallurgy, 185 (2019) 93-101.

[65] Pan J., Nie T., Vaziri Hassas B., Rezaee M., Wen Z., Zhou C. Recovery of rare earth elements from coal fly ash by integrated physical separation and acid leaching. Chemosphere 248 (2020) 126112.

[66] Wang Z., Dai S., Zou J., French D., Graham I.T. Rare earth elements and yttrium in coal ash from the Luzhou power plant in Sichuan, Southwest China: concentration, characterization and optimized extraction. International Journal of Coal Geology, 203 (2019) 1-14.

[67] Phuoc T.X., Wang P. Laser separation of rare earth elements from coal ashes. World of Coal Ash Conference, Lexington, May 8-11 (2017).

[68] Taggart R.K., King J.F., Hower J.C., Hsu-Kim H. Rare earth element recovery from coal fly ash by roasting and leaching methods. World of Coal Ash Conference, Lexington, May 8-11 (2017).

[69] King J.F., Taggart R.K., Smith R.C., Hower J.C., Hsu-Kim H. Aqueous acid and alkaline extraction of rare earth elements from coal combustion ash. International Journal of Coal Geology, 195 (2018) 75-83.

[70] Liu P., Huang R., Tang Y. Comprehensive understandings of rare earth element (REE) speciation in coal fly ashes and implication for REE extractability. Environmental Science and Technology, 53 (2019) 5369-5377.

[71] Lin R., Stuckman M., Howard B.H., Bank T.L., Roth E.A., Macala M.K., Lopano M.K., Soong Y., Granite E.J. Application of sequential extraction and hydrothermal treatment for characterization and enrichment of rare earth elements from coal fly ash. Fuel, 232 (2018) 124-133.

[72] Eggert R., Wadia C., Anderson C., Bauer D., Fields F., Meinert L., Taylor P. Rare earths: market disruption, innovation, and global supply chains. Annual Review of Environment and Resources, 41 (2016) 199-222.

[73] Smolka-Danielowska D. Rare earth elements in fly ashes created during the coal burning process in certain coal-fired power plants operating in Poland–Upper Silesian industrial region. Journal of Environmental Radioactivity, 101 (2010) 965-968.

[74] Seredin V.V. Rare earth element-bearing coals from the Russian far east deposits. International Journal of Coal Geology, 30 (1996) 101-129.

[75] Mardon S.M., Hower J.C. Impact of coal properties on coal combustion by-product quality: examples from a Kentucky power plant. International Journal of Coal Geology, 59 (2004) 153-169.

[76] Stuckman M.Y., Lopano C.L., Granite E.J. Distribution and speciation of rare earth elements in coal combustion by-products via synchrotron microscopy and spectroscopy. International Journal of Coal Geology, 195 (2018) 125-138.

[77] Chemistry Libretexts. Nuclear magic number. https://chem.libretexts.org/Bookshelves/Physical_and_Theoretical_Chemistry_Textbook_Maps/Supplemental_Modules_(Physical_and_Theoretical_Chemistry)/Nuclear_Chemistry/Nuclear_Energetics_and_Stability/Nuclear_Magic_Numbers (2020) (accessed 6 September 2020)

[78] Chemistry Libretexts. Patterns of nuclear stability. https://chem.libretexts.org/Courses/Valley_City_State_University/Chem_122/Chapter_9%3A_Nuclear_Chemistry/9.3%3A_Patterns_of_Nuclear_Stability (2020) (accessed 6 September 2020).

[79] L'Annunziata, M.F. Radioactivity: introduction and history. Amsterdam: Elsevier (2007).

[80] Raymond Murray Keith Holbert. Nuclear energy: an introduction to the concepts, systems, and applications of nuclear processes (7th edition). Oxford: Butterworth-Heinemann (2015).

[81] Gilmore, G.R. Practical gamma-ray spectrometry (2nd edition). Chichester: John Wiley & Sons (2008).

[82] National Council on Radiation Protection and Measurements . A handbook of radioactivity measurements procedures (2nd edition). Report No. 58, Maryland. (1985).

[83] Krane, K.S. Introductory nuclear physics, Chichester: John Wiley & Sons (1988).

[84] Choppin G., Liljenzin J., Rydberg, J. Radiochemistry and nuclear chemistry (3rd edition). USA: Butterworth-Heinemann (2002).

[85] Prince, J.H. Comments on equilibrium, transient equilibrium, and secular equilibrium in serial radioactive decay. Journal of Nuclear Medicine 20 (1979) 162-164.

[86] Cember, H., Johnson, T.E. Introduction to Health Physics (4th edition). New York: McGraw-Hill. (2009).

[87] Lilley, J. Nuclear Physics: principles and applications. Chichester: John Wiley & Sons (2001).

[88] World Nuclear Association. Naturally occurring radioactive material (NORM). https://www.world-nuclear.org/information-library/safety-and-security/radiation-and-health/naturally-occurring-radioactive-materials-norm.aspx (2020) (accessed 4 September 2020).

[89] Nancy E.L., James C.H., Heileen H.-K., Ross K. Taggart, Vengosh A. Naturally occurring radioactive materials in coals and coal combustion residuals in the United States. Environmental Science and Technology, 49 (2015) 11227-11233.

[90] Ruhl L., Vengosh A., Dwyer G.S., Hsu-Ki, H., Deonarine A., Bergin M., Kravchenko J. Survey of the potential environmental and health impacts in the immediate aftermath of the coal ash spill in Kingston, Tennessee. Environmental Science and Technology, 43 (2009) 6326-6333.

[91] Chen J., Chen P., Yao D., Huang W., Tang S., Wang K., Liu W., Hu Y., Zhang B., Sha J. Abundance, distribution, and modes of occurrence of uranium in Chinese coals. Minerals 7 (2017) 239.

[92] Arbuzov S.I., Maslov S.G., Volostnov A.V., Il'enok S.S., Arkhipov V.S. Modes of occurrence of uranium and thorium in coals and peats of northern Asia. Solid Fuel Chemistry 46 (2012) 52-66.

[93] Chen J., Chen P., Yao D., Huang W., Tang S., Wang K., Liu W., Hu Y., Li Q., Wang R. Geochemistry of uranium in Chinese coals and the emission inventory of coal-fired power plants in China. International Geology Review, 60 (2017) 621-637.

[94] Karangelos D., Petropoulos N., Anagnostakis M., Hinis E., Simopoulos S. Radiological characteristics and investigation of the radioactive equilibrium in the ashes produced in lignite-fired power plants. Journal of Environmental Radioactivity, 77 (2004) 233-246.

[95] Manolopoulou M., Papastefanou C. Behavior of natural radionuclides in lignites and fly ashes. Journal of Environmental Radioactivity, 16 (1992) 261-271.

[96] Isinkaye O.M., Jibiri N.N., Olomide A.A. Radiological health assessment of natural radioactivity in the vicinity of Obajana cement factory, North Central Nigeria. Journal of Medical Physics, 40 (2015) 52-59.

[97] Santawamaitre T., Malain D., Al-Sulaiti H.A., Matthews M., Bradley D.A., Regan P.H. Study of natural radioactivity in riverbank soils along the Chao Phraya river basin in Thailand. Nuclear Instruments and Methods in Physics Research Section A, 652 (2011) 920-924.

[98] International Atomic Energy Agency. Radioactive particles in the environment: Sources, particle characteristics and analytical techniques. IAEA-TECDOC-1663 Vienna (2011) p. 2.

[99] McGuire C., Dale P., Copplestone D., Wilson C., Tyler A. Characterising radium-226 particles from legacy contamination to support radiation dose assessments. Journal of Environmental Radioactivity, 212 (2020) 106-127.

[100] Salbu B., Kashparov V., Lind O.C., Garcia-Tenorio R., Johansen M.P., Child D.P., Roos P., Sancho C. Challenges associated with the behaviour of radioactive particles in the environment. Journal of Environmental Radioactivity, 186 (2018) 101-115.

[101] Salbu B., Lind O.C., Skipperud L. Radionuclide speciation and its relevance in environmental impact assessments. Journal of Environmental Radioactivity, 74 (2004) 233-242.

[102] Simopoulos S.E., Angelopoulos M.G. Natural radioactivity releases from lignite power plants in Greece. Journal of Environmental Radioactivity, 5 (1987) 379-389.

[103] Lu X., Jia X., Wang F. Natural radioactivity of coal and its by-products in the Baoji coal-fired power plant, China. Current Science, 91 (2006).

[104] Mandal A., Sengupta D. Radioelemental study of Kolaghat thermal power plant, West Bengal, India: Possible environmental hazards. Environmental Geology, 44 (2003) 180-186.

[105] Kisić D.M., Miletić S.R., Radonjić V.D., Radanović S.B., Filipovic J.Z., Gržetić I.A. Natural radioactivity of coal and fly ash at the Nikola Tesla B TPP. Hemijska Industrija, 67 (2013) 729-738.

[106] Cevik U., Damla N., Nezir S. Radiological characterization of Cayirhan coal-fired power plant in Turkey. Fuel, 86 (2007) 2509-2513.

[107] Nancy L., Vengosh A., Dai S. Naturally occurring radioactive materials in uranium-rich coals and associated coal combustion residues from China. Environmental Science and Technology, 51 (2017) 13487-13493.

[108] Parzentny H.R., Róg L. The role of mineral matter in concentrating uranium and thorium in coal and combustion residues from power plants in Poland. Minerals, 9 (2019) 312.

[109] Tian Q., Guo B., Nakama S., Sasaki K. Distributions and leaching behaviors of toxic elements in fly ash. ACS Omega, 3 (2018) 13055-13064.

[110] Goodarzi F., Huggins F.E., Sanei H. Assessment of elements, speciation of As, Cr, Ni and emitted Hg for a Canadian power plant burning bituminous coal. International Journal of Coal Geology, 74 (2008) 1-12.

[111] Sun Y., Wu M., Zheng L., Zheng L., Wang B., Wang Y. Uranium speciation in coal bottom ash investigated via, x-ray absorption fine structure and x-ray photoelectron spectra. Journal of Environmental Sciences, 74 (2018) 88-94.

Chapter 3

Research materials and methods

This chapter introduces the sampling strategies, sample preparation processes and the suite of analytical techniques used to obtain the results presented in this thesis.

3.1 Study area

The coal samples characterised in this study were sourced from three open-pit coal mines located in Kogi State, Nigeria, (as shown in Figure 3.1). The Okaba (OK) and Odagbo (OD) mines are located in Okaba and Odagbo, respectively, within the Ankpa Local Government Area (LGA), the Omelewu (OM) coal mine is located in Imane, within the Olamaboro LGA.

Kogi State lies in the north-central geopolitical zone of Nigeria, with the confluence of River Niger and River Benue at its capital, Lokoja. Kogi State has an average maximum temperature of 33.2 °C and average minimum of 22.8 °C, with two distinct seasons, the 'cold, windy and dusty' dry season, which lasts from November to February, and a rainy season, from March to October. Annual rainfall ranges from 1016 mm to 1524 mm [1].

The state has a land area of 29,833 km^2, with the geological exposures of the state comprised of two primary rock types; namely the significantly older basement complex rocks of Precambrian era in the western part of the state, and Cretaceous sedimentary rocks in the eastern half [1]. The basement complex is made up of metasediments (migmatite, gneiss, schist, granites), and iron formations (rich in magnetite and haematite) with prominent outcrops south-east of Kabba, Kogi State [2]. The sedimentary formations in the eastern half

of the state are divided into a number of sedimentary basins, namely; the Benue (central), Sokoto (north-west border), Chad (north-east), Bida (central), Dahomey (south-west) and Anambra (south-east) Basins [2]. The Anambra basin is mainly made of different Formations, namely; the Nkporo, Mamu, Ajali and Nsukka formations [3]. These Formations are inter-bedded marine sandstones, siltstones, carboniferous-shale, coal and sandstones of a fluvial nature. These Formations control the formation of coal, kaolin, clay, limestone, gemstones, slate, phosphate, gypsum and other associated minerals [3].

The OK, OD and OM coal mines all host sub-bituminous coal (part of the Mamu Formation) and belong to the Kogi mining district – a major coal resource within the Anambra basin, comprising an area of 225,000 ha [4-6]. The estimated reserve (in million tonnes) for OK and OD coal mines are 99 and 250, respectively [5,6]; the estimated reserve for OM coal mine is unknown as little data is available.

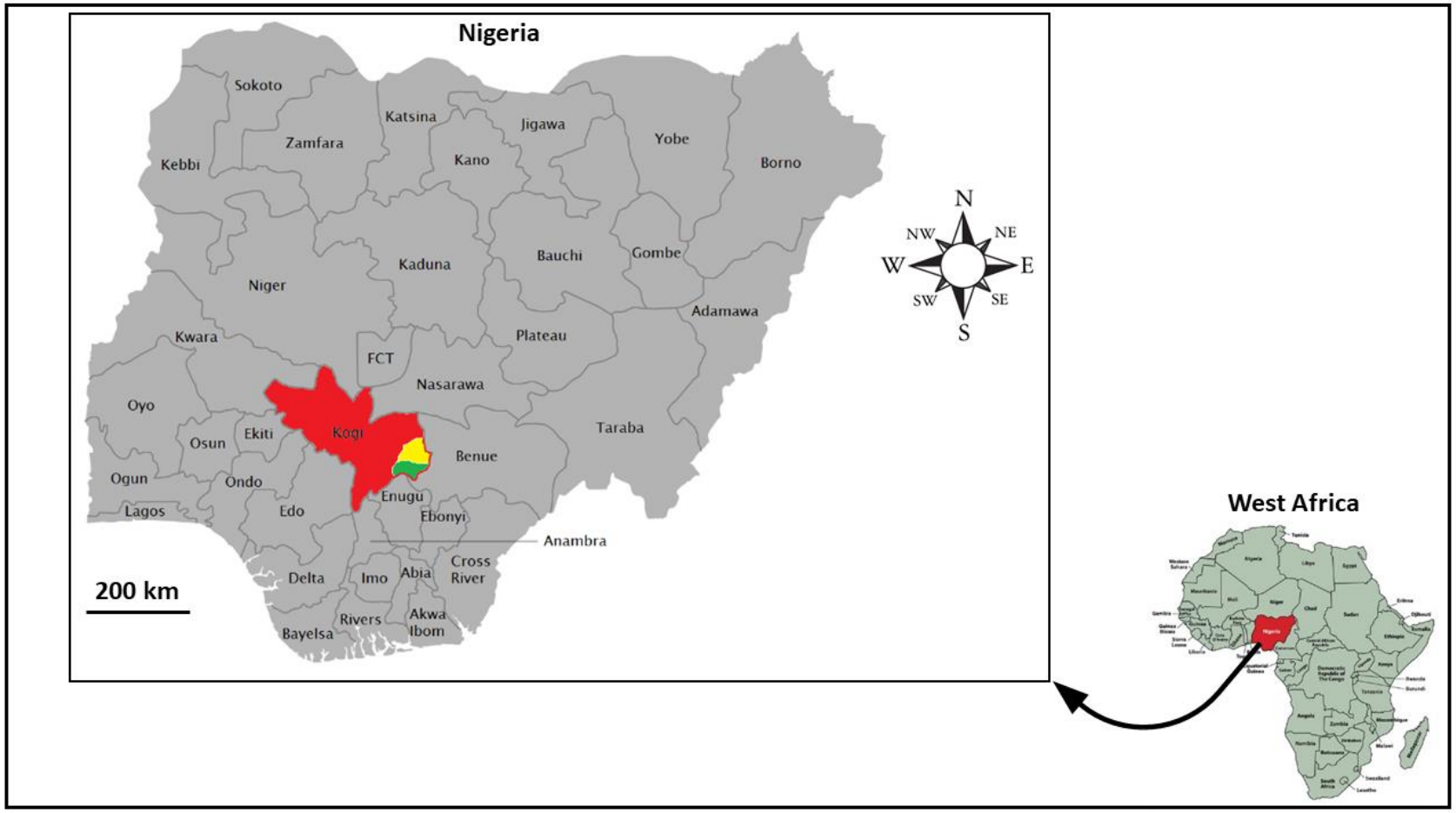

Figure 3.1: Map of Nigerian states showing the location of Ankpa LGA (yellow) and Olamaboro LGA (green), both in Kogi state (red). Modified from [7].

3.2 Coal sample collection and preparation

In this study, coal samples were collected from each mine using a stratified random sampling methodology to ensure that samples collected were representative of the full compositional variability within the mine. This was achieved by dividing the coal field to be sampled into subareas followed by random sampling of each subareas. In other to cover the whole mine site, a total of 15 coal samples per mine were collected at 200 m intervals.

The raw samples (each approximately 1 kg) were packed in polythene bags and transported to the UK for analysis. Figure 3.2 shows photographs from the sample collection field trip.

Figure 3.2: Photos from the field trip to the coal mines for sample collection.

Prior to subsequent technique-specific coal and coal fly ash sample preparation, the individual coal samples collected from the three mines were each crushed before being oven-dried at 100 °C for a period of 30 min to remove any moisture. The crushed samples were then pulverised and homogenised before being passed through a 150 µm wire mesh sieve (to simulate the pulverised coal particle size range fed into coal-fired power plants). The crushing and pulverising was performed using an agate mortar and pestle.

3.2.1 Simulant coal fly ash preparation

Because Nigeria's coal-fired power plants are only at an advanced stage of planning (that is, no operational coal-fired power plants yet exist in Nigeria from which to obtain coal fly ash samples), simulant coal fly ash samples were produced and subsequently studied in this work. To simulate coal fly ash within the laboratory, sub-samples of each pulverised and sieved coal sample (200 to 400 g) were (in turn) combusted in crucibles using a Lenton^{TM} ECF 12/6 muffle furnace (for treatments in air with a maximum operating temperature of 1,200 °C) at 1,100 °C (below the fusion temperature of the ash, while completely removing the organic matter content). This was achieved by combusting each coal sample in the furnace from room temperature at the rate of 10 °C/min; the max temperature (1,100 °C) was maintained for 30 min, and the oven was thereafter cooled down to room temperature at the rate of 10 °C/min. This selected combustion temperature approximates to the temperature used in coal-fired power plants burning coal (especially low-rank coal such as lignite, sub-bituminous) at temperature between 800 °C and 1,200 °C [8,9]. The implication of burning low-rank coal (at a low temperature) over high-rank coal is that it is more likely for the rare earth and radioactive mineral particles to exist discretely, rather than being encapsulated in the glassy component of coal fly ash, since the melting temperatures of glass-forming aluminosilicate

minerals are higher than this coal combustion temperature. Following ashing, the samples were left to cool. Results of sieve analysis (Table 3.1) revealed that approximately 80% of these coal ash materials fell in the particle size range of 1 µm to 300 µm, which corresponds to 80% fly ash and 20% bottom ash. The sieve analysis was performed using a set of sieves (45 µm, 75 µm, 150 µm and 300 µm) and a mechanical sieve shaker. Each composite sample was, in turn, packed into the 300 µm (with the other sieve sizes placed beneath) and loaded onto the mechanical shaker and vibrated for 3 hr for complete separation of the particle sizes.

Table 3.1: Results of sieve analysis of OMA, OKA and ODA simulant coal fly ash.

Source mine	Particle size (%)			
	45 µm	75 µm	150 µm	300 µm
OMA	15.6	41.1	21.2	22.1
OKA	15.1	43.5	21.1	20.3
ODA	17.2	38.6	23.2	21.0

3.3 Analytical techniques

3.3.1 Inductively coupled plasma mass spectrometry

Inductively coupled plasma mass spectrometry (ICP-MS) is a quantitative analytical technique that is used for trace elemental analysis of aqueous and solid samples. Within an ICP-MS, nebulised sample is introduced into high temperature argon plasma, resulting in ionisation of the sample solution. The generated ions are then deflected on the basis of their mass:charge ratio (using a mass spectrometer), detected and the signal processed and read out using fast counting digital electronics.

The advantages of ICP-MS over other elemental analysis techniques, such as inductively coupled plasma optical emission spectrometry, inductively coupled plasma atomic emission spectrometry and atomic absorption spectroscopy, include very low detection limit (parts per trillion; ppt), high sample throughput and productivity, multi-element capability and isotopic analysis capability. ICP-MS has seen application in forensic, environmental, clinical, pharmaceutical and nuclear analysis, and is well suited to quantitative analysis of toxic heavy metals, radionuclides and rare earth elements. However, the capital and running costs of the ICP-MS instrumentation are high on comparison to the aforementioned techniques due to a higher cost of the components such as the detector, cones and reaction cell.

Operation principles

As shown in Figure 3.3, the basic ICP-MS system is divided in to four main functional components: (i) sample introduction; (ii) plasma ion source; (iii) plasma-mass spectrometer interface; (iv) mass separation and detection.

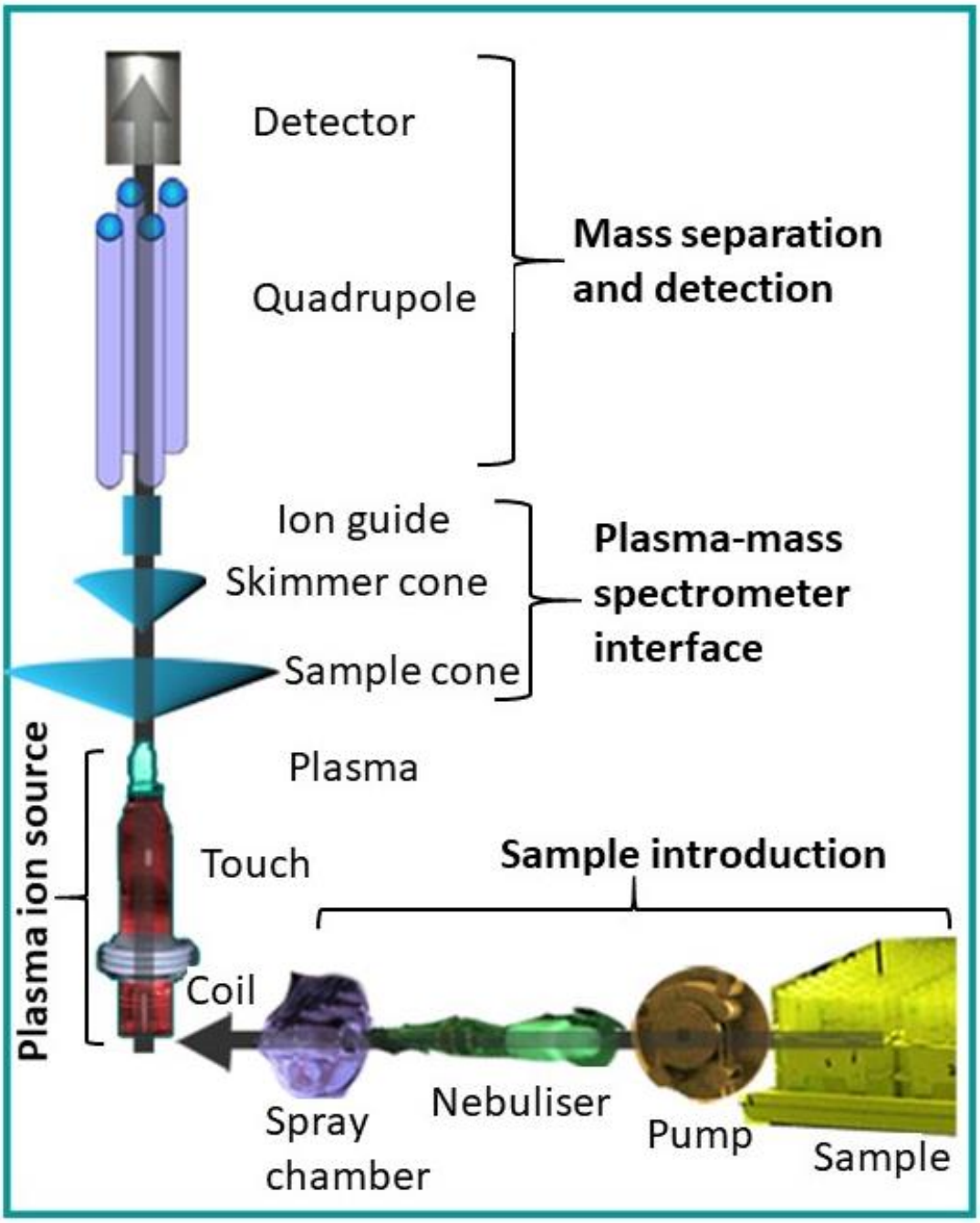

Figure 3.3: Typical internal layout of an ICP-MS system [10].

Sample introduction

To effectively perform trace elemental analysis using ICP-MS, a given sample needs to be efficiently introduced into the head-end of the ICP-MS system. With a liquid sample, a nebuliser is used to convert this into a fine aerosol by pneumatic action of a stream of Ar gas

(~1 $L.min^{-1}$). To avoid the plasma being extinguished or cooled (which would cause matrix interferences) and solvents loading into the plasma during operation, the optimal aerosol particle size for plasma processes to occur is circa 10 µm, enough for efficient vaporisation to occur [11]. To achieve this, the aerosols generated using the nebuliser are passed through a spray chamber (fitted with a thermostat regulated water jacket) to remove droplets larger than 10 µm and reduce solvent content. Typically, only a small portion (<2%) of the sample reaches the plasma torch after the separation process within the spray chamber. For solid samples, a laser ablation system is used; a laser beam focused on the solid sample generates fine particles by ablation, and the ablated particles are carried into the plasma via a stream of Ar gas.

Plasma ion source

Once the sample is partially desolvated and the aerosol is sorted within the spray chamber, particles of the right size (circa 10 µm) are injected into the plasma torch, where they are mixed with Ar carrier gas. In the plasma torch at atmospheric pressures, an inductively-coupled high-temperature (7,000 K – 10,000 K) Ar plasma is produced within the confines of three concentric glass tubes by the interaction of a strong magnetic field (produced by a radio frequency generator induction coil) and Ar gas. Aerosol particles carried through the centre of the plasma is desolvated, dissociated, atomised and ionised, before being subsequently passed into the mass analyser through the interface region – comprised of a series of apertures/cones (circa 1mm diameter).

Plasma-mass spectrometer interface

The ions generated then pass through the atmospheric pressure plasma source and high-vacuum (~10^{-7} mbar) mass spectrometer interface. The interface consists of two metallic cones with small orifices (~1 mm) - sampler/extraction and skimmer cones, which help to direct the expanding jet of ionised gas into the ion-focusing region. In the ion-focusing region, electrostatic lenses focus the ion beam and separate the unwanted photons and neutral species from the gas jet with remaining ions subsequently passed into reaction cell (located behind the skimmer cone) where polyatomic interferences are removed. In the reaction cell operated in He mode, the larger polyatomic species collide more with He molecules and lose kinetic energy; subsequently, a potential barrier at the exit of the reaction cell passes only the high energy analyte ions into the mass spectrometer while preventing the low energy polyatomic species by energy discrimination. The mass spectrometer is maintained at high vacuum (≤10^{-6} mbar) to keep the velocity of the ions at optimal speed to prevent undesired ion-air molecule collisions that would lead to signal deterioration.

The mass spectrometer

The mass spectrometer (MS) acts as a filter, passing and counting the ions based on their mass (m):charge (z) ratio. A number of MS include quadrupole, sector-field, ion-trap and time-of-flight mass, with the commonly used being that of the quadrupole MS. The quadrupole MS consists of two pairs of straight cylindrical rods to which varying alternating current (AC) and direct current (DC) voltages are applied. Ions beneath or above the set mass of the quadrupole enter an unstable trajectory and are lost from the stream. By varying the AC and DC voltages, different masses can be selectively allowed to pass through. Quadrupole scan rates are typically in the order of 2500 atomic mass units per second; in practice, a total of 25

elements can be determined with good precision within 30 s - 60 s. One of the inefficiencies of quadrupole MS is its resolution, which is limited to unity, making the technique prone to interferences resulting from polyatomic ions generated during plasma-solvent-sample matrix interaction.

Once passed through the ion detector, the sorted ions are then detected and converted into electrical signals for display. The ion detector is typically an electron multiplier device made up of a series of dynodes within which a cascade of electron multiplication processes takes place, resulting in the production of a measurable signal pulse. The magnitude of the ion current is used to provide quantification of the elements in a sample. In order to accurately quantify the trace elements in a sample, the ICP-MS must be calibrated (prior to sample analysis) using certified reference materials containing known amounts of the analytes of interest.

3.3.2 Gamma-ray spectrometry

Gamma-ray spectrometry is the measurement (using an appropriate detector/spectrometer) of the energy spectrum generated when gamma-rays from decaying radionuclides contained in a sample interact with the detector. Irrespective of the detector type, this interaction of gamma-rays with the detector results in the excitation and/or indirect ionisation of atoms in the detector and, subsequently, the generation of an electrical signal, which is then further processed and displayed as the resulting gamma-ray spectrum. The gamma spectrum, which is characteristic of the gamma-emitting nuclides, is typically used to **identify** and **quantify** the gamma emitters present in a sample. Typically, the **gamma-rays** from radioactive sources range from a few keV to ~8 MeV in energy [12].

Generally, there are two main classes of solid-state gamma spectrometers: scintillation and semiconductor. Scintillation detectors convert the kinetic energy of incident ionising radiation into flashes of visible light through the process of excitation and de-excitation of the atoms of the detector material. these light flashes are then converted to electrical signal pulse using a photomultiplier. One of the oldest and most frequently used scintillation detector types is thallium-activated sodium iodide (NaI(Tl)). These detectors have a high efficiency for detecting gamma radiation and require no cooling. However, scintillation detectors have relatively poor energy resolution, which is a key advantage of semiconductor detectors. Semiconductor detectors work by direct generation of electric signal pulses from charge carriers created when gamma photons impinge on the detector active semiconductor crystal volume. The common types of semiconductor detectors include high-purity germanium (HPGe), Si(Li) and Ge(Li). These materials require active cooling to cryogenic temperatures to reduce thermal noise to manageable levels. The experimental work presented in this thesis used an HPGe detector which provides the highest energy resolution possible.

Theory

Gamma-ray photons interactions with matter occur via three mechanisms namely; (i) photoelectric absorption; (ii) Compton scattering; and (iii) pair production. These mechanisms combined (called “full-energy events”) all contribute to the formation of gamma-ray energy peaks in a resulting spectrum through the transfer of all or part of the gamma-rays energy to electrons in the volume of the detector material. The probability of a gamma photon interacting with a detector material of atomic number Z is proportional to Z^n ($4 < n < 5$) for photoelectric absorption, Z for Compton scattering and Z^2 for pair production [13]. The energy dependence of these three mechanisms is as shown in Figure 3.4.

(i) In the process of **photoelectric absorption**, a gamma-ray photon with energy greater than the electron binding energy interacts with a bound inner shell electron in the detector material, whereby the photon is completely absorbed, leading to the ejection from the inner shell of an energetic electron (termed “photoelectron”). This creates a temporary vacancy in a shell of the atom, resulting in an excited state; the subsequent de-excitation of the atom can occur by electron rearrangement from higher shells to fill in the vacancy, leading to the emission of a characteristic ‘fluorescence’ x-ray (Figure 3.5a). The de-excitation process could result in the release of other (Auger) electrons from the atom (as also shown in Figure 3.5a). Photoelectric absorption is the ideal process for detector operation as, unlike the other interaction processes, it involves total absorption of the energy of an incident gamma photon by the detector material, resulting in the most-efficient energy transfer. The photoelectric process is significant at low photon energies (< 0.1 MeV), becoming less dominant at higher energies.

(ii) **Compton scattering** describes a collision between the incident gamma-ray photon and a weakly-bound or free electron in the absorbing material - resulting to the incomplete transfer (or only a portion) of the photons energy to the recoiling electron. The result of this interaction is the incident gamma-ray photon is degraded in energy and deflected from its original direction, with an (recoil/photo) electron created (Figure 3.5b). Since Compton scattering involves incomplete energy transfer to the detector, energy transfer is less efficient compared to the photoelectric process. Compton scattering is the dominant interaction process for intermediate gamma-ray energies (0.1 MeV to 10 MeV).

(iii) The third interaction mechanism of gamma-rays with matter is that of **pair production**. This process becomes increasingly important when the incident gamma-ray photon has

energy significantly greater than twice the rest mass energy of an electron (1.022 MeV). This interaction occurs within the Coulomb field of a nucleus, in which the gamma-ray photon is absorbed into the vacuum and converted into an electron-positron pair (Figure 3.5c). After the electron and positron pair is created, they can traverse the medium, losing their kinetic energy through collisions with electrons in the surrounding material via ionisation, excitation and/or Bremsstrahlung generation. Once the positron slows down, it can interact with an atomic electron in the surrounding material and annihilate - forming two (annihilation) photons, each with an energy of about 0.511 MeV. This process has the least energy transfer efficiency.

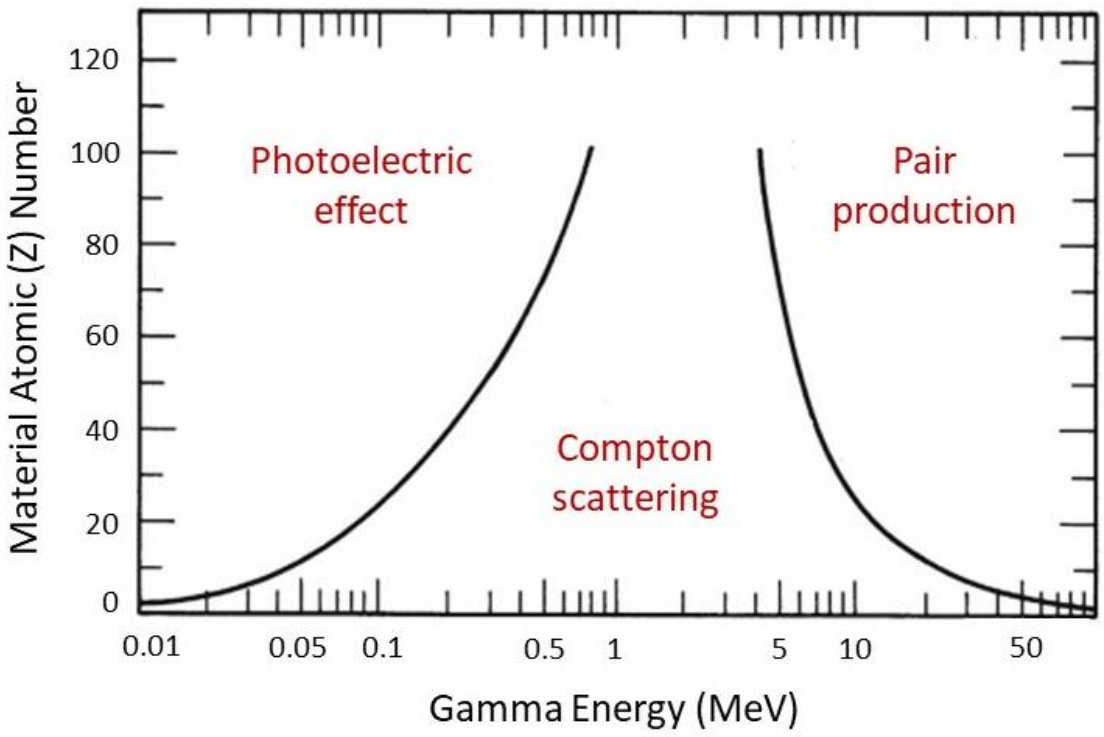

Figure 3.4: Plot depicting the energy dependence of photoelectric, Compton and pair production processes. From [14].

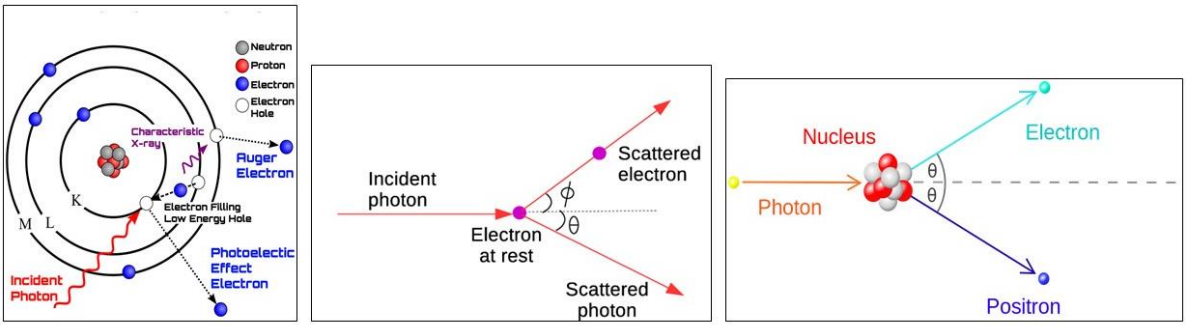

Figure 3.5: Gamma photon interaction with matter: (a) Photoelectric effect (b) Compton scattering (c) pair production. From [15].

High-purity germanium detector operation principles

A HPGe detectors operate via the production of charge carriers (electron-hole pairs) when electrons are promoted from the valence band to the conduction band due to gamma-ray interaction with the semiconductor detector material. The number of charge carriers produced is directly proportional to the energy of the incident gamma photon and, in the presence of an applied electric voltage, these charge carriers migrate to the oppositely-charged electrodes (cathode and anode), generating a measurable electrical signal pulse. An HPGe detector is a reverse-biased p-type and n-type (pn) junction, with the depletion region acting as the detector active volume [16]. The relatively small energy (2.96 eV at 77 K temperature) required to create an electron-hole pair, the very narrow band gap (0.67 eV) and the excellent resolution (1.71 keV at 1.33 MeV ^{60}Co) are the main advantages of an HPGe detector. However, the very narrow band gap results in substantial thermal excitation (at room temperature), leading to leakage current induced noise, which deteriorates the detector's energy resolution. The detector is, therefore, operated at below room temperature by cooling to cryogenic temperatures (77 K) to greatly reduce thermal excitation. HPGe detectors are commonly used in a variety of applications, including

environmental monitoring for radioactive contamination, radiometric assay, medical and nuclear security.

Figure 3.6a shows a Pb shielded HPGe gamma-ray spectrometer with a liquid nitrogen Dewar; and Figure 3.6b shows the generic functional block diagram of an HPGe detector. Following the interaction of a gamma-ray with the detector active volume, production of ion pairs and migration to the electrodes (by the application of a reverse bias voltage between 2500 kV and 3000 kV), the electron-hole pairs are collected by the preamplifier and converted into a voltage pulse. The voltage pulse is conditioned, shaped, corrected for pile-up and summing effects and further amplified within the pre-amplifier and amplifier unit.

The voltage pulses from the amplifier are sorted by their pulse height (which is proportional to the gamma energy deposited in the detector) and then assigned to a digital channel number by the analogue-to-digital converter (ADC) in the multichannel analyser (MCA). Finally, a spectrum of counts versus gamma energy is output. To identify and **quantify** the gamma emitters present in a sample, energy and efficiency calibration of the HPGe detector must be performed prior to sample analysis using the appropriate gamma reference standards containing the radionuclides of interest with known activity, and covering the energy range of interest. To reduce unwanted background contribution (to photo-peak intensity) from external sources, the detector crystal is shielded in a 10 cm Pb wall.

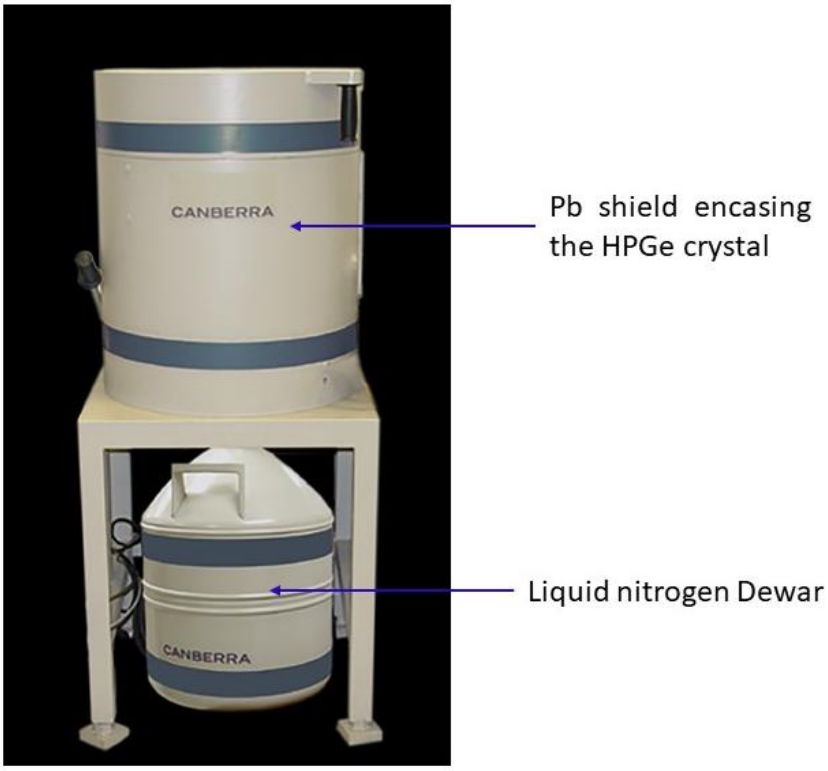

Figure 3.6a: Photo of a typical Pb shielded HPGe gamma-ray spectrometer with a liquid nitrogen Dewar [17].

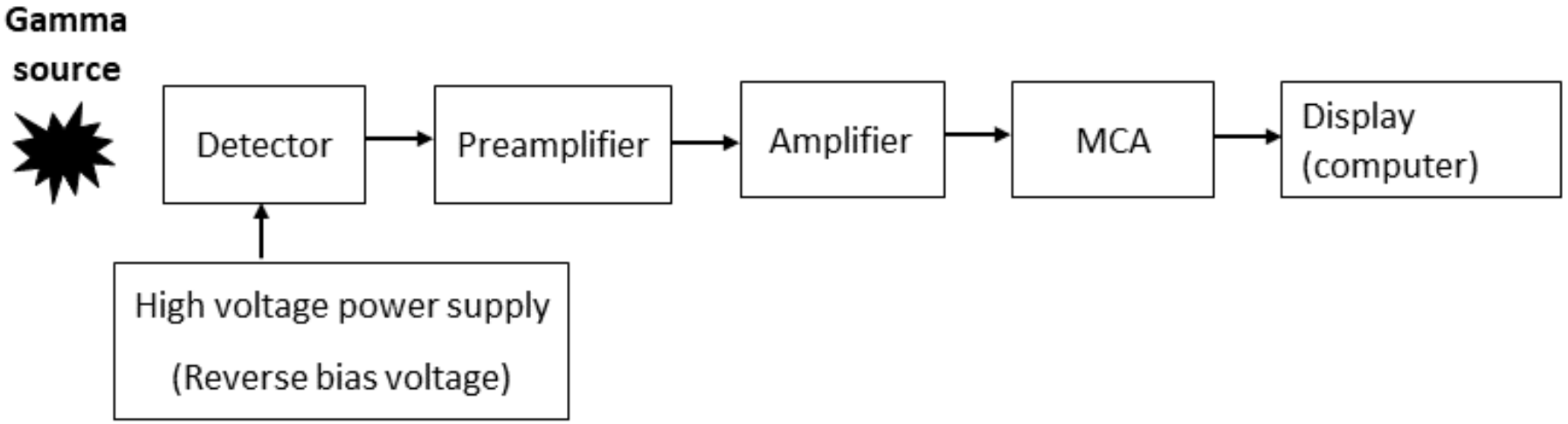

Figure 3.6b: Generic functional block diagram of an HPGe detector. Modified from [16].

3.3.3 Scanning electron microscopy

Scanning electron microscopy (SEM) is a powerful technique that is used to reveal textural, structural and compositional information about a sample. This vacuum technique uses a finely-focused energetic beam of electrons to bombard the surface of a sample, generating information-laden signals which are then detected using various scintillation or solid-state detectors coupled to it at different positions and angles. The signals generated include secondary electrons (SE), backscattered electrons (BSE), characteristic/fluorescence x-rays, Auger electrons and cathodoluminescence, with the common and most important being SE, BSE and characteristic x-rays (Figure 3.7). These signals originate from different depths within the sample (Figure 3.7). The advantage of SEM over optical microscopy (which is limited by the wavelength of visible light (400 nm - 700 nm)) is its ability to produce nanometre resolution and high magnification images of material surfaces, owing to the shorter wavelength of electrons (~1 nm).

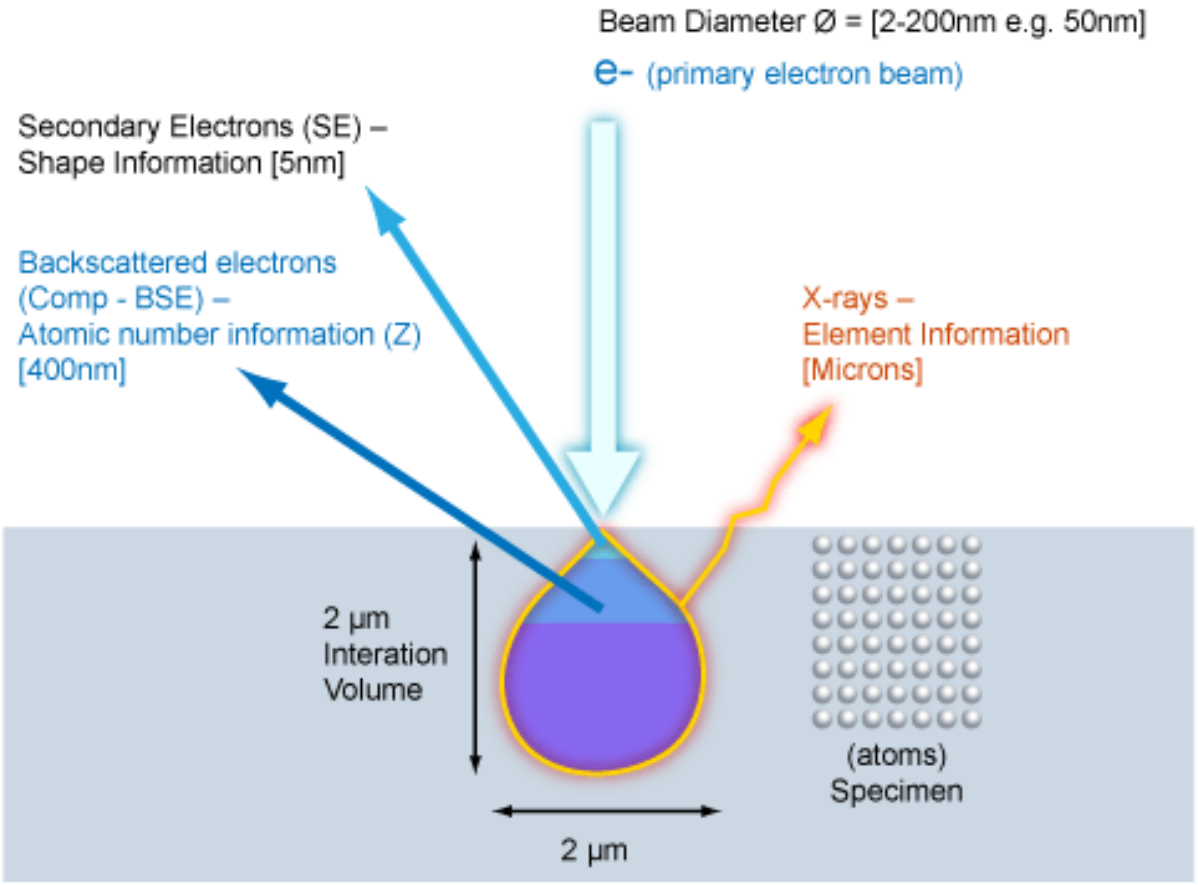

Figure 3.7: Types of SEM signals generated following electron beam-sample interaction, showing signal interaction depths [18].

Operation principles

Shown in Figure 3.8 is a schematic of a field emission gun (FEG) SEM showing its operational parts and the relative position of the installed detectors. The SEM produces an initial unrefined energetic beam of electrons (typically 1 kV - 40 kV) in the gun via field emission [19]. The electrons produced are focused, shaped, guided and controlled down the column towards the sample (in the sample chamber) by the combined action of the condensor, magnetic, objective and electrostatic lenses. The electron beam focused onto the sample surface is raster-scanned across the region of interest, producing signals that carry morphological and compositional information about the sample. To maintain a consistent

electron beam by preventing scattering and attenuation, the SEM is typically operated at a high vacuum.

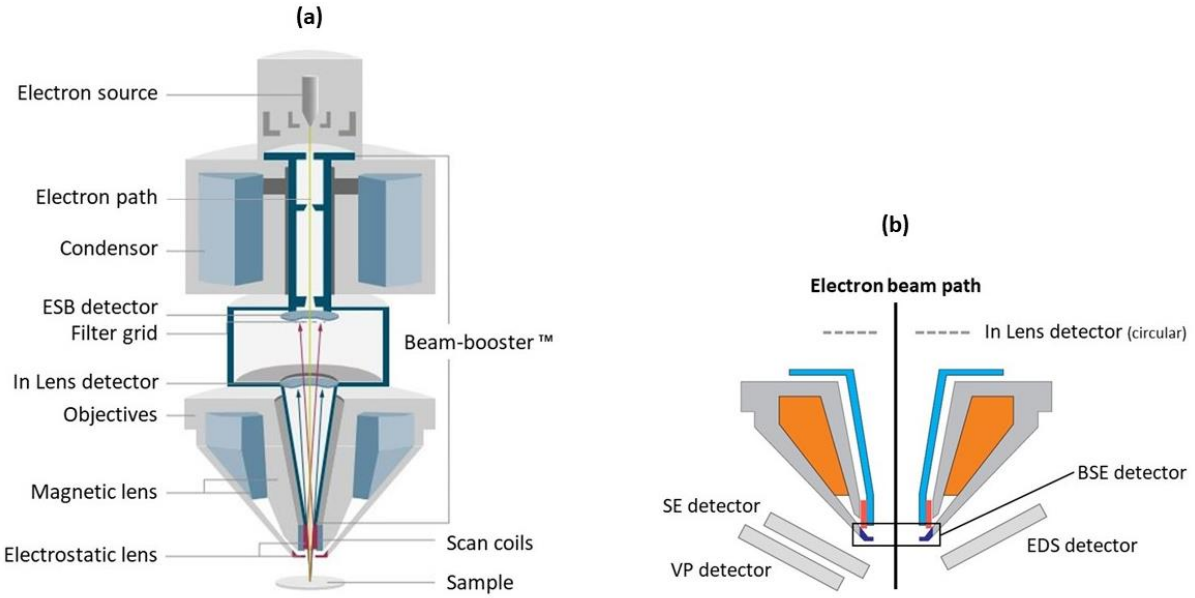

Figure 3.8: FEGSEM schematic showing the (a) various components (b) position of the detectors installed relative to the lower portion of its optics [14].

Figure 3.9 illustrates the three most important phenomena resulting from the primary electrons-sample interactions:

(i) SE result from ionisation of the atoms in the sample due to the impact of the energetic electron beam. They are low energy (<50 eV) electrons produced at the surface of the sample; SE emissions are, therefore, used to image sample surfaces (to reveal morphological details) with resolution approximating the size of the focused electron beam [20].

(ii) BSE result from elastic scattering of primary electrons by the nucleus of a scattering atom due to the strong columbic repulsive force of the nucleus. BSE are a function of the Z number of the scattering atom; high-Z atoms scatter the

primary electrons more because of their greater cross-sectional area. Thus, a contrast compositional map (made up of bright (high-Z) and dark (low-Z) spots) of the sample is generated, which helps to distinguish different phases in a sample.

(iii) Characteristic x-rays are emitted during SE production, where there is ionisation/ejection of inner shell electrons and refilling of the vacancies created by the ejected electrons by other electrons from the outer shells. The emitted characteristic x-rays are detected using energy dispersive spectrometry (EDS), typically making use of a Peltier-cooled solid-state silicon drift detector (SDD). Analysis of the characteristic x-rays in spot/point and/or mapping modes can yield information on the identity, distribution and concentration of elements in the sample. One drawback of most SEMs is the need to coat a non-conductive sample with a thin layer of conductor (e.g. Au or C) to negate surface charging that distorts the generated signal. Alternatively, an SEM can be operated in variable pressure (VP) mode to reduce surface charging without the need for coating.

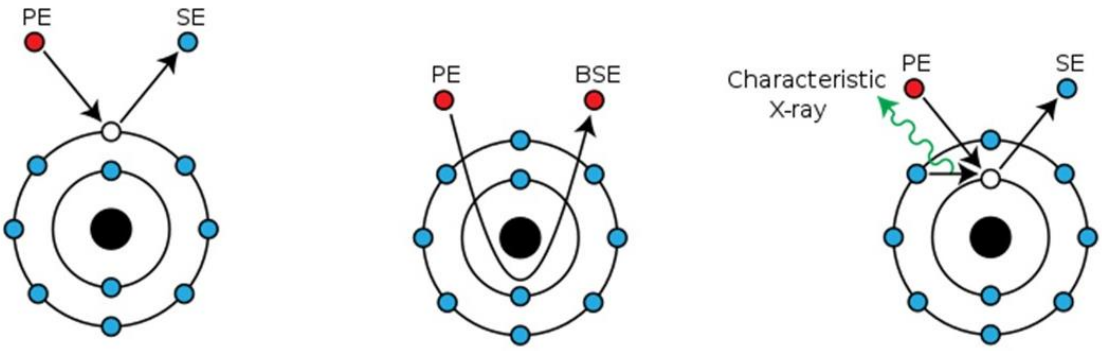

Figure 3.9: Three principal modes of electron emission following primary electron-sample interaction. PE: Primary electron; SE: Secondary electron; BSE: Backscattered electron [14].

3.3.4 X-ray analysis

X-rays are a type of electromagnetic radiation (ER) with the same properties (reflection, diffraction, interference, speed of light) as the other types of ER (gamma-ray, microwave, radiowave, etc). While gamma-rays originate from nuclear decay processes, x-rays arise from the processes of excitation or ionisation of atomic electrons [21] but interact with matter in a similar manner (as discussed in Section 3.3.2), leading to the generation of secondary x-rays characteristic of the elemental composition of the sample. These ER properties, alongside the generated secondary characteristic x-rays when the primary x-rays interact with a sample, are used to study materials, providing information on the morphology, structure (amorphous or crystalline) and elemental composition of such material.

X-ray generation

The primary X-rays, in a laboratory x-ray tube maintained at high vacuum, are produced by two principal processes: (i) rearrangement of electrons within shells following excitation or ionisation of the atoms in the target material (anode) when bombarded with electrons thermionically-emitted from the cathode, resulting in the production of characteristic X-rays, etc; (ii) deceleration of the thermionically-emitted electrons by the strong columbic attractive force of the nucleus of atoms in the target material, resulting in the production of bremsstrahlung x-rays.

However, x-rays produced at a synchrotron facility compared to typical laboratory sources are 10 orders of magnitude more intense and collimated, with fluxes of up to 10^{12} photons per second. As shown in Figure 3.10, in a synchrotron maintained at high vacuum electrons are first produced in an electron gun ((1) in Figure 3.10) and accelerated (within a linear

accelerator (2)) to a high energy (MeV) using radio frequency (RF) cavities and injected into the booster ring (3). The beam of electrons is further focused and the energy increased (MeV) within the booster ring before being injected into the storage ring (4), where the curving/deflection in a circular path, and focusing of the electron beam under the action of further magnets and RF cavities take place (5). Bending magnets and insertion devices – consisting of undulators and wigglers (6) are used to curve the electron beam around the storage ring, producing a broad spectrum of highly intense x-ray beams. The x-rays generated are emitted tangentially, passing through the beamlines optics cabin (7), where they are further focused and tuned prior to finally entering the experiment hutch (8) for controlled work from the safety of the beamline control cabin (9).

The highly-collimated and intense flux x-ray beam is also tunable, which makes synchrotron techniques more suited for material characterisation than laboratory equivalents. The main limitations of a synchrotron facility are the very high capital and running costs. In the following sections, the operation principles of laboratory and synchrotron techniques used in this study are explained.

Figure 3.10: Main components of a third-generation synchrotron facility [14].

Laboratory x-ray techniques

X-ray fluorescence

Laboratory-based XRF, which works on the principle of photoelectric absorption (explained in Section 3.3.2), can provide information on the elemental composition of bulk samples. In this study, a Niton^{TM} 950 series field x-ray lab system was used to determine the major elements (as oxide ratios) and trace heavy toxic metals in the bulk coal fly ash samples. This XRF analyser has a Ag anode with 50 kV / 80 µA (maximum) x-ray tube, a Si-p-i-n semiconductor detector (a silicon pn diode with an intrinsic layer sandwiched between the pn junction), alongside an integrated camera used to monitor sample position during analysis. It is self-calibrating, running factory-installed calibration software (called "Fundamental Parameter"), to quickly and accurately measure major and trace elemental concentrations and automatically correct

for matrix and inter-element effects. The analyser also has in-built filters (**main** filter for the transition elements; **high** filter for the heavy elements with atomic number, (Z) = 47 to 56; **light** filter for the light elements with Z<17), that allows modification of the x-ray energy to preferentially boost the fluorescence of certain elements in certain matrices. This analyser (with a stated limit of detection less than 5 $mgkg^{-1}$) [22], is suitable for both pelletised samples and powdered samples (in an xrf sample cup).

X-ray diffraction

X-ray diffraction (XRD) is a bulk analytical technique suited for the identification and quantification of crystalline content and phases in a powder sample made up of randomly-oriented crystallites, using the characteristic diffraction pattern produced when a collimated beam of mono energetic x-rays interacts with atomic planes in such material. This technique has applications in the pharmaceutical and glass industries, forensics, materials and earth sciences.

Operation principles

A crystalline material has a well-ordered and periodically arranged atomic (lattice) planes; when such material is illuminated with a monochromatic x-ray beam, the x-rays (with wavelength comparable to interatomic spacing) are coherently scattered and reflected (Figure 3.11). The reflected x-rays constructively interfere along certain lattice planes within the material to produce a diffraction pattern made up of intensity peaks, characteristic of the material. The samples for XRD analysis are typically finely powdered to enhance x-ray penetration and diffraction.

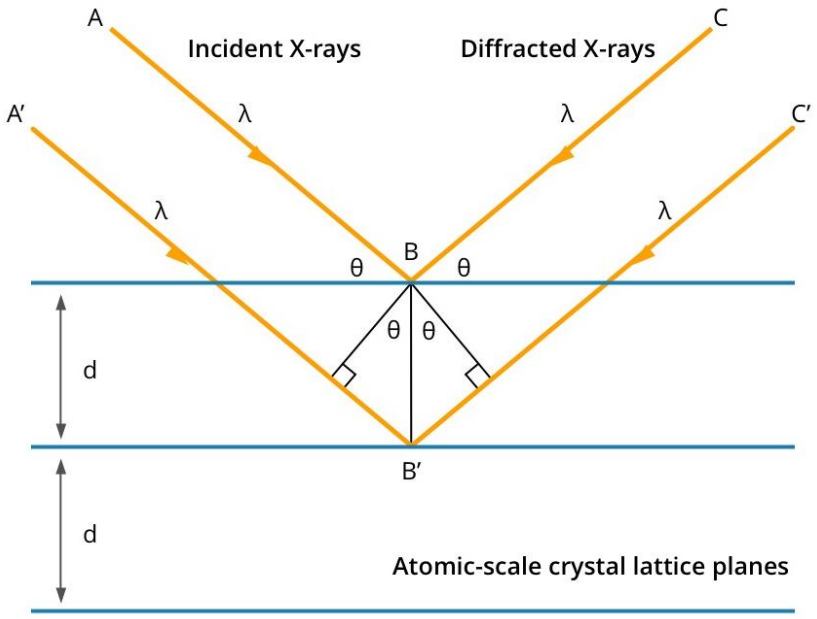

Figure 3.11: XRD beam schematic [23].

The condition for constructive interference leading to the production of an XRD pattern is described by Bragg's law (Equation 3.1), relating the wavelength (λ), angle of incidence (θ) and lattice spacing (d), where n is a whole integer. For diffraction to occur at a given angle, the wavelengths of the incident and diffracted beams must be the same.

$$\mathbf{n\lambda = 2dsin\theta} \tag{3.1}$$

A standard XRD instrument is made up of five main components (Figure 3.12), namely: (i) x-ray source, an evacuated x-ray tube which generates an x-ray beam; copper K_α radiation (λ=51.5418Å) is the most commonly used incident x-ray radiation; (ii) primary optics, which focus and fine tune the x-rays into a more collimated and monochromatic beam, using slits and monochromators; (iii) sample stage, where the sample is positioned to be irradiated; (iv) secondary optics with detector, which receive and record the diffracted x-rays coming from the sample; and (v) equipment goniometer to change the angle of the x-ray source and the detector relative to the sample.

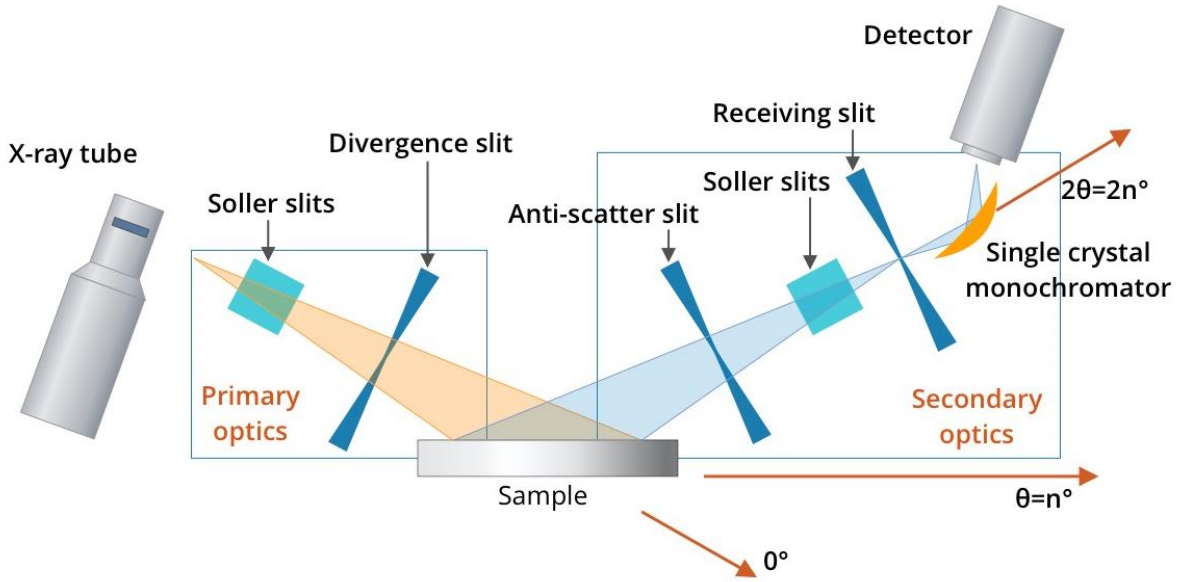

Figure 3.12: XRD setup schematic showing main parts [24].

Synchrotron x-ray techniques

In this study, µ-XRF, µ-XRF tomography, micro x-ray absorption near-edge structure (µ-XANES) and µ-XRD analyses of coal fly ash derived monazite particles were performed at the Diamond Light Source (DLS) on the micro-focus spectroscopy beamline (I18). Located in Harwell, Oxfordshire, the DLS is a medium-energy third-generation synchrotron with the storage ring operating at 3 GeV and has a nominal beam current of 300 mA, with typical fluxes of 2 x 10^{12} photons per second at 10 keV [25]. A schematic is shown earlier in Figure 3.10.

I18 beamline

The I18 beamline (at DLS), with an energy range of 2.05 keV to 20.5 keV, is equipped with a cryogenically-cooled double crystal Si[111] monochromator (for energy tuning) and Kirkpatrick-Baez mirrors for focusing of the beam (to a spot of 2 µm × 2 µm) onto the sample, and harmonic rejection. The beamline was equipped with a Vortex-ME4™ multi-element SDD and a high-resolution photonic science™ scientific complementary metal-oxide-

semiconductor (sCMOS) x-ray camera for μ-XRF, μ-XRF tomography, μ-XANES and μ-XRD. To prevent detector saturation, a 0.1 mm Al foil was inserted prior to all the analyses performed on the beamline. Throughout all sample analyses, consistent beam, sample and detector geometry were maintained. Figure 3.13 is a labelled photograph showing the experimental setup of the I18 beamline.

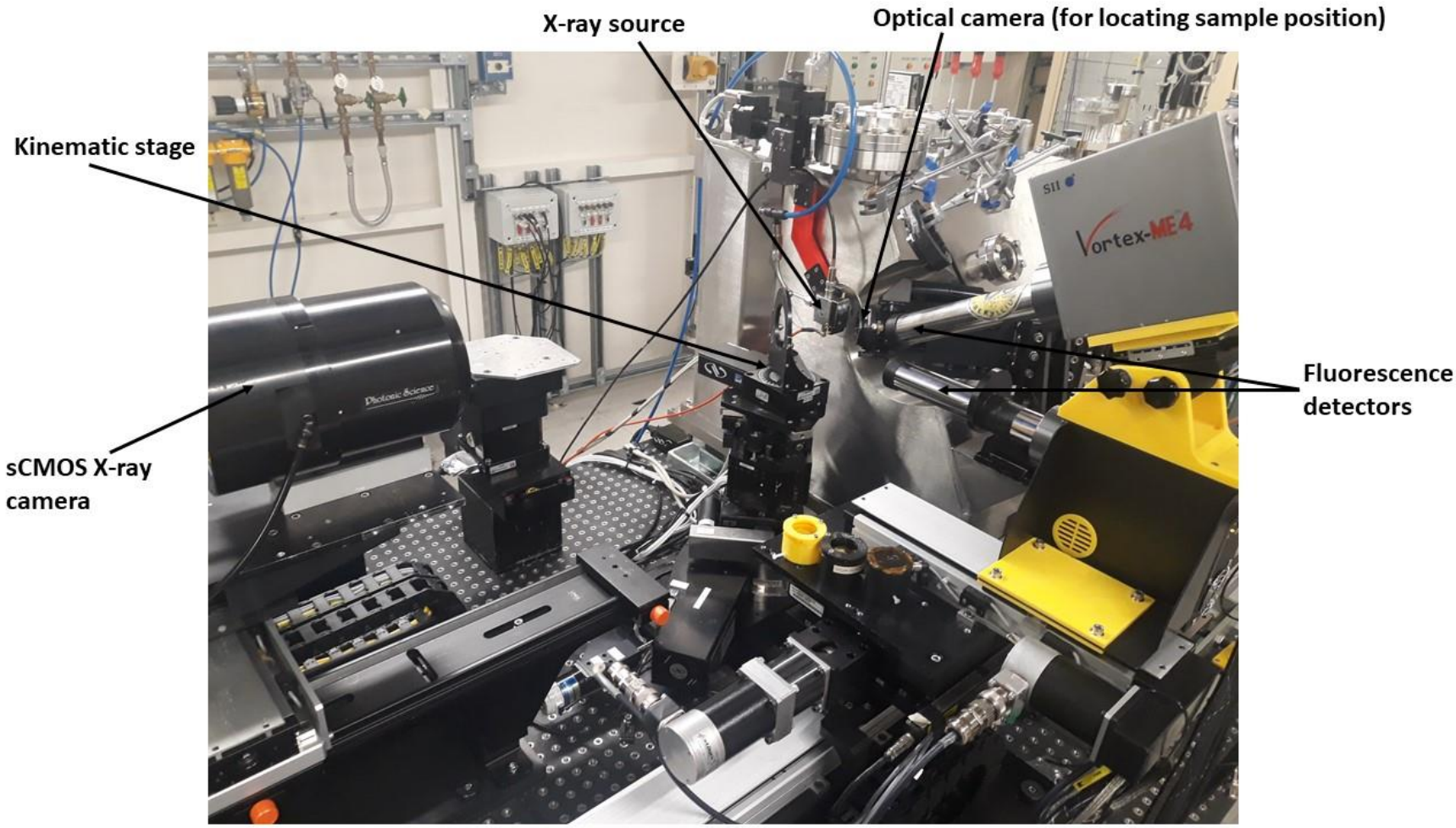

Figure 3.13: Labelled photograph of experimental setup on the I18 beamline.

μ-XRF mapping

In μ-XRF mapping, a tuned and focused synchrotron x-ray beam is used to illuminate and raster-scan a small user-defined region on a sample, and the secondary x-rays/fluorescence x-rays produced from the sample are collected using an SDD and processed to produce a 2D elemental compositional map of the sample over the region illuminated. Each fluorescence x-ray produced has specific energy which is a fingerprint of the atom that produced it.

μ-XRF tomography

μ-XRF tomography is a non-destructive and non-invasive technique which provides information (in a 3D view) of the interior features and the spatial distribution of elements within a sample. This basically involves bombarding a sample with the highly-focused and penetrating synchrotron x-ray beam while the sample is translationally raster-scanned while being rotated (180°) through the x-ray beam at a set angular step size. Fluorescence x-rays emitted by the sample are collected as 2D radiograph images (slices) from each fluorescence projection and then reconstructed into a 3D volumetric rendering of the sample using iterative algorithms. While μ-XRF tomography provides information on both the structure and distribution of elements within the interior of a sample, 'non-XRF' tomography provides only structural information based on the decrease in intensity (attenuation) of the x-ray beam within a sample due to variation in density of the sample. This decrease in intensity is described by Beer's law (Equation 3.2) as a function of linear attenuation coefficient (μ) of the absorbing material, energy of the x-ray, density and atomic number (Z) of the material. Therefore, a 3D contrast image is formed, with dense regions and less dense regions (such as cracks and voids) within the sample appearing dark and bright, respectively; the dense regions absorb more x-rays and the less dense regions are more transparent to x-rays:

$$I = I_0 . e^{-\mu . x} \quad (3.2)$$

where I and I_0 represent the incident and transmitted x-ray beam intensities, respectively.

μ-XANES

X-ray absorption spectroscopy theory

X-ray absorption spectroscopy (XAS) is a non-destructive technique that uses synchrotron radiation to reveal information about the local atomic structure as well as the oxidation state of elements in a sample from the absorption spectrum. This technique relies on photoelectric absorption (discussed in Section 3.3.2).

At energies equal to or above the binding energy of the core electron, an abrupt rise in x-ray absorption is observed, leading to what is called an absorption edge (Figure 3.14). As shown in Figure 3.14, an XAS spectrum is made up of three parts, namely: pre-edge; XANES; extended x-ray absorption fine structure (EXAFS) [26]. The pre-edge region, lying about 10 eV below the absorption edge, provides information on coordination chemistry and disorder around the absorbing atom. The XANES region, which spans ~10 eV below and ~20 eV above the absorption edge, is dominated by intense and narrow oscillations resulting from the constructive and destructive interferences of x-rays scattered by atoms neighbouring to the absorbing atom. From the shape and position of the absorption edge, this region of the spectrum provides information on the oxidation state of elements in a sample. This region was used here to investigate the oxidation state of some rare earth elements (REEs) and actinide (U), to invoke the impact of combustion on their oxidation states and to understand how that influences their subsequent environmental mobility and fate. Finally, the EXAFS region typically starts ~50 eV from the absorption edge with less pronounced oscillatory

behaviour, and reveals information on the local structure and surrounding atoms of the studied element.

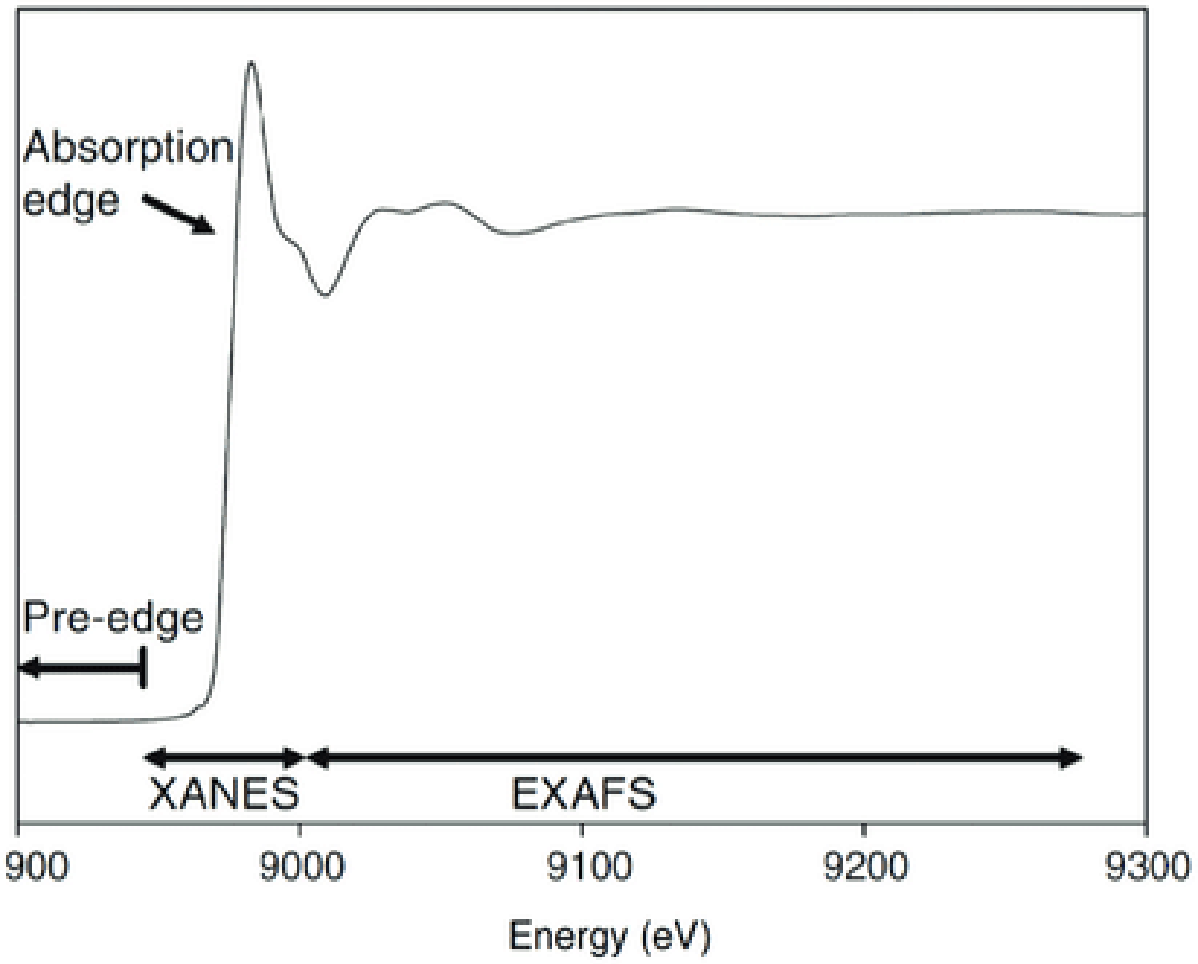

Figure 3.14: XAS spectrum showing the three regions [26].

μ-x-ray diffraction (μ-XRD)

As explained in Section 3.3.4.1, XRD relies on the constructive interference of x-rays reflected from atomic planes within a material, governed by Bragg's law. Compared to laboratory-based XRD, synchrotron μ-XRD uses a highly-focused x-ray beam to illuminate a very small volume of a sample, using a pencil beam. This is ideal for mapping μ- and nm-size mineral particles and thin foils, to reveal crystallographic information. In this study, the crystal structure of coal fly ash derived monazite micro particles post-combustion was studied to

investigate the effect of the high combustion temperature, with the aim of providing valuable information relevant for REE recovery method optimisation and/or development.

3.4 Summary

This chapter has described the coal materials, the simulant coal fly ash materials and the array of complementary analytical techniques used for the interrogation of the coal and simulant coal fly ash materials presented in this thesis. The selection of techniques is suited specifically to sub-millimetre size particles, to either be analysed as bulk powders or, as individual particles.

It is the isolation and micro-analysis of individual microparticles which is particularly challenging and novel for the analytical component of this thesis. Table 3.2 is a summary of the techniques and the information derived from each technique.

Table 3.2: Summary of techniques used in this study.

Method	**Scale**	**Information provided**
Laboratory XRF	Bulk	Major and trace elemental composition
Laboratory XRD	Bulk	Major mineral phases
SEM-EDS	μm to nm	Identification of micro mineral phases (mainly REE-bearing and radioactive mineral particles), their distribution and morphology
ICP-MS	Bulk	1. REEs concentration 2. REEs partitioning in coal and simulant coal fly ash
Gamma spectrometry	Bulk	Specific activity concentration of ^{226}Ra, ^{228}Ra, ^{228}Th and ^{40}K, and the associated radiological health risks
Synchrotron μ-XRF	μm to nm	2D mapping of REEs and radionuclides distribution within isolated REE, U and Th mineral particles
Synchrotron μ-XANES	μm to nm	REE, U oxidation state
Synchrotron μ-XRF tomography	μm to nm	3D mapping of REEs and radionuclides distribution within isolated REE, U mineral particles
Synchrotron μ-XRD	μm to nm	Crystallography of isolated REE-bearing particles

3.5 References

[1] Final report on resettlement action plan (RAP) for Adumu road - Ogugu erosion site, Olamaboro local government area, submitted to Kogi State Nigeria erosion and watershed management project (KSG-NEWMAP). http://documents1.worldbank.org/curated/en/248831545297215514/pdf/Final-World-Bank-Cleared-Report-for-ADUMU-Gully-Erosion-Site-Copy.pdf (2018) (accessed 28 September 2020).

[2] Aizebeokhai A.P. Potential impacts of climate change and variability on groundwater resources in Nigeria. African Journal of Environmental Science and Technology, 5 (2011) 760-768.

[3] Fatoye Felix Bamidele. Geology and Mineral Resources of Kogi State, Nigeria. International Journal of Multidisciplinary Sciences and Engineering, 9 (2018) 7-13.

[4] Onoduku U.S. Geochemical evaluation of Okaba (Odagbo) coal deposit, Anambra Basin, Nigeria. Research Journal of Science and IT Management, 03 (2014) 11-16.

[5] Ministry of Solid Minerals Development, Federal Republic of Nigeria. Feasibility study: Nigerian coal resource development. https://electricityinnigeria.com/ (2006) (accessed 18 March 2019).

[6] Chukwu M., Folayan C.O., Pam G.Y., Obada D.O. Characterisation of some Nigerian coals for power generation. Journal of Combustion, 2016 (2016) 11 pages.

[7] Okeme I.C., Scott T.B., Martin P.G., Satou Y., Ojonimi T.I., Olaluwoye M.O. Assessment of the mode of occurrence and radiological impact of radionuclides in Nigerian coal and resultant post-combustion coal ash using scanning electron microscopy and gamma-ray spectroscopy. Minerals, 10 (2020) 241p.

[8] Honaker R.Q., Zhang W., Werner J. Acid Leaching of Rare Earth Elements from Coal and Coal Ash: Implications for using fluidized bed combustion to assist in the recovery of critical materials. Energy & fuels, 33 (2019) 5971-5980.

[9] Pulverised coal combustion (PCC). https://www.iea-coal.org/pulverised-coal-combustion-pcc/ (Accessed 4 January 2018).

[10] Radboud University. General instrumentation - ICP-MS. https://www.ru.nl/science/gi/facilities-activities/elemental-analysis/icp-ms/#:~:text=Atomic%20elements%20are%20lead%20through,Extremely%20low%20detection%20limits (accessed 7 September 2020).

[11] Dean JR.. Practical inductively coupled plasma spectroscopy. Chichester: John Wiley & Sons (2005).

[12] Radiation dosimetry: what is gamma spectroscopy-definition? https://www.radiation-dosimetry.org/what-is-gamma-spectroscopy-definition/ (2019) (accessed 7 September 2020).

[13] Semiconductors and semimetals semiconductors for room temperature nuclear detector applications; edited by Schlesinger T.E., B. James R.B. 43 (1995) 1-606.

[14] Martin, Peter George. The 2011 Fukushima Daiichi Nuclear Power Plant accident: an analysis over 10 orders of magnitude (Doctoral dissertation, University of Bristol). Institution repository https://research-information.bris.ac.uk/en/studentTheses/the-2011-fukushima-daiichi-nuclear-power-plant-accident (2018).

[15] Oncology Medical Physics. Basic radiation physics. https://oncologymedicalphysics.com/basic-radiation-physics/ (accessed 7 September 2020).

[16] Gordon Gilmore. Practical gamma-ray spectrometry. Chichester: John Wiley & Sons (1995).

[17] Mirion technologies. The Mirion 777 lead shield system. https://www.mirion.com/products/777-ultra-low-background-shield (accessed 26 December 2020).

[18] Myscope. Generation of x-rays in the electron microscope. https://myscope.training/legacy/analysis/eds/xraygeneration/ (accessed 25 September 2020).

[19] Myscope. Scanning electron microscopy. https://myscope.training/#/SEMlevel_3_5 (accessed 25 September 2020).

[20] Joseph G., Dale N., David J., Charles L., Patrick E., Eric L., Linda S., Joseph M. SEM and x-ray microanalysis. 3rd edition. Kluwer Academic / Plenum publishers (2003).

[21] Murray R., Holbert K. Nuclear energy: an introduction to the concepts, systems, and applications of nuclear processes (7th edition). Oxford: Butterworth-Heinemann (2015).

[22] Thermo Fisher Scientific. Thermo Scientific Niton FXL 950 series analyser. Tech. rep. Winchester: Niton UK limited; 2017, P1.

[23] Myscope. Xray diffraction. https://myscope.training/#/XRDlevel_2_10 (accessed 21 September 2020).

[24] Myscope. Xray diffraction. https://myscope.training/#/XRDlevel_3_3 (accessed 21 September 2020).

[25] Diamond Light Source (DLS). How DLS works. https://www.diamond.ac.uk/Home/About/How-Diamond-Works.html (accessed 12 September 2020).

[26] Mottana A., Marcelli A. The historical development of x-ray absorption fine spectroscopy and of its applications to materials science; in: History of mechanism and machine science, vol. 27. Dordrecht: Springer (2015).

Chapter 4

Elemental composition and mineralogical analysis of simulant coal fly ash samples

One vital stage during REE recovery from both conventional and unconventional sources is the beneficiation phase where the elements of interest are separated from the gangue materials and concentrated. This phase, which can include magnetic, electric, gravitational and/or froth floatation processes, is used to further concentrate REE minerals (to between 50% and 80%) prior to acid leach treatment and selective extraction of each REE. The cost-effectiveness of the beneficiation processes is dependent on the physical and chemical natures of the source material derived from the elemental and mineralogical characteristics of the REE minerals and associated gangue minerals.

Evaluation of the cost implications of REE recovery from coal fly ash and the radiological health risks posed by coal fly ash depend on the concentration and forms of occurrence of the chemo- and radio-toxic trace elements, such as U, Th, As, Cr, Cd and Pb. Since these elements are highly regulated, this information is vital for the assessment of the cost and potential negative environmental and health impacts resulting from the extraction and separation of rare earths from coal fly ash, or disposal of the coal fly ash. For example, due to lax environmental standards and poor management, the Government of both China and Malaysia are grappling with the negative environmental impacts and the high clean-up costs of pollutants and radioactive wastes from REE processing operations in both countries [1].

This chapter focuses on the elemental and mineralogical analysis of the simulant coal fly ash samples (OMA, OKA, ODA), their implications on REE recovery from coal fly ash and the hazards associated with handling these materials. Results of bulk and micro elemental composition and mineralogy analyses using laboratory XRF, XRD and SEM-EDS are presented and discussed with respect to the implications on REE recovery, and the environmental and human impacts. In addition, the effect of the coal combustion temperature on the formation of secondary mineral and amorphous phases is highlighted.

The methods and results presented in this chapter have formerly been published in the peer-reviewed literature:

Ilemona C. Okeme, Thomas B. Scott, Peter G. Martin, Yukihiko Satou, Theophilus I. Ojonimi, Moromoke O. Olaluwoye. Assessment of the mode of occurrence and radiological impact of radionuclides in Nigerian coal and resultant post-combustion coal ash using scanning electron microscopy and gamma-ray spectroscopy. *Minerals*, 10 (2020) 241p.

Ilemona C. Okeme, Peter G. Martin, Christopher Jones, Richard A. Crane, Theophilus I. Ojonimi, Konstantin Ignatyev, Dave Megson-Smith, Thomas B. Scott. An advanced analytical assessment of rare earth element concentration, distribution, speciation, crystallography and solid-state chemistry in fly ash. *Spectrochimica Acta Part B: Atomic Spectroscopy*, 2020.

4.1 Experimental Methods

4.1.1 X-ray fluorescence (XRF)

In this study, a benchtop Niton™ 950 series field x-ray fluorescence system was used to determine the major elements (as oxide ratios) and trace heavy toxic metals in the bulk fly ash samples. A total of 15 fly ash samples per coal mine were analysed by XRF. Prior to sample analysis, the calibration of the analyser was confirmed by running two reference materials (USGS SdAR-M2, NIST 2709a). For analysis, the pulverised, homogenised and sieved fly ash samples (preparation detailed in chapter 3, Section 3.2.1) were each packaged into single open-ended polyethylene XRF sample cups (inner diameter 32 mm; height 24 mm), with the open end sealed using a polypropylene thin film with gauge thickness of 4 µm. To ensure an accurate reading, each sample was scanned for 2 minutes (live time); the analysis (peak identification, fitting and quantification) of the XRF spectra obtained was performed using the Thermo Scientific Inc. NDT™ analysis package.

4.1.2 X-ray Diffraction (XRD)

Mineralogical analysis of the bulk fly ash samples was performed on composite OMA, OKA and ODA bulk fly ash samples (packed level into aluminium XRD stubs) using a Philips X'pert™ diffractometer system with a Cu anode operated at 40 kV / 30 mA. The diffractometer uses a θ:θ arrangement where, during data acquisition, the sample remains stationary while the x-ray source and detector both move simultaneously over the angular range of θ, with the x-ray beam maintained on the sample. The scans were run from 10° to 80° 2θ, with increments of 0.07° and a counting time of 10 s per step. Identification and quantification of the mineral phases was performed using the Match™ phase identification package; XRD can

only provide analysis of crystalline phases within materials whilst amorphous (or glass) phases are not identified.

4.1.3 Scanning electron microscopy with energy dispersive spectroscopy (SEM-EDS)

SEM-EDS was used to study the REE-bearing and actinide-bearing micro-mineral phases in the coal and fly ash samples. To do this, representative composite samples were prepared by depositing a fine layer (<1 g) onto a 12 mm low elemental background adhesive carbon (Leit) disc mounted on a standard SEM pin-stub. 10 subsamples each for the coal (OMC, OKC, ODC) and simulant coal fly ash (OMA, OKA, ODA) samples were prepared as described above for analysis. The samples were then examined using a Zeiss SIGMA™ field emission SEM fitted with secondary electron, SE (Everhart Thornley SE2) and backscattered electron, BSE (AsB) detectors. Samples examination was performed using the instrument's VP mode, thereby avoiding the need for a conductive coating to negate surface charging that distorts the generated signal. Figure 4.1 shows a labelled image of the electron microscope's chamber detailing the relative positions of the primary x-ray source, sample stage, detectors and a Kleindiek MM3A^{TM} micromanipulator (explained and used in chapter five).

Using the AsB BSE detector, mineral particles containing trace levels of high-Z elements in the samples (e.g. REE minerals and actinides) appeared as bright (white) spots against the otherwise dark (low Z) sample background. REE and actinide mineral particles were then identified based on their characteristic elemental composition following confirmatory EDS analysis. The elemental composition and, subsequently, the mass fraction (wt% ± absolute error, δ) were determined using an EDAX™ Octane Plus high-resolution EDS system comprising an electronically-cooled silicon drift detector, SDD. At a voltage of 30 keV,

aperture of 120 µm (in high current mode) and acquisition time of 200 s, the whole surface of each identified REE and actinide mineral particle was raster-scanned, and data analysis undertaken using the associated EDAX (AMETEK Inc.) TEAM™ software.

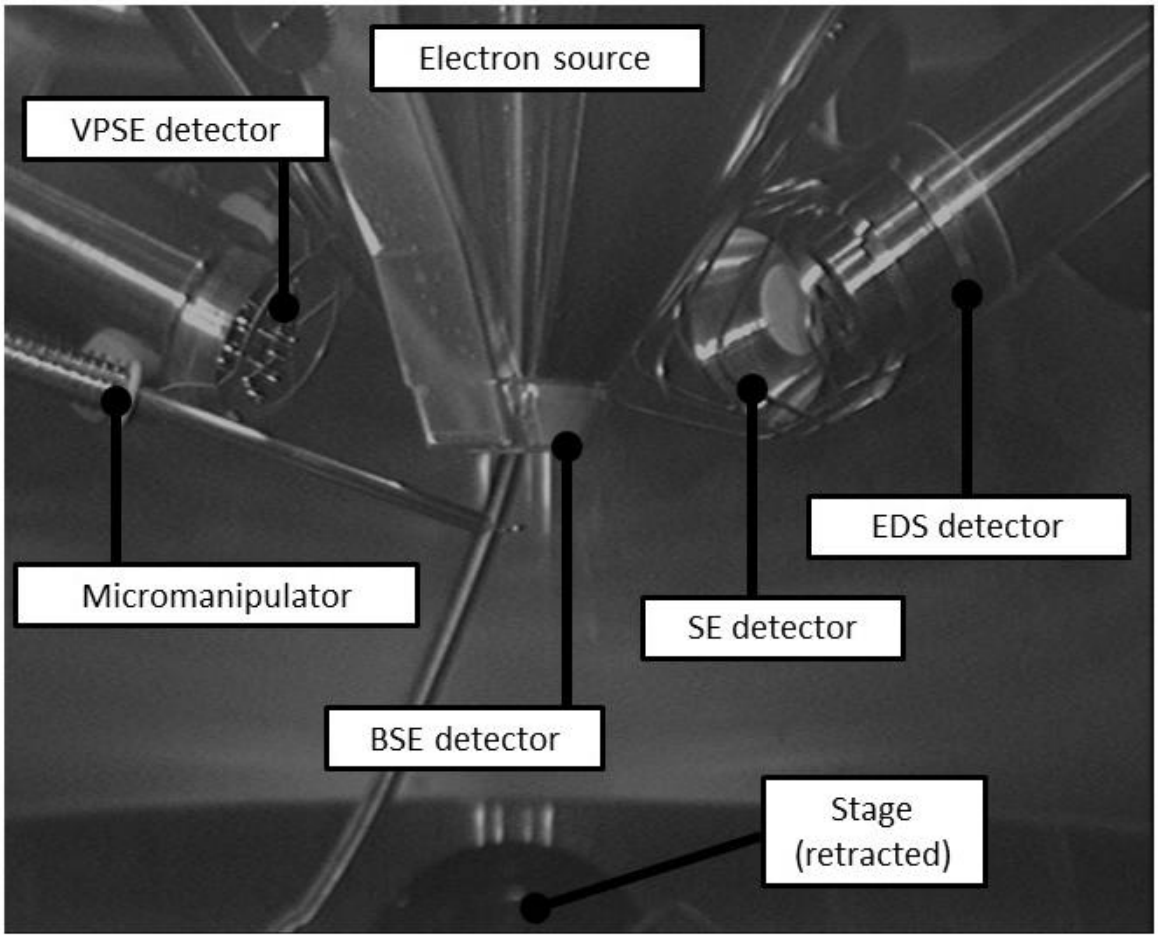

Figure 4.1: Labelled image of the Zeiss SIGMA™ electron microscope chamber. From [2].

4.2 Results and discussion

4.2.1 XRF

Table 4.1 shows the XRF results for OMA, OKA and ODA simulant coal fly ash samples. The XRF results (wt% ± 2σ) show that the fly ash samples are largely composed of SiO_2 (>54%) and Al_2O_3 (>19%), with less amounts (2% to 7%) of Fe_2O_3, TiO_2 and CaO (except for OMA samples with less than 1% CaO). In OMA, OKA and ODA samples, the sum of SiO_2, Al_2O_3 and Fe_2O_3 were greater than 70%, with CaO also less than 8%; this, according to the ASTM reference standard defines OMA, OKA and ODA fly ash as class F, suitable for use as cement supplement due to its cementitious properties [3]. A previous study has shown that high calcium concentration (as in the case of OKA and ODA) increases extractability of REE associated with calcium-bearing phases in the fly ash, due to the high solubility of the calcium-bearing phases in nitric acid [4]. These results are comparable with studies on fly ash sourced from coal-fired power plants [5,6].

The U contents ($mg.kg^{-1}$) of OMA, OKA and ODA were 12.1 $mg.kg^{-1}$, 11.4 $mg.kg^{-1}$and 10.5 $mg.kg^{-1}$, respectively, with Th content ($mg.kg^{-1}$) of 30.0 $mg.kg^{-1}$, 25.5 $mg.kg^{-1}$ and 28.6 $mg.kg^{-1}$, respectively. The U and Th content in these coal fly ash materials are in the range found in most granitic and phosphate rocks, as well as shales; but, relative to the ash volume, these concentrations are significant and can be considered as potential added value to the REEs if also recovered, but do not pose a level of radioactive risk associated with the fly ash that must be managed and reduced if deemed unacceptably high. The development of Th-based nuclear reactors is gaining significant momentum, a consequence of the several notable advantages of Th-based fuel over U fuels (such as core-meltdown-proof, less waste generation, higher

energy efficiency and little or no weapons-grade by-products) [7]. A recent study led by the United States Department of Energy [7] has developed a Th-based nuclear fuel, ANEEL ('Advanced Nuclear Energy for Enriched Life'), which combines Th and high assay Low Enriched U), a potential breakthrough in the revival of Th-based reactors. This development in addition to the deal between the Nigerian Government and the Russian government for the construction and operation of two nuclear power plants in Nigeria [8], gives credence to profitability of Th and U recovery from coal fly ash.

The highest value for Pb (95.6 $mg.kg^{-1}$) was recorded for ODA; with the lowest value of As (6.5 $mg.kg^{-1}$) recorded for OMA. While Cd was not detected, Cr had concentrations with values of 255.7 $mg.kg^{-1}$, 200.6 $mg.kg^{-1}$ and 185.2 $mg.kg^{-1}$ in OMA, OKA and ODA, respectively. Studies have shown that while these trace elements are associated with mineral forms, they are more concentrated in the very fine particulate fly ash, adsorbed on the surfaces of fine particles during combustion [9,10]. The toxicity (such as carcinogenesis and mutagenesis) of Cr is oxidation state dependent, with Cr (VI) – being the more soluble and bioavailable, much more toxic compared to Cr (III) [11]. Studies have shown that Cr exist in mixed oxidation states in coal fly ash following the oxidation of Cr (III) in the precursor coal, to Cr (IV) during combustion [11,12]. The valence state(s) of Cr in the simulant coal fly ash would be proven in future work using X-ray absorption near edge spectroscopy (XANES) to establish the risk posed by inhalation or escape into nearby water sources.

Although occurring only as tens up to hundreds of $mg.kg^{-1}$, because of the large volume of fly ash generated annually, the trace chemo- and radio-toxic heavy metals (Pb, As, Cr, U, Th) are of environmental concern if the fly ash is not stored correctly, which comes at a financial cost. During fly ash disposal or utilisation in different environmental conditions, these toxic metal-

laden particles may become (re)suspended and, if inhaled, would be deposited in the lungs, potentially leading to respiratory illnesses and internal radiation exposure [13]. Leaching of these metals into local water bodies could cause contamination and harm to aquatic life forms [14]. Equally, rare earth extraction is also typically capital-intensive; for example, during REE extraction using acid leaching these trace elements become concentrated in the wastewater and, if not properly contained in surface impoundments may seep into the ground or local river courses. For this reason, wastewater from the REE extraction process is held in bonded ponds with impermeable liners, which is capital-intensive due to high operating costs involved in the surveillance and maintenance of the ponds.

Table 4.1: Average elemental composition of simulant coal fly ash, derived from XRF analysis.

Oxide	Mean elemental composition (wt%)		
	OMA	OKA	ODA
SiO_2	54.4 ± 0.1	56.1 ± 0.2	54.3 ± 0.2
Al_2O_3	19.6 ± 0.1	19.30 ± 15	19.1 ± 0.2
Fe_2O_3	6.40 ± 0.02	3.80 ± 0.02	5.10 ± 0.02
CaO	0.66 ± 0.01	5.60 ± 0.03	5.80 ± 0.03
K_2O	0.49 ± 0.01	0.78 ± 0.01	0.50 ± 0.02
TiO_2	2.70 ± 0.01	2.50 ± 0.01	2.60 ± 0.01
ZrO_2	0.10 ± 0.001	0.08 ± 0.001	0.07 ± 0.001
MgO	0.32 ± 0.01	0.70 ± 0.01	0.35 ± 0.01
MnO	0.02 ± 0.002	0.06 ± 0.002	0.06 ± 0.002
BaO	0.01 ± 0.002	0.06 ± 0.01	0.05 ± 0.01
SrO	0.01 ± 0.001	0.04 ± 0.001	0.03 ± 0.001
SO_3	0.11 ± 0.005	0.95 ± 0.01	0.87 ± 0.01
P_2O_5	0.04 ± 0.007	0.09 ± 0.01	0.07 ± 0.01
U ($mg.kg^{-1}$)	12.1 ± 1.8	11.4 ± 2.4	10.5 ± 2.5
Th ($mg.kg^{-1}$)	30.0 ± 1.8	25.5 ± 1.7	28.6 ± 2.0
Pb ($mg.kg^{-1}$)	17.4 ± 2.3	20.3 ± 2.3	95.6 ± 3.8
As ($mg.kg^{-1}$)	6.5 ± 1.6	18.2 ± 1.6	20.4 ± 2.7
Cr ($mg.kg^{-1}$)	255.7 ± 14.1	200.6 ± 12.5	185.2 ± 16.2
Cd ($mg.kg^{-1}$)	ND	ND	ND

ND: Not detected; Reported error: 2 sigma (2σ).

4.2.2 XRD

Figures 4.2, 4.3 and 4.4 show the results (in wt%) of XRD analysis of OMA, OKA and ODA simulant coal fly ash samples, respectively. The results show quartz (SiO_2) and mullite ($3Al_2O_3.2SiO_2$) exist as the major mineral phases alongside trace amounts (less than 1%) of haematite (formed from the oxidation of pyrite during the high temperature combustion process) and cristobalite (a polymorph of quartz formed during the high temperature combustion process). These results are comparable with XRD studies on fly ash samples from coal-fired power plants [6,15]; these show the mineralogy of coal fly ash to consist of primary mineral phases from the precursor coal (such as crystalline quartz), secondary mineral phases (such as mullite, cristobalite, haematite) and amorphous glassy phase – the largest component formed during the high temperature combustion process.

Though the presence of Ti and Zr (identified by XRF analysis) is indicative of the heavy minerals ilmenite and zircon, these mineral phases were not detected during XRD analysis as a result of their low concentrations. For all fly ash samples, compared to fly ash sourced from coal-high temperature (≥1,700 °C) fired electric power plants the XRD spectra show only a very small hump (indicative of low amount of amorphous glassy phases) between 20° to 30° 2θ. This is attributable to the low combustion temperature of the coal and hence, glass was not substantially formed. This indicates little or no encapsulation of the REE minerals in glassy phases, which is an advantage for REE recovery as harsh organic acid treatment is required to libertate REE minerals otherwise encapsulated in such glassy phases [6]. To further probe the micro mineral phases the REEs, U and Th were associated with, microanalysis of the fly ash samples was carried out using SEM-EDS, the results of which are presented in the next section (4.3).

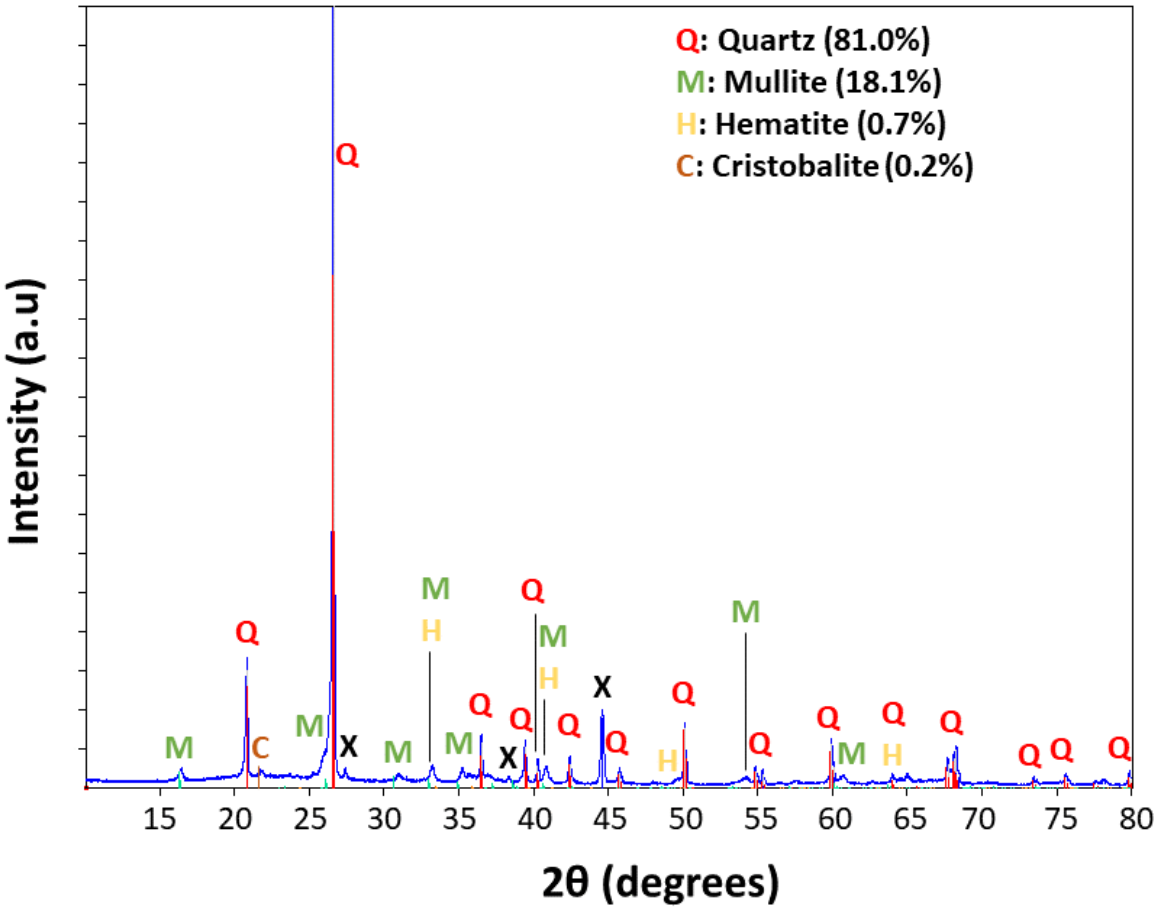

Figure 4.2: XRD plot of composite OMA simulant coal fly ash. **X**: Peaks arising from aluminium sample holder. Quartz (SiO_2); Mullite ($3Al_2O_3{\cdot}2SiO_2$); Hematite (Fe_2O_3); Cristobalite (SiO_2).

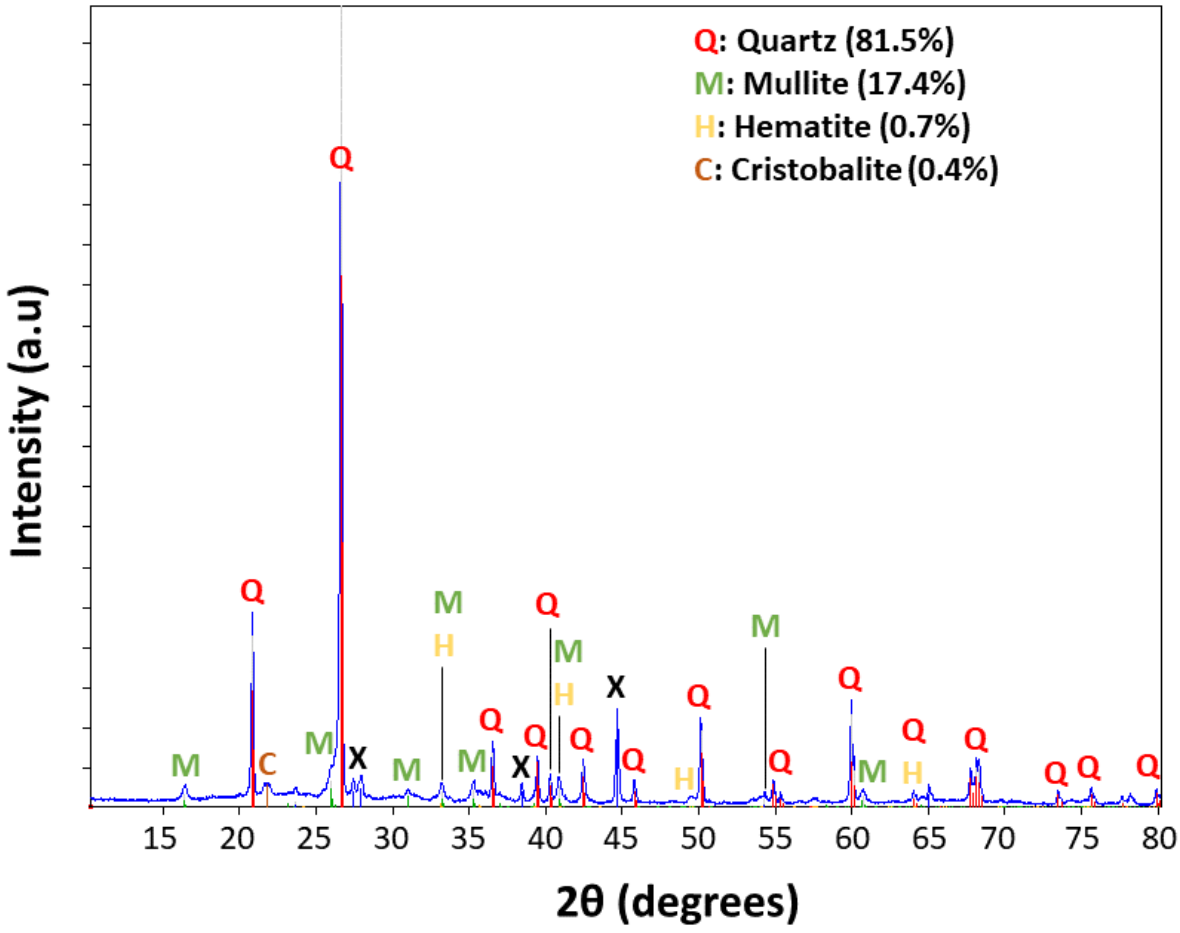

Figure 4.3: XRD plot of composite OKA simulant coal fly ash. **X**: Peaks arising from aluminium sample holder.

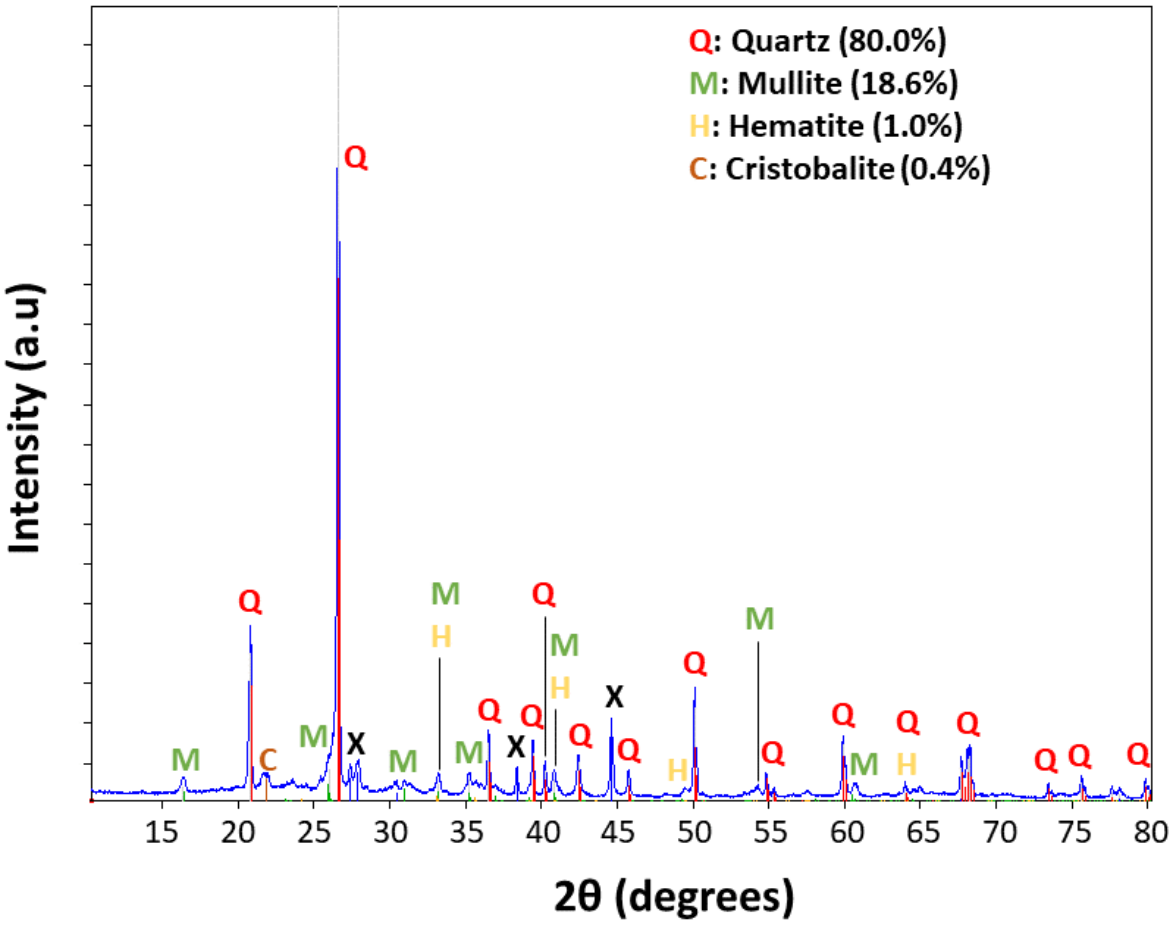

Figure 4.4: XRD plot of composite ODA fly ash. **X**: Peaks arising from aluminium sample holder.

4.2.3 SEM-EDS analysis of simulant coal fly ash

The results of SEM-EDS analysis of fly ash samples reveal the abundant presence of micron-scale mineral particles containing REE; micro-particles of monazite (a LREE mineral), xenotime and zircon (both HREE minerals)), alongside actinide minerals (uraninite and thorite), Fe and Ti minerals (ilmenite, rutile, haematite) all within the fly ash samples. However, despite extensive analysis of the precursor coal samples within the SEM using the backscattered electron detector (AsB) and EDS, REE, U or Th composition mineral particles were not observed; this implies the mineral particles occur entrapped within the carbonaceous coal

material, bound within the organic matrix by adsorption with humic acid components. It is following combustion of the coal materials that such particle fragments are liberated into the coal ash material. This entrapment, on the one hand, is a disadvantage for direct REE recovery from the feedstock coal, as little can be done to extract these REEs until after combustion. On the other hand, the encapsulation serves to partially protect U in the coal from the prevalent oxidising environmental conditions, significantly reducing its environmental mobility over the oxidised (VI) species of U [16].

REE-bearing minerals

Figure 4.5 shows a backscattered electron image detailing the distribution and abundance of dense REE minerals monazite, xenotime and zircon in a simulant coal fly ash sample; occurring discretely and scattered within the sample. Figure 4.6 shows backscattered electron images and EDS spectra of three example monazite particles **A**, **B** and **C** from OMA, OKA and ODA, respectively; the EDS spectra show characteristic peaks of the light REEs (Ce, La, Pr, Nd - a critical REE) and actinides (Th, U), alongside Ca, Al, Si peaks. Strong Al and Si peaks (from the bulk material matrix) signify the occurrence of quartz and mullite, the major mineral phases in simulant coal fly ash. The mass fraction (wt% ± absolute error) elemental composition of ten monazite particles identified within composite OMA, OKA and ODA samples, respectively, is shown in Table 4.2, which reveal Ce as having the highest mean fraction in OMA (19.3 $mg.kg^{-1}$), OKA (19.9 $mg.kg^{-1}$), ODA (21.9 $mg.kg^{-1}$), identifying the monazite particles as monazite-(Ce). The backscattered electron image and EDS spectra of xenotime (X1, X2, X3) and Y-bearing zircon (Z1, Z2, Z3) particles are shown in Figures 4.7 and 4.8, with their corresponding mass fraction (wt% ± absolute error) elemental composition in Table 4.3; these xenotime and zircon particles contain the heavy REEs (Dy, Yb, Er, Y, Gd), of which Dy, Y, Er are critical REEs.

Trace monazite particles rich in the light REEs (with trace levels of Th, U, Ca) were observed as the predominant REE mineral within the fly ash samples, followed by zircon and xenotime. REE-Ca substitution in monazite ([Ce,La,Nd,Th]PO_4) is due to the similar atomic radii [17]. The respective REE mineral particles detected in OMA, OKA, ODA were the same in composition and morphology, being mainly angularly and sub-angularly shaped with weathering-induced pitted surfaces, ascribed to a detrital source, transported by water or wind from a nearby granitic highland, deposited and subsequently incorporated into the coal during coalification [18]. The particles also have cracked surface morphologies evidence of the high combustion temperature. While U and Th were detected in the monazite micro-particles, the xenotime (YPO_4) and zircon ($ZrSiO_4$) micro-particles do not contain measurable U and Th. The EDS maps of monazite particles from OMA, OKA and ODA (as shown in Figure 4.9) reveal a homogenous distribution of REEs, U and Th; with the REEs being the more prominent. This is possible indication that the REEs are distributed towards the surface of the monazite matrix, while U and Th occur deep or within the monazite matrix (i.e., depleted within the surface).

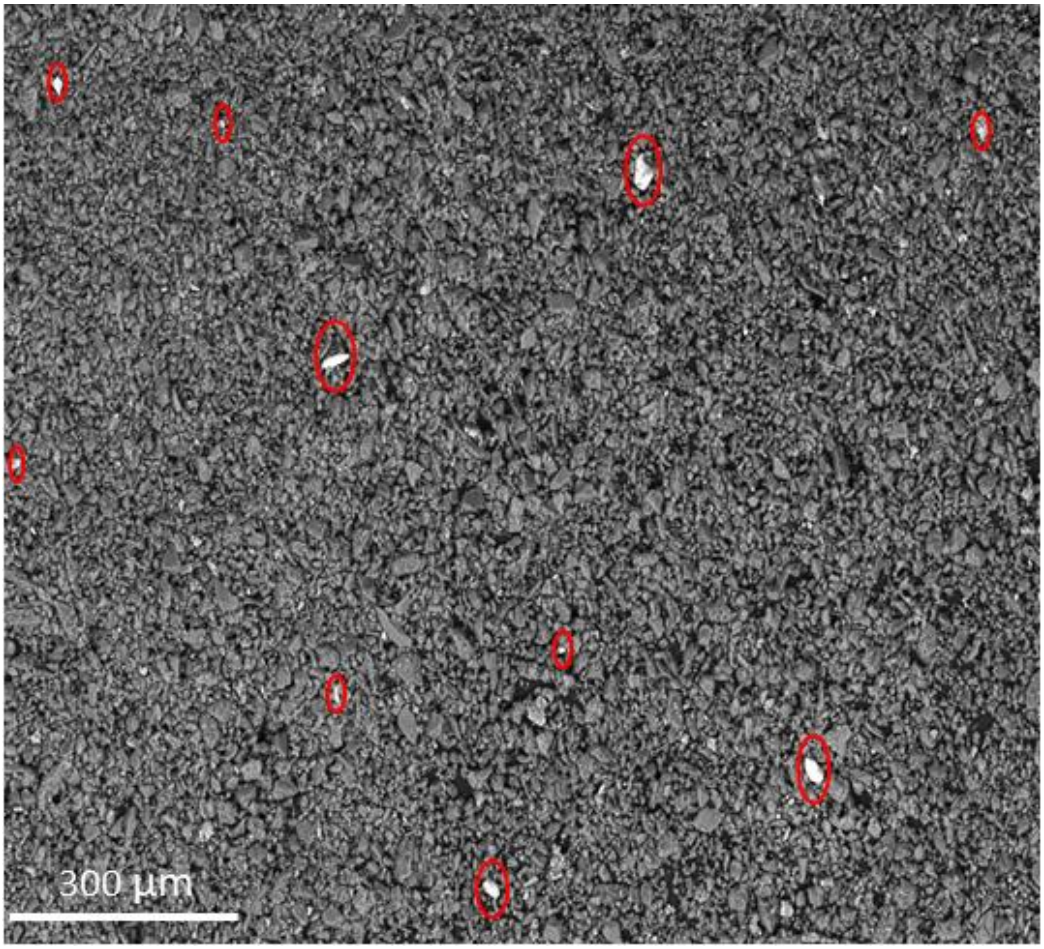

Figure 4.5: Backscattered electron image showing distribution and abundance of micro REE mineral particles in OMA simulant fly ash sample, with the particles appearing white in contrast to the surrounding material.

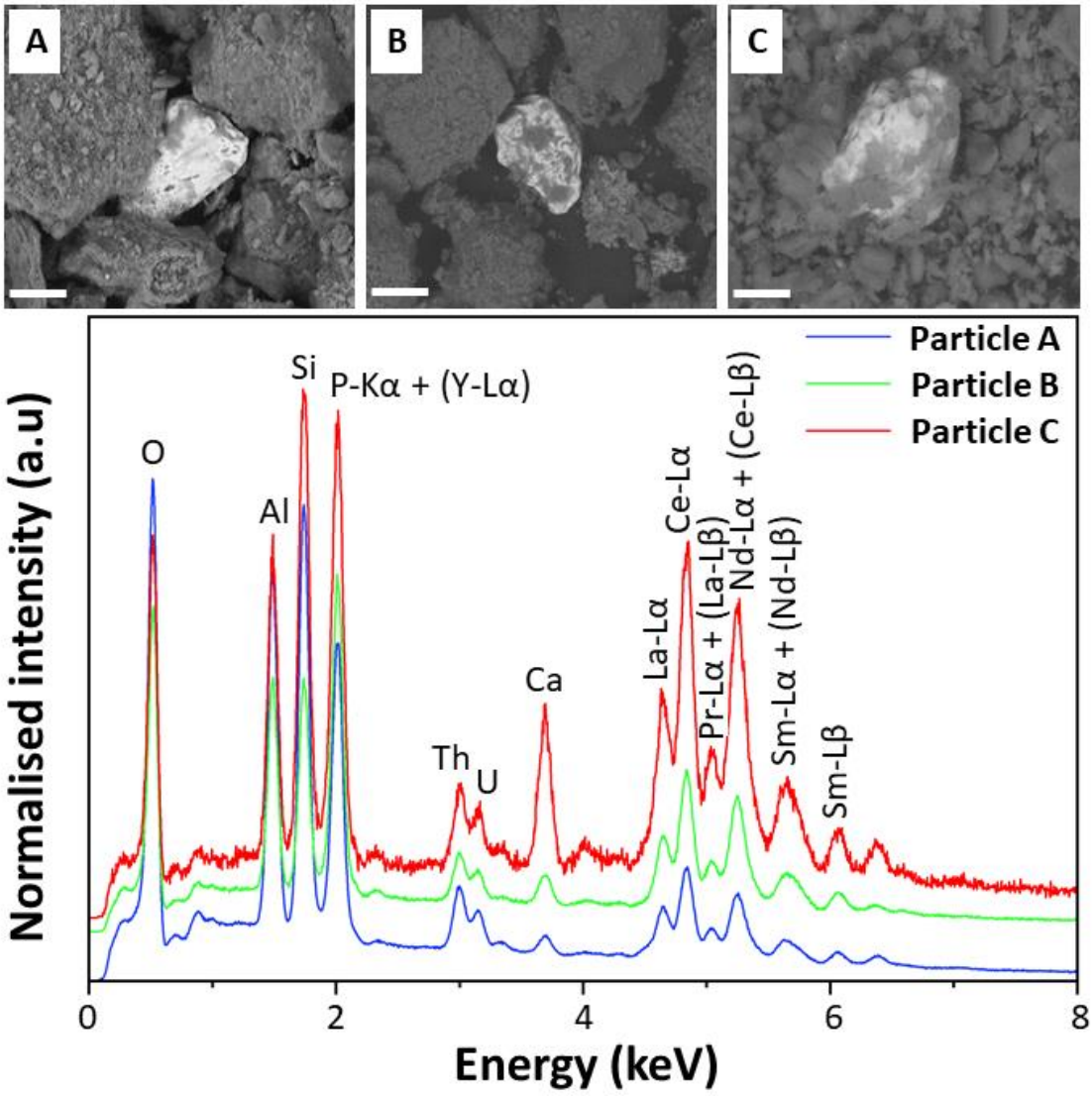

Figure 4.6: (top) Backscattered electron images of monazite particles (A, B, C) in OMA, OKA, ODA, respectively;
(bottom) Associated EDS spectra, with emission peaks identified. Scale bars = 50 μm

Table 4.2: REEs, Th and U composition (wt% ± absolute error) for 10 monazite particles from composite bulk OMA, OKA and ODA samples.

OMA	1	2	3	4	5	6	7	8	9	10	Mean ± s.d
La	9.18 ± 0.33	7.01 ± 0.29	11.2 ± 0.68	10.14 ± 0.33	8.91 ± 0.37	7.82 ± 0.30	9.76 ± 0.22	12.1 ± 0.38	6.65 ± 0.27	7.54 ± 0.39	9.03 ± 0.16
Ce	16.5 ± 0.49	15.1 ± 0.37	26.2 ± 0.84	17.3 ± 0.42	18.8 ± 0.42	19.1 ± 0.57	20.6 ± 0.43	18.7 ± 0.45	21.3 ± 0.59	23. 1 ± 0.72	19.3 ± 0.62
Nd	5.86 ± 0.59	8.34 ± 0.44	6.25 ± 0.34	9.11 ± 0.29	4.56 ± 0.19	4.34 ± 0.18	6.81 ± 0.21	5.53 ± 0.15	7.47 ± 0.23	4.76 ± 0.25	6.30 ± 0.10
Sm	3.20 ± 0.27	5.31 ± 0.33	5.15 ± 0.33	7.21 ± 0.30	4.76 ± 0.24	7.44 ± 0.17	5.83 ± 0.25	6.63 ± 0.45	7.15 ± 0.30	4.66 ± 0.25	5.73 ± 0.08
Pr	1.32 ± 0.15	1.76 ± 0.18	1.96 ± 0.24	2.16 ± 0.20	4.13 ± 0.35	1.77 ± 0.18	2.67 ± 0.25	3. 85 ± 0.51	2.10 ± 0.30	3.22 ± 0.27	2.34 ± 0.02
Th	4.01 ± 0.24	2.54 ± 0.16	1.44 ± 0.12	1.87 ± 0.29	2.56 ± 0.33	2.25 ± 0.19	1.55 ± 0.16	3.11 ± 0.17	2.19 ± 0.17	2.31 ± 0.27	2.38 ± 0.02
U	1.32 ± 0.11	0.56 ± 0.05	0.44 ± 0.05	0.67 ± 0.05	1.05 ± 0.15	0.26 ± 0.03	0.76 ± 0.06	0.44 ± 0.04	1.21 ± 0.15	0.89 ± 0.10	0.76 ± 0.003
OKA	1	2	3	4	5	6	7	8	9	10	Mean ± s.d
La	8.68 ± 0.33	9.52 ± 0.21	12.3 ± 0.52	6.55 ± 0.30	9.32 ± 0.25	8.76 ± 0.31	11.1 ± 0.29	6.40 ± 0.14	5.87 ± 0.16	9.77 ± 0.28	8.83 ± 0.18
Ce	17.3 ± 0.48	15.5 ± 0.53	26.2 ± 0.47	20.4 ± 0.49	23.0 ± 0.49	17.3 ± 0.56	22.4 ± 0.65	20.4 ± 0.48	21.6 ± 0.74	16.3 ± 0.76	19.9 ± 0.71
Nd	7.71 ± 0.30	7.21 ± 0.33	9.23 ± 0.33	10.42 ± 0.48	8.32 ± 0.30	12.2 ± 0.42	9.21 ± 0.21	7.45 ± 0.24	11.52 ± 0.73	6.23 ± 0.21	8.59 ± 0.14
Sm	3.01 ± 0.31	4.12 ± 0.27	2.45 ± 0.11	2.45 ± 0.18	5.32 ± 0.34	3.47 ± 0.13	2.15 ± 0.16	1.87 ± 0.06	3.66 ± 0.20	4.21 ± 0.14	3.27 ± 0.04
Pr	2.26 ± 0.20	0.87 ± 0.12	2.12 ± 0.22	1.56 ± 0.15	2.45 ± 0.18	0.95 ± 0.15	3.65 ± 0.24	2.76 ± 0.24	4.87 ± 0.41	3.23 ± 0.24	2.47 ± 0.03
Th	2.67 ± 0.20	1.51 ± 0.07	2.56 ± 0.21	1.23 ± 0.07	2.01 ± 0.09	0.87 ± 0.06	2.54 ± 0.09	3.23 ± 0.21	1.25 ± 0.05	1.87 ± 0.05	1.97 ± 0.01
U	0.93 ± 0.09	0.34 ± 0.03	1.12 ± 0.11	0.55 ± 0.05	1.23 ± 0.05	0.43 ± 0.03	0.87 ± 0.06	1.22 ± 0.04	1.18 ± 0.04	0.44 ± 0.02	0.83 ± 0.003
ODA	1	2	3	4	5	6	7	8	9	10	Mean ± s.d
La	11.0 ± 0.76	11.1 ± 0.36	9.70 ± 0.42	9.21 ± 0.29	7.32 ± 0.18	6.89 ± 0.31	12.23 ± 0.30	7.26 ± 0.18	8.87 ± 0.31	7.34 ± 0.21	9.09 ± 0.17
Ce	20.9 ± 0.82	22.3 ± 0.47	18.3 ±v0.57	23.1 ± 0.49	19.8 ± 0.50	26.1 ± 0.46	20.2 ± 0.69	19.3 ± 0.47	24.2 ± 0.62	24.5 ± 0.63	21.9 ± 0.56
Nd	9.13 ± 0.71	7.21 ± 0.17	6.45 ± 0.24	10.3 ± 0.34	7.43 ± 0.18	8.46 ± 0.27	7.51 ± 0.18	9.33 ± 0.33	6.39 ± 0.21	8.22 ± 0.28	8.05 ± 0.10
Sm	2.80 ± 0.24	4.86 ± 0.21	3.96 ± 0.22	7.61 ± 0.30	5.60 ± 0.22	4.55 ± 0.22	7.54 ± 0.18	8.93 ± 0.22	7.45 ± 0.32	3.15 ± 0.17	5.65 ± 0.12
Pr	2.66 ± 0.52	2.05 ± 0.13	4.31 ± 0.14	1.93 ± 0.15	5.23 ± 0.23	3. 17 ± 0.07	3.76 ± 0.12	2.97 ± 0.13	3.78 ± 0.16	4.23 ± 0.35	3.44 ± 0.04
Th	2.53 ± 0.31	1.43 ± 0.08	1.55 ± 0.07	2.55 ± 0.09	1.44 ± 0.06	3.12 ± 0.17	1.87 ± 0.06	0.97 ± 0.08	1.22 ± 0.05	0.85 ± 0.06	1.75 ± 0.01
U	0.52 ± 0.06	0.87 ± 0.06	0.62 ± 0.06	1.13 ± 0.11	0.82 ± 0.07	0.76 ± 0.07	0.89 ± 0.11	1.05 ± 0.14	0.56 ± 0.05	0.68 ± 0.03	0.79 ± 0.02

s.d.: Standard deviation

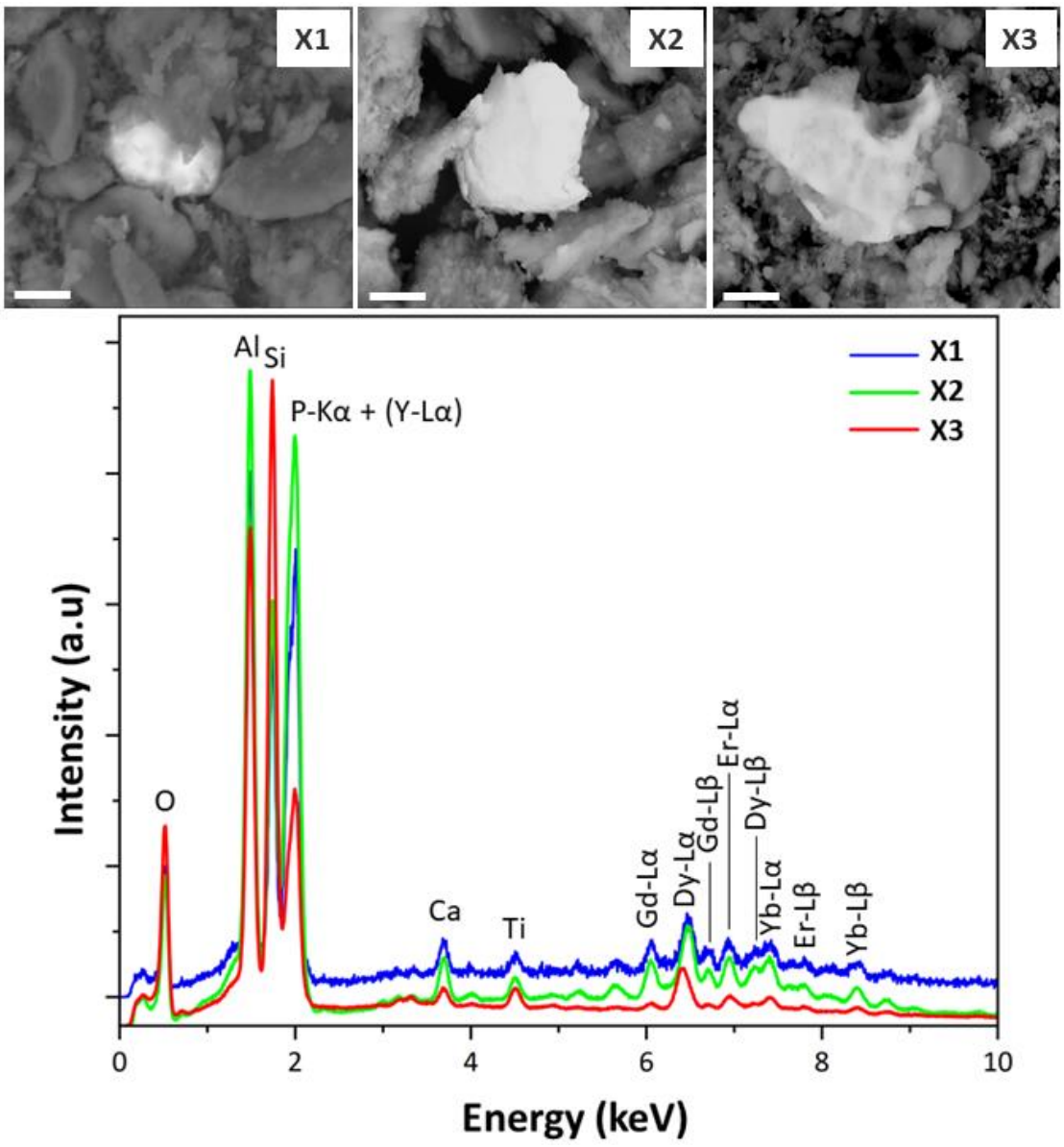

Figure 4.7: (top) Backscattered electron images of xenotime particles (X1, X2, X3) in OMA, OKA, ODA, respectively;
(bottom) Associated EDS spectra, with emission peaks identified; the elemental composition of the xenotime particles is shown in Table 4.3. Scale bars = 10 μm.

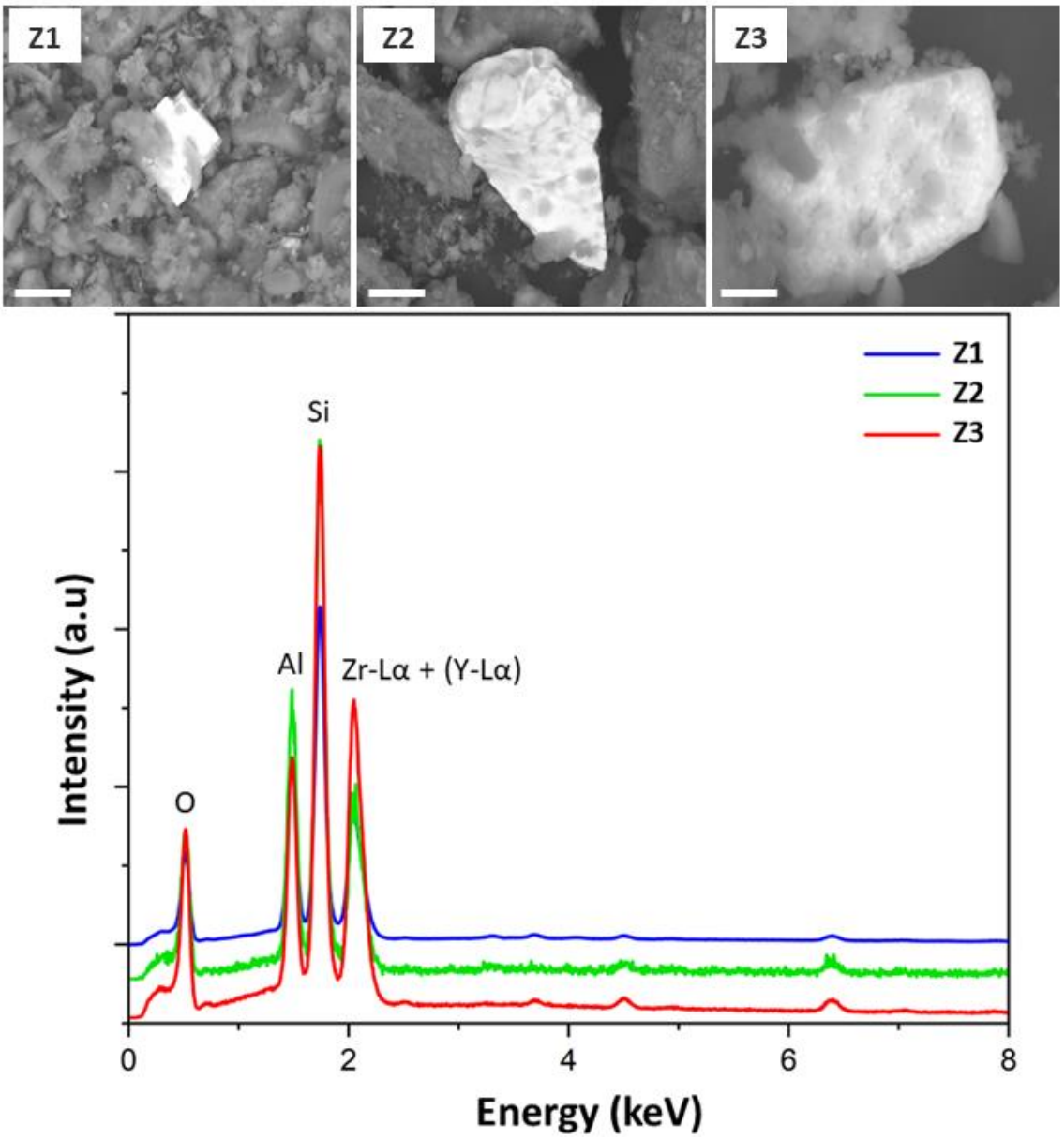

Figure 4.8: (top) Backscattered electron images of zircon particles (Z1, Z2, Z3) in OMA, OKA, ODA, respectively;
(bottom) Associated EDS spectra, with emission peaks identified; the elemental composition of the zircon particles is shown in Table 4.3. Scale bars = 20 μm.

Table 4.3: Elemental composition for xenotime (X1, X2, X3) and zircon (Z1, Z2, Z3) particles each from composite bulk OMA, OKA and ODA samples, respectively.

Particle identity	Elemental composition (wt% ± absolute error)					
	Y	Zr	Gd	Dy	Er	Yb
X1	20.1 ± 0.82	ND	3.57 ± 0.19	5.67 ± 0.37	5.22 ± 0.53	6.99 ± 0.76
X2	18.3 ± 0.77	ND	6.91 ± 0.82	13.3 ± 1.31	3.43 ± 0.18	6.65 ± 1.05
X3	22.4 ± 1.27	ND	3.49 ± 0.15	7.70 ± 0.24	4.17 ± 0.17	3.52 ± 0.19
Z1	2.56 ± 0.13	23.3 ± 0.82	ND	ND	ND	ND
Z2	2.71 ± 0.14	22.5 ± 1.43	ND	ND	ND	ND
Z3	1.94 ± 0.16	27.3 ± 0.90	ND	ND	ND	ND

ND: Not detected

(a) OMA

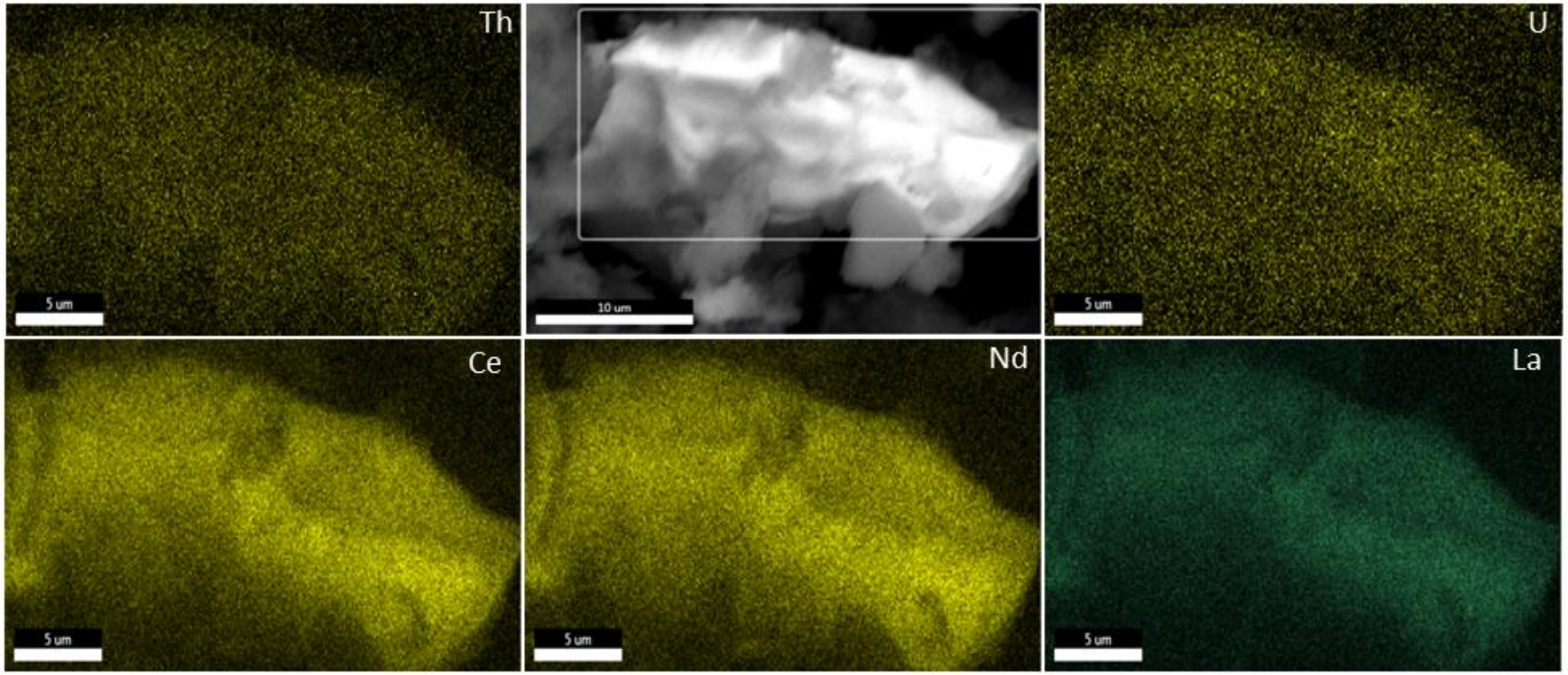

(b) OKA

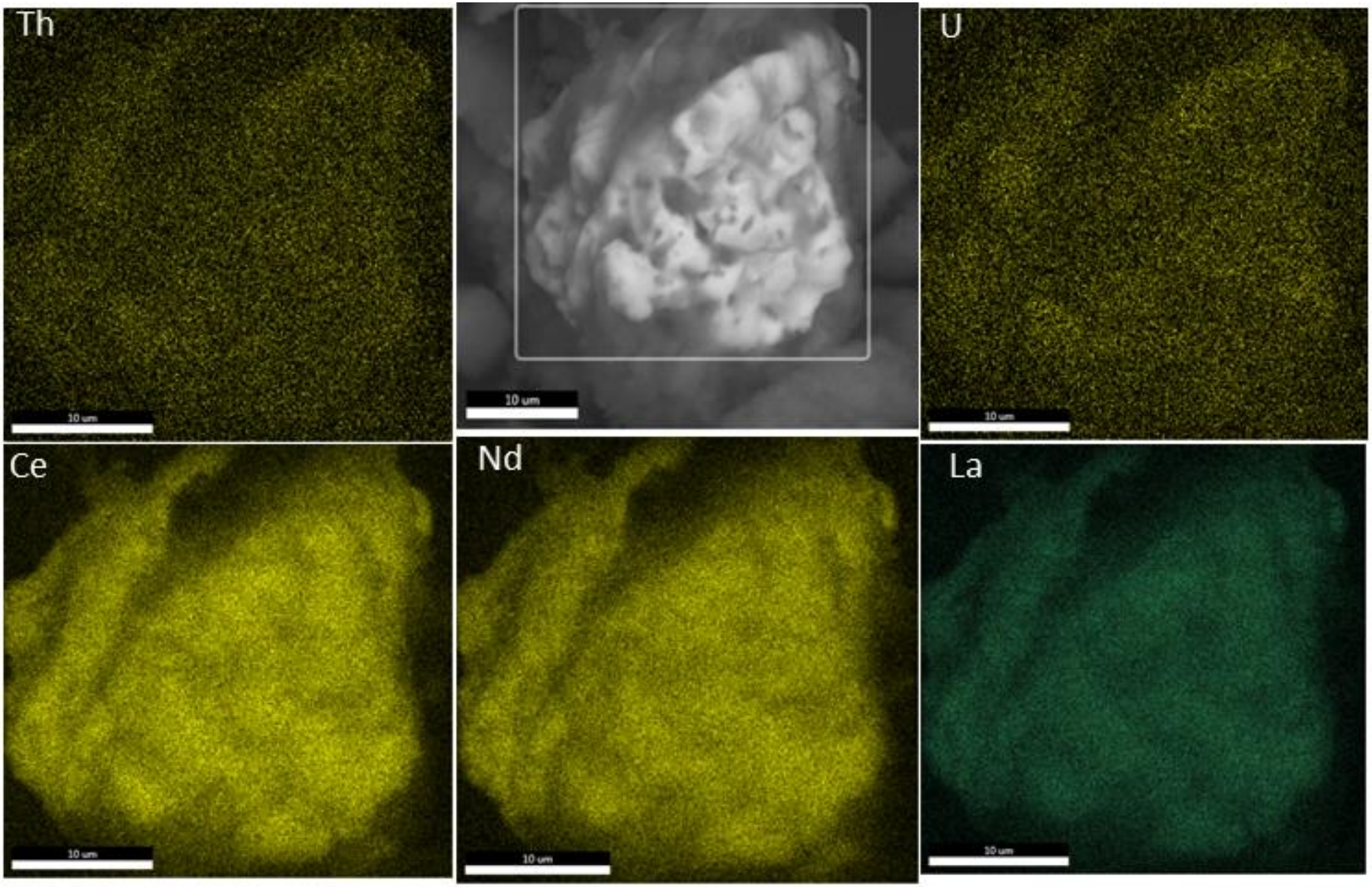

(c) ODA

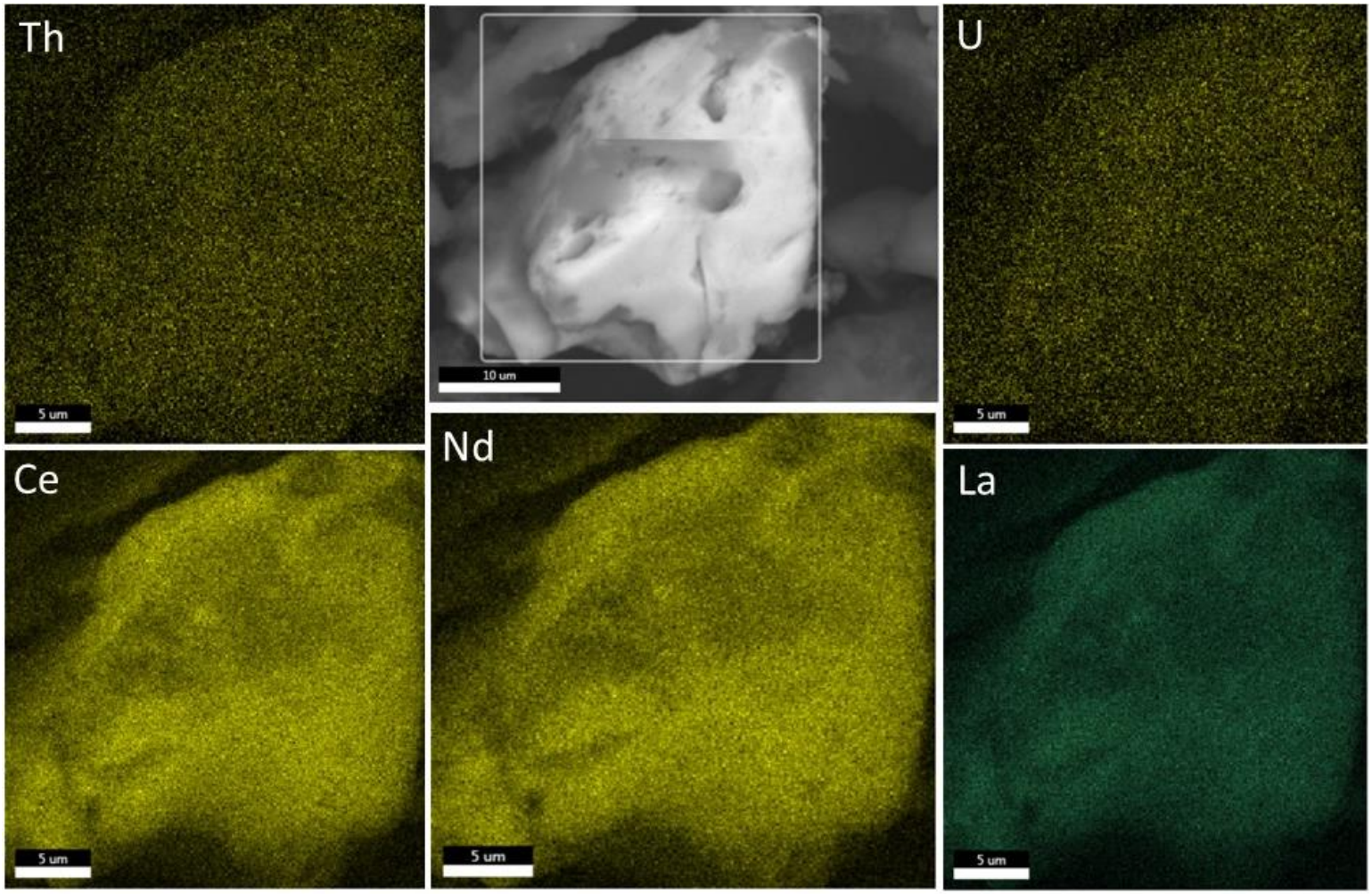

Figure 4.9: backscattered electron image (grey) with EDS elemental maps of monazite particles in (a) OMA (b) OKA and (c) ODA, showing the distribution of Ce, Nd, La, Th and U. Scale bars = 5 µm, 10 µm and 5 µm, respectively.

These REE minerals (between 10 µm and 80 µm in diameter) were found to exist largely as discrete particles and not encapsulated in glassy phases. The extraction and isolation of these discrete particles is more cost-effective, as leaching rare earth mineral particles encapsulated in glassy phases consumes more costly reagents and generates significant volumes of waste products [6,19]. Studies have shown that REE mineral particles can become encapsulated in aluminosilicate glass phases during coal combustion, mainly during coal combustion at high temperatures between 1400°C and 1700°C [4,6]. Hence, combustion of low rank coal at temperatures between 900°C and 1200°C greatly reduces the formation of glassy phases and the sequestration of REE minerals into these phases, therefore making REE extraction from fly ash cost effective. Our results agreed with previous studies on fly ash (sourced from coal-fired plants burning high-rank coal) that REE mineral particles were either dispersed throughout the glass phase or exist as independent mineral particles [20].

These (resistate) REE minerals are tough to dissolve, requiring a conventional total acid digestion using concentrated sulphuric acid prior to REEs separation, a costly and environmentally damaging process [21]. However, studies have shown that high-temperature pre-treatment (at 600 °C and above) of these REE-bearing minerals greatly enhances leaching of REEs contained in their matrix [19].

Actinide minerals

Both Figures 4.10 and 4.11 show backscattered electron images and EDS spectra of particles (P1, P2) ascribed as uraninite and a calcium-rich thorite particle (P3) ascribed as thorite detected in the simulated OMA, OKA, ODA fly ash samples from the three mines. The compositional breakdown (in wt% ± absolute error, δ) of these particles is shown in Table 4.4. Such discrete uraninite and thorite minerals, with weathered surfaces, were found within

OMA, OKA, ODA. The uraninite and thorite particles were thought to be either of detrital origin or to have precipitated from hydrothermal fluids during coalification [22]. P1 has a botryoidal surface morphology (partially altered by the combustion process) - characteristic of U of hydrothermal origin [23].

These radioactive particles (with sizes between 10 μm and 80 μm) have cracked surface morphologies (due to the high combustion temperature), with the tendency to further fragment into more smaller fragments (particulate matter, PM2.5), thereby increasing the risk of inhalation and localised radiation dose if particulates should be carried into the air. The occurrence of these radioactive mineral microparticles in discrete form in the coal fly ash materials is a consequence of the lower combustion temperature used. At low combustion temperatures, a less substantial amount of dense glassy amorphous materials - considered to reduce radon emanation rate and the leaching rate of the radioactive particles, is formed. Non-entrapment of the radioactive mineral microparticles glassy amorphous materials implies increased radioactivity of the coal fly ash materials, a consequence of increased radon gas emanation rate and radionuclides being weakly bonded to fly ash particle surfaces [24].

The uraninite particles detected were found to contain residual Pb thought to be from the decay of U, alongside Fe and Nb present in the bulk material or indicative of possible substitution of radiogenic Pb from later fluid-circulation events after initial formation of the uraninite during coalification [25]. Though REEs can be found as trace impurities in uraninite and thorite, the particles detected in this study do not contain any measurable REE using EDS analysis.

In acidic aerated waters, the less soluble and immobile UO_2 (U^{4+}) can become oxidised to form the more soluble and mobile (VI) species (UO_2^{2+}) [26]; this reaction is expressed as:

$$U^{4+} + 2H_2O = UO_2^{2+} + 4H^+ + 2e^- \quad (4.1)$$

This has consequences for storage of fly ash wastes that will arise from burning Nigerian coal deposits; if the fly ash is not suitably protected from interaction with meteoric waters, then leaching will occur leading to acid generation, with negative feedback for driving further/faster leaching of U and its decay products alongside toxic heavy metals (such as Cd, As, Cr, etc) into the environment, contaminating land and water over long periods of time.

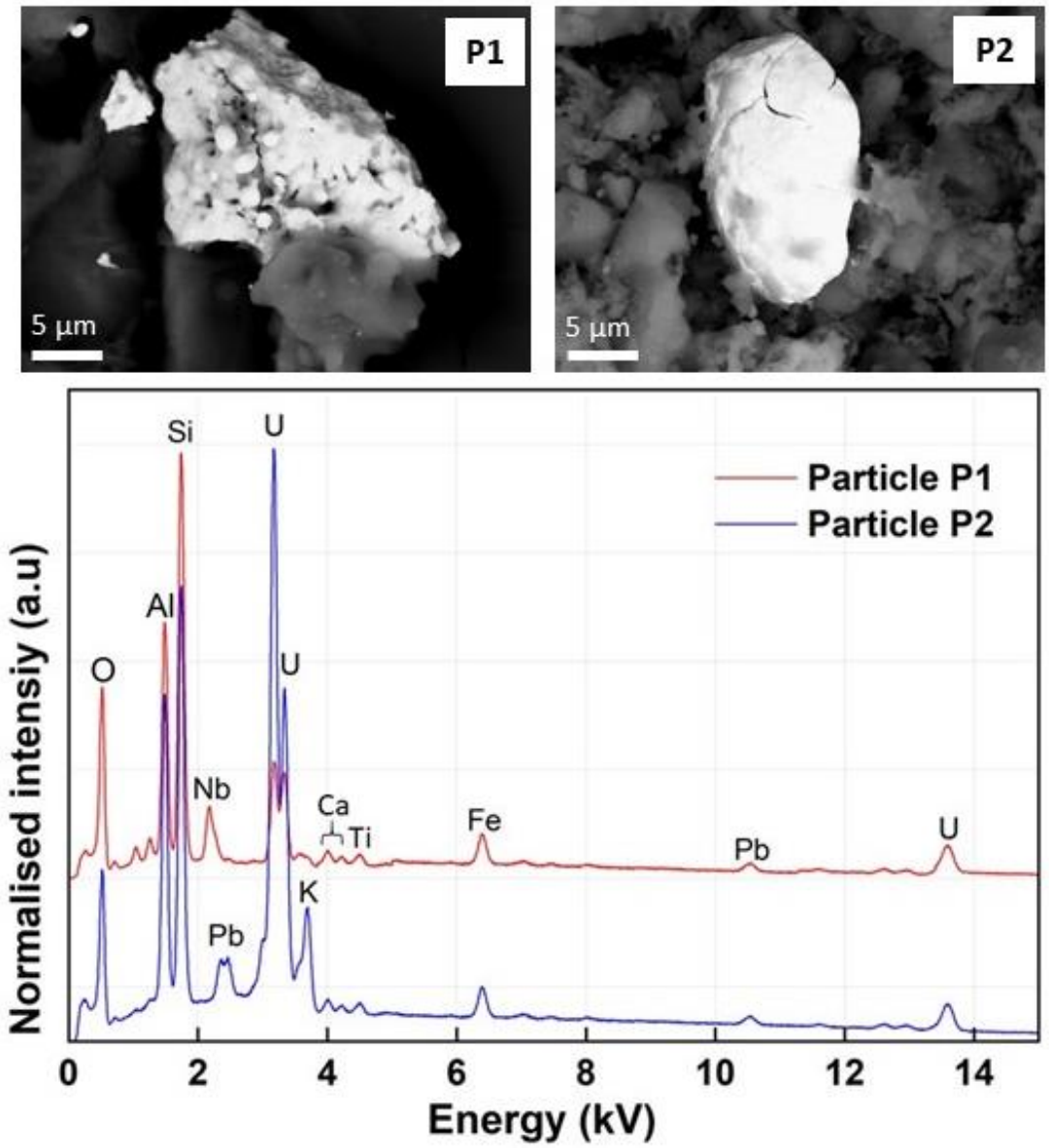

Figure 4.10: (top) Backscattered electron images of two uraninite particles (P1 in OKA, P2 in OMA). (bottom) Associated EDS spectra with emission peaks identified.

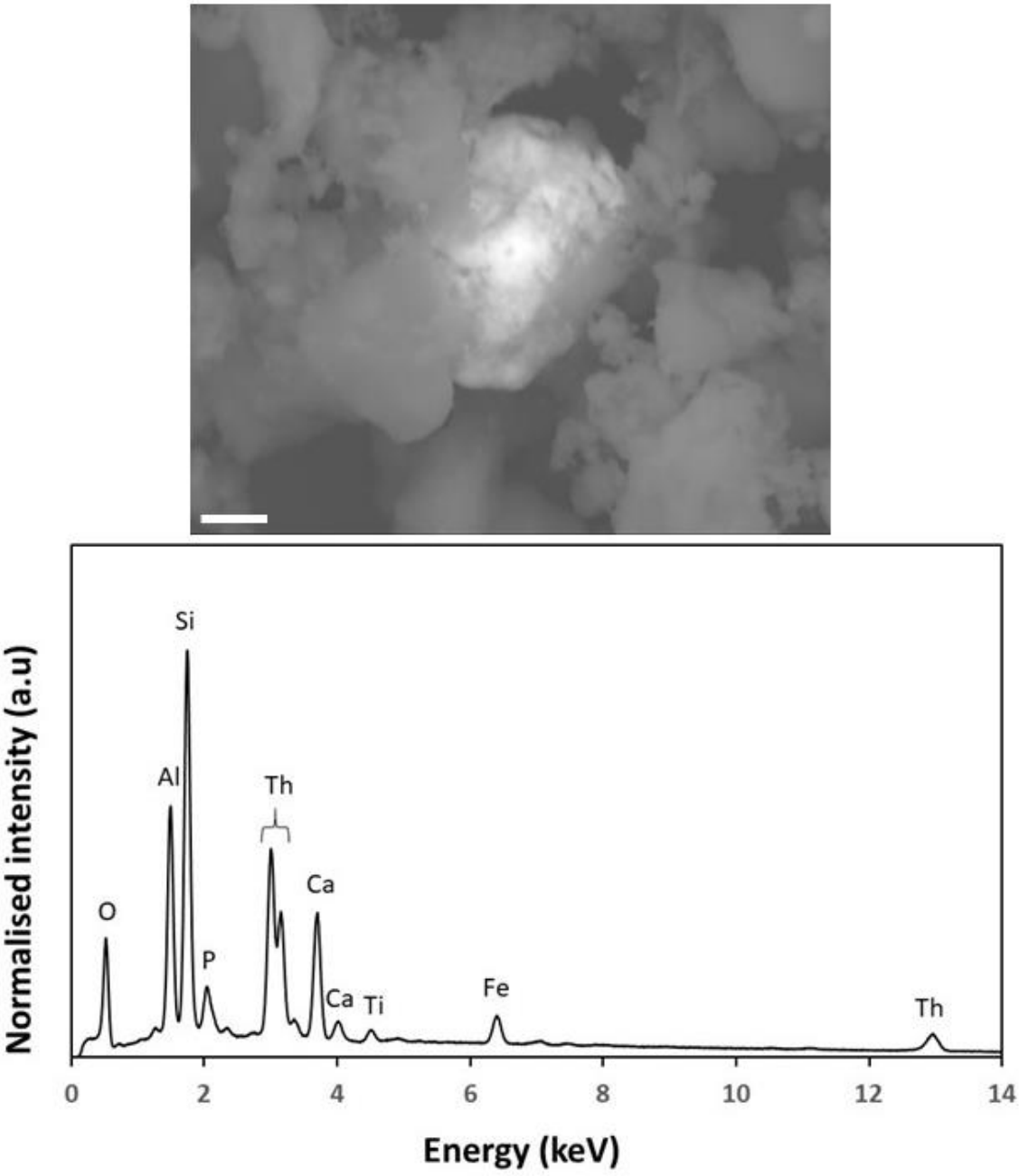

Figure 4.11: (top) Backscattered electron image of Thorite particle (P3 in OMA). (bottom) Associated EDS spectrum with emission peaks identified. Scale bar = 2 µm.

Table 4.4: Elemental composition of particles P1, P2 and P3, as determined via EDS analysis, and as shown in Figures 4.10 and 4.11.

Element	Elemental composition (wt% ± absolute error)		
	P1	**P2**	**P3**
O	27.3 ± 2.54	20.1 ± 1.50	25.4 ± 2.40
Al	4.99 ± 0.38	5.12 ± 0.39	10.67 ± 0.67
Si	20.0 ± 1.34	33.8 ± 2.31	19.0 ± 1.10
P	ND	ND	3.47 ± 0.22
Nb	14.3 ± 0.64	ND	ND
Pb	2.45 ± 0.27	8.32 ± 0.73	ND
Fe	4.36 ± 0.13	1.39 ± 1.00	5.11 ± 0.18
Ti	0.18 ± 0.03	0.13 ± 0.02	ND
Th	ND	ND	26.0 ± 0.89
U	28.9 ± 0.42	34.9 ± 0.73	ND
K	0.12 ± 0.02	2.37 ± 0.16	ND
Ca	0.10 ± 0.02	0.15 ± 0.03	10.3 ± 0.41

ND: Not detected.

Non REE-bearing heavy minerals

Figure 4.12 presents a typical backscattered electron image and EDS spectrum of ODA simulant coal fly ash, showing the elements Fe and Ti, indicative of the occurrence of heavy minerals ilmenite, rutile and haematite (formed during the thermal decomposition of pyrite) in the fly ash samples. These results, which confirm the XRF results reported earlier, are common to all the fly ash samples. Although no detectable level of toxic heavy metals (e.g. As, Cd, Pb or U) were found associated with haematite particles, studies have shown that these elements become adsorbed onto the surface of (oxyhydr)oxides of Fe (e.g. haematite) during coal combustion, thereby immobilising them [27,28]. In addition to adsorption, U association with (oxyhydr)oxides of Fe is also reported to occur during coalification via the reduction of the highly mobile U(VI) to the poorly soluble and immobile U(IV) [29]. However, these toxic heavy metals could still be leached into the environment under favourably acidic

redox conditions, hence, the need for proper containment and management of fly ash must be enforced.

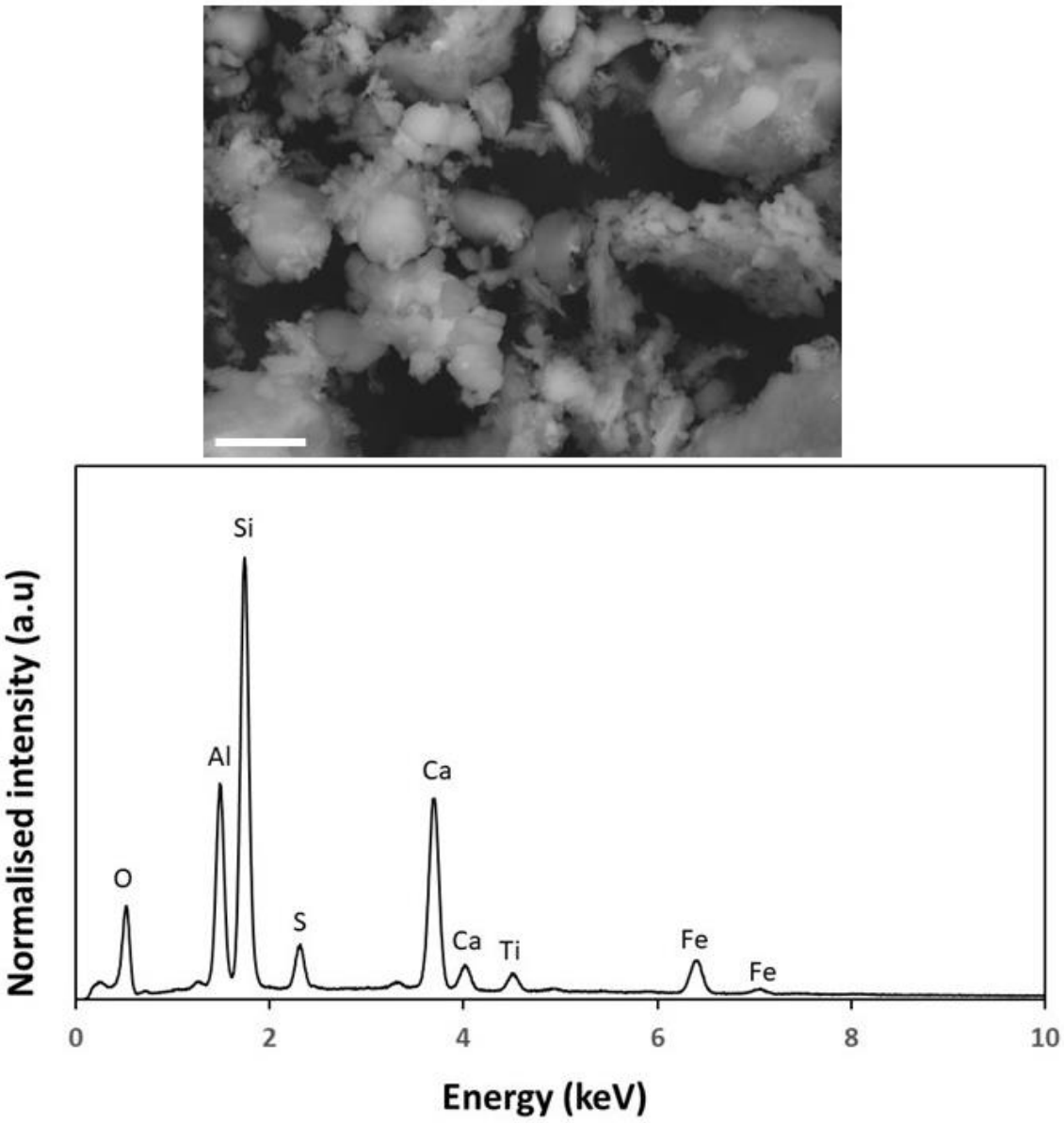

Figure 4.12: (top) Backscattered electron image of ODA fly ash. (Bottom) Associated EDS spectrum with emission peaks identified. Scale bar = 500 µm.

Implication for REE-bearing minerals beneficiation

The results of XRF and XRD analysis show that OMA, OKA and ODA fly ash samples do not possess a complex gangue and widely varied REE mineralogy. The advantage of the gangue minerals (quartz, mullite, cristobalite, haematite) in the simulant coal fly ash alongside the

occurrence of REEs in heavy minerals such as monazite, xenotime and Y-bearing zircon is the potential simplicity of beneficiation via a combination of physical methods, such as density, magnetic and electrostatic separation, which avoid the need for large quantities of flotation chemicals such as hydroxamates and phosphoric acid esters [21]. These methods rely on the difference in density, and magnetic and electrostatic properties of the heavy gangue and REE-bearing minerals [21,30]. A flowsheet for the potential physical beneficiation procedure for OMA, OKA and ODA coal fly ash is shown in Figure 4.13. On dry ash basis, the uncompacted fly ash is beneficiated via high intensity magnetic separation to remove the weakly magnetic haematite and ilmenite, followed by high intensity electrostatic separation to remove rutile [31,32]. Finally, the gangue minerals (quartz (2.65 g/cc), mullite (3.05 g/cc), cristobalite (2.27 g/cc)) being less dense compared to monazite (5.15 g/cc), xenotime (4.75 g/cc) and Zircon (4.56 g/cc), are then removed via density separation to produce a final concentrate rich in the REE-bearing minerals [32-34].

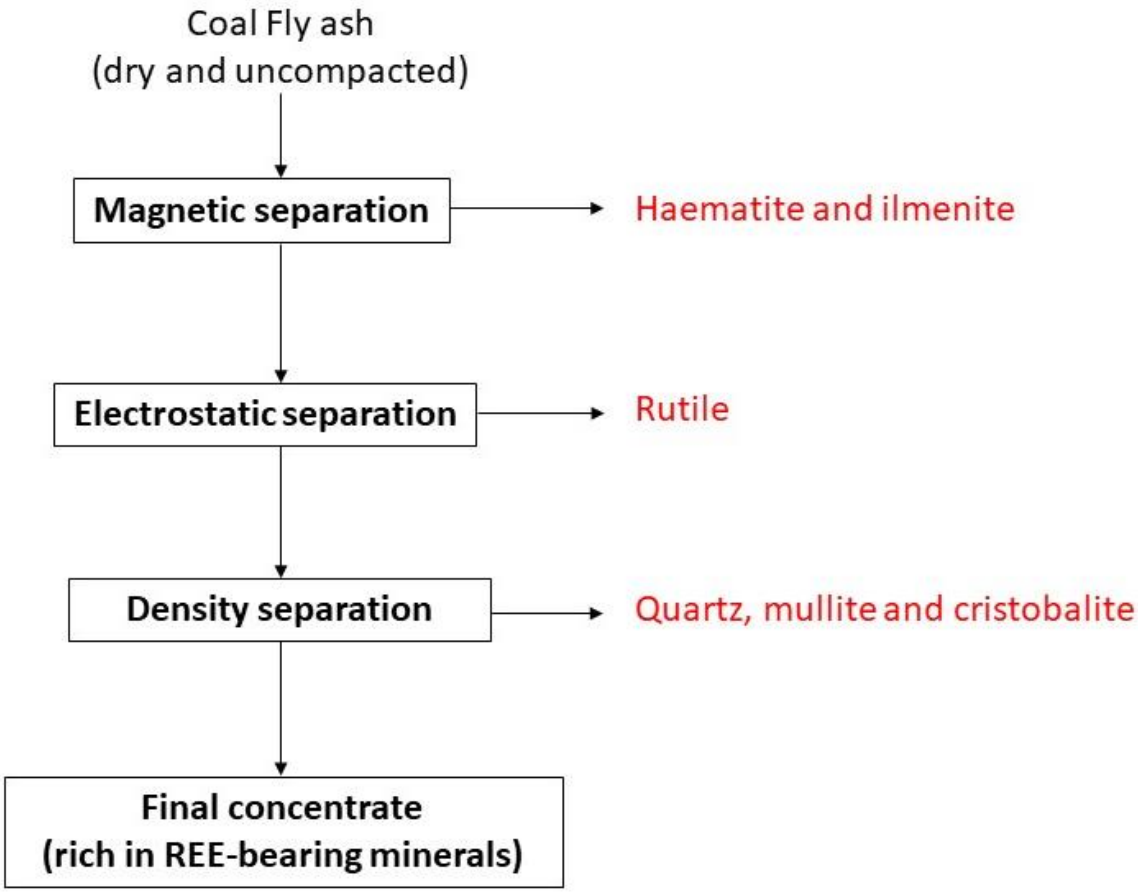

Figure 4.13: Flowsheet for potential physical beneficiation of REE-bearing minerals in simulant coal fly ash.

4.3 Summary

Results of elemental and mineralogical analysis of OMA, OKA and ODA fly ash samples have been presented and discussed from the perspective of resource recovery and environmental impacts. The ash materials were composed mainly of SiO_2, Al_2O_3, Fe_2O_3, TiO_2 and CaO, and, based on these, are denoted as class F fly ash materials. Although no calcium-rich REE phases were detected, the detection of CaO invokes the presence of REE-bearing Ca phases in the fly ash materials which favours high REE extractability due to their high solubility in nitric acid.

The chemo- and radio-toxic trace elements (Cr, Cd, As, Pb, U and Th) were detected in the fly ash materials, with Cr the most-enriched in the fly ash materials. Although occurring only up to a few hundred $mg.kg^{-1}$, because of the large volume of fly ash generated annually the trace chemo- and radio-toxic heavy metals (Pb, As, Cr, U, Th) are of serious environmental concern and capital-intensive during fly ash storage or rare earth extraction.

The simulant coal fly ash materials have a less complex mineralogy, with the major (non REE-bearing) mineral phases being quartz, mullite, haematite and cristobalite, alongside trace amounts of ilmenite and rutile. This favours cost effective REE beneficiation through density, magnetic and electrostatic physical beneficiation techniques. The results of SEM-EDS analysis reveal REE micro mineral particles of monazite (a LREE mineral and the most predominant) plus xenotime and zircon (both of which are HREE minerals), alongside potentially inhalable radioactive particles, namely uraninite and thorite. EDS maps of monazite particles invoke the concentration of REEs at the particle surfaces, making the REEs more susceptible to chemical attack with increased solubility. This surface distribution of REEs in the monazite particles favours more cost-effective and environmentally friendly REE leaching methods as only the outer regions of the monazite particles is leached by using a less aggressive dilute mineral

acid at a lower temperature and in less time, compared to the conventional processes that utilise harsh acids at high temperature, a more cost intensive process. The encapsulation within carbonaceous matter of the rare earth minerals in the feedstock coal is a challenge for direct REE recovery from coal as combustion is required to free these micro mineral particles, a process which releases CO_2 and contributes to global warming.

In the next chapter, the results of bulk analysis of fly ash materials via acid digestion and sequential extraction are presented, providing information on the economic feasibility of REE extractability from the simulant fly ash materials, valuable for the optimisation and/or development of methods for REE recovery.

4.4 References

[1] Yale Environment 360. Boom in Mining Rare Earths Poses Mounting Toxic Risks. https://e360.yale.edu/features/boom_in_mining_rare_earths_poses_mounting_toxic_risks (accessed 12 January 2021).

[2] Martin, Peter George. The 2011 Fukushima Daiichi Nuclear Power Plant accident: an analysis over 10 orders of magnitude (Doctoral dissertation, University of Bristol). Institution repository https://research-information.bris.ac.uk/en/studentTheses/the-2011-fukushima-daiichi-nuclear-power-plant-accident (2018).

[3] ASTM C618-19: Standard specification for coal fly ash and raw or calcined natural pozzolan for use in concrete. ASTM International, West Conshohocken, Pennsylvania. https://compass.astm.org/ (2019) (Accessed 6 April 2018).

[4] Taggart R.K., Hower J.C., Dwyer G.S., Hsu-Kim H. Trends in the rare earth element content of U.S-based coal combustion fly ashes. Environmental Science and Technology, 50 (2016) 5919-5926.

[5] Stuckman M.Y., Lopano C.L., Granite E.J. Distribution and speciation of rare earth elements in coal combustion by-products via synchrotron microscopy and spectroscopy. International Journal of Coal Geology, 195 (2018) 125-138.

[6] Wang Z, Dai S, Zou J, French D, Graham I.T. Rare earth elements and yttrium in coal ash from the Luzhou power plant in Sichuan, Southwest China: concentration, characterisation and optimised extraction. International Journal of Coal Geology, 203 (2019) 1-14.

[7] OilPrice energy news. Could Thorium revive the nuclear energy industry? https://oilprice.com/Alternative-Energy/Nuclear-Power/Could-Thorium-Revive-The-Nuclear-Energy-Industry.html/ (accessed 17 September 2020).

[8] BBC news. Russia to build nuclear power plants in Nigeria.

https://www.bbc.co.uk/news/world-africa-41818933 (accessed 13 June 2020).

[9] Querol X., Fernandez T.J.L., Lopez S.A. Trace elements in coal and their behaviour during combustion in a large station. Fuel, 74 (1995) 331-343.

[10] Clarke L.B., Sloss L.L. Trace elements - emissions from coal combustion and gasification. London: IEA Coal Research (1992).

[11] Huggins F.E., Rezaee M., Honaker R.Q., Hower J.C. On the removal of hexavalent chromium from a Class F fly ash. Waste Management, 51 (2016) 105-110.

[12] Arthur F. Stam, Ruud Meij, Henk te Winkel, Ronald J. van Eijk, Frank E. Huggins, Gerrit Brem. Chromium Speciation in Coal and Biomass Co-Combustion Products. Environmental science and technology, 45 (2011) 2450-2456.

[13] Finkelman R.B., Orem W., Castranova V., Tatu C.A., Belkin H.E., Zheng B., Lerch H.E., Maharaj S.V., Bates A.L. Health impacts of coal and coal use: possible solutions. International Journal of Coal Geology, 50 (2002) 425-443.

[14] Kim A., Kazonich G., Dahlberg M. Relative solubility of cations in class F fly ash, Environmental Science and Technology, 37 (2003) 4507-4511.

[15] National Energy Technology Laboratory, U.S. Department of Energy. Characterization of rare earth element minerals in coal utilization by-products. https://edx.netl.doe.gov/dataset/characterization-of-rare-earth-element-minerals-in-coal-utilization-byproducts (2017) (Accessed 8 May 2019).

[16] Wang Y., Bagnoud A., Suvorona E., McGivney E. Geochemical control on uranium (IV) mobility in a mining-impacted wetland. Environmental Science and Technology, 48 (2014) 10062-10072.

[17] Thompson W., Lombard A., Santiago E., Singh A. Mineralogical studies in assisting beneficiation of rare earth element minerals from carbonatite deposits. In: Proceedings of the 10th International Congress for Applied Mineralogy (ICAM), Trondheim, (2012) 665-672.

[18] Hower J.C., Eble C.F., Dai S.,Belkin H.E. Distribution of rare earth elements in eastern Kentucky coals: indicators of multiple modes of enrichment? International Journal of Coal Geology, 160-161 (2016) 73-81.

[19] Honaker R.Q., Zhang W., Werner J. Acid Leaching of Rare Earth Elements from Coal and Coal Ash: Implications for using fluidized bed combustion to assist in the recovery of critical materials. Energy and Fuels, 33 (2019) 5971-5980.

[20] Hood M.M., Taggart R.K., Smith R.C., Hsu-Kim H., Henke K.R., Graham U., Groppo J.G., Unrine J.M., Hower J.C. Rare earth element distribution in fly ash derived from the Fire Clay coal, Kentucky. Coal Combustion and Gasification Products, 9 (2017) 22-33.

[21] Archana Kumari, Rekha Panda, Manis Kumar Jha, Rajesh Kumar J., Jin Young Lee. Process development to recover rare earth metals from monazite mineral: A review. Minerals Engineering, 79 (2015) 102-115.

[22] Chen J., Chen P., Yao D., Huang W., Tang S., Wang K., Liu W., Hu Y., Zhang B., Sha J. Abundance, distribution, and modes of occurrence of uranium in Chinese coals. Minerals, 7 (2017) 239p.

[23] Pohjolainen E. Uranium deposits of Finland. W.D. Maier, R. Lahtinen, H. O'Brien (Eds.), Mineral Deposits of Finland, Elsevier, Amsterdam (2015), pp. 659-683.

[24] Jadambaa Temuujin, Enkhtuul Surenjav, Claus Henning Ruescher, Jan Vahlbruch. Processing and uses of fly ash addressing radioactivity (critical review). Chemosphere, 216 (2019) 866-882.

[25] Alexandre P., Kyser T.K. Effects of cationic substitutions and alteration in uraninite, and implications for the dating of uranium deposits. The Canadian Mineralogist, 43 (2005) 1005-1017.

[26] Burns P.C., Finch R. Uranium: mineralogy, geochemistry, and the environment. Reviews in Mineralogy, volume 38; Mineralogical Society of America: Washington, DC, USA (1999).

[27] Ainsworth C., Pilon J., Gassman P., Van der Sluys W. Cobalt, cadmium, and lead sorption to hydrous iron oxide: residence time effect. Soil science Society of America journal, 58 (1994) 1615-1623.

[28] Ames L., McGarrah J., Walker B., Salter P. Uranium and radium sorption on amorphous ferric oxyhydroxide. Chemical geology, 40 (1983) 135-148.

[29] Marshall T.A., Morris K., Law G.T.W., Livens F.R., Mosselmans J.F.W., Pieter Bots P., Shaw S. Incorporation of uranium into hematite during crystallization from ferrihydrite. Environmental Science and Technology, 48 (2014) 3724-3731.

[30] Ananda Subramani Kannan, Klas Jareteg, Niels Christian Krieger Lassen, Jens Michael Carstensen, Michael Adsetts Edberg Hansen, Flemming Dam, Srdjan Sasic. Design and performance optimization of gravity tables using a combined CFD-DEM framework. Powder Technology, 318 (2017) 423-440.

[31] 911 metallurgist. Titanium ore processing and beneficiation. https://www.911metallurgist.com/blog/titanium-flotation (2016) (accessed 20 December 2020).

[32] Ronghong Lin, Bret H. Howard, Elliot A. Roth, Tracy L. Bank, Evan J. Granite, Yee Soong, Enrichment of rare earth elements from coal and coal by-products by physical separations. Fuel, 200 (2017) 506-520.

[33] The engineering toolbox. Densities of minerals. https://www.engineeringtoolbox.com/mineral-density-d_1555.html (2009) (accessed 13 December 2020).

[34] Zhang W, Noble A, Yang X, Honaker R. A Comprehensive Review of Rare Earth Elements Recovery from Coal-Related Materials. Minerals, 10 (2020) 451p.

Chapter 5

Bulk characterisation of rare earth elements and toxic heavy metals in simulant coal fly ash

The economic viability of fly ash material as an unconventional source of rare earth elements (REEs) is hinged primarily on the concentration and effective extraction of these elements. In Chapter four, REEs were reported to be mainly associated with discrete micro mineral particles of monazite, xenotime and zircon, in addition to other forms of occurrence, undetected in electron microscopy analysis due to low concentrations. In this chapter, results of bulk total acid digestion and sequential extraction analyses of coal (MC, KC, DC) and simulant coal fly ash (OMA, OKA, ODA) samples are presented and discussed, aimed at evaluating the economic viability of REE recovery by determining the REEs content and the influence of fractionation and combustion temperature on extractability within the fly ash materials.

The methods and results presented in this chapter have been published in the peer-reviewed literature:

Ilemona C. Okeme, Peter G. Martin, Christopher Jones, Richard A. Crane, Theophilus I. Ojonimi, Konstantin Ignatyev, Dave Megson-Smith, Thomas B. Scott. An advanced analytical assessment of rare earth element concentration, distribution, speciation, crystallography and solid-state chemistry in fly ash. *Spectrochimica Acta Part B: Atomic Spectroscopy*, 2020.

5.1 Experimental Methods

In this study, an Agilent 7700x ICP-MS was used to determine the mass and phase fractions of REEs, toxic heavy metals and actinides (U, Th) in coal and fly ash samples following full acid digestion and sequential extraction. The Agilent 7700x utilises a special third-generation collision/reaction cell (ORS3 octopole reaction system, operating in He-mode) to remove spectral interferences that might otherwise bias results. These spectral interferences result from polyatomic ions (with m/z ratios identical to those of the elements of interest) formed during sample digestion process. Calibration was performed using an Inorganic Ventures ICP-71A multi-elemental ICP-MS calibration standard, which contained REEs, trace heavy metals, U and Th, among others. Indium was used as an internal standard and was added inflow whilst samples were being ran. During sample analyses, blanks, duplicates and replicates of a United States Geological Survey (USGS) reference material (AGV-1, DNC-1) were run every 10 samples to detect any variance or instrumental drift during analysis and to provide a measure of accuracy.

5.1.1 Total acid digestion

Acid digestion and ICP-MS analysis were performed at the Camborne School of Mines, (University of Exeter, UK), using the method of Garbe-Schönberg [1]. A total of 45 fly ash samples (15 per coal mine) were prepared, hereafter termed OMA, OKA and ODA fly ash samples. Each sample was first homogenised by gentle agitation and 100 mg were transferred into an individual 50 mL screw cap Teflon digestion vessel. Following this, 4 mL of HF (47wt% - 51wt% trace metal grade; Fisher Scientific) followed by 3 mL of HCl (34wt% - 37wt% trace metal grade; Fisher Scientific) and finally 1 mL of HNO_3 (67wt% - 69wt% trace metal grade; Fisher Scientific) were added to each sample using a micropipette. Time (~5 mins) was

allowed between each step for any exo- and endothermic reactions to subside. The sample vessels were then sealed, placed in DigiPrep digestion blocks (preheated to 160 °C) and digested for 18 h. The vessels were then removed from the DigiPrep system and allowed to cool to room temperature. Following this, 1 mL of $HClO_4$ (65wt% Normatom; VWR^{TM}) was added to each sample, which were then returned to the DigiPrep system and heated to 180 °C until incipient dryness. The samples were then removed again from the DigiPrep system and allowed to cool to room temperature. This step was repeated, this time using 1 mL of HNO_3 (67% - 69% trace metal grade; Fisher Scientific). Then, 1 mL of concentrated HNO_3 (67wt% - 69wt% trace metal grade; Fisher Scientific) and 5 mL of MilliQ deionised water were added to each of the samples, which were returned to the DigiPrep system and heated to 100 °C for 30 min. The samples were then removed from the DigiPrep system and allowed to cool to room temperature. Finally, 44 mL of MilliQ deionised water was added to each sample, with the samples then prepared for ICP-MS analysis by diluting a 5 mL aliquot using 45 mL of 5% HNO_3 (67% - 69% trace metal grade; Fisher Scientific), to yield a 50 mL analysis volume.

5.1.2 Sequential extraction

While full acid digestion followed by ICP-MS provides detailed quantitative information about elements of interest, sequential extraction, provides crucial information on the mode of occurrence, bonds and mobility (or immobility) of the REEs, toxic heavy metals and actinides (U, Th), vital for understanding the geochemical processes that control their extractability, transport, leachability and bioavailability in the environment. The results of sequential extraction can inform cost-effective reagents to use in REE leaching and extraction. In this study, the Community Bureau of Reference (BCR) four-step method [2], was used.

The first step of the BCR sequential extraction method uses ethanoic acid to extract all metals and metalloids which are: (i) bound to carbonates; and (ii) found in their ionic or exchangeable form. Metal(loid)s removed in this stage are considered more mobile as they are water-soluble or exchangeable and so are more likely to be bioavailable. This makes potentially-ecotoxic elements that fall into this category a problem, if observed to occur in considerable concentrations. Conversely, this also makes them much easier to remove with selective leaching, making the fly ash waste easier to treat.

The second step of the BCR sequential extraction method uses hydroxylamine hydrochloride ($NH_2OH.HCl$) to extract all the chemically reducible fractions, such as those bound to iron and manganese oxides and hydroxides. These metals and metalloids are considered less mobile than those extracted in Step 1 and so are less of a concern if identified within the fly ash samples. However, they can still be mobilised under certain (acid) environmental conditions and so may still represent a problem.

The third step of the sequential extraction uses hydrogen peroxide (H_2O_2) and ammonium acetate ($C_2H_7NO_2$) to extract all oxidisable phases, metal(loid)s bound to sulphides and organic material. These phases are, again, less mobile than those removed in the previous steps, though they could still be mobilised if the environmental conditions change.

The fourth step of the sequential extraction uses aqua regia - a mixture of nitric acid (HNO_3) and hydrochloric acid (HCl) in a ratio of 1:3 - to extract the residual fractions, metal(loid)s bound to silicates or crystalline iron and manganese oxides. These are considered immobile and are unlikely to be released under natural conditions. As such, they do not present a danger to humans or the environment [2].

The sequential extraction analysis in this work was also performed at the Camborne School of Mines, (University of Exeter, UK). A total of six composite coal and fly ash samples (one composite coal sample and one composite fly ash sample per coal mine) were prepared and tested, namely OMC, OKC and ODC composite coal samples and the corresponding composite fly ash samples OMA, OKA and ODA. For each mine, the composite coal and fly ash samples were prepared by mixing equal amounts of the respective 15 coal samples and 15 fly ash samples, respectively. The sequential extraction procedure is detailed below, with each step completed in triplicate to assess reproducibility.

Step 1: Acid-soluble fractions

A 1 L solution of 0.11 M ethanoic acid was made by adding 6.38 mL of concentrated ethanoic acid to a volumetric flask, which was then filled to 1 L using MilliQ deionised water. This was thoroughly mixed and left to stand before use.

A sample of 0.5 g mass was added to a 50 mL centrifuge tube. To this tube, 20 mL of the 0.11 M ethanoic acid (CH_3COOH) was added using an auto-pipette. Once the ethanoic acid had been added to the samples, they were loaded into a rotary mixer and mixed for 16 h. After this time, the samples were centrifuged at 3,000 rpm for 2 min to form a plug of solid material at the base of the centrifuge tube. The supernatant was then carefully decanted to beakers, from which it was filtered using 0.45 µm PTFE syringe filters into plastic 50 mL flat-bottomed test tubes. These were acidified using concentrated HNO_3 and stored in a fridge ahead of dilution. A 10 mL volume of MilliQ deionised water was added to each of the centrifuge tubes and shaken vigorously to wash the solid residue. These were again centrifuged at 3,000 rpm for 2 min with the supernatant decanted into beakers, from which

it was filtered using 0.45 µm PTFE syringe filters into plastic 50 mL flat-bottomed test tubes. These were again acidified using concentrated HNO_3 and stored in a fridge ready for dilution.

Step 2: Reducible fractions

A 250 mL solution of 0.5 M $NH_2OH.HCl$ was made by adding 8.686 g of $NH_2OH.HCl$ salt to a volumetric flask, which was then filled to the 250 mL level using MilliQ deionised water.

An auto-pipette was used to add 20 mL of 0.5 M $NH_2OH.HCl$ solution to each of the washed solids from Step 1. These were then loaded into the rotary mixer and agitated for 16 h, after which the samples were then centrifuged at 3,000 rpm for 2 min. The resulting supernatant was decanted and filtered using 0.45 µm PTFE syringe filters, with the solid washed using 10 mL of MilliQ deionised water and centrifuged at 3,000 rpm for 2 min. The supernatant was decanted and filtered using 0.45 µm PTFE syringe filters. The filtered supernatants were then again acidified using concentrated HNO_3 and refrigerated prior to dilution.

Step 3: Oxidisable fractions

A 250 mL solution of 1 M $C_2H_7NO_2$ was made by adding 19.27 g of $C_2H_7NO_2$ salt to a 250 mL volumetric flask and filling to the 250 mL level with MilliQ deionised water. This was decanted to a beaker on a stirring plate. While stirred, the solution was adjusted to a pH of 1.8 using concentrated HNO_3.

An auto-pipette was used to add 5 mL of 8.82 M H_2O_2 to each sample, which were put in a water bath at 65 °C until near dryness. A further 5 mL of 8.82 M H_2O_2 were added using an auto-pipette. The samples were again left in a water bath at 65 °C, until near dryness. An auto-pipette was used to add 25 mL of the 1 M $C_2H_7NO_2$ solution to each sample. These were loaded into the rotary mixer and agitated for 16 h. The samples were then centrifuged at

3,000 rpm for 2 min. The supernatant was decanted and filtered using 0.45 µm PTFE syringe filters, with the solid washed using 10 mL of MilliQ deionised water and centrifuged again at 3,000 rpm for 2 min. Then, the supernatant was decanted and filtered using 0.45 µm PTFE syringe filters, with the filtered supernatants acidified using concentrated HNO_3 and refrigerated ahead of dilution.

Step 4: Residual fractions

The remaining solid was fully digested using aqua regia. In polypropylene centrifuge tubes, 6 mL of concentrated HCl was added to each residual sludge sample. Once the reaction subsided, 2 mL of concentrated HNO_3 was added to each sample. Each centrifuge tube was covered with a watch glass and left for 15 min to allow for the reaction to reach completion. The centrifuge tubes were then placed into a DigiPrep digestion block for 60 min at 95 °C. Once removed from the digestion block and allowed to cool, each sample was made up to a volume of 50 mL with MilliQ deionised water. The samples were filtered using 0.45 µm cellulose nitrate filters, after which they were diluted for ICP-MS by adding 0.5 mL of the sample to 49.5 mL of 5% HNO_3 (100x dilution).

5.2 Results and discussion

5.2.1 Rare earth concentration in simulant coal fly ash samples

Shown in Tables 5.1, 5.2 and 5.3, respectively, are the complete results of REE measurement with ICP-MS for fly ash samples (OMA, OKA, ODA) following full acid digestion. The mean total REE (plus Y and Sc) mass fraction for OMA, OKA and ODA were 623 $mg.kg^{-1}$, 442 $mg.kg^{-1}$ and 441 $mg.kg^{-1}$, respectively. The fraction of the critical REE (Nd, Eu, Tb, Dy, Y, Er) in OMA, OKA and ODA were 43%, 34% and 33%, respectively. Compared to bastnaesite ores - including the Bayan Obo rare earth deposit in China with only about 10% critical REE content - these fly ash materials are three to four times enriched in the critical REEs [3]. The most abundant REE in the fly ash materials were Ce, Y, Nd and La, with the highest values of these REEs (164 $mg.kg^{-1}$, 126 $mg.kg^{-1}$, 100 $mg.kg^{-1}$ and 86 $mg.kg^{-1}$, respectively) recorded in OMA fly ash materials (Table 5.1). The amount of Y confirms the SEM-EDS observations of xenotime and zircon occurrence in the fly ash materials (chapter four, section 4.2.3), and also suggests its association with combustion products of Y-bearing minerals such as bastnaesite, synchysite; though Y is abundant in the fly ash samples (being highest in OMA (126 $mg.kg^{-1}$)), its extraction will be difficult if it is mainly associated with zircon, a refractory mineral. The samples were highly-concentrated in the light REEs (LREEs), with Ce, followed by Nd, being the most abundant LREE in all samples. Out of the heavy REEs (HREEs), Y, Sc, Gd and Dy were the most abundant, with Eu, Tb, Ho, Tm and Lu each being just a few $mg.kg^{-1}$ (characteristic of non-ore HREE sources), indicating low occurrence of HREE minerals in the studied fly ash samples.

When compared with the upper continental crust abundance (UCCA), the total REE contents in OMA, OKA and ODA fly ash materials were two to four times enriched (with Ce being six times enriched in the OMA fly ash). This abundance pattern of the light and the heavy REE in

the fly ash samples conforms to the Oddo-Harkins Rule [4], where, in this case, REEs with even atomic number (Z) are more abundant than those with odd Z. Though these concentrations were generally well below concentrations in conventional REE ores [5], the large volumes of fly ash generated annually, in addition to the little or no additional cost of ore mining and waste rock handling, is a significant advantage. These results are very enriched for critical REE but in terms of total REE content, it is only seasonable but comparable to previously studied fly ash materials from the USA, China and Indian (Table 5.4).

Table 5.1: REE concentration ($mg.kg^{-1}$) in **OMA** simulant coal fly ash (compared with UCCA [6,7]), showing also TREE and critical REE (%).

	La	Ce	Pr	Nd	Sm	Sc	Y	Eu	Gd	Tb	Dy	Ho	Er	Tm	Yb	Lu	TREE	Critical REE (%)
OMA1	87	161	23	101	21	22	124	5	24	3	20	4	11	1	8	1	616	43
OMA2	83	147	23	98	20	22	121	5	24	3	19	4	10	1	8	1	589	43
OMA3	80	147	21	92	19	23	116	5	22	3	19	4	10	1	8	1	571	43
OMA4	77	141	21	92	19	24	123	5	23	3	20	4	11	1	8	1	573	44
OMA5	74	159	19	84	17	21	109	4	21	3	17	3	10	1	8	1	551	41
OMA6	67	119	18	80	17	19	101	4	19	3	16	3	9	1	7	1	484	44
OMA7	91	183	25	108	22	23	132	5	25	4	21	4	11	1	9	1	665	42
OMA8	74	146	21	93	20	21	119	5	23	3	19	4	11	1	8	1	569	44
OMA9	91	187	24	105	22	27	136	5	26	4	22	4	12	1	9	1	676	42
OMA10	94	181	25	106	22	26	130	5	25	4	21	4	11	1	9	1	665	42
OMA11	95	173	26	111	23	24	137	5	27	4	22	4	12	1	9	1	674	43
OMA12	93	178	24	100	20	26	115	5	23	3	18	4	10	1	7	1	628	40
OMA13	96	177	26	113	23	25	140	6	27	4	22	4	12	1	9	1	686	43
OMA14	82	165	22	96	20	24	132	5	24	3	21	4	11	1	9	1	620	43
OMA15	105	203	29	127	26	28	161	6	31	4	25	5	14	2	10	1	777	43
Mean	**86**	**164**	**23**	**100**	**21**	**24**	**126**	**5**	**24**	**3**	**20**	**4**	**11**	**1**	**8**	**1**	**623**	**43**
UCCA	**30**	**64**	**7.1**	**26**	**4.5**	**13.6**	**22**	**0.88**	**3.8**	**0.64**	**3.5**	**0.8**	**2.3**	**0.33**	**2.2**	**0.32**		

Critical REE: Nd, Eu, Tb, Dy, Y and Er. TREE: Lanthanides+Sc+Y. UCCA: Upper continental crust abundance.

Table 5.2: REE concentration (mg.kg^{-1}) in **OKA** fly ash (compared with UCCA [6,7]), showing also TREE and critical REE (%).

	La	Ce	Pr	Nd	Sm	Sc	Y	Eu	Gd	Tb	Dy	Ho	Er	Tm	Yb	Lu	TREE	Critical REE (%)
OKA1	82	140	17	63	12	26	63	3	12	2	11	2	6	1	5	1	446	33
OKA2	82	147	18	67	13	24	58	3	12	2	10	2	6	1	5	1	451	32
OKA3	80	141	16	60	11	27	62	3	11	2	10	2	6	1	5	1	438	33
OKA4	77	120	15	57	11	26	63	3	11	2	10	2	6	1	5	1	410	34
OKA5	83	151	19	71	14	24	67	3	13	2	12	2	7	1	6	1	476	34
OKA6	81	143	18	70	14	23	65	3	13	2	11	2	6	1	5	1	458	34
OKA7	79	123	16	61	12	25	62	3	11	2	10	2	6	1	5	1	419	34
OKA8	75	113	15	56	10	26	63	2	11	2	10	2	6	1	5	1	399	35
OKA9	72	96	14	55	11	24	60	3	11	2	10	2	6	1	5	1	373	36
OKA10	78	112	16	62	12	23	61	3	12	2	11	2	6	1	5	1	407	36
OKA11	86	131	18	69	13	27	73	3	14	2	13	2	7	1	6	1	465	36
OKA12	88	149	18	70	13	28	70	3	13	2	12	2	7	1	6	1	483	34
OKA13	81	156	18	67	13	24	58	3	12	2	10	2	6	1	5	1	460	32
OKA14	85	143	17	64	12	29	68	3	12	2	11	2	7	1	6	1	462	34
OKA15	90	153	17	65	12	31	71	3	12	2	12	2	7	1	6	1	485	33
Mean	**81**	**135**	**17**	**64**	**12**	**26**	**64**	**3**	**12**	**2**	**11**	**2**	**6**	**1**	**5**	**1**	**442**	**34**
UCCA	**30**	**64**	**7.1**	**26**	**4.5**	**13.6**	**22**	**0.88**	**3.8**	**0.64**	**3.5**	**0.8**	**2.3**	**0.33**	**2.2**	**0.32**		

Table 5.3: REE concentration (mg.kg^{-1}) in **ODA** fly ash (compared with UCCA [6,7]), showing also TREE and critical REE (%).

	La	Ce	Pr	Nd	Sm	Sc	Y	Eu	Gd	Tb	Dy	Ho	Er	Tm	Yb	Lu	TREE	Critical REE (%)
ODA1	75	138	17	65	12	20	54	3	12	2	10	2	5	1	5	1	422	33
ODA2	86	149	17	64	12	31	73	3	13	2	12	2	7	1	6	1	479	34
ODA3	85	152	18	70	14	23	61	3	13	2	11	2	6	1	5	1	467	33
ODA4	77	144	17	68	13	20	57	3	13	2	10	2	6	1	5	1	439	33
ODA5	76	140	17	67	13	19	55	3	12	2	10	2	5	1	5	1	428	33
ODA6	85	139	17	62	12	27	65	3	12	2	11	2	6	1	5	1	450	33
ODA7	77	131	15	58	11	25	58	3	11	2	10	2	6	1	5	1	416	33
ODA8	81	146	19	72	14	21	61	3	13	2	11	2	6	1	5	1	458	34
ODA9	84	155	19	71	14	22	62	3	13	2	11	2	6	1	5	1	471	33
ODA10	77	137	16	59	11	24	59	3	11	2	10	2	6	1	5	1	424	33
ODA11	78	137	18	69	13	22	60	3	13	2	11	2	6	1	5	1	441	34
ODA12	76	141	17	65	13	21	55	3	12	2	10	2	6	1	5	1	430	33
ODA13	79	133	16	59	11	25	60	3	11	2	10	2	6	1	5	1	424	33
ODA14	77	122	15	57	11	24	59	2	11	2	10	2	6	1	5	1	405	34
ODA15	82	152	19	72	14	21	59	3	13	2	11	2	6	1	5	1	463	33
Mean	**80**	**141**	**17**	**65**	**13**	**23**	**60**	**3**	**12**	**2**	**11**	**2**	**6**	**1**	**5**	**1**	**441**	**33**
UCCA	**30**	**64**	**7.1**	**26**	**4.5**	**13.6**	**22**	**0.88**	**3.8**	**0.64**	**3.5**	**0.8**	**2.3**	**0.33**	**2.2**	**0.32**		

Table 5.4: Comparison of mass concentration (mg.kg^{-1}) of total REE (TREE) in simulant coal fly ash with those of top coal-consuming countries.

Coal source	TREE	Critical REE (%)	Reference
Omelewu coal, Nigeria	623	43	This study
Okaba coal, Nigeria	442	34	This study
Odagbo coal, Nigeria	441	33	This study
Jungar, Inner Mongolia, China	293.5	28.3	Dai et al., 2014b [8]
Bhusawal coal plant (unspecified mine), India	384.1	26.3	Modal et al., 2019 [9]
Central Appalachian (Fire Clay), USA	1667.6	36.5	Mardon and Hower, 2004 [10]
Central Appalachian, USA	401.5	38.6	Hower et al., 2013b [11]
Illinois Basin, USA	312.1	36.2	Hower et al., 2013b [11]
Central Appalachian, USA	563.6	38.1	Hower et al., 2013b [11]
Powder River Basin, USA	283.2	32.8	Taggart et al., 2016 [3]

5.2.2 Economic valuation of REE content of simulant coal fly ash

Table 5.6 shows the REE mass fractions expressed as rare earth oxide (REO). These results are comparable to the REO content of the following types of REE ore deposits: ion adsorption clay deposits, South China (500 mg.kg^{-1} to 4,000 mg.kg^{-1}); round top peralkaline igneous deposits, USA (630 mg.kg^{-1}); and Canali heavy mineral sand deposits, Turkey (700 mg.kg^{-1}) [12]. The highest mean REO value was recorded for OMA (744.9 mg.kg^{-1}). On an REO basis, the economic valuation shows that these fly ash samples have very strong potential of yielding REO worth millions of US dollars (US$) per year. Using the ash content values of OMA, OKA and ODA fly ash samples (14.8wt%, 10.7wt% and 5.3wt%, respectively; Table 5.5), and an initial projected annual consumption of 27 million metric tonnes of coal by the proposed power plants [13], this amounts to 1330 thousand, 960 thousand and 480 thousand metric tonnes of fly ash generated annually from OMA, OKA and ODA coal mines, respectively (assuming equal supply of coal from all mines). Using the REO values (Table 5.6), we estimate that a total of 1,752 t.yr^{-1} (1,751,844.7 kg.yr^{-1}) of REO is recoverable from Nigerian fly ash,

translating into an annual value of US$41,204,000 (Table 5.7). Though this economic valuation does not include costs of recovery (with cost-effective technologies currently under development) and it is subject to the volatility of REE prices, it however, provides the basis for evaluating viability of REE extraction from fly ash. One major advantage of using fly ash as an alternative source of REE is the minimal expense associated with the mining processes, such as blasting, prospecting and transport. The results also show that the potential value of REE in fly ash is dependent on REE class (LREE vs HREE), with the high prices of Sc, Nd and HREE contributing considerably to the REE value in fly ash. This is an extremely positive observation and one which is potentially lucrative for the country of Nigeria or mining companies, provided a suitable extraction process, that is affordable and environmentally acceptable, can be identified or developed.

Table 5.5: Proximate analysis of **OMA**, **OKA** and **ODA** coals, from existing literature.

	OMA [14]	OKA [15]	ODA [16]
Moisture content (wt%)	14.8	5.4	14.9
Ash content (wt%)	14.8	10.7	5.3
Volatile matter (wt%)	45.9	21.5	38.7
Fixed carbon (wt%)	39.3	54.9	41.1

Table 5.6: Conversion of mean REE concentration to mean rare earth oxide (REO).

	Mean REE ($mg.kg^{-1}$)				Mean REO ($mg.kg^{-1}$)		
	OMA	**OKA**	**ODA**	REE to REO conversion factor [17]	**OMA**	**OKA**	**ODA**
La	86	81	80	1.17	100.6	94.8	93.6
Ce	164	135	141	1.17	191.9	158	165
Pr	23	17	17	1.17	26.9	19.9	19.9
Nd	100	64	65	1.16	116	74.2	75.4
Sm	21	12	13	1.16	24.4	13.9	15.1
Sc	24	26	23	1.53	36.7	39.8	35.2
Y	126	64	60	1.27	160.0	81.3	76.2
Eu	5	3	3	1.16	5.8	3.48	3.48
Gd	24	12	12	1.15	27.6	13.8	13.8
Tb	3	2	2	1.15	3.45	2.3	2.3
Dy	20	11	11	1.15	23	12.7	12.7
Ho	4	2	2	1.15	4.6	2.3	2.3
Er	11	6	6	1.14	12.5	6.84	6.84
Tm	1	1	1	1.14	1.14	1.14	1.14
Yb	8	5	5	1.14	9.12	5.7	5.7
Lu	1	1	1	1.14	1.14	1.14	1.14
Total	**621**	**442**	**442**		**744.9**	**531.3**	**529.8**

Table 5.7: Total annual mass and estimated value of REO per year.

	Total REO (kg.yr^{-1})					Total value (US$.yr^{-1}) to the nearest thousand			
	OMA	OKA	ODA	Total	REO price per kg (US$) [18]	OMA	OKA	ODA	Total
La	133,798	91,008	44,928	269,734	1.67	223,000	152,000	75,000	450,000
Ce	255,227	151,680	79,200	486,107	1.63	416,000	247,000	129,000	792,000
Pr	35,777	19,104	9,552	64,433	47.56	1,702,000	909,000	454,000	3,064,000
Nd	154,280	71,232	36,192	261,704	40.96	6,319,000	2,918,000	1,482,000	10,719,000
Sm	32,452	13,344	7,248	53,044	1.77	57,000	24,000	13,000	94,000
Sc	48 811	38,208	16,896	103,915	46.86	2,287,000	1,790,000	792,000	4,869,000
Y	212,800	78,048	36,576	327,424	2.84	604,000	222,000	104,000	930,000
Eu	7,714	3,340.8	1,670.4	12,725.2	30.53	236,000	102,000	51,000	389,000
Gd	36,708	13,248	6,624	56,580	22.58	829,000	299,000	150,000	1,278,000
Tb	4,588.5	2,208	1,104	7,900.5	489.14	2,244,000	1,080,000	540,000	3,864,000
Dy	30,590	12,192	6,096	48,878	235.7	7,210,000	2,874,000	1,437,000	11,504,000
Ho	6,118	2,208	1,104	9,430	44.37	271,000	98,000	49,000	418,000
Er	16,625	6,566.4	3,283.2	26,474.6	23.07	384,000	151,000	76,000	611,000
Tm	-	-	-	-	NA	-	-	-	-
Yb	12,129.6	5,472	2,736	20,337.6	20.16	245,000	110,000	55,000	410,000
Lu	1,516.2	1,094.4	547.2	3,157.8	567.94	861,000	622,000	311,000	1,793,000
Total	**989,134.3**	**508,953.6**	**253,756.8**	**1,751,844.7**		**23,889,000**	**11,597,000**	**6,717,000**	**41,204,000**

NA: Not available.

5.2.3 REE fractionation

Figures 5.1, 5.2 and Table 5.8 show the results of sequential extraction for the light REEs (LREEs) and heavy REEs (HREEs) in the simulant coal fly ash (OMA, OKA, ODA) and coal (OMC, OKC, ODC) samples.

Coal sample

In the coal samples, while the LREEs and the HREEs were recovered to a limited extent in the initial acid-soluble fraction (~1%), they were mainly contained in the oxidisable fraction (42% to 64% for LREEs; 63% to 77% for HREEs), followed by the residual fraction (27% to 47% for LREEs; 13% to 22% for HREEs), and then the reducible fraction (8% to 13% for LREEs; 7% to 14% for HREEs). While the concentrations of both LREEs and HREEs in the residual and reducible fractions confirm the occurrence of rare earth minerals and possible adsorption of REEs onto Fe (hydr)oxides in the coal samples, the very high concentrations of both LREEs and HREEs in the oxidisable fraction indicate that REEs in the coal samples were significantly associated with sulphides and organic matter. Studies have shown that coal organic matter may become REE-enriched, occurring during coalification when REE-enriched leachates infiltrated the coal bed and became absorbed by the organic matter, with HREEs having a higher affinity to the organic matter [7,19-21], hence the weighting to the HREE observed in the samples.

It is notable that only a very small amount (~1%) of the critical REEs (Nd, Eu, Tb, Dy, Y, Er) were recovered in the exchangeable fraction for all coal samples, being mostly concentrated in the oxidisable fraction (52% to 78%), residual fraction (10% to 28%) and reducible fraction (7% to 18%). The implication of these results for REE recovery from pulverised raw coal is that

REEs in coal cannot be easily recovered using ethanoic acid, as only just ~1% of REEs will be recovered with the remainder staying chemically locked inside the coal.

Simulant coal fly ash samples

In the fly ash samples, while both the LREEs and HREEs were mainly associated with the residual fraction (39% to 68%) - a confirmation of the SEM-EDS results presented in Chapter Four - significant amounts of both were associated with the acid-soluble fraction (14% to 31%). The amounts of both LREEs and HREEs in the oxidisable fraction (13% to 22%) were comparable to the acid-soluble fraction, with the least amounts being in the chemically reducible fraction (3% to 8%). While REEs in the residual fraction were attributed to a combination of REE-containing silicate minerals and rare earth metal oxides (formed during decomposition of REE-bearing organic matter in coal during combustion), REEs in the oxidisable fraction result from the REE-bearing sulphide minerals [22]. Compared with the mean values of REEs from the total dissolution analysis (tables 5.1, 5.2 and 5.3), the total values of REEs extracted in the sequential analysis of OMA, OKA and ODA (Table 5.8) translates to 24 wt%, 44 wt% and 45 wt% percent recovery, respectively, an indication of non-dissolution of significant amounts of REEs in the residual fractions.

The amounts of the critical REEs recovered in the acid-soluble fraction were significant and comparable to the amounts of the LREEs and HREEs in the acid-soluble fractions of all the fly ash samples, except for OMA (5%). Compared to the other critical REEs, the contents of Eu in the acid-soluble fraction of all fly ash samples were relatively low (9% to 10%), except for OMA (23%). The significantly high amount of REEs recovered in the acid-soluble fractions is attributable to: (i) the occurrence of easily soluble calcium oxide, periclase, and other basic oxides (formed from the decomposition of REE carbonate minerals such as bastnaesite and

synchysite) - although not detected in this study, previous studies have detected REE-bearing oxide of Ca in coal fly ash [22]; and (ii) increased solubility of difficult-to-leach rare earth minerals due to thermal decomposition and amorphisation of their matrix during combustion, while also reducing the formation of glassy phases and encapsulation of REE minerals in such phases. Honaker et al. [23], in their study of fly ash sourced from fluidised bed combustion (FBC) coal-fired power plant (operated at between 750 °C to 900 °C) reported improved REE extractability due to thermal decomposition. This supports the finding in this current study, and provides evidence for the advantage of burning coal at low temperatures (below 1200 °C), or using FBC coal-fired power plant that, by design, operate at temperatures below 1200 °C. Although most sequential extraction studies [24-26] on coal fly ash (sourced from PCC coal-fired power plant), reported over 70% of REEs to be in the insoluble residual fraction and less than 4% in the acid soluble fraction, the results from this present study on simulant coal fly ash agree with a previous study by Taggart et al. [27], on coal fly ash sourced from PCC coal-fired power plant. Taggart et al. [27] in their sequential extraction study, reported a 14% REEs recovery from the acid soluble fraction; however, a higher amount of REE was recovered from the oxidisable fraction (16.9%), which was attributed to a higher amount of unburnt carbon in the coal fly ash samples.

Implication for REE recovery

The implication of these results for REE recovery from fly ash samples is that REEs (especially the critical REEs) can be easily and cost-effectively recovered using ethanoic acid (a biodegradable and environmentally-friendly acid, which is the main component of cheap, and readily available vinegar), compared to sulphuric and hydrochloric acids. To maximise REE recovery from these fly ash materials while minimising costs, a combination of magnetic,

electrostatic and density beneficiation methods (to concentrate the REE-bearing minerals), followed by cost-effective heap-leaching (using ethanoic acid) and selective extraction, to recover the acid-soluble fraction of the REEs, is hereby proposed as a potentially economical and environmentally friendly procedure for the recovery of REEs from the simulant coal fly ash.

The heap-leaching method is a low-cost industrial metal extraction process during which a large heap of (pulverised) ore or sample of interest (placed on an impermeable liner) is treated with chemical solutions (lixiviants), producing a metal-laden (pregnant) leach solution [28]. The dissolved metals in the leach solution are then potentially recovered via a selective extraction process such as the conventional solvent and liquid membrane extraction. Owing to its low operating costs, fewer handling procedures, low energy requirement and low solvent consumption, Liquid membrane extraction (LME) process has been projected as a promising alternative to solvent extraction process for the recovering REEs from coal fly ash [28-30]. However, the development of customised and cost effective methods for REEs recovery from coal fly ash is still challenging; no method has been perfected and commercialised. Figure 5.3 shows a typical flowsheet of a heap-leach operation. As the fly ash materials need no pulverisation, and only a cheaply-available acid (ethanoic acid) is required to extract the REEs, this process is highly cost-effective. Compared to REE recovery via total acid digestion of fly ash materials, the proposed process greatly reduces the toxic waste to be handled during REE recovery, which translates to lower cost. This proposed process of using ethanoic acid in a heap leach process is potentially suitable for the cost-effective recovery of significant amounts of REEs from a substantial proportion of the millions of tonnes of fly ash materials (generated from FBC coal-fired power plant) that exist globally. Although PCC power

plants dominate globally, there are more than 6,000 FBC power plants in operation largely concentrated in China, with many more under construction or planned [31].

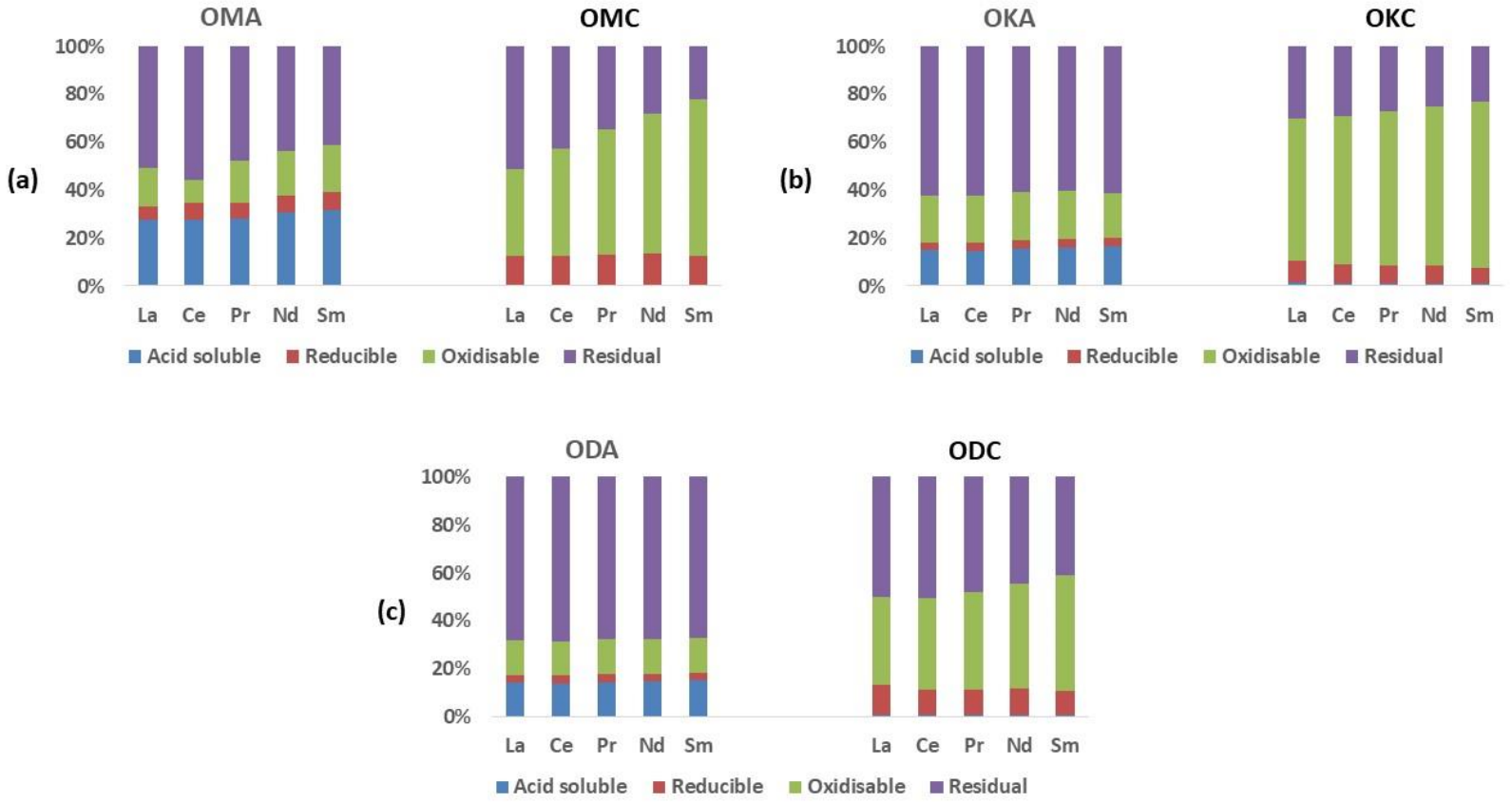

Figure 5.1: Results of sequential extraction for LREEs; (a) simulant coal fly ash (OMA) and the corresponding coal (OMC); (b) simulant coal fly ash (OKA) and the corresponding coal (OKC); (c) simulant coal fly ash (ODA) and the corresponding coal (ODC).

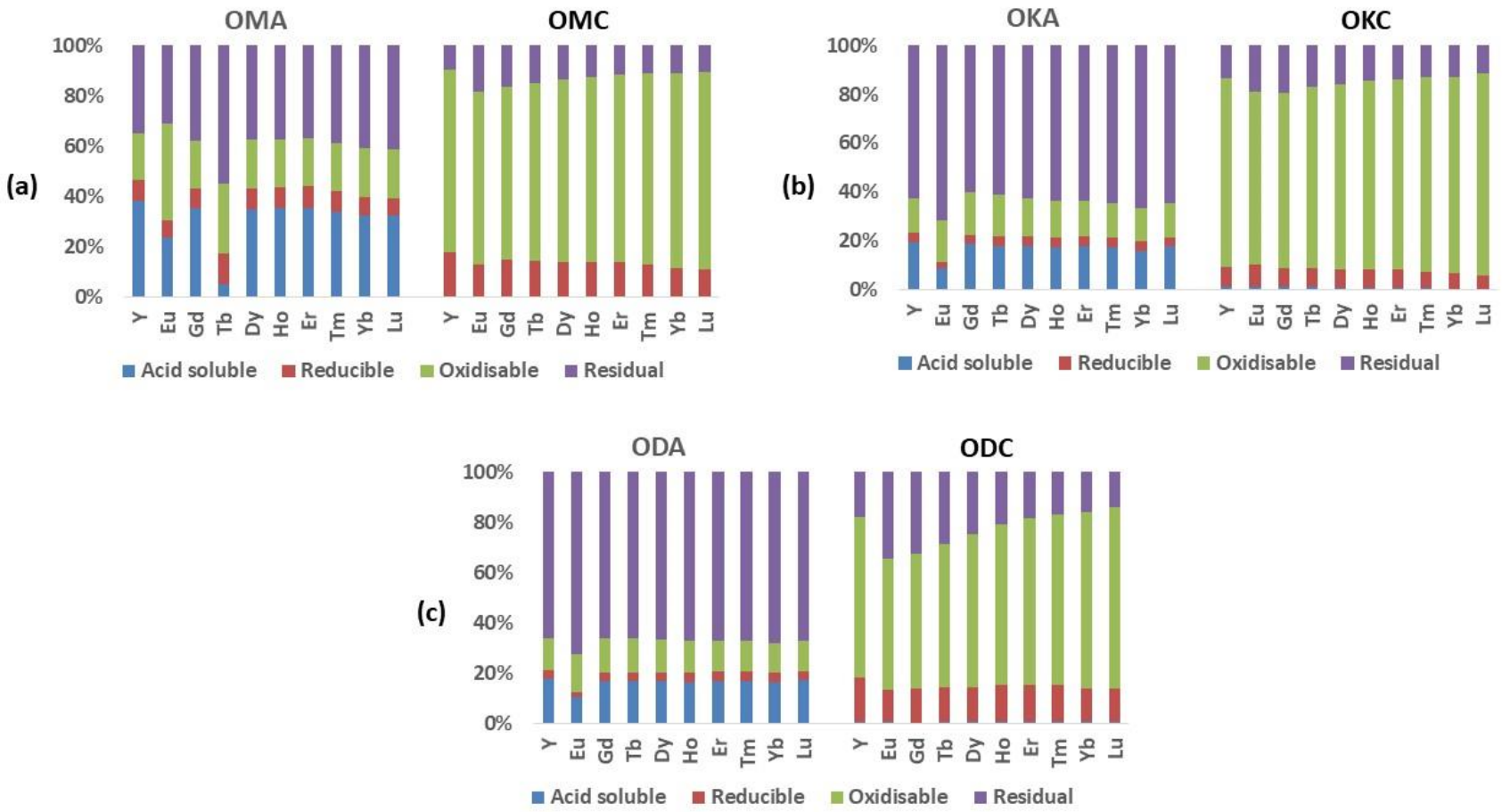

Figure 5.2: Results of sequential extraction for HREEs; (a) simulant coal fly ash (OMA) and the corresponding coal (OMC); (b) simulant coal fly ash (OKA) and the corresponding coal (OKC); (c) simulant coal fly ash (ODA) and the corresponding coal (ODC).

Table 5.8: Absolute values (mg.kg^{-1}) of REEs in the various sequential extraction fractions for the simulant fly ash samples (OMA, OKA, ODA).

Sample/Fractions	La	Ce	Pr	Nd	Sm	Y	Eu	Gd	Tb	Dy	Ho	Er	Tm	Yb	Lu
OMA															
F1	5.57	10.87	1.56	7.60	1.67	11.90	0.33	2.26	0.03	1.76	0.35	0.92	0.11	0.53	0.08
F2	1.15	2.77	0.38	1.78	0.39	2.47	0.10	0.51	0.08	0.44	0.09	0.22	0.03	0.13	0.02
F3	3.18	3.73	0.98	4.64	1.04	5.78	0.54	1.21	0.17	0.97	0.19	0.49	0.06	0.32	0.05
F4	10.24	22.07	2.65	11.00	2.16	10.80	0.43	2.43	0.34	1.90	0.37	0.96	0.12	0.67	0.10
Total	**20.14**	**39.44**	**5.57**	**25.02**	**5.26**	**30.95**	**1.40**	**6.41**	**0.62**	**5.07**	**1.00**	**2.59**	**0.32**	**1.65**	**0.25**
OKA															
F1	5.02	9.48	1.18	4.68	0.91	4.82	0.14	1.00	0.14	0.78	0.15	0.41	0.05	0.29	0.05
F2	1.17	2.35	0.27	1.00	0.20	0.94	0.03	0.21	0.03	0.18	0.03	0.09	0.01	0.07	0.01
F3	6.48	13.04	1.50	5.73	1.06	3.53	0.27	0.94	0.13	0.72	0.13	0.34	0.04	0.25	0.04
F4	21.17	41.10	4.57	17.32	3.42	15.56	1.11	3.24	0.48	2.80	0.56	1.50	0.20	1.21	0.16
Total	**33.84**	**65.97**	**7.52**	**28.73**	**5.59**	**24.85**	**1.55**	**5.39**	**0.78**	**4.48**	**0.87**	**2.34**	**0.30**	**1.82**	**0.26**
ODA															
F1	4.87	9.17	1.12	4.43	0.90	4.45	0.17	0.94	0.14	0.76	0.15	0.40	0.05	0.30	0.04
F2	1.05	2.11	0.24	0.93	0.19	0.87	0.04	0.19	0.03	0.16	0.03	0.09	0.01	0.07	0.01
F3	5.04	9.36	1.15	4.41	0.85	3.09	0.24	0.77	0.11	0.60	0.11	0.29	0.04	0.22	0.03
F4	23.29	45.63	5.28	20.23	4.01	16.42	1.18	3.74	0.54	3.05	0.59	1.58	0.21	1.26	0.17
Total	**34.25**	**66.27**	**7.79**	**30.00**	**5.95**	**24.83**	**1.63**	**5.64**	**0.82**	**4.57**	**0.88**	**2.36**	**0.31**	**1.85**	**0.25**

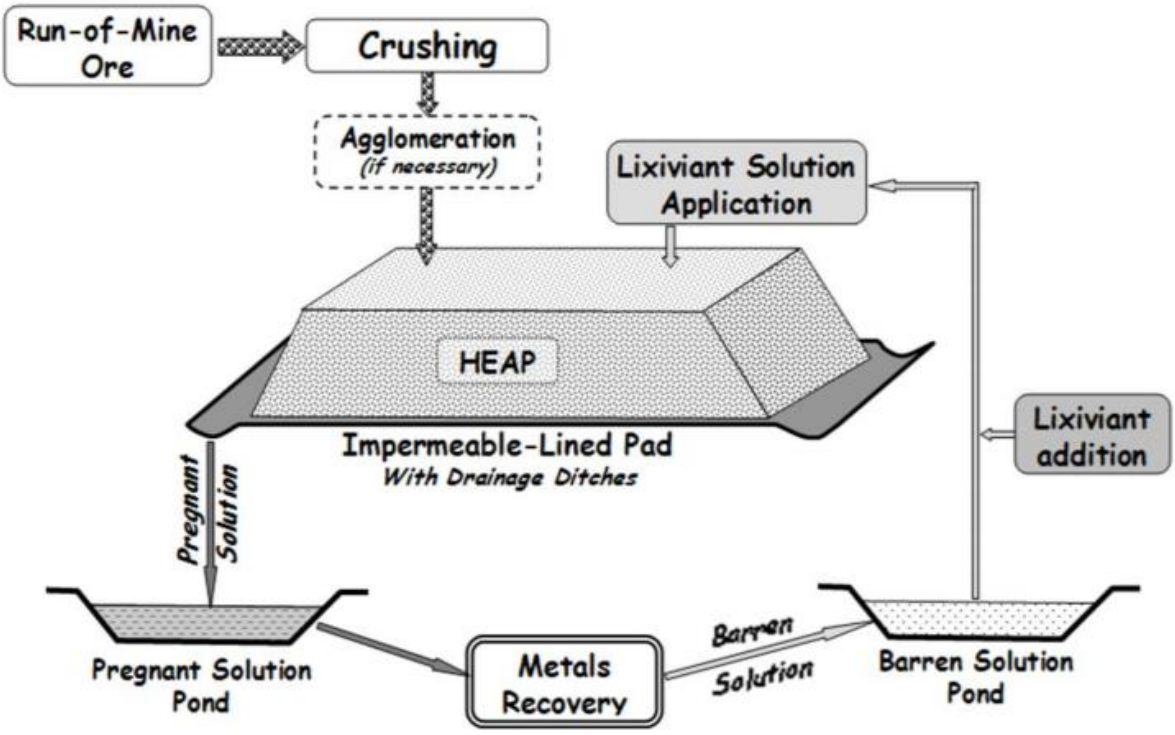

Figure 5.3: Generalised flowsheet of a heap leach operation [32].

5.2.4 Toxic heavy metal fractionation

Figure 5.4 shows the results of sequential extraction of the toxic heavy metals Cr, As, Pb, Cd, Th and U from coal and fly ash samples.

Coal sample

In OMC, only As (11%), Pb (4%) and Cd (15%) were significantly recovered in the acid-soluble fraction, with only very small amounts (~1%) of Cr, Th and U recovered in the same fraction. Cr (96%), Pb (53%), Cd (60%), Th (59%) and U (87%) were most recovered in the oxidisable fraction, alongside As (37%). This indicates high organic affinity of these toxic heavy metals for organic matter, occurring as coordination complexes (chelates) within the organic structure of the coal [33], and the occurrence of sulphide minerals of Pb (e.g. galena). While the amount of U (0.3%) recovered in the reducible fraction of OMC indicates very little U

adsorption onto the surface of (hydr)oxides of Fe and Mn, the high amount of U (87%) in the oxidisable fraction indicates less mobility and less solubility. As (52%) was most recovered in the reducible fraction, alongside significant amounts of Pb (25%) and Cd (24%); these results are indications of: (i) occurrence of arsenopyrite and pyrite in the coal samples; and to a lesser extent (ii) adsorption of As, Pb, Cd onto the surface of (hydr)oxides of Fe and Mn during coalification. Studies have shown that (hydr)oxides of Fe and Mn are good scavengers of toxic heavy metals [34,35]. Th (41%), Pb (18%) and U (13%) were also associated with the residual fraction, an indication of the occurrence of Th and U in silicate minerals (e.g. zircon, coffinite, thorite) alongside radiogenic Pb from the decay of Th and U.

In OKC and ODC, a similar distribution of the toxic heavy metals was recorded, with As in the acid-soluble fractions of OKC (27%) and ODC (23%) being about two times higher than in OMC (11%). These results indicate strong similarity in the mineralogy and geochemistry of OMC, OKC and ODC coal samples.

Simulant coal fly ash sample

In OMA, OKA and ODA, the amounts of the toxic heavy metals were generally higher compared to OMC, OKC and ODC, due to the destruction of organic matter in the coal samples during combustion, and subsequent preconcentration of the heavy metals into the residual fly ash. The amounts of Cr recovered in the acid-soluble fraction for OMA (~2%), OKA (~3%) and ODA (~4%) were two to four times higher compared to OMC, OKC and ODC (in which ~1% Cr was recovered). In the acid-soluble fraction of the fly ash samples, As (46% to 60%) was the most enriched, followed by Cd (15% to 34%). In the acid-soluble fraction, the amount of Pb recovered from ODA (4%) was three to five times lower compared to its amounts in OMA (21%) and OKA (13%). The greatest amounts of U (53% to 62%) and Th (89% to 96%)

were recovered in the highly immobile and insoluble residual fraction, followed by the oxidisable fraction (34% to 41% for U; 4% to 10% for Th). Compared with OMC, OKC and ODC, (with 0.2%, 0.1% and 0.5%, respectively, of U recovered in the acid-soluble fraction), U recovered in the same fraction from OMA (5%), OKA (3%) and ODA (13%) was 25 to 30 times higher but still proportionately low. Compared to the U recovered in the other fractions, the amount of U in the acid-soluble fraction (being very mobile and soluble), although low, is of most concern for human health and the environment. These results agree with previous studies on fly ash sourced from a coal-fired thermal plant [27,36].

Implications

From the perspective of health and environmental hazards, As, Pb, Cd, Cr and U in the acid-soluble fraction (due to their high mobility, solubility and bioavailability) are of serious human and environmental concern, as these metals are carcinogenic, mutagenic and teratogenic in humans and aquatic organisms [37]. U causes mutation, lowering of reproduction rate and mass mortality in aquatic animals (e.g. fish, crabs) [34]; As, Pb, Cd and Cr also bioaccumulates in aquatic life forms, and subsequently in humans via consumption, leading to health concerns such as cancer, kidney disfunction and growth impairment in children [37].

With respect to REE recovery, the low concentration Of Cr in all the fly ash samples studied, and the relatively low amount of Pb in ODA, translates to lower costs, as smaller amounts of toxic wastes will be generated, to require handling. Following the heap-leaching process, the fly ash residue (now with a reduced radioactivity level due to beneficiation of the radioactive REE-bearing minerals and actinides) can then be processed into bricks or concrete, locking the toxic heavy metals in the brick and concrete matrices. While recycling the residual fly ash

(post heap-leaching) adds extra value, it also reduces the health and environmental hazards of the toxic heavy metals, and the carbon footprint of using conventional cement in brick and concrete production.

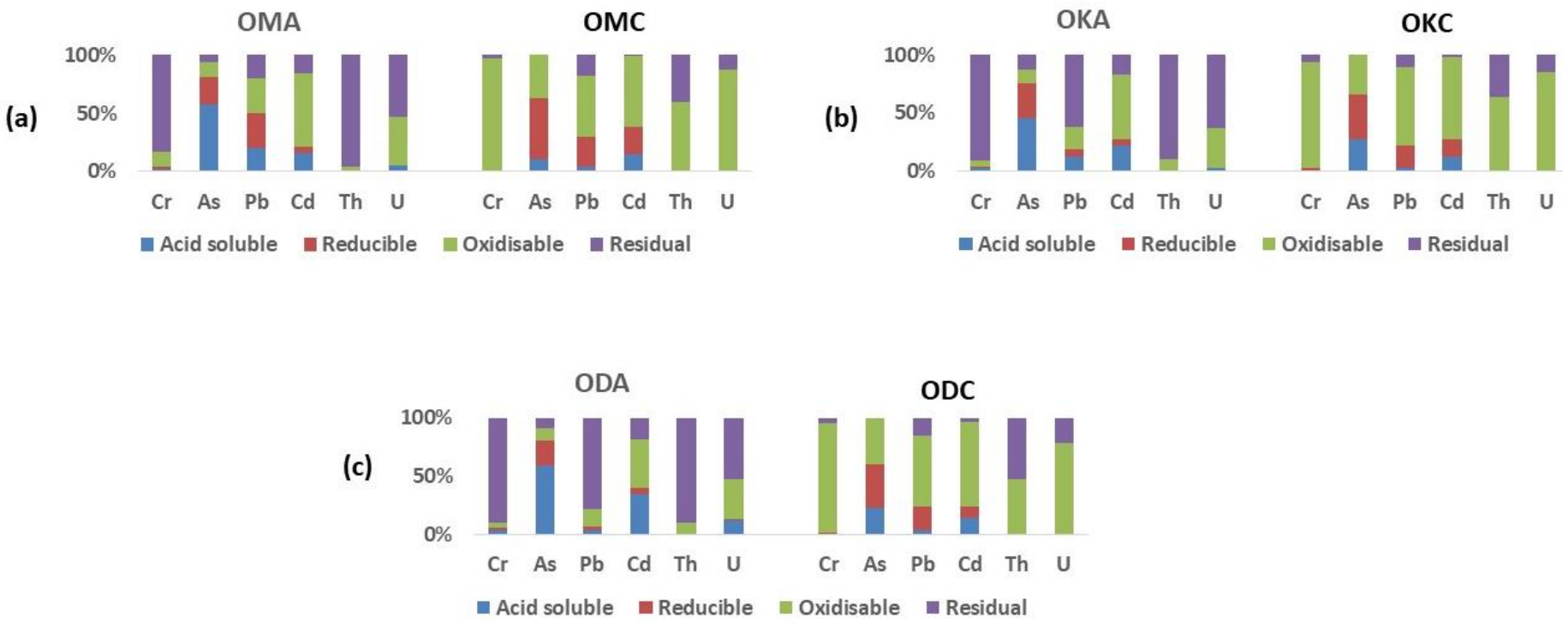

Figure 5.4: Results of sequential extraction of toxic heavy metals from coal and simulant coal fly ash; (a) simulant coal fly ash (OMA) and the corresponding coal (OMC); (b) simulant coal fly ash (OKA) and the corresponding coal (OKC); (c) simulant coal fly ash (ODA) and the corresponding coal (ODC)

5.3 Summary

The results of total acid digestion and sequential extraction of REEs from Nigerian fly ash and coal samples have been presented and discussed. The average total REE mass fractions (plus Y and Sc) in OMA, OKA and ODA fly ash samples were 623 $mg.kg^{-1}$, 442 $mg.kg^{-1}$ and 441 $mg.kg^{-1}$, respectively, which translate to a two to four times enrichment when compared with average upper continental crust abundance. Compared with China's Bayan Obo HREE bastnaesite ore deposit, the fly ash samples were found to be relatively enriched in the critical REEs (Nd, Eu, Tb, Dy, Y, Er), with the values of 43%, 34% and 33% in OMA, OKA and ODA, respectively. Although the amount of REEs (including the critical REEs) recovered from the acid-soluble fraction in the coal samples was very low (~1%), significant amounts of the REEs (14% to 31%) were recovered from the same fraction in the corresponding fly ash materials. The greatest amounts of REEs were contained in the residual fraction of the fly ash (39% to 68%).

In all the coal samples, the toxic heavy metals were most concentrated in the stable oxidisable fraction (53% to 96%) and residual fractions (24% to 54%); only As (11%), Pb (4%) and Cd (15%) were significantly recovered in the acid-soluble fraction, with very low (~1%) amounts of Cr, Th and U recovered in the same fraction. In the fly ash samples, As (46% to 60%) was the most enriched in the acid-soluble fraction, followed by Cd (15% to 34%). While the greatest amounts of U (53% to 62%) and Th (89% to 96%) were only recovered from the difficult-to-leach residual fraction, small but not insignificant amounts of U were recovered in the acid-soluble fraction from OMA (5%), OKA (3%) and ODA (13%). The implication of these results for REE recovery from these fly ash samples is that REEs (especially the critical REEs) in the fly ash can be easily and cost-effectively recovered using a combination of physical separation

techniques and heap-leaching (using ethanoic acid), while also reducing the health and environmental hazards of the toxic heavy metals by recycling the residual fly ash (post beneficiation and heap-leaching) into bricks or concrete. Total recovery of the REEs in these fly ash materials can potentially yield an estimated annual revenue of US$41,204,000 (costs of recovery inclusive) to the Nigerian government; but just using simple ethanoic acid (or similar), a significant amount of the REEs would be recovered for relatively little cost or effort.

Further work is recommended to explore available and cost effective processes for REE separation from leach solutions. This is needed in order to generate market grade products for onwards sale recognising that efficiently separated REE products attract higher market price.

5.4 References

[1] Garbe-Schönberg C.-D. Simultaneous determination of thirty-seven trace elements in twenty-eight international standards by ICP-MS. Geostandards Newsletter, 17 (1993) 81-97.

[2] Ure A., Quevauviller Ph., Muntau H., Griepink B. Euro Report EUR 14763 EN, Improvement and harmonisation of extraction techniques for soil and sediment analysis, Office for Official Publications of the European Communities, Luxembourg, (1993) 85p.

[3] Taggart R.K., Hower J.C., Dwyer G.S., Hsu-Kim H. Trends in the rare earth element content of U.S.-based coal combustion fly ashes. Environmental Science and Technology, 50 (2016) 5919-5926.

[4] A Dictionary of Earth Sciences (3 ed.). Edited by Michael Allaby; Oxford; Oxford university press (2008).

[5] British Geological Survey. Rare earth elements. https://www.bgs.ac.uk/downloads/start.cfm?id=1638 (2011) (accessed 18 July 2019).

[6] Taylor S.R., McLennan S.M. The geochemical evolution of the continental crust. Reviews of Geophysics, 33 (1995), 241–265.

[7] Taylor S.R., McLennan S.M. The continental crust: its composition and evolution. Blackwell, Oxford, 1985.

[8] Dai S.F., Zhao L., Hower J.C., Johnston M.N., Song W.J., Wang P.P., Zhang S.F. Petrology, mineralogy, and chemistry of size-fractioned fly ash from the Jungar power plant, Inner Mongolia, China, with emphasis on the distribution of rare earth elements. Energy and Fuels, 28 (2014) 1502-1514.

[9] Modal S., Ghar A., Satpati A.K., Sinharoy P., Singh D.K., Sharma J.N., Sreenivas T., Kain V. Recovery of rare earth elements from coal fly ash using TEHDGA impregnated resin. Hydrometallurgy, 185 (2019) 93-101.

[10] Mardon, S. M., Hower, J.C. Impact of coal properties on coal combustion by-product quality: examples from a Kentucky power plant. International Journal of Coal Geology, 59 (2004) 153-169.

[11] Hower J.C., Groppo J.G., Joshi P., Dai S., Moecher D.P., Johnston M. Location of cerium in coal combustion fly ashes: implications for recovery of lanthanides. Coal Combustion and Gasification Products, 5 (2013) 73-78.

[12] United States Geological Survey. Rare-earth elements. https://pubs.usgs.gov/pp/1802/o/pp1802o.pdf (2017) (accessed 30 August 2020).

[13] Ministry of Solid Minerals Development, Federal Republic of Nigeria. Feasibility Study: Nigerian Coal Resource Development. http://www.inceptholdings.com.au/wp-content/uploads/2015/03/Nigeria_Coal_Feasibility_Study_-_USTDA.pdf 2006 (accessed 18 March 2019).

[14] Afu D.J., Ifeola E.O. Adesida P.A. Omelewu coal characterisation for powering power plant at Dangote cement factory, Obajana, Kogi state, Nigeria. American Journal of Engineering Research, 7 (2018) 143-152.

[15] Garba M.U., Musa U., Azare P.E., Ishaq K., Onoduku U.S., Mohammad Y.S. Characterisation and ash chemistry of selected Nigerian coals for solid fuel combustion. Petroleum and Coal. 58 (2016) 646-654.

[16] Chukwu M., Folayan C.O., Pam G.Y., Obada D.O. Characterisation of some Nigerian coals for power generation. Journal of Combustion, 2016 (2016) 11p.

[17] James Cook University. Element-to-stoichiometric oxide conversion factors. https://www.jcu.edu.au/advanced-analytical-centre/services-and-resources/resources-and-extras/element-to-stoichiometric-oxide-conversion-factors (accessed 4 January 2020).

[18] Institute of Rare Earths and Strategic Metals. Rare earth prices. https://en.institut-seltene-erden.de/Rare-earth-prices-in-december-2019/ (accessed 19 December 2019; REO prices were as of 19 December 2019).

[19] Seredin V.V., Dai S. Coal deposits as potential alternative sources for lanthanides and yttrium. International Journal of Coal Geology, 94 (2012) 67-93.

[20] Lin R., Bank T.L., Roth E.A., Granite E.J., Soong Y. Organic and inorganic associations of rare earth elements in central Appalachian coal. International Journal of Coal Geology, 179 (2017) 295-301.

[21] Dai S., Ren D., Chou C.L., Li S., Jiang Y. Mineralogy and geochemistry of the No. 6 coal (Pennsylvanian) in the Jungar Coalfield, Ordos Basin, China. International Journal of Coal Geology, 66 (2006) 253-270.

[22] Scott N. Montross, Circe A. Verba, Han Ling Chan, Christina Lopano. Advanced characterization of rare earth element minerals in coal utilization by-products using multimodal image analysis. International journal of coal geology, 195 (2018) 362-372.

[23] Honaker R.Q., Zhang W., Werner J. Acid Leaching of Rare Earth Elements from Coal and Coal Ash: Implications for using fluidized bed combustion to assist in the recovery of critical materials. Energy and Fuels, 33 (2019) 5971-5980.

[24] J. Pan, C. Zhou, M. Tang, S. Cao, C. Liu, N. Zhang, M. Wen, Y. Luo, T. Hu, W. Ji. Study on the modes of occurrence of rare earth elements in coal fly ash by statistics and a sequential chemical extraction procedure. Fuel, 237 (2019) 555-565.

[25] Z. Wang, S. Dai, J. Zou, D. French, I.T. GrahamRare earth elements and yttrium in coal ash from the Luzhou power plant in Sichuan, Southwest China: Concentration, characterization and optimized extraction. Int. J. Coal Geol., 203 (2019), pp. 1-14.

[26] R. Lin, M. Stuckman, B.H. Howard, T.L. Bank, E.A. Roth, M.K. Macala, C. Lopano, Y. Soong, E.J. GraniteApplication of sequential extraction and hydrothermal treatment for characterization and enrichment of rare earth elements from coal fly ash. Fuel, 232 (2018), pp. 124-133.

[27] Taggart R.K., Rivera N.A., Levard C., Ambrosi J.P., Borschneck D., Hower J.C., Hsu-Kim H. Differences in bulk and microscale yttrium speciation in coal combustion fly ash. Environmental Science: Processes and Impacts, 20 (2018) 1390-1403.

[28] Ryan C. Smith, Ross K. Taggart, James C. Hower, Mark R. Wiesner, and Heileen Hsu-Kim. Selective Recovery of Rare Earth Elements from Coal Fly Ash Leachates Using Liquid Membrane Processes. Environmental Science & Technology, 53 (2019), 4490-4499.

[29] P.K. Parhi. Supported Liquid Membrane Principle and Its Practices: A Short Review. Journal of Chemistry, 2013 (2013) 11p.

[30] Pont N., Salvadó V., Fontàs C. Applicability of a Supported Liquid Membrane in the Enrichment and Determination of Cadmium from Complex Aqueous Samples. Membranes, 8 (2018) 21p.

[31] Biao Fu, Guijian Liu, Mei Sun, James C. Hower, Md Manik Mian, Dun Wu, Ruwei Wang, Guangqing Hu. Emission and transformation behavior of minerals and hazardous trace elements (HTEs) during coal combustion in a circulating fluidized bed boiler. Environmental Pollution, 242, part B (2018) 1950-1960.

[32] Zanbak C. Heap leaching technique in mining, within the context of best available techniques (BAT). Supported by Euromines - The European Association of Mining Industries, Metal Ores and Industrial Minerals. http://www.euromines.org/files/mining-europe/mining-techniques/batforheapleaching-feb2013-c.zanbak-euromines.pdf (2012) (accessed 17 November 2020).

[33] Jackson B.P., Ranville J.F., Bertsch P.M., Sowder A.G. 2005.Characterization of colloidal and humic-bound Ni and U in the dissolved fraction of contaminated sediment extracts. Environmental Science and Technology, 39 (2005) 2478-2485.

[34] Shailendra K.S., Subramanian V., Ronald J.G. Hydrous Fe and Mn oxides - scavengers of heavy metals in the aquatic environment, Critical Reviews in Environmental Control, 14 (1984) 33-90.

[35] Gadde R.R., Laitinen H.A. Studies of heavy metal adsorption by hydrous iron and manganese oxides. Analytical Chemistry, 46 (1974) 2022-2031.

[36] Tian Q., Guo B., Nakama S., Sasaki K. Distributions and leaching behaviors of toxic elements in fly ash. ACS Omega, 3 (2018) 13055-13064.

[37] Hazrat A., Ezzat K., Ikram I. Environmental chemistry and ecotoxicology of hazardous heavy metals: environmental persistence, toxicity, and bioaccumulation. Journal of Chemistry, 2019 (2019) 14p.

Chapter 6

Synchrotron speciation analysis of rare earth containing microparticles in simulant coal fly ash

The development of customised, environmentally-friendly and economical extraction technologies for the recovery of rare earth elements (REEs) from coal fly ash is directly dependent on the distribution and location of the REEs within the mineral matrix within which they are entrapped, and the physicochemical and structural transformations (such as crystallographic transformation and matrix decomposition) that occurred within the mineral particles during the high-temperature combustion process. Currently, REE recovery is achieved through conventional acid digestion process at high temperature – a relatively uneconomical and environmentally-unfriendly processes due to the large amounts of energy consumed and large volumes of chemicals (such as hydrofluoric acid) used. This process involves the breaking of chemical bonds by dissolving the REE from the mineral matrix, and subsequently selectively extracting the REEs out of the leach solution. This dissolution process is dependent on the distribution and location of the REEs within the REE mineral matrix, with the surface-bound REEs more easily leached compared to the ones distributed deep within the mineral matrix, thereby impacting the volume of chemicals/reagents, temperature and time used during the recovery.

Energy dispersive spectroscopy (EDS) maps of the more abundant monazite particles within the simulant coal fly ash samples presented in Chapter Four (Section 4.2.3) highlight a surface distribution of REEs within the mineral matrix that favours rapid and economical extraction.

Therefore, further research into the distribution and location of the REEs, alongside the physicochemical and structural transformations of REE-bearing mineral phases in coal fly ash during coal combustion, is vital for understanding the processing properties of each REE-bearing mineral phase present in the coal fly ash and how best to cost-effectively tune the acids and treatment conditions to optimise REE recovery, in terms of time, cost and wastes produced.

In this chapter, results of speciation analysis of monazite particles A, B and C (detailed in Chapter Four, Section 4.2.3) isolated from the simulant coal fly ash materials OMA, OKA, ODA, are presented and discussed. These analyses, aimed at determining REE oxidation states (at the micron scale), distribution and location within REE minerals and alterations to crystallographic structure, were performed via the synchrotron-based techniques micro-x-ray fluorescence (μ-XRF) mapping, μ-XRF tomography, micro-x-ray absorption near edge spectroscopy (μ-XANES) and micro-x-ray diffraction (μ-XRD). The synchrotron radiation techniques μ-XRF tomography and μ-XRD, which could reveal structural and crystallographic transformations within REE-bearing mineral particles in coal fly ash, vital for the optimisation and/or development of recovery methods, have not been used in previous studies on REE-bearing minerals in coal fly ash.

The methods and results presented in this chapter have been published in the peer-reviewed literature:

Ilemona C. Okeme, Peter G. Martin, Christopher Jones, Richard A. Crane, Theophilus I. Ojonimi, Konstantin Ignatyev, Dave Megson-Smith, Thomas B. Scott. An advanced analytical assessment of rare earth element concentration, distribution, speciation, crystallography and solid-state chemistry in coal fly ash. *Spectrochimica Acta Part B: Atomic Spectroscopy*, 2020.

6.1 Experimental Methods

6.1.1 REE particle isolation procedure

Following identification of monazite particles A, B and C using both backscattered electron imaging and EDS (detailed in Chapter Four, section 4.1.3), in-situ removal from the bulk was performed using a Kleindiek Nanotechnik MM3A micromanipulator [1], installed within the SEM instrument (shown in Chapter Four, Figure 4.1). This piezo-electric device, capable of stepwise vertical, retractive, rotational and lateral motion at minimum incremental movements of 1 nm, was used to control an extruded glass capillary with a tip diameter of approximately 1 µm. To negate the effects of electron beam induced charging effects, the non-conductive extruded glass capillary was coated with approximately 2 nm of sputter-deposited gold.

The lift-out process reported in Martin et al [2] for uranium particles was used in this work to extract the monazite particles, utilising the electron-beam hardening adhesive SEMGlu™, also made by Kleindiek [3]. A schematic of the isolation process is presented in Figure 6.1. Each of the monazite particles extracted from the bulk simulant coal fly ash (still adhered to a glass capillary needle) was securely enclosed in Kapton™ tape (Figure 6.2) in preparation for subsequent synchrotron radiation analysis. In this study, only three monazite particles (A, B, C) were prepared in this way for synchrotron analysis owing to the morphological and compositional similarities of the suite of monazite particles identified in the composite OMA, OKA and ODA simulant coal fly ash samples, and the limited beam time available at the synchrotron facility.

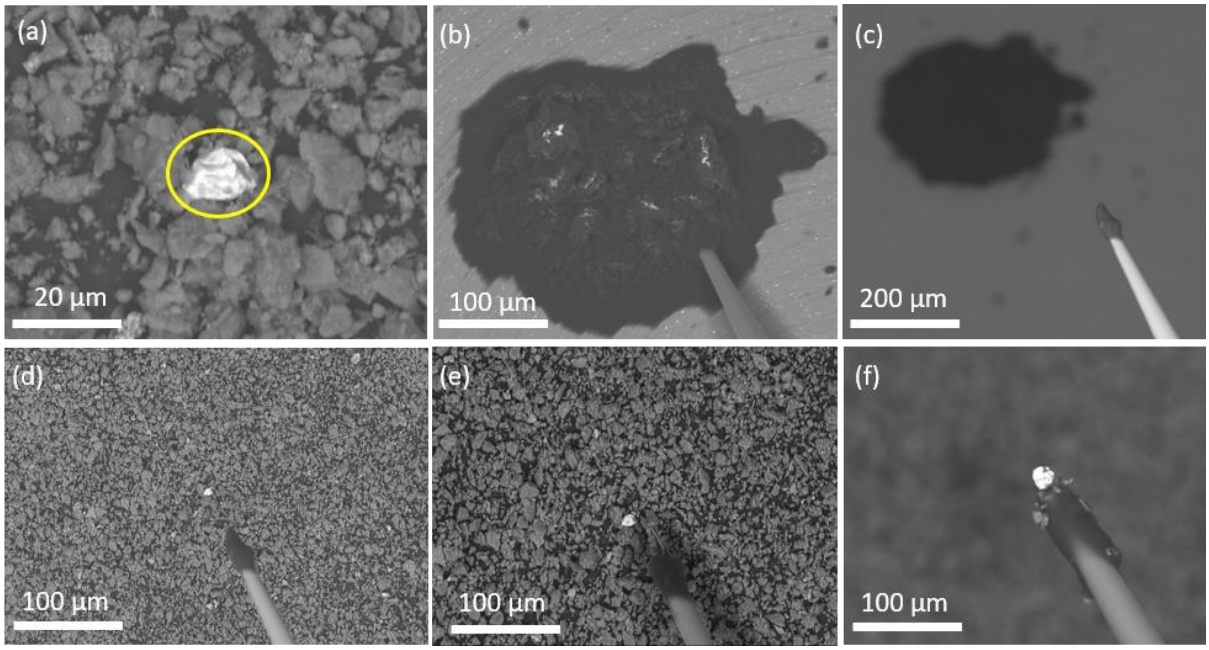

Figure 6.1: In-situ mineral particle isolation process performed within Zeiss SIGMA VP SEM using Kleindiek MM3A micromanipulator: (a) locating particle using BSE detector and co-incident EDS; (b) and (c) applying small quantity of electron-beam-hardening SEMGlu™ to extruded tip of glass capillary; (d) and (e) progressively lowering glass capillary to approach particle; (f) removing particle from surrounding bulk material, attached to capillary tip.

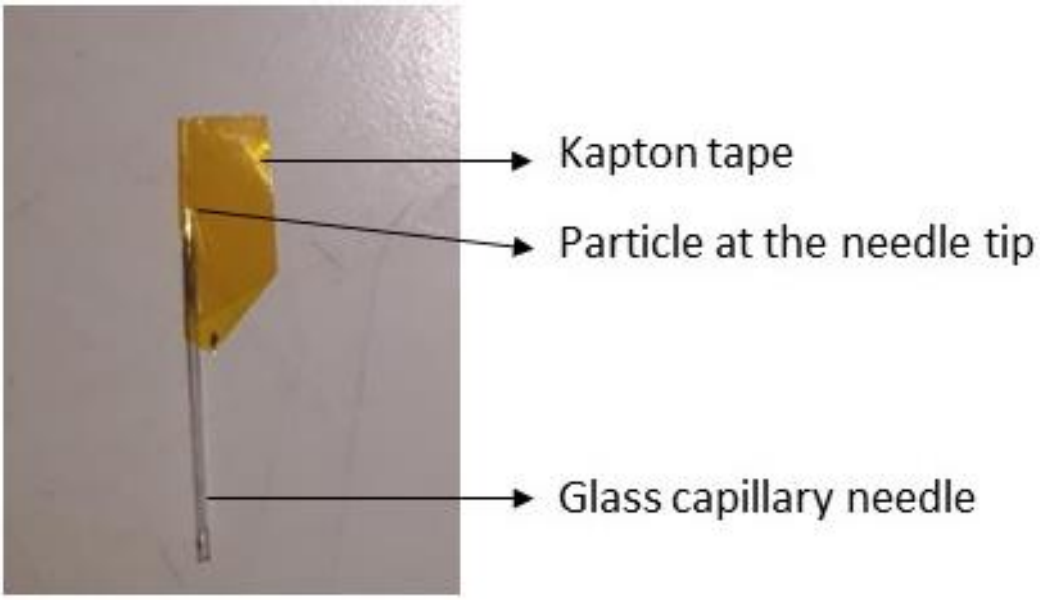

Figure 6.2: Monazite particle (adhered to tip of glass capillary needle) enclosed in Kapton™ tape.

6.1.2 Monazite particle analysis on the I18 beamline

μ-XRF, μ-XRF tomography, μ-XANES and μ-XRD analyses were performed on the monazite particles on the I18 beamline. Prior to analysis, preliminary sample positioning was performed using a camera on-board the I18 beamline experimental setup. To prevent detector saturation and allow for reasonable detector dead time (~20%), a 0.1 mm Al foil was placed over the face of the μ-XRF detector prior to all the μ-XRF analyses performed on the beamline. Throughout all sample analysis and for each technique, consistent beam, sample and detector geometries were maintained; rare earth metal foils (from the National Institute of Standards and Technology (NIST)) were used for energy calibration during the μ-XANES analysis. Figure 6.3 is a photograph taken at the I18 beamline during sample mounting.

Due to similarities in emission and edge energies, elements within the bulk simulant coal fly ash can interfere with the μ-XRF and μ-XANES data of the REEs of interest, leading to biases and reduction in the quality of results. For example, the V K_α (4,838 eV) and Ba L_α (4,828 eV, 4,852 eV, 4,926 eV) emission energies interfere with the μ-XRF data of Ce (4,839 eV L_α emission energy), and the Cr K-edge energy (5,989 eV) interferes with Ce L_{III}-edge energy (5,723 eV) in μ-XANES analysis. To ensure high quality results, interferences from other elements within the background bulk material in REE μ-XRF maps and μ-XANES were avoided by isolating the REE-bearing monazite particles prior to synchrotron analysis.

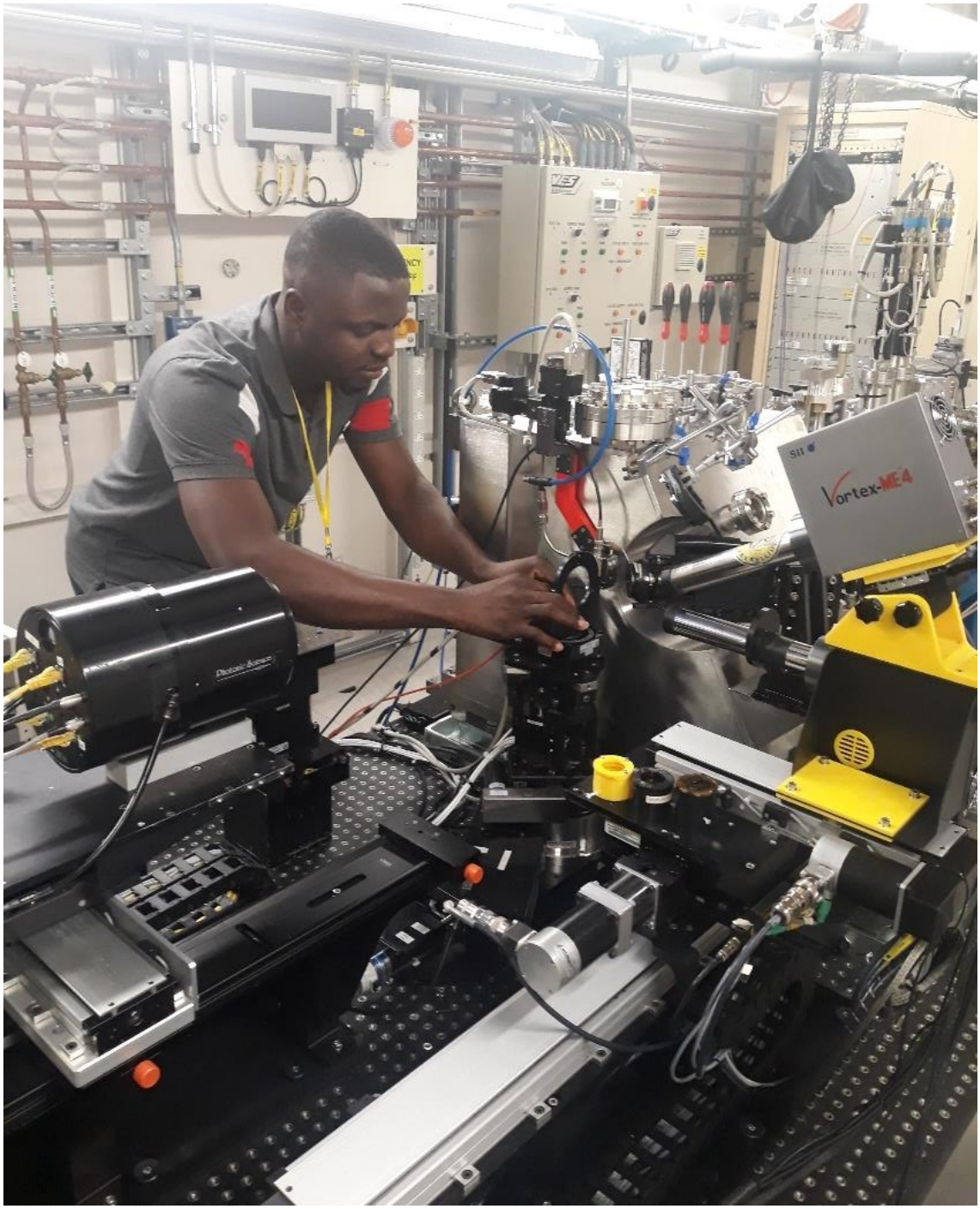

Figure 6.3: Sample being mounted on the I18 beamline.

µ-XRF mapping

To reduce the amount of scattered photons and maximise the signal from the sample reaching the detector, each particle was mounted on a kinematic stage at 45° to the incident beam, with the fluorescence detector oriented at 90° (perpendicular) to the incident beam. Each

particle was raster-scanned through the beam at an energy of 18 keV (above the L_{III} edge energies of Ce (5,723 eV), Nd (6,208 eV), La (5,483 eV), U (17,166 eV) and Th (16,300 eV)) using a step size of 2.5 μm and dwell-time of 30 s per step. Resulting from the relatively-thin sample thickness, elemental composition data were acquired in fluorescence mode using the Vortex-ME4™ multi-element silicon drift detector (SDD), fitted using PyMCa and visualised in 2D using DLS' in-house DAWN software [4].

The μ-XRF technique provides a depth-averaged 2D representation of a 3D distribution of elements. Hence, it does not reveal 3D information on the location of elements on the surface or within a particle. This limitation is resolved through μ-XRF tomography.

μ-XRF tomography

μ-XRF tomography analysis was performed on monazite particle A from the OMA simulant coal fly ash sample to obtain 3D information on REE, U and Th distribution. For each fluorescence tomographic scan, the particle was raster-scanned while progressively being translated through the beam (using a step size of 2.5 μm), and then rotated through 180° (with constant angular steps of 3°) at a dwell-time of 60 ms. Fluorescence projections were acquired using an sCMOS X-ray camera coupled with a gadolinium oxysulphide scintillator screen. Corrections for absorption within the particle matrix and reconstruction of the fluorescence projections collected were completed using iterative algorithms, with a 3D volumetric rendering of the particle performed using FEI Avizo™ software [5].

μ-XANES

μ-XANES data were acquired (at respective L_{III} edge energies) for Ce (5,723 eV), Nd (6,208 eV) and La (5,483 eV) at spots identified as containing high concentrations of these elements

within each monazite particle. For each of the elements, in the pre- and post-edge regions, energy steps of 0.25 eV were used, with steps of 0.1 eV across the main edge region using a dwell-time of 30 s per step. μ-XANES data were processed (calibrated against respective Ce, La and Nd L_{III} edge energies, deglitched, normalised and fitted) using the ATHENA software suite [6]. The quantification of Ce (III) and Ce (IV) in the normalised μ(E) Ce μ-XANES spectra was undertaken in ATHENA by linear combination fitting (LCF), using a fit range of -30 eV to 70 eV around the Ce L_{III} edge. The standards $CeTiO_3$ (Ce III) and CeO_2 (Ce IV) were used for the LCF; the weights of the standards were forced to be between 0 and 1, with no restriction on the edge energy, E_0.

μ-x-ray diffraction (μ-XRD)

For μ-XRD, the sCMOS X-ray camera was aligned directly downstream of the sample along the path of the beam of energy 18 keV. Samples were rotated through 180° during exposure and data were acquired in transmission mode. Calibration was performed using LaB6 NIST reference material. Data processing (background correction, visualisation and azimuthal integration of the 2D images to 1D patterns) was additionally performed using DAWN software.

6.2 Results and discussion

6.2.1 μ-XRF

Figure 6.4 shows the elemental composition maps of monazite particles A, B and C. From the results, the monazite particles show a core-shell pattern, with the shell rich in strongly colocalised Ce, La and Nd, and a Th/U-rich core. U and Th were both observed to colocalise strongly together. However, both were poorly colocalised with respect to the LREE. The chemical similarities (such as atomic radius) account for this observed colocalisation of the LREE [7]. The core-shell zonation of the actinides and LREE in the monazite particles is characteristic of detrital monazite, formed during magmatic growth or recrystallisation of the monazite particles [8].

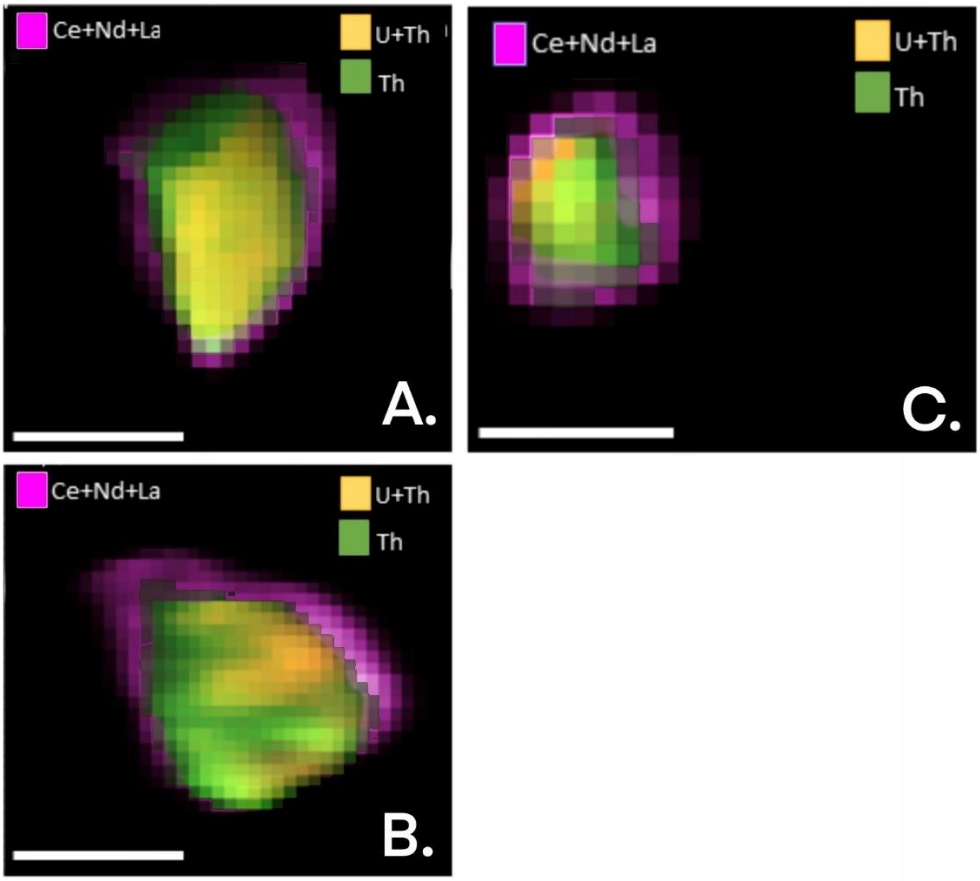

Figure 6.4: μ-XRF maps (Ce, Nd, La, U, Th) of monazite particles A, B and C, illustrating compositional variance of these elements (scale bars = 50 μm).

6.2.2 μ-XRF tomography

Renderings of the μ-XRF tomography data from monazite particle A are shown in Figures 6.5, 6.6 and 6.7. The results highlight the core-shell distribution of elements within the particle (Figures 6.5), with the REE Ce, La and Nd confirmed to be surface bound, surrounding Th and U (Figures 6.6 and 6.7). Both Th and U were observed to exist strongly colocalised in the core of the monazite particle, while being simultaneously depleted around its shell (Figures 6.5 and 6.7), confirming the earlier μ-XRF results, and SEM-EDS results (earlier reported in Chapter Four, Section 4.2.3). Being surface bound, these REE would have the potential to be preferentially leached during an extraction process (compared to U and Th, that are conversely located within the particle centre). This finding is significant in the development

of a selective extraction methodology, targeting the strongly colocalised and (easily leached) surface-bound REE in the simulant coal fly ash monazite particles. The μ-XRF tomography results have also illustrated that the monazite particle is of high density and non-porous; implying that the surface pits (identified by the SEM imaging) do not permeate significantly into the underlying monazite structure.

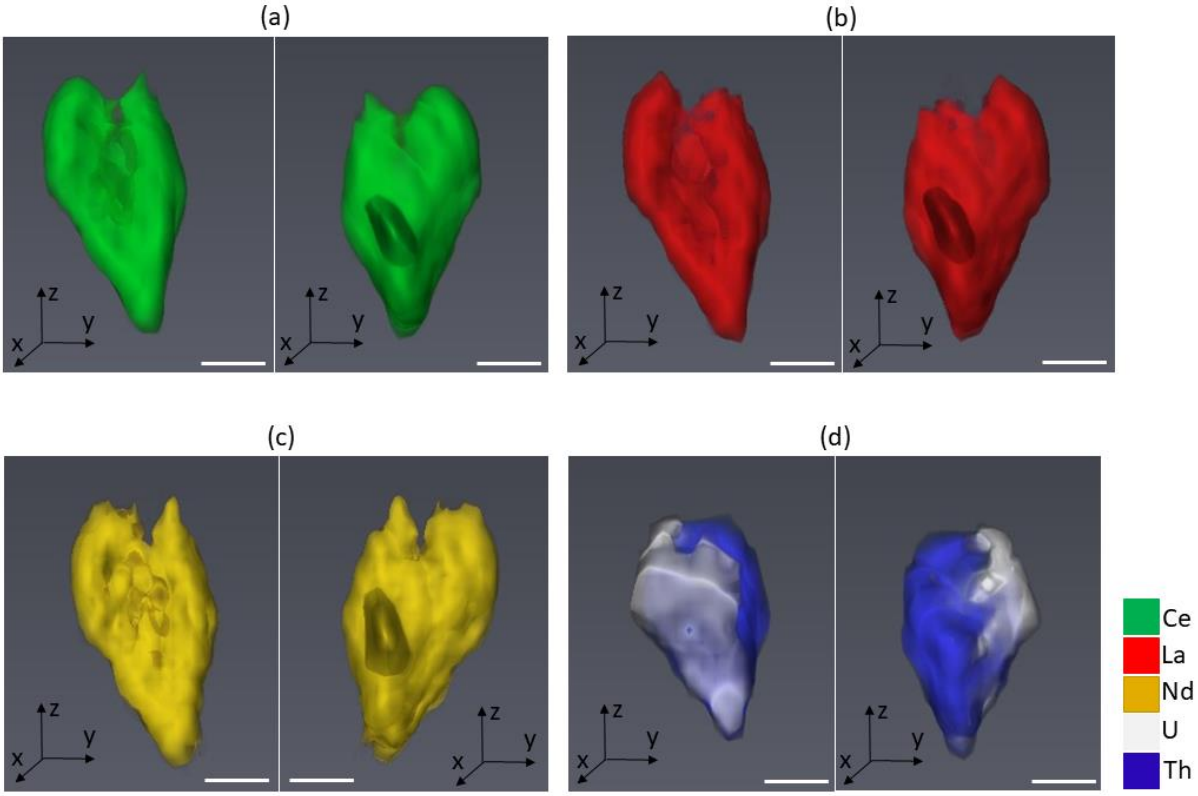

Figure 6.5: 3D volumetric rendering (front and back views) of (a) Ce, (b) La, (c) Nd, (d) U and Th in monazite particle A. Scale bars = 25 μm.

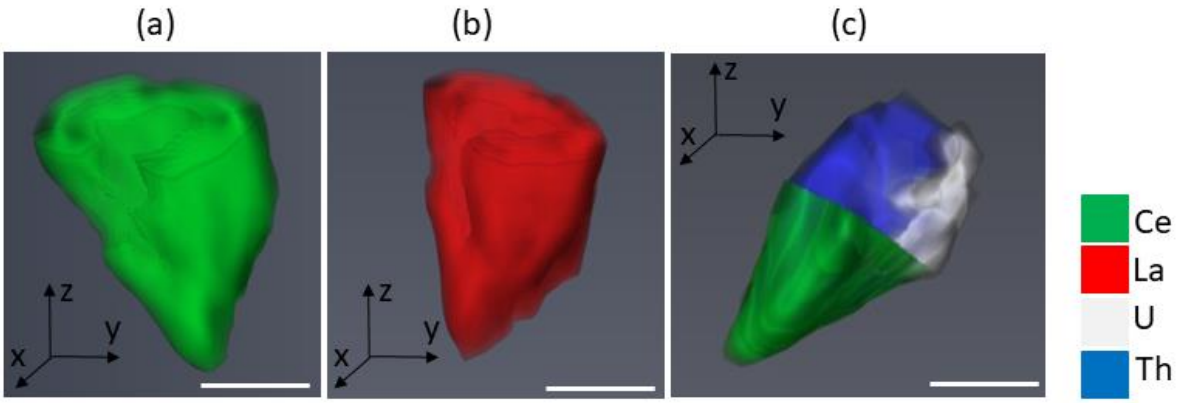

Figure 6.6: Cut sections of 3D volumetric renderings of monazite particle A showing the core-shell pattern. (a) and (b): REE-depleted interior within Ce and La volumetric renderings. (c): Ce outer shell with U and Th components within the core. Scale bars = 25 µm.

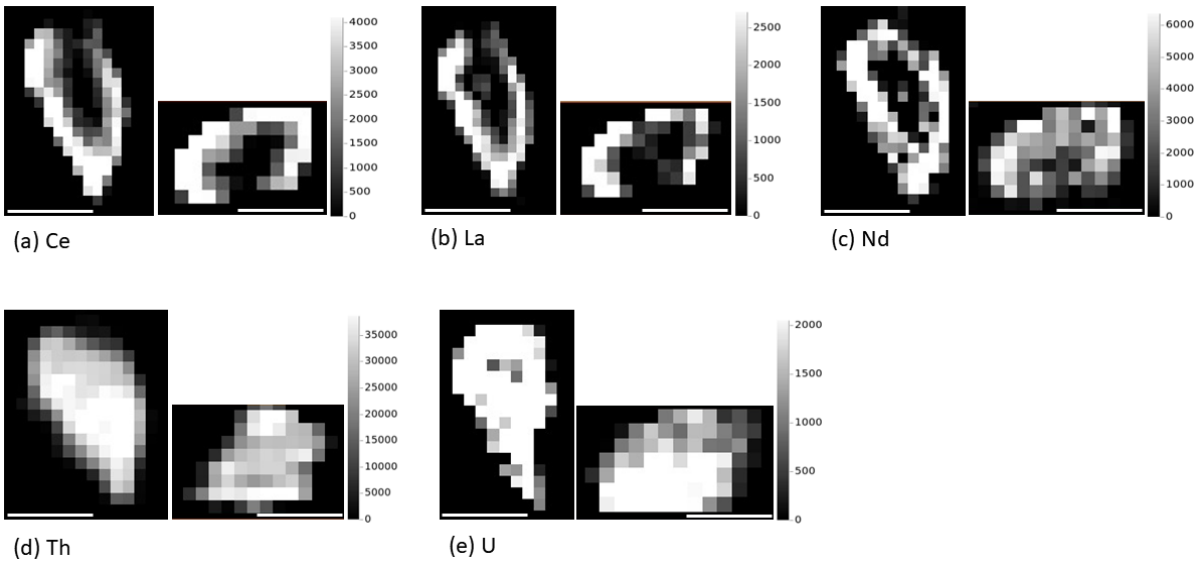

Figure 6.7: Greyscale plots in the xy and xz planes (arbitrary units) showing monazite particle A with an REE-rich rim ((a), (b), (c)) and Th and U rich core ((d) and (e)).

Scale bars = 25 µm.

6.2.3 µ-XANES

The µ-XANES spectra across the Ce, La and Nd L_{III}-edge in monazite particles A, B and C, alongside their reference spectra, are shown in Figures 6.8a-6.8c. from Figure 6.8a, the Ce (III) reference has a single peak at *P* (5,727.5 eV) with the peaks at *Q* (5,731 eV) and *R* (5,738 eV) representing the Ce (IV) reference. The µ-XANES spectrum of Ce in particle A (Figure 6.8a)

displays two peaks, an intense peak at 5,727.5 eV (position *P*), corresponding to Ce (III) and a subtle peak at 5,738 eV (position *R*), corresponding to a Ce (IV) minor contribution. This implies micro-scale oxidation of Ce (transitioning from III to IV) resulting from thermal decomposition of the detrital monazite particles, during the high-temperature combustion process, and illustrates that Ce existed in mixed oxidation states of III and IV. Ce (III) has the thermodynamic tendency to lose an electron to become $4f^0$ and, hence, form stable Ce (IV) [7]. LCF using Ce (III) ($CeTiO_3$) and Ce (IV) (CeO_2) references revealed a Ce (III) and Ce (IV) ratio 80%:20% (Table 6.1), which affirms micro scale partial oxidation (that is thermal decomposition of the monazite matrix) due to the high-temperature combustion process. These results agree with an earlier work, noting possible processing differences [9].

Both La and Nd in particles A, B and C (Figures 6.8 and 6.9) were found to exist only in the 3+ oxidation state, with distinct peaks at 5,485 eV and 6,214 eV, respectively. This result, coupled with the existence of good similarity in the pre- and post-edge features between the particles and reference La and Nd spectra, suggests that the La and Nd chemistries for the particles are unaffected by the high-temperature combustion process and resistant to oxidation. The similarity in chemical properties of the REE explains the prevalence of the 3+ oxidation state.

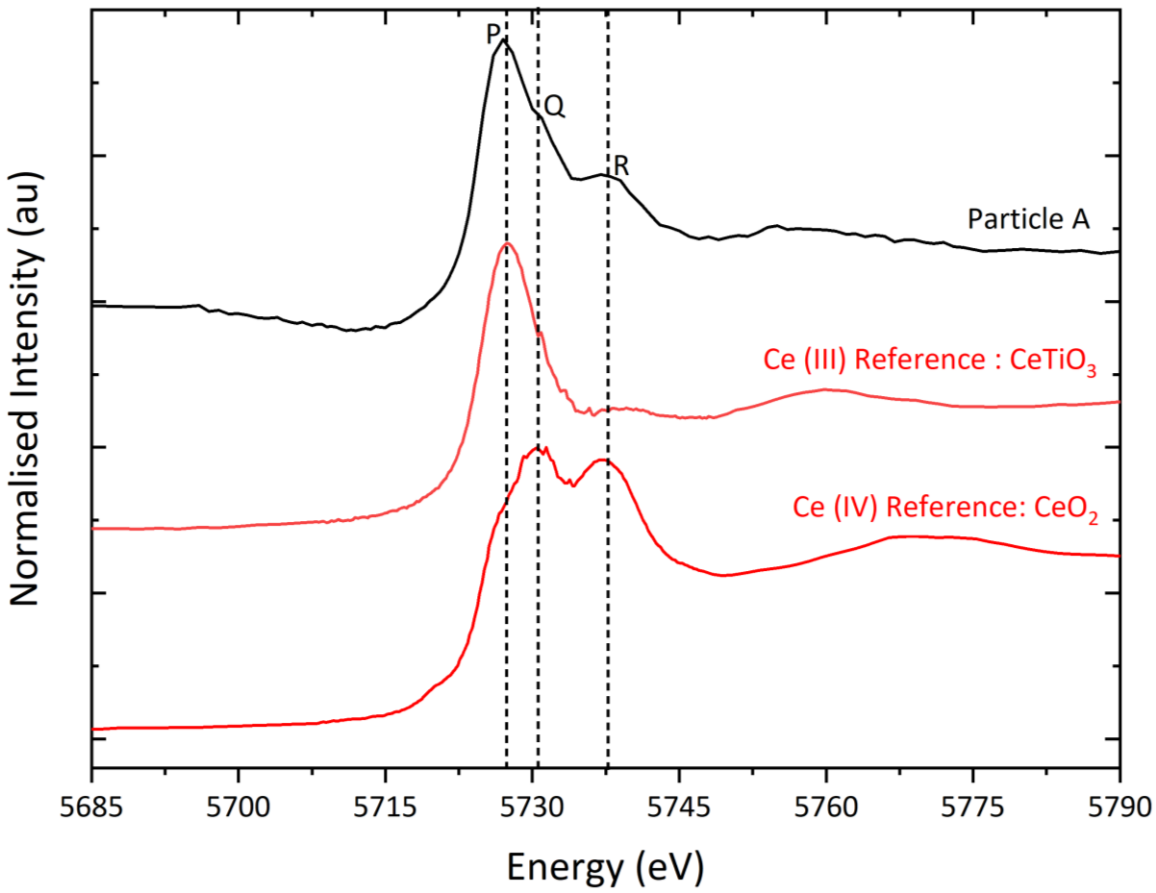

Figure 6.8: XANES spectrum of Ce in monazite particle A alongside reference spectra [10]. P represents Ce (III) peak. Q and R represent Ce (IV) peaks.

Table 6.1: LCF results of Ce μ-XANES detailing the weight of Ce oxidation states.

	Component	Component weight (in % ± uncertainty)	R-factor
Particle A	$CeTiO_3$ (Ce III)	80.2 ± 0.044	0.038
	CeO_2 (Ce IV)	19.8 ± 0.062	
		Sum: 100	

R-factor defines the goodness of a fit, given as $\frac{sum\,[(data-fit)^2]}{sum\,(data^2)}$. Smaller R- factor represents a better fit.

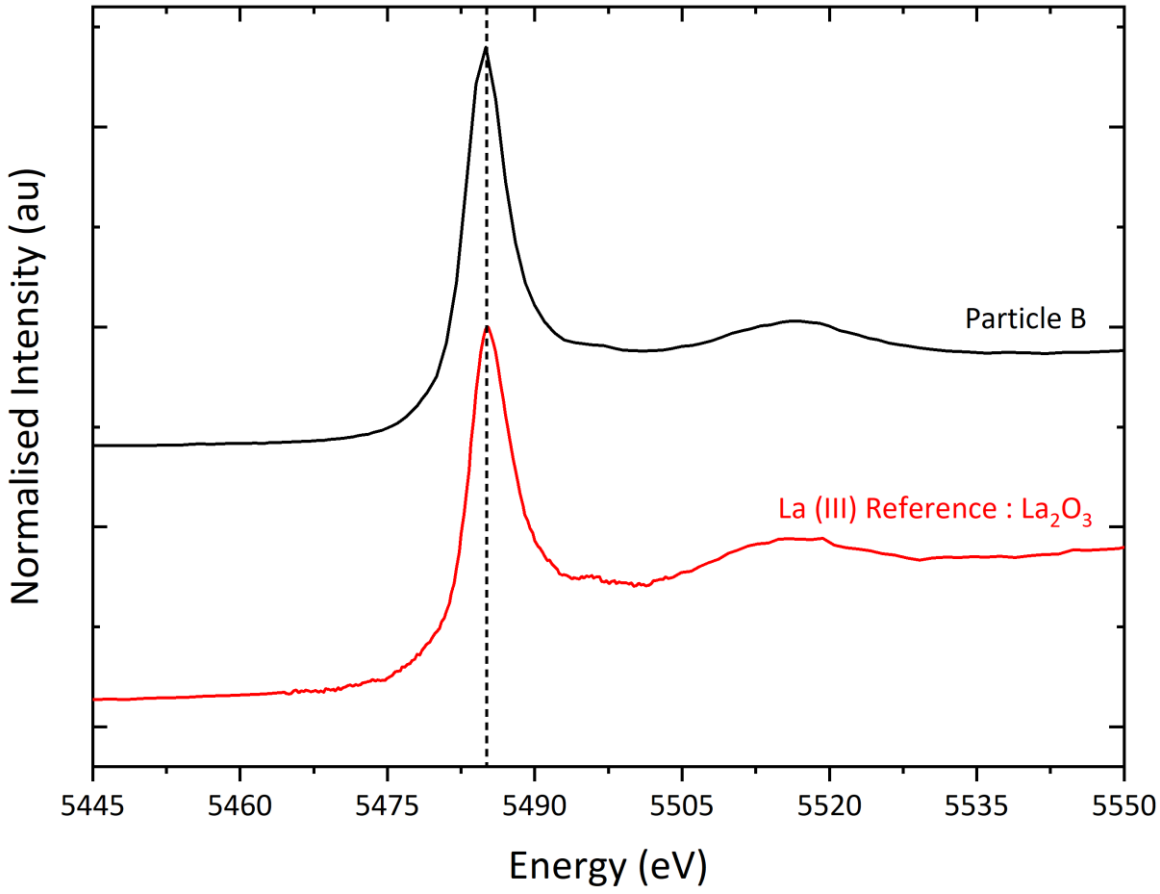

Figure 6.9: XANES spectrum of La in monazite particle A alongside reference spectrum [10].

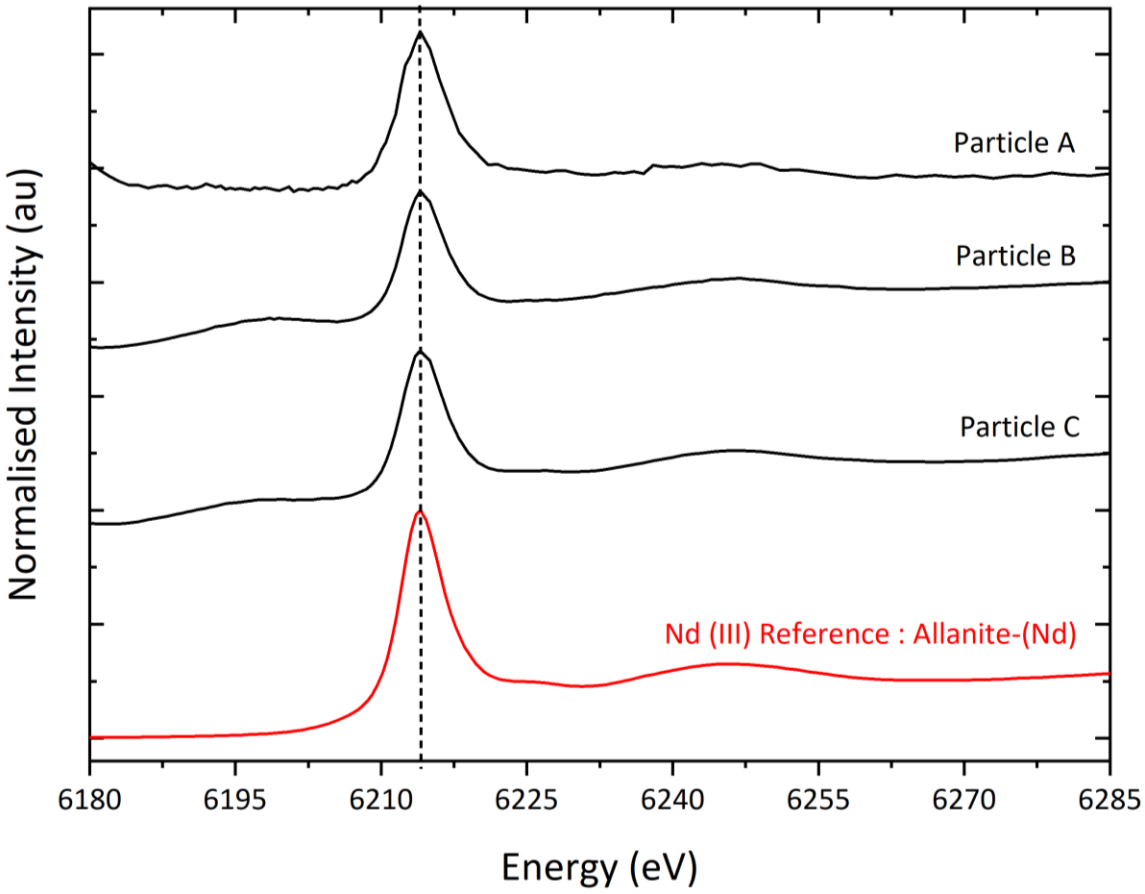

Figure 6.10: XANES spectrum of Nd in monazite particles A, B and C alongside reference spectrum [10].

6.2.4 µ-XRD

The 2D and 1D µ-XRD patterns of particles A, B and C (Figure 6.11) showed poorly-formed diffuse diffraction rings, broad haloes and a lack of well-defined diffraction peaks, characteristic of amorphous materials. This implies partial or total amorphisation/metamictisation of the (naturally-crystalline) monazite particle due to the combined effects of alpha-irradiation from the uranium and thorium of the particles, and/or the high-temperature ashing/combustion process. This radiation- and/or high-temperature-induced structural transformation post-combustion is vital in understanding the chemical reactivity, solubility and extractability of REE from coal fly ash. Studies have reported improved REE extractability due to thermal decomposition and

amorphisation, as these transformations lower the hardness of monazite, thereby making it more susceptible to chemical attack with increased solubility [11]. Therefore, monazite leaching can be achieved using a less-aggressive dilute mineral acid at a lower temperature and in less time, which is more economical and with a higher REE extraction efficiency than the conventional processes.

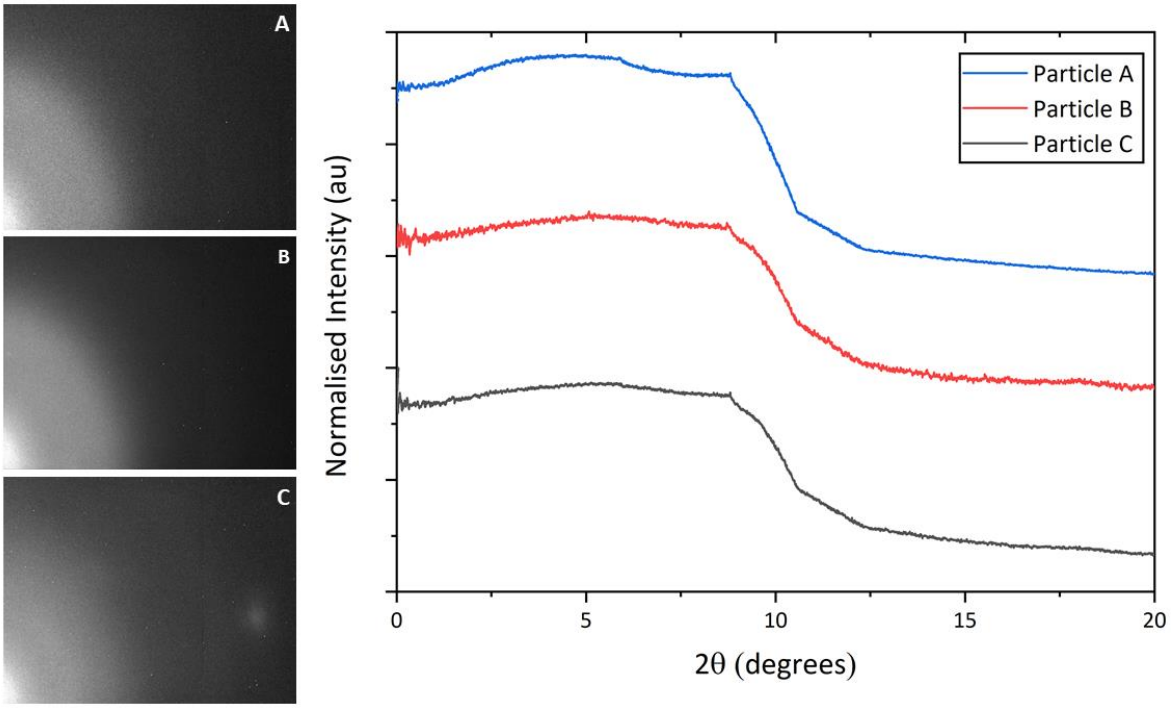

Figure 6.11: 2D and 1D μ-XRD patterns of monazite particles A, B and C.

6.3 Summary

This work has determined the REE distribution and speciation in monazite particles isolated from Nigerian simulant coal fly ash via synchrotron techniques. This study has also demonstrated a new method whereby individual monazite particles are removed from bulk samples using an SEM-mounted micromanipulator (prior to synchrotron radiation analysis), which has been demonstrated as being able to significantly enhance the resolution and quality of the results obtained when compared to conventional speciation analysis of REE mineral particles within 'bulk' coal fly ash materials.

The light REE in the monazite particles were strongly colocalised and surface-bound, enveloping the actinides in a core-shell pattern. Ce was found to exist in mixed oxidation states (but predominantly in the (III) oxidation state), with Nd and La being very stable in state III and unaffected by the high-temperature combustion process; this is indicative of thermal decomposition of the monazite matrix and oxidation of the REEs. Both U and Th were observed to be strongly colocalised, concentrated in the particle interiors and depleted around the circumference. Such identification of elemental zonation (REEs, U, Th) within isolated monazite particles derived from simulant coal fly ash material represents the first complementary synchrotron radiation μ-XRF and μ-XRF tomography study on coal fly ash. The monazite particles were metamict/amorphous, attributable to irradiation- and thermally-induced structural transformation (due to the high coal combustion temperature). These results of surface distribution of the REEs and structural transformation of the monazite matrix are indicative of higher solubility, which translates to more cost-effective REE leaching from monazite, using a less-aggressive dilute mineral acid at a lower temperature and in less time, than the conventional processes. Therefore, REE extraction methods should target the

more abundant monazite particles, which revealed a surface distribution of the REEs. However, other particle types have not been studied to confirm REE location and hence potential leachability. While based only on an indicative sample set, these initial results are very significant for the optimisation and development of rare earth extraction methods and represent a potentially highly valuable source for prized REE from an otherwise pure waste product.

6.4 References

[1] Kleindiek Nanotechnik GmbH. MM3A-EM micromanipulator product brochure. Technical report.

[2] Martin P.G., Griffiths I., Jones C.P., Stitt C.A., Davies-Milner M., Mosselmans J.F.W., Yamashiki Y., Richards D.A., Scott T.B. In-situ removal and characterisation of uranium-containing particles from sediments surrounding the Fukushima Daiichi Nuclear Power Plant. Spectrochimica Acta Part B: Atomic Spectroscopy, 117 (2016) 1-7.

[3] Kleindiek Nanotechnik GmbH. SEMGlu product brochure.

[4] Basham M., Filik J., Wharmby M.T., Chang P.C.Y., El Kassaby B., Gerring M., Aishima J., Levik K., Pulford B.C.A., Sikharulidze I., Sneddon D., Webber M., Dhesi S.S., Maccherozzi F., Svensson O., Brockhauser S., Náray G., Ashton A.W. Data Analysis WorkbeNch (DAWN). Journal of Synchrotron Radiation, 22 (2015) 853-858.

[5] Thermo Fisher Scientific. Amira-Avizo software: 3D visualization and analysis software. (2019) (accessed 4 January 2019).

[6] Ravel B., Newville M. Athena, Artemis, Hephaestus: data analysis for x-ray absorption spectroscopy using IFEFFIT. Journal of Synchrotron Radiation, 12 (2005) 537-541.

[7] Cotton S. Lanthanide and actinide chemistry. Chichester, England: John Wiley and Sons; 2006.

[8] Catlos E.J.. Generalisations about monazite: implications for geochronologic studies. American Mineralogist, 98 (2013) 819-832.

[9] Stuckman M.Y., Lopano C.L., Granite E.J. Distribution and speciation of rare earth elements in coal combustion by-products via synchrotron microscopy and spectroscopy. International Journal of Coal Geology, 195 (2018) 125-138.

[10] International X-ray Absorption Society, XAFS materials database. http://ixs.iit.edu/database/data/Farrel_Lytle_data/RAW/index.html. (Accessed 6 March 2019).

[11] Honaker R.Q., Zhang W., Werner J. Acid leaching of rare earth elements from coal and coal ash: Implications for using fluidized bed combustion to assist in the recovery of critical materials. Energy and Fuels, 33 (2019) 5971-5980.

Chapter 7

Bulk and particulate radiological analysis of coal and simulant coal fly ash

Several factors are responsible for the radiological hazards associated with the release of large volumes of coal fly ash into the environment (in the form of accidental release from ash ponds, direct disposal to landfills and mine land reclamation) and its recycling into bricks for the construction of residential buildings. These factors include the mode of occurrence of the radionuclides, particle size, distribution, activity concentration of the gamma-emitting radionuclides (such as ^{226}Ra, ^{228}Ra, ^{228}Th) and the chemical speciation [1]. Due to heterogeneity of radionuclide concentration in particles at the micro- and nano-scales [2], activity concentration analysis (via gamma spectrometry) alone is inadequate in establishing links between the source terms and deposition, fate, transport, bioavailability and ensuing health risks [3,4].

To overcome this inadequacy, there is a need to complement gamma spectrometry with sub-micron spatial resolution techniques such as synchrotron radiation micro-x-ray fluorescence (μ-XRF) and micro-x-ray absorption near edge spectroscopy (μ-XANES) analyses, that provide valuable information (on particle size, radionuclide distribution and oxidation state) that controls deposition, transport, leaching, bioavailability and uptake in the ecosystem [1].

Previously in Chapter Four, uraninite microparticles were identified in the residual simulant coal fly ash. These particles - observed to have high atomic number with high concentration of U, were isolated following the same procedure used for the isolation of the monazite microparticles (as earlier reported in chapter six) in preparation for non-destructive X-ray analysis. This current chapter seeks to combine the gamma-ray spectrometric analysis of bulk coal (OMC, OKC, ODC) and simulant coal fly ash (OMA, OKA, ODA) materials with non-destructive synchrotron μ-XRF and μ-XANES analyses of the isolated uraninite particles (P1, P2), aimed at providing deeper understanding on the associated radiological hazards and informing the best disposal and recycling strategies for these materials.

The methods and results presented in this chapter have previously been published in the peer-reviewed literature:

Ilemona C. Okeme, Thomas B. Scott, Peter G. Martin, Yukihiko Satou, Theophilus I. Ojonimi, Moromoke O. Olaluwoye. Assessment of the mode of occurrence and radiological impact of radionuclides in Nigerian coal and resultant post-combustion coal ash using scanning electron microscopy and gamma-ray spectroscopy. *Minerals*, 10 (2020) 241p.

7.1 Experimental Methods

7.1.1 Gamma-ray spectrometry

In this work, gamma-ray spectrometry was performed using a high-resolution P-type coaxial ORTEC, GEM-13180 HPGe detector (10% relative efficiency, 1.71 keV resolution at 1.33 MeV Co-60, ORTEC, Oak Ridge, TN, USA), shielded by a 10 cm Pb wall with a 2 mm inner lining of copper and cadmium foils (to reduce the background contribution to photo-peak intensity). The detector was coupled to a multichannel analyser with installed Maestro™ software (version 7.0) for gamma-ray spectral analysis. The setup is as shown in Figure 7.1.

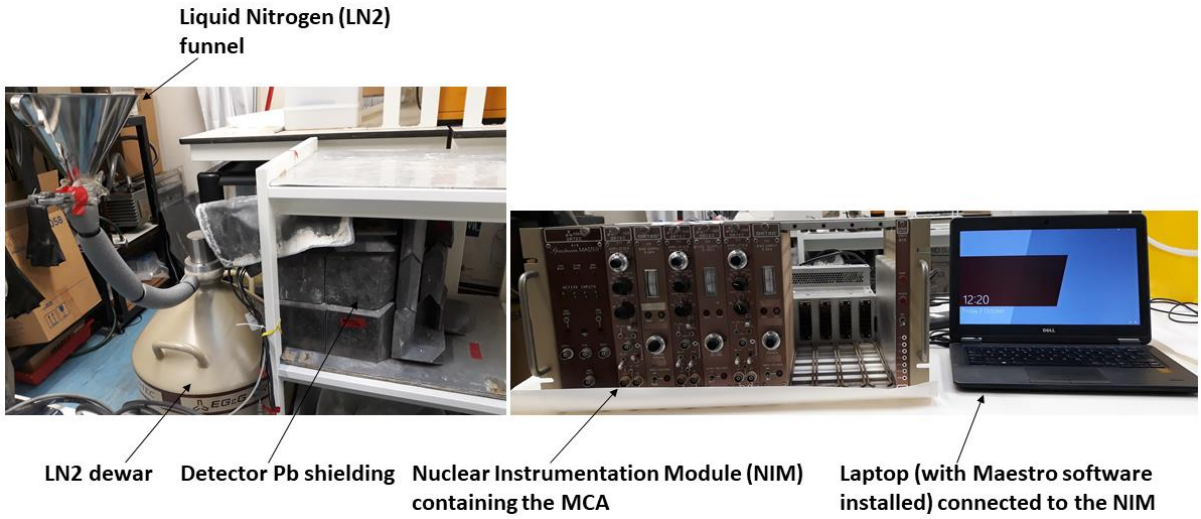

Figure 7.1: Experimental setup of the HPGe detector used in this study.

Energy and efficiency calibration

To be able to identify radionuclides in the samples by their gamma-ray energies, the detector was energy-calibrated using a multi-nuclide point-source (model 7603, Eckert and Ziegler™; Table 7.1) with gamma-ray emission lines spanning the full range of the radionuclides of interest (40 keV to 1836 keV). The multi-nuclide point-source, being of high activity, was

placed 7 cm from the detector cap within the lead shielding and a spectrum collected for 20 min.

To quantify the activity of gamma-emitting radionuclides in the samples, the full-energy/photo-peak efficiency calibration was performed using IAEA certified reference material (IAEA-385, sea sediment; Table 7.2), containing the specific radionuclides of interest (^{226}Ra (^{238}U series), ^{228}Ra and ^{228}Th (^{232}Th series), ^{40}K). The use of multi-nuclide point-sources (not containing the radionuclides of interest and, therefore, relying on interpolation) for efficiency calibration has been reported as introducing large errors (>10%) [5,6]; hence, IAEA-385, containing the radionuclides of interest, was used in the efficiency calibration. Prior to analysis, IAEA-385 material was repackaged and sealed in the same geometry as the experimental samples, and kept for 30 days under non humid conditions to ensure that secular equilibrium was re-established between the decay products of ^{226}Ra, ^{228}Ra and ^{228}Th [7]. To achieve the American Society for Testing and Materials standard (E181) criterion of at least 20,000 net counts for the efficiency calibration [8], the IAEA-385 reference sample was counted for 24 h and the full energy efficiency (Ɛ) of the radionuclides of interest was determined using Equation 7.1 [5]:

$$\varepsilon = \frac{N}{A.M.T.\gamma} \qquad (7.1)$$

where N is the background corrected net count, A is radionuclide activity (in Bq.kg^{-1}), M is mass of the reference sample (in kg), T is counting time (in s) and γ is gamma yield of the radionuclide source.

Decay corrections were also made during efficiency calibration using Equation 7.2 [5]:

$$\mathbf{A(t)\ (Bq.kg^{-1}) = A_0 e^{\frac{-(ln2)t}{t_{\frac{1}{2}}}}} \quad (7.2)$$

where A(t) is activity at count time, A_0 is activity at date of preparation of standard, t is decay time (in y) and $t_{\frac{1}{2}}$ is half-life (in y).

The suitability of IAEA-385 as a reference material for efficiency calibration was based on a 90% match between its matrix and elemental composition and that of the experimental samples following a prior laboratory-based XRF analysis.

Table 7.1: Gamma-ray lines of the energy calibration multi-nuclide point-source [9].

Nuclide	Gamma-ray energy (keV)
^{210}Pb	47
^{241}Am	60
^{109}Cd	88
^{57}Co	122
^{139}Ce	166
^{203}Hg	279
^{113}Sn	392
^{85}Sr	514
^{137}Cs	662
^{88}Y	898
	1,836
^{60}Co	1,173
	1,333

Table 7.2: IAEA-385 reference material showing the radionuclides of interest (bold) [10].

Radionuclide	Certified value ($Bq.kg^{-1}$)
^{40}K	607
^{137}Cs	33.0
^{226}Ra	21.9
^{228}Ra	32.0
^{232}Th	33.7
^{238}U	29

Preparation of coal and simulant coal fly ash samples

To ensure that secular equilibrium was attained between the decay products of ^{226}Ra and ^{228}Ra in the samples prior to analysis, 200 g of coal (detailed in Chapter Three, Section 3.2) in snap-on lid re-usable re-entrant mini Marinelli beakers (from GA-MA and Associates Inc., Ocala, FL, USA) and 40 g of simulant coal fly ash (detailed in Chapter Three, Section 3.2.1) in petri-style dishes were kept for 30 days under non humid condition [7,11]. The beakers and petri-style dishes were made airtight by sealing using PVC tape to prevent the escape of gaseous ^{222}Rn and ^{220}Rn from the samples, thereby maintaining secular equilibrium [7]. For large-volume samples like the 200 g samples, re-usable re-entrant mini Marinelli beakers give higher geometric detection efficiencies by positioning greater amounts of sample (by volume) as close to the detector as possible [5]. A total of 30 samples (15 coal and 15 simulant coal fly ash) per coal mine were prepared for analysis. Figure 7.2 shows the sample preparation desk, with the apparatus used and samples.

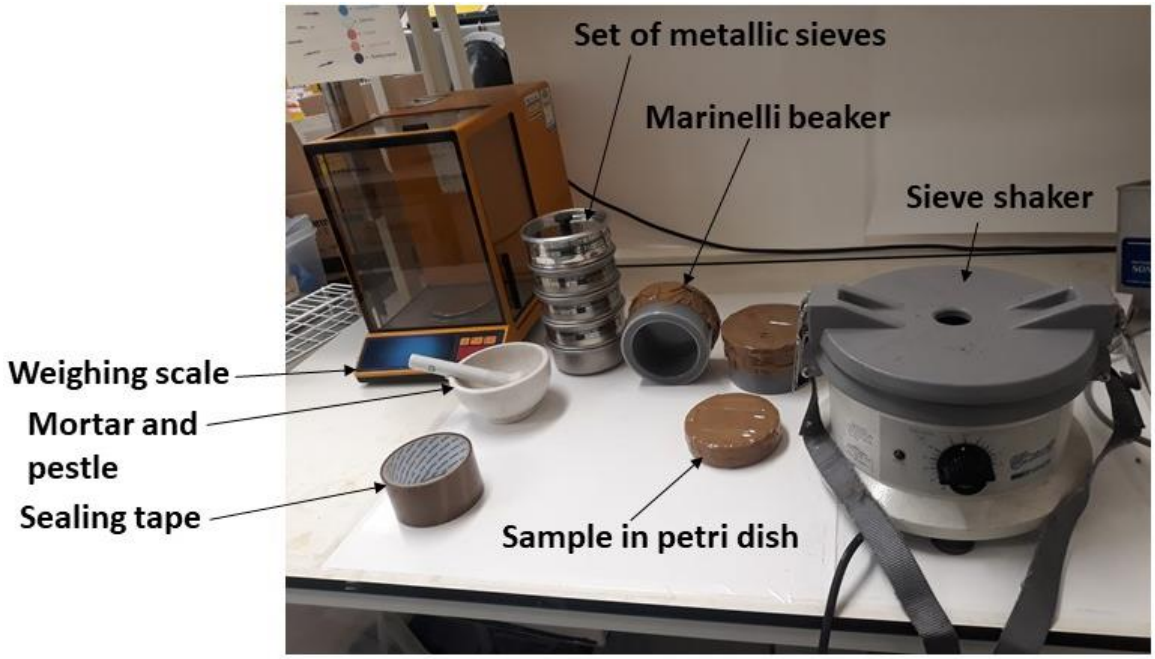

Figure 7.2: Preparation desk, showing apparatus and samples.

Sample and background measurement

Once secular equilibrium was attained, each sample was counted for 24 h to ensure sufficient photo-peak count while also minimising statistical counting error. Background measurement was also carried out over 24 h (with no radioactive source close to the detector) with an empty sample container mounted inside lead shielding; this was done at the start, mid-point and end of the experiment, and the mean of the measurements taken. Radionuclide specific activities were then calculated from the background-corrected photo-peak intensity (i.e. gross count of photo-peak minus background count for each photo-peak).

Determination of activity concentrations

To indirectly determine the activity concentrations of ^{226}Ra, ^{228}Ra and ^{228}Th via their strong gamma-emitting decay products, and also that of ^{40}K, the following equation [12] was used:

$$\mathbf{A\ (Bq.kg^{-1})} = \frac{N}{\varepsilon . M . T . Y} \qquad (7.3)$$

where N is background corrected net count, Ɛ is radionuclide photo-peak efficiency, M is mass of the sample (in kg), T is counting time (in s) and γ is gamma yield of the radionuclide.

The activity concentration of ^{226}Ra was determined by averaging the activity concentrations of its decay products, ^{214}Pb (352 keV) and ^{214}Bi (609 keV), that occurred in secular equilibrium; similarly, the activity concentrations of ^{228}Ra and ^{228}Th were determined from their decay products ^{228}Ac (911 keV) and ^{208}Tl (583 keV), respectively [13,14]. To negate gamma-ray attenuation within the sample volume and to register significant counts (≥20,000 counts) under each radionuclide photo-peak, decay products (as above) with energies greater than 350 keV and gamma yield greater than 25% were used to compute activity concentrations. The activity concentration of ^{232}Th was determined from the mean activity concentrations of ^{228}Ra and ^{228}Th. The ^{40}K activity was determined using its characteristic gamma emission energy of 1,461 keV. The gamma yield for each radionuclide was obtained from NuDat 2.7 (National Nuclear Data Center, Brookhaven National Laboratory, Upton, NY, USA) [15]. Table 7.3 presents the natural radionuclides of interest and their gamma-ray-emitting decay products used for the determination of activity concentration.

Table 7.3: Natural radionuclides of interest and their decay products [15].

Radionuclide	Main gamma-emitting decay product	Gamma energy (keV)	Gamma yield of decay product
^{226}Ra (^{238}U series)	^{214}Pb	352	0.3560
	^{214}Bi	609	0.4549
^{228}Ra (^{232}Th series)	^{228}Ac	911	0.2580
^{228}Th (^{232}Th series)	^{208}Tl	583	0.8500
^{40}K	Not applicable	1,461	0.1066

Radiological hazard indices

To determine hazards associated with the precursor coal and the subsequent disposal of large volumes of coal ash into the environment (in the forms of both direct disposals to landfill and mine site reclamation), the radiation doses arising from radionuclides present in the studied samples were assessed in terms of several different, but related, dose indices. All radiation doses were calculated using dose conversion coefficients and occupancy factors provided by the United Nations Scientific Committee on the Effects of Atomic Radiation (UNSCEAR) 2000 [16].

(i) Radium equivalent

Resulting from the non-uniform distribution of the radionuclides in each sample, to represent total activity due to all the radionuclides (^{40}K, ^{226}Ra, ^{232}Th) in a sample by a single value a common index, termed the radium equivalent (Ra_{eq}), was used [14]. Ra_{eq} activity is a widely-used radiation hazard index employed to estimate the suitability of any material to be utilised as a component within building construction based on the total activity concentration of the radionuclides and the possible external exposure risks to inhabitants of such buildings [14]. To calculate Ra_{eq}, Equation 7.4 was used [17]:

$$Ra_{eq}\ (Bq.kg^{-1}) = A_{Ra} + 1.43A_{Th} + 0.077A_K \quad (7.4)$$

where A_{Ra}, A_{Th} and A_K are activity concentrations of ^{226}Ra, ^{232}Th and ^{40}K, respectively. This estimates that 370 $Bq.kg^{-1}$ of ^{226}Ra, 259 $Bq.kg^{-1}$ of ^{232}Th and 4,810 $Bq.kg^{-1}$ of ^{40}K equate to the same gamma-ray dose rate [17]. For any material to be suitable as a component within building construction, a Ra_{eq} upper limit of 370 $Bq.kg^{-1}$ is recommended [14,17].

(ii) Absorbed dose

To calculate the amount of ionising energy deposited in an exposed person per unit mass at 1 m above the ground surface (termed absorbed dose, D), the following equation was used:

$$D\ (nGy.h^{-1}) = (0.462A_{Ra} + 0.604A_{Th} + 0.0417A_K) \quad (7.5)$$

where A_{Ra}, A_{Th} and A_K are activity concentrations of ^{226}Ra, ^{232}Th and ^{40}K, respectively. The dose coefficients of A_{Ra}, A_{Th} and A_K in Equation 3.5 (in units of $nGy.h^{-1}$ per $Bq.kg^{-1}$) were obtained from [16].

(iii) Annual effective dose equivalent

The severity of any radiological hazard may be estimated based on the annual radiation dose received by a person working or living in the radiation environment. The outdoor annual effective dose depends upon the conversion coefficient from D in air to the effective dose, alongside outdoor occupancy factors. To calculate the biological impact of such exposure, D is converted to an annual effective dose equivalent (AEDE) using Equation 7.6 [14]:

$$AEDE\ (\mu Sv.y^{-1}) = D \times 8760 \times 0.2 \times 0.7 \times 10^{-3} \quad (7.6)$$

where D (in $nGy.h^{-1}$) is absorbed dose calculated using Equation 3.5, 8760 is hours in a year (in h), 0.2 is outdoor occupancy factor and 0.7 (in $Sv.Gy^{-1}$) is the dose conversion coefficient from D to effective dose.

7.1.2 Synchrotron micro-analysis of uraninite particles

Synchrotron radiation μ-XRF and μ-XANES analyses were performed on the uraninite particles, P1 and P2 (see Chapter Four, Section 4.2.3) that were taken as representative U-bearing microparticles. The procedures for particle isolation, characterisation and data processing

used for the monazite particles (see Chapter Five, Section 6.1) were also used for P1 and P2; however, an Y metal foil (from the National Institute of Standards and Technology) with K-edge at 17.038 keV was used for μ-XANES U energy calibration (L_{III} edge at 17.166 keV).

7.2 Results and discussion

7.2.1 Gamma-ray spectrometry

Investigation of radioactive secular equilibrium

The activity concentration results assume secular equilibrium for the decay products of ^{226}Ra, ^{228}Ra and ^{228}Th used for the determination of activity concentrations of ^{226}Ra and ^{232}Th. To validate this assumption of secular equilibrium, the activity concentration ratio between ^{214}Bi and ^{214}Pb was used for ^{226}Ra, and also as proxy for ^{232}Th, since ^{228}Ra(^{228}Ac) and ^{228}Th (^{208}Tl) are not direct decay products of each other in the ^{232}Th decay chain [18,19]. Appendices A1 to A6 present the activity concentrations of ^{214}Bi, ^{214}Pb (alongside their ratio), ^{228}Ra(^{228}Ac) and ^{228}Th (^{208}Tl) for OMC, OMA, OKC, OKA, ODC and ODA, respectively. From Appendices A1 and A2, we see that the activity ratios between ^{214}Bi and ^{214}Pb in OMC and OMA varied from 1.06 to 1.25 and 1.03 to 1.18, respectively, with mean values of 1.11 ± 0.05 and 1.09 ± 0.05, respectively. In OKC and OKA (Appendices A3 and A4), the activity ratios were found to vary from 0.95 to 1.28 and 0.90 to 1.24, respectively, with mean values of 1.12 ± 0.10 and 1.10 ± 0.10, respectively. Similarly, the activity ratios in ODC and ODA (Appendices A5 and A6) varied from 0.88 to 1.30 and 0.83 to 1.17, respectively, with mean values of 1.06 ± 0.13 and 1.03 ± 0.10, respectively. These results of activity concentration ratios of ^{214}Bi and ^{214}Pb approximate to unity, indicating that secular equilibrium was attained in all samples.

^{40}K, ^{232}Th and ^{226}Ra activity concentrations in coal samples

Results of activity concentration analysis for ^{40}K, ^{232}Th and ^{226}Ra in native coal samples (OMC, OKC and ODC, respectively) are presented in Tables 7.4, 7.5 and 7.6. The mean activity concentrations of ^{40}K, ^{232}Th (mean of ^{228}Ra and ^{228}Th) and ^{226}Ra (mean of ^{214}Pb and ^{214}Bi) in

OMC (Table 7.4) were 79.32 ± 16.91 Bq.kg^{-1}, 41.76 ± 9.17 Bq.kg^{-1} and 42.51 ± 8.54 Bq.kg^{-1}, respectively. Conversely, the mean activity concentrations of ^{40}K, ^{232}Th and ^{226}Ra in OKC (Table 7.5) were 122.96 ± 50.80 Bq.kg^{-1}, 18.43 ± 5.54 Bq.kg^{-1} and 16.19 ± 5.33 Bq.kg^{-1}, respectively; in ODC (Table 7.6), the mean activity concentration of ^{40}K, ^{232}Th and ^{226}Ra were 53.39 ± 20.53 Bq.kg^{-1}, 13.64 ± 4.76 Bq.kg^{-1} and 8.69 ± 4.76 Bq.kg^{-1}, respectively. Compared with the adopted UNSCEAR World mean concentrations in soil (400 Bq.kg^{-1}, 35 Bq.kg^{-1} and 30 Bq.kg^{-1} for ^{40}K, ^{232}Th and ^{226}Ra, respectively, [16]), the mean activity concentrations of ^{232}Th and ^{226}Ra in OMC were marginally higher while those in OKC and ODC were two to three times lower; the higher concentration of ^{232}Th and ^{226}Ra in OMC compared to OKC and ODC implies higher levels of U and Th in OMC. While the total Ra in OMC (77.64 Bq.kg^{-1}) was slightly higher than the World mean in soil (65 Bq.kg^{-1}), total Ra in OKC (33.69 Bq.kg^{-1}) and ODC (22.40 Bq.kg^{-1}) was half and one-third of that mean value, respectively. The low spread in ^{232}Th, ^{228}Ra and ^{226}Ra and large spread in ^{40}K activity concentration values for the series of individual subsamples in OMC, OKC and ODC, indicate an approximately uniform distribution of ^{232}Th, ^{228}Ra and ^{226}Ra and a significantly nonuniform distribution of ^{40}K in the coal samples from each mine. The source of ^{40}K suspected to be from the percolation of K-rich groundwaters and K-feldspar minerals – common in granitic rocks and potentially present in the coal as larger particles because of their lower density. These activity concentrations in the coal samples (OMC, OKC, ODC) represent a low contribution to natural background radiation and are comparable to similar studies in China, India, Serbia and Turkey [20-23]. These coal samples do not pose any radiological hazard.

Table 7.4: Activity concentrations (Bq.kg^{-1}) of ^{40}K, ^{232}Th and ^{226}Ra in OMC.

Sample	^{40}K	^{232}Th	^{228}Ra	^{226}Ra	Total radium
OMC1	81.40 ± 4.98	32.23 ± 1.27	27.00 ± 1.67	32.35 ± 1.17	59.35
OMC2	80.24 ± 4.84	31.94 ± 1.25	27.33 ± 1.67	30.22 ± 1.09	57.55
OMC3	53.40 ± 3.64	28.77 ± 1.14	24.92 ± 1.53	28.56 ± 1.03	53.48
OMC4	105.95 ± 5.67	46.88 ± 1.74	37.93 ± 2.21	47.06 ± 1.64	84.99
OMC5	90.09 ± 5.15	44.71 ± 1.68	36.89 ±2.17	45.03 ± 1.57	81.92
OMC6	88.75 ± 5.08	43.72 ± 1.64	36.33 ± 2.13	46.74 ± 1.63	83.07
OMC7	90.10 ± 5.00	46.37 ± 1.72	38.56 ± 2.23	45.74 ± 1.59	84.30
OMC8	96.52 ± 5.50	48.25 ± 1.81	41.54 ± 2.42	50.99 ± 1.78	92.53
OMC9	84.10 ± 4.93	36.55 ± 1.40	31.43 ± 1.88	40.46 ± 1.42	71.89
OMC10	50.35 ± 3.31	66.56 ± 2.40	55.98 ± 3.14	59.22 ± 2.03	115.20
OMC11	45.91 ± 3.39	33.06 ± 1.29	27.55 ± 1.69	30.95 ± 1.11	58.50
OMC12	83.02 ± 4.87	41.25 ± 1.56	35.28 ± 2.08	43.97 ± 1.54	79.25
OMC13	80.19 ± 4.85	41.85 ± 1.59	35.14 ± 2.09	45.34 ± 1.59	80.48
OMC14	78.12 ± 4.76	42.07 ± 1.60	35.47 ± 2.10	45.44 ± 1.60	80.91
OMC15	81.68 ± 4.91	42.20 ± 1.60	35.60 ± 2.11	45.57 ± 1.60	81.17
Minimum Maximum	45.91 ± 3.39 105.95 ± 5.67	28.77 ± 1.14 66.56 ± 2.40	27.00 ± 1.67 55.98 ± 3.14	28.56 ± 1.03 59.22 ± 2.03	53.48 115.20
Mean ± s.d.	79.32 ± 16.91	41.76 ± 9.17	35.13 ± 7.32	42.51 ± 8.54	77.64
UNSCEAR 2000 mean [16]	400	30	30	35	65
% of UNSCEAR 2000	20	139*	117*	121*	119*

*: % of UNSCEAR 2000 greater than 100%.

s.d.: standard deviation.

Table 7.5: Activity concentrations (Bq.kg^{-1}) of ^{40}K, ^{232}Th and ^{226}Ra in OKC.

Sample	^{40}K	^{232}Th	^{228}Ra	^{226}Ra	Total radium
OKC1	82.09 ± 6.31	18.43 ± 0.92	16.83 ± 1.30	13.84 ± 0.63	30.67
OKC2	46.60 ± 3.80	12.57 ± 0.63	13.26 ± 0.98	19.43 ± 0.76	32.69
OKC3	77.11 ± 6.50	16.59 ± 0.90	16.52 ± 1.34	12.08 ± 0.59	28.60
OKC4	165.99 ± 9.74	22.11 ± 1.04	20.89 ± 1.50	20.12 ± 0.83	41.01
OKC5	174.21 ± 10.27	21.27 ± 1.03	19.43 ± 1.45	16.21 ± 0.70	35.64
OKC6	116.26 ± 7.69	21.10 ± 1.00	18.87 ± 1.40	23.52 ± 0.95	42.39
OKC7	224.58 ± 12.48	27.14 ± 1.26	27.68 ± 1.92	16.86 ± 0.74	44.54
OKC8	139.32 ± 8.53	25.38 ± 1.14	21.80 ± 1.53	27.52 ± 1.07	49.32
OKC9	145.05 ± 9.02	16.97 ± 0.87	18.42 ± 1.37	12.67 ± 0.59	31.09
OKC10	119.32 ± 7.97	17.99 ± 0.91	18.05 ± 1.36	15.57 ± 0.69	33.62
OKC11	127.04 ± 7.43	16.27 ± 0.77	14.07 ± 1.04	18.23 ± 0.73	32.30
OKC12	192.01 ± 11.66	23.04 ± 1.13	19.66 ± 1.52	16.20 ± 0.74	35.86
OKC13	74.63 ± 5.75	19.36 ± 0.94	18.55 ± 1.37	13.95 ± 0.62	32.50
OKC14	87.53 ± 6.86	4.82 ± 0.40	5.03 ± 0.61	5.02 ± 0.32	10.05
OKC15	72.61 ± 5.65	13.50 ± 0.72	13.47 ± 1.07	11.63 ± 0.54	25.10
Minimum Maximum	46.60 ± 3.80 224.58 ± 12.48	4.82 ± 0.40 27.14 ± 1.26	5.03 ± 0.61 27.68 ± 1.92	5.02 ± 0.32 27.52 ± 1.07	10.05 49.32
Mean ± s.d.	122.96 ± 50.80	18.43 ± 5.54	17.50 ± 4.99	16.19 ± 5.33	33.69
UNSCEAR 2000 soil mean [16]	400	30	30	35	65
% of UNSCEAR 2000	31	61	58	46	52

s.d.: standard deviation

Table 7.6: Activity concentrations (Bq.kg^{-1}) of ^{40}K, ^{232}Th and ^{226}Ra in ODC.

Sample	^{40}K	^{232}Th	^{228}Ra	^{226}Ra	Total radium
ODC1	17.63 ± 2.79	13.18 ± 0.75	12.91 ± 1.10	8.16 ± 0.44	21.07
ODC2	56.75 ± 4.99	12.89 ± 0.70	11.09 ± 0.95	11.23 ± 0.53	22.32
ODC3	81.79 ± 6.38	12.15 ± 0.69	10.95 ± 0.97	9.29 ± 0.47	20.24
ODC4	68.94 ± 5.79	21.43 ± 1.07	23.54 ± 1.70	17.02 ± 0.74	40.56
ODC5	53.02 ± 5.19	8.77 ± 0.60	9.73 ± 0.94	4.91 ± 0.32	14.64
ODC6	52.97 ± 5.24	24.31 ± 1.18	21.49 ± 1.63	18.48 ± 0.82	39.97
ODC7	19.93 ± 2.88	13.99 ± 0.77	13.69 ± 1.14	8.10 ± 0.42	21.79
ODC8	86.73 ± 6.95	17.94 ± 0.96	19.91 ± 1.54	10.85 ± 0.54	30.76
ODC9	64.79 ± 5.39	14.59 ± 0.73	13.52 ± 1.05	6.88 ± 0.37	20.40
ODC10	48.10 ± 4.76	13.00 ± 0.75	14.46 ± 1.19	10.61 ± 0.53	25.07
ODC11	60.90 ± 5.43	13.25 ± 0.76	14.60 ± 1.20	3.37 ± 0.25	17.97
ODC12	32.04 ± 3.70	6.95 ± 0.48	6.29 ± 0.68	2.25 ± 0.19	8.54
ODC13	40.96 ± 4.16	9.97 ± 0.61	11.07 ± 0.96	3.68 ± 0.25	14.75
ODC14	43.03 ± 4.24	7.57 ± 0.50	6.62 ± 0.68	4.41 ± 0.28	11.03
ODC15	73.32 ± 5.94	14.68 ± 0.80	15.73 ± 1.24	11.10 ± 0.53	26.83
Minimum Maximum	17.63 ± 2.79 86.73 ± 6.95	6.95 ± 0.48 24.31 ± 1.18	6.29 ± 0.68 23.54 ± 1.70	2.25 ± 0.19 18.48 ± 0.82	8.54 40.56
Mean ± s.d.	53.39 ± 20.53	13.64 ± 4.76	13.71 ± 4.96	8.69 ± 4.76	22.40
UNSCEAR 2000 soil mean [16]	400	30	30	35	65
% of UNSCEAR 2000	13	45	46	25	34

s.d.: standard deviation

^{40}K, ^{232}Th and ^{226}Ra activity concentrations in simulant coal fly ash samples

For the simulant coal fly ash samples (OMA, OKA, ODA), activity concentrations of ^{40}K, ^{232}Th, ^{228}Ra and ^{226}Ra are presented in Tables 7.7, 7.8 and 7.9, respectively. The mean activity concentrations of ^{40}K, ^{232}Th, ^{228}Ra and ^{226}Ra in OMA were 312.96 ± 62.88 Bq.kg^{-1}, 131.92 ± 12.35 Bq.kg^{-1}, 121.25 ± 11.13 Bq.kg^{-1} and 240.89 ± 24.53 Bq.kg^{-1}, respectively. For OKA, the mean activity concentrations of ^{40}K, ^{232}Th, ^{228}Ra and ^{226}Ra were 995.65 ± 301.03 Bq.kg^{-1}, 153.28 ± 34.15 Bq.kg^{-1}, 138.41 ± 7.67 Bq.kg^{-1} and 153.44 ± 29.36 Bq.kg^{-1}, respectively. Similarly, the mean activity concentrations of ^{40}K, ^{232}Th, ^{228}Ra and ^{226}Ra in ODA were 448.91 ± 156.04 Bq.kg^{-1}, 100.02 ± 23.80 Bq.kg^{-1}, 96.84 ± 5.87 Bq.kg^{-1} and 97.03 ± 18.64 Bq.kg^{-1}, respectively. In OMA, while the mean activity concentration of ^{232}Th was about two times higher than the UNSCEAR 1988 World mean value in coal fly ash, the mean activity concentration values for ^{40}K, ^{228}Ra and ^{226}Ra were approximately equal to the World mean value. While the mean activity concentration of ^{228}Ra in OKA was approximately equal to the UNSCEAR 1988 World coal fly ash mean for ^{228}Ra (130 Bq.kg^{-1}), those for ^{40}K and ^{232}Th were four and two times, respectively, higher than the World mean; ^{226}Ra concentration was about half the World mean (240 Bq.kg^{-1}). Conversely, while the mean activity concentration values of ^{40}K (448.91 Bq.kg^{-1}) and ^{232}Th (100.02 Bq.kg^{-1}) in ODA were slightly higher than the UNSCEAR 1988 coal fly ash World mean values, ^{228}Ra (96.84 Bq.kg^{-1}) and ^{226}Ra (97.03 Bq.kg^{-1}) were one to three times lower than the UNSCEAR 1988 values. The low spread in ^{232}Th, ^{228}Ra and ^{226}Ra and large spread in ^{40}K activity concentration values for the series of individual subsamples in the simulant coal fly ash samples (OMA, OKA, ODA) imply a uniform distribution of ^{232}Th, ^{228}Ra and ^{226}Ra and a largely non-uniform distribution of ^{40}K within each mine.

To evaluate the hazards associated with the disposal of these simulant coal fly ash materials into the environment, the activity concentration results were compared with the UNSCEAR 2000 mean values in soil. Compared with the UNSCEAR 2000 values, the mean activity concentrations of ^{226}Ra and ^{232}Th in OMA were seven and four times higher, respectively. Both ^{232}Th and ^{226}Ra were observed to be concentrated in OMA by a factor of three and six, respectively, relative to the precursor coal. In OKA, the mean activity concentrations of ^{232}Th, ^{228}Ra and ^{226}Ra were five times higher than the UNSCEAR 2000 mean values in soil. ^{226}Ra, ^{232}Th and ^{228}Ra were observed to have been concentrated in OKA relative to the precursor coal by a factor of between nine and ten. Conversely, the mean activity concentrations of ^{232}Th, ^{228}Ra and ^{226}Ra in ODA were approximately three times higher than the UNSCEAR 2000 mean values in soil, with ^{228}Ra and ^{226}Ra concentrated in ODA by a factor of seven and eleven, respectively, relative to the precursor coal.

Using the mean values, the ^{226}Ra and ^{228}Ra in OKA was higher than OMA by a factor of two, while being approximately the same as with ODA. This implies greater association of ^{226}Ra and ^{228}Ra in OKA and ODA precursor coals with organic matter than in OMA precursor coal, where ^{226}Ra and ^{228}Ra are ascribed to be more associated with mineral matter; following the high temperature combustion process, ^{226}Ra and ^{228}Ra encapsulated within carbonaceous organic matter were released into the ash. This is supported by the lower percentage ash contents of OKC (10.7 wt%) and ODC (5.3 wt%) compared to OMC (14.8 wt%) [24,25]. Similarly, compared to ^{228}Ra, it was found that ^{226}Ra was more pre-concentrated in the simulant coal fly ash samples from all three mines, a consequence of the longer half-life (slower decay rate) of ^{226}Ra (^{214}Pb and ^{214}Bi) compared to ^{228}Ra (^{228}Ac).

The mean total radium value of 362.14 Bq.kg^{-1} recorded for OMA (Table 7.7) represents an approximate five-fold increase relative to the 77.64 Bq.kg^{-1} in the precursor coal (Table 7.4). Similarly, the mean total radium values of 291.86 Bq.kg^{-1} and 193.87 Bq.kg^{-1} recorded for OKA and ODA (Tables 7.5 and 7.6), respectively, represent approximate nine-fold concentrations relative to the 33.69 Bq.kg^{-1} and 22.40 Bq.kg^{-1}, respectively, in the precursor coals (Tables 7.5 and 7.6). In OMA (Table 7.7), the mean ^{226}Ra/^{228}Ra ratio was found to be 2.00, which implies a higher concentration of ^{226}Ra compared to ^{228}Ra. Similarly, mean values of ^{226}Ra/^{228}Ra in OKA (0.85) and ODA (0.77) (Tables 7.8 and 7.9) indicate approximately equal concentrations of ^{226}Ra and ^{228}Ra. These Ra isotope ratio results are useful in tracing material provenance in the case of coal fly ash accidental spillage or leakage during storage or transport.

The activity concentrations in the simulant coal fly ash samples imply that OMA, OKA and ODA were enriched (though not anomalously) in ^{226}Ra, ^{228}Ra and ^{228}Th; in a case of accidental release of these fly ashes into the environment, they would add significantly to natural background radiation. Compared to UNSCEAR 2000, elevated values of total radium activity concentration in OMA and OKA (with means of 291.86 Bq.kg^{-1} and 362.14 Bq.kg^{-1}, respectively) suggest potentially high radon release rates from buildings constructed using such coal fly ash materials, which would consequently represent a serious health hazard for occupants of such buildings due to exposure to gamma radiation from radium, alongside radon inhalation [26]. The activity concentrations (of U and Th progenies) for OMA, OKA and ODA are also comparable to non-uraniferous coal fly ash samples from the Appalachian, Illinois and Powder River Basin coal mines (USA) and coal mines in Xijiang, Guangxi and Sichuan provinces in China [7,27]. In summary, the residual simulant coal fly ash is enriched in NORMs (naturally occurring radioactive materials) relative to its parent coal; this is a logical concentration of refractory and non-combustible material.

Table 7.7: Activity concentrations (Bq.kg^{-1}) of ^{40}K, ^{232}Th and ^{226}Ra in OMA, and radium isotope ratio.

Sample	^{40}K	^{232}Th	^{228}Ra	^{226}Ra	Total radium	^{226}Ra/^{228}Ra
OMA1	295.00 ± 21.68	130.49 ± 5.50	124.48 ± 8.02	222.84 ± 7.95	347.32	1.79
OMA2	280.90 ± 23.34	127.58 ± 5.78	140.06 ± 9.27	225.17 ± 8.22	365.23	1.61
OMA3	395.27 ± 25.74	122.17 ± 5.18	117.32 ± 7.59	201.43 ± 7.24	318.75	1.72
OMA4	332.90 ± 25.31	123.73 ± 5.46	111.64 ± 7.64	215.51 ± 7.87	327.15	1.93
OMA5	451.19 ± 31.07	120.53 ± 5.46	125.88 ± 8.47	216.81 ± 7.93	342.69	1.72
OMA6	371.47 ± 24.79	112.07 ± 4.80	98.39 ± 6.58	212.78 ± 7.62	311.17	2.16
OMA7	199.53 ± 19.75	129.73 ± 5.83	121.90 ± 8.41	230.72 ± 8.48	352.62	1.89
OMA8	324.30 ± 25.68	137.84 ± 6.05	128.01 ± 8.65	253.57 ± 9.18	381.58	1.98
OMA9	351.50 ± 25.87	155.93 ± 6.53	131.69 ± 8.67	261.51 ± 9.34	393.20	1.99
OMA10	299.89 ± 24.48	157.59 ± 6.73	141.05 ± 9.36	283.75 ± 10.19	424.80	2.01
OMA11	232.33 ± 18.93	129.90 ± 5.47	111.01 ± 7.33	272.47 ± 9.63	383.48	2.45
OMA12	310.47 ± 22.31	140.72 ± 5.82	124.83 ± 8.03	257.19 ± 9.10	382.02	2.06
OMA13	298.25 ± 20.97	135.88 ± 5.56	118.41 ± 7.56	257.92 ± 9.07	376.33	2.18
OMA14	267.12 ± 19.06	129.90 ± 5.29	111.33 ± 7.10	250.21 ± 8.79	361.54	2.25
OMA15	284.26 ± 19.83	124.72 ± 5.13	112.78 ± 7.18	251.42 ± 8.83	364.20	2.23
Minimum Maximum	199.53 ± 19.75 451.19 ± 31.07	112.07 ± 4.80 155.93 ± 6.53	98.39 ± 6.58 141.05 ± 9.36	201.43 ± 7.24 283.75 ± 10.19	311.17 424.80	1.61 2.45
Mean ± s.d.	312.96 ± 62.88	131.92 ± 12.35	121.25 ± 11.13	240.89 ± 24.53	362.14	2.00 ± 0.23
UNSCEAR 1988 coal fly ash mean [28]	265	70	130	240	-	-
UNSCEAR 2000 soil mean [16]	400	30	30	35	65	-
% of UNSCEAR 2000	78	440*	404*	688*	557*	-

*: % of UNSCEAR 200 greater than 100%

s.d.: standard deviation

Table 7.8: Activity concentrations (Bq.kg^{-1}) of ^{40}K, ^{232}Th and ^{226}Ra in OKA, and radium isotope ratio.

Sample	^{40}K	^{232}Th	^{228}Ra	^{226}Ra	Total radium	^{226}Ra/^{228}Ra
OKA1	1330.79 ± 68.14	241.29 ± 7.56	218.87 ± 11.86	187.93 ± 7.08	406.80	0.86
OKA2	1146.74 ± 60.37	160.13 ± 6.88	146.84 ± 9.74	190.42 ± 7.09	337.26	1.30
OKA3	991.76 ± 54.23	169.20 ± 7.14	140.09 ± 9.31	180.38 ± 6.79	320.26	1.29
OKA4	900.92 ± 51.20	127.69 ± 5.75	114.43 ± 7.98	143.12 ± 5.55	257.55	1.25
OKA5	1159.41 ± 62.15	152.40 ± 6.68	135.92 ± 9.23	156.34 ± 6.06	292.26	1.15
OKA6	1165.76 ± 62.68	161.95 ± 7.03	141.50 ± 9.57	140.71 ± 5.53	282.21	0.99
OKA7	698.89 ± 41.08	177.87 ± 7.32	151.83 ± 9.76	172.86 ± 6.47	324.69	1.14
OKA8	882.02 ± 49.40	180.89 ± 7.51	147.79 ± 9.67	176.79 ± 6.63	324.58	1.20
OKA9	1,412.72 ± 74.87	163.33 ± 7.32	158.41 ± 10.77	176.85 ± 6.85	335.26	1.12
OKA10	1,360.02 ± 71.68	136.41 ± 6.29	133.83 ± 9.31	154.85 ± 6.08	288.68	1.16
OKA11	1,137.84 ± 62.58	133.34 ± 6.12	125.18 ± 8.79	157.93 ± 6.15	283.11	1.26
OKA12	1,119.74 ± 64.46	145.70 ± 6.77	138.15 ± 9.79	145.71 ± 5.87	283.86	1.05
OKA13	485.95 ± 33.47	145.12 ± 6.34	137.55 ± 9.18	116.86 ± 4.67	254.41	0.85
OKA14	622.25 ± 41.66	103.56 ± 5.09	104.09 ± 7.65	99.38 ± 4.24	203.47	0.95
OKA15	519.97 ± 35.55	100.30 ± 4.78	81.99 ± 6.21	101.49 ± 4.23	183.48	1.24
Minimum Maximum	485.95 ± 33.47 1,360.02 ± 71.68	100.30 ± 4.78 241.29 ± 7.56	81.99 ± 6.21 218.87 ± 11.86	99.38 ± 4.24 190.42 ± 7.09	183.48 406.80	0.85 1.30
Mean ± s.d.	995.65 ± 301.03	153.28 ± 34.15	138.41 ± 29.72	153.44 ± 29.36	291.86	1.12 ± 0.15
UNSCEAR 1988 coal ash mean [28]	265	70	130	240	-	-
UNSCEAR 2000 soil mean [16]	400	30	30	35	65	-
% of UNSCEAR 2000	249*	511*	461*	438*	449*	-

*: % of UNSCEAR 200 greater than 100%

s.d.: standard deviation.

Table 7.9: Activity concentrations (Bq.kg^{-1}) of ^{40}K, ^{232}Th and ^{226}Ra in ODA, and radium isotope ratio.

Sample	^{40}K	^{232}Th	^{228}Ra	^{226}Ra	Total radium	^{226}Ra/^{228}Ra
ODA1	583.30 ± 41.17	97.01 ± 4.95	94.72 ± 7.29	118.40 ± 4.95	213.12	1.25
ODA2	457.81 ± 32.14	166.35 ± 7.12	166.65 ± 10.73	128.56 ± 5.05	295.21	0.77
ODA3	369.31 ± 30.69	101.20 ± 5.10	102.33 ± 7.70	89.23 ± 3.94	191.56	0.87
ODA4	638.35 ± 41.83	113.47 ± 5.45	116.42 ± 8.33	116.83 ± 4.77	233.25	1.00
ODA5	635.02 ± 38.86	109.46 ± 5.00	102.01 ± 7.17	99.49 ± 4.01	201.50	0.98
ODA6	499.11 ± 33.49	83.40 ± 4.19	93.51 ± 6.75	98.25 ± 4.00	191.76	1.05
ODA7	730.93 ± 47.37	96.80 ± 4.91	85.65 ± 6.80	80.90 ± 3.62	166.55	0.94
ODA8	392.57 ± 31.46	75.92 ± 4.14	81.73 ± 6.48	68.53 ± 3.18	150.26	0.84
ODA9	417.23 ± 29.10	81.15 ± 3.94	75.52 ± 5.64	92.32 ± 3.74	167.84	1.22
ODA10	226.83 ± 21.60	74.65 ± 3.93	79.35 ± 6.12	75.64 ± 3.36	154.99	0.95
ODA11	306.34 ± 21.37	79.94 ± 3.65	80.19 ± 5.51	89.55 ± 3.50	169.74	1.12
ODA12	201.90 ± 18.14	97.74 ± 4.44	77.50 ± 5.64	94.12 ± 3.76	171.62	1.21
ODA13	396.67 ± 25.86	94.29 ± 4.21	93.25 ± 6.30	82.55 ± 3.29	175.80	0.89
ODA14	324.99 ± 22.55	98.23 ± 4.33	96.01 ± 6.42	91.08 ± 3.57	187.09	0.95
ODA15	553.31 ± 35.97	130.64 ± 5.76	107.75 ± 7.50	130.03 ± 5.11	237.78	1.21
Minimum Maximum	201.90 ± 18.14 730.93 ± 47.37	74.65 ± 3.93 166.35 ± 7.12	75.52 ± 5.64 166.65 ± 10.73	68.53 ± 3.18 130.03 ± 5.11	150.26 295.21	0.77 1.25
Mean ± s.d.	448.91 ± 156.04	100.02 ± 23.80	96.84 ± 5.87	97.03 ± 18.64	193.87	1.02 ± 0.04
UNSCEAR 1988 coal ash mean [28]	265	70	130	240	-	-
UNSCEAR 2000 soil mean [16]	400	30	30	35	65	-
% of UNSCEAR 2000	112*	333*	323*	277*	298*	-

*: % of UNSCEAR 200 greater than 100%

s.d.: standard deviation.

Radiological hazard indices

Tables 7.10, 7.11 and 7.12 present results of estimated D, AEDE and Ra_{eq} for OMC, OKC and ODC, respectively. Similarly, Tables 7.13, 7.14 and 7.15 show results of estimated D, AEDE and Ra_{eq} for OMA, OKA and ODA, respectively. The mean values of D, AEDE and Ra_{eq} in OMC, OKC and ODC coal samples (Tables 7.10, 7.11, 7.12) were respectively: 48.17 $nGy.h^{-1}$, 59.08 $\mu Sv.y^{-1}$ and 108.33 $Bq.kg^{-1}$; 23.74 $nGy.h^{-1}$, 29.12 $\mu Sv.y^{-1}$ and 52.02 $Bq.kg^{-1}$; 14.48 $nGy.h^{-1}$, 17.76 $\mu Sv.y^{-1}$ and 32.31 $Bq.kg^{-1}$. These values were well below the World mean values of 59 $nGy.h^{-1}$, 70 $\mu Sv.y^{-1}$ and 370 $Bq.kg^{-1}$ for D, AEDE and Ra_{eq}, respectively. In OMA, OKA and ODA simulant coal fly ash (Tables 7.13, 7.14, 7.15), the mean values of D, AEDE and Ra_{eq} (respectively: 204.02 $nGy.h^{-1}$, 250.21 $\mu Sv.y^{-1}$, 453.63 $Bq.kg^{-1}$; 204.99 $nGy.h^{-1}$, 251.40 $\mu Sv.y^{-1}$, 449.30 $Bq.kg^{-1}$; 123.96 $nGy.h^{-1}$, 152.02 $\mu Sv.y^{-1}$, 274.62 $Bq.kg^{-1}$) were higher than the World mean; the mean AEDE, being two to four times higher than the World mean, represents 6% to 10% of the annual natural background effective dose – with the value of 2.4 mSv [29]. The Ra_{eq} values for OMA (453.63 $Bq.kg^{-1}$) and OKA (449.30 $Bq.kg^{-1}$) being higher than the recommended upper limit of 370 $Bqkg^{-1}$ imply using large volumes (>50%) of these fly ash materials for the construction of residential buildings, has the implication of potentially increasing internal exposure (and to a lesser extent, external exposure) to U, Th, radon gas and related decay products [30,31]. However, factors such as gamma-rays attenuation by the bricks or concrete used and radon emanation rates strongly influence radiation-related hazards from high volume fly ash bricks and concrete [31].

Also, the radiological hazard data for OMA, OKA, ODA imply that indiscriminate disposal of large volumes of coal fly ash from all three mines into landfills and use for agronomic purposes could under acidic conditions, potentially leach radionuclides and toxic heavy metals into the

soil and contaminate groundwater [32]. These results imply that caution should be taken during the disposal and use of these coal ash materials; they should be properly stored in slurry ponds to prevent exposure to gamma radiation, ingestion and inhalation of (re)suspended particles, and leaching of radionuclides and toxic heavy metals into the environment especially given the high surface area of the material, leaching will be rapid. These potential health impacts are a significant finding and represent major safety implications for the Nigerian people if such coal fly ash material is not properly stored, exposing the people to radiation via inhalation and ingestion. Alternatively, this material could be used as filler in asphalt pavements and in the production of geopolymers (with improved compressive strength and fire resistance) for nuclear waste encapsulation [32,33].

Table 7.10: Radiological hazard indices for radionuclides in OMC.

Sample	Absorbed dose ($nGy.h^{-1}$)	Annual effective dose equivalent ($\mu Sv.y^{-1}$)	Radium equivalent ($Bq.kg^{-1}$)
OMC1	37.81 ± 0.96	46.37 ± 1.18	84.71 ± 2.19
OMC2	36.60 ± 0.93	44.89 ± 1.14	82.07 ± 2.13
OMC3	32.80 ± 0.85	40.22 ± 1.04	73.81 ± 1.95
OMC4	54.48 ± 1.32	66.81 ± 1.62	122.26 ± 3.01
OMC5	51.57 ± 1.27	63.24 ± 1.55	115.90 ± 2.90
OMC6	51.70 ± 1.26	63.41 ± 1.55	116.09 ± 2.88
OMC7	52.90 ± 1.29	64.87 ± 1.58	118.99 ± 2.95
OMC8	56.73 ± 1.39	69.57 ± 1.70	127.42 ± 3.17
OMC9	44.28 ± 1.09	54.30 ± 1.34	99.20 ± 2.48
OMC10	69.66 ± 1.73	85.43 ± 2.12	158.28 ± 4.00
OMC11	36.18 ± 0.94	44.37 ± 1.16	81.76 ± 2.17
OMC12	48.69 ± 1.20	59.71 ± 1.47	109.35 ± 2.74
OMC13	49.57 ± 1.23	60.79 ± 1.50	111.36 ± 2.80
OMC14	49.66 ± 1.23	60.90 ± 1.51	111.62 ± 2.82
OMC15	49.95 ± 1.23	61.26 ± 1.51	112.21 ± 2.82
Minimum Maximum	32.80 ± 0.85 69.66 ± 1.73	40.22 ± 1.04 85.43 ± 2.12	73.81 ± 1.95 158.28 ± 4.00
Mean ± s.d.	48.17 ± 9.18	59.08 ± 11.66	108.33 ± 21.63
World mean [16,17]	59	70	<370
% of World mean	82	84	29

s.d.: standard deviation

Table 7.11: Radiological hazard indices for radionuclides in OKC.

Sample	Absorbed dose ($nGy.h^{-1}$)	Annual effective dose equivalent ($\mu Sv.y^{-1}$)	Radium equivalent ($Bq.kg^{-1}$)
OKC1	20.95 ± 0.68	25.69 ± 0.83	46.52 ± 1.54
OKC2	18.51 ± 0.54	22.70 ± 0.66	40.99 ± 1.21
OKC3	18.82 ± 0.67	23.08 ± 0.82	41.74 ± 1.50
OKC4	29.57 ± 0.84	36.27 ± 1.03	64.52 ± 1.86
OKC5	27.60 ± 0.82	33.85 ± 1.01	60.04 ± 1.81
OKC6	28.46 ± 0.81	33.90 ± 1.00	62.65 ± 1.82
OKC7	33.55 ± 0.98	41.14 ± 1.21	72.96 ± 2.17
OKC8	33.85 ± 0.92	41.52 ± 1.13	74.54 ± 2.06
OKC9	22.15 ± 0.70	27.17 ± 0.86	48.11 ± 1.54
OKC10	23.03 ± 0.72	28.25 ± 0.88	50.48 ± 1.60
OKC11	23.55 ± 0.65	28.88 ± 0.80	51.28 ± 1.44
OKC12	29.41 ± 0.91	36.07 ± 1.11	63.93 ± 1.99
OKC13	21.25 ± 0.68	26.06 ± 0.83	47.38 ± 1.55
OKC14	8.88 ± 0.40	10.89 ± 0.49	18.65 ± 0.84
OKC15	16.55 ± 0.55	20.30 ± 0.68	36.53 ± 1.24
Minimum Maximum	8.88 ± 0.40 33.85 ± 0.92	10.89 ± 0.49 41.52 ± 1.13	18.65 ± 0.84 74.54 ± 2.06
Mean ± s.d.	23.74 ± 6.78	29.12 ± 8.31	52.02 ± 14.81
World mean [16,17]	59	70	<370
% of World mean	40	42	14

s.d.: standard deviation

Table 7.12: Radiological hazard indices for radionuclides in ODC.

Sample	Absorbed dose (nGy.h^{-1})	Annual effective dose equivalent (µSv.y^{-1})	Radium equivalent (Bq.kg^{-1})
ODC1	12.47 ± 0.51	15.29 ± 0.63	28.36 ± 1.18
ODC2	15.34 ± 0.53	18.81 ± 0.65	34.03 ± 1.20
ODC3	15.04 ± 0.54	18.45 ± 0.66	32.96 ± 1.20
ODC4	23.68 ± 0.77	29.04 ± 0.94	52.97 ± 1.76
ODC5	9.78 ± 0.45	11.99 ± 0.55	21.53 ± 1.00
ODC6	25.43 ± 0.84	31.19 ± 1.03	57.32 ± 1.92
ODC7	13.02 ± 0.52	15.97 ± 0.64	29.64 ± 1.20
ODC8	19.47 ± 0.69	23.87 ± 0.85	43.18 ± 1.57
ODC9	14.69 ± 0.52	18.02 ± 0.64	32.73 ± 1.18
ODC10	14.76 ± 0.55	18.10 ± 0.68	32.90 ± 1.25
ODC11	12.10 ± 0.52	14.84 ± 0.64	27.01 ± 1.19
ODC12	6.57 ± 0.34	8.06 ± 0.42	14.66 ± 0.77
ODC13	9.43 ± 0.42	11.57 ± 0.52	21.09 ± 0.96
ODC14	8.40 ± 0.37	10.31 ± 0.46	18.55 ± 0.83
ODC15	17.05 ± 0.60	20.91 ± 0.73	37.74 ± 1.34
Minimum Maximum	6.57 ± 0.34 25.43 ± 0.84	8.06 ± 0.42 31.19 ± 1.03	14.66 ± 0.77 57.32 ± 1.92
Mean ± s.d.	14.48 ± 5.32	17.76 ± 6.52	32.31 ± 11.95
World mean [16,17]	59	70	<370
% of World mean	25	25	9

s.d.: standard deviation

Table 7.13: Radiological hazard indices for radionuclides in OMA.

Sample	Absorbed dose ($nGy.h^{-1}$)	Annual effective dose equivalent ($\mu Sv.y^{-1}$)	Radium equivalent ($Bq.kg^{-1}$)
OMA1	194.07 ± 5.03	238.01 ± 6.17	432.16 ± 11.31
OMA2	192.80 ± 5.25	236.45 ± 6.44	429.24 ± 11.80
OMA3	183.33 ± 4.70	224.84 ± 5.77	406.57 ± 10.54
OMA4	188.18 ± 5.02	230.78 ± 6.16	418.08 ± 11.26
OMA5	191.78 ± 5.10	235.20 ± 6.25	423.91 ± 11.38
OMA6	181.48 ± 4.67	222.57 ± 5.73	401.64 ± 10.43
OMA7	193.27 ± 5.33	237.03 ± 6.54	431.60 ± 12.00
OMA8	213.93 ± 5.70	262.36 ± 6.99	475.65 ± 12.77
OMA9	229.66 ± 5.94	281.65 ± 7.29	511.56 ± 13.36
OMA10	238.78 ± 6.30	292.84 ± 7.73	532.20 ± 14.15
OMA11	214.03 ± 5.60	262.49 ± 6.86	476.12 ± 12.49
OMA12	216.76 ± 5.56	265.84 ± 6.82	482.33 ± 12.45
OMA13	213.67 ± 5.44	262.04 ± 6.67	475.19 ± 12.17
OMA14	205.20 ± 5.23	251.65 ± 6.41	456.54 ± 11.69
OMA15	203.34 ± 5.19	249.38 ± 6.36	451.66 ± 11.58
Minimum Maximum	181.48 ± 4.67 238.78 ± 6.30	222.57 ± 5.73 292.84 ± 7.73	401.64 ± 10.43 532.20 ± 14.15
Mean ± s.d.	204.02 ± 16.90	250.21 ± 20.73	453.63 ± 38.20
World mean [16,17]	59	70	<370
% of World mean	346*	357*	123*

*: % of World mean greater than 100%

s.d.: standard deviation

Table 7.14: Radiological hazard indices for radionuclides in OKA.

Sample	Absorbed dose ($nGy.h^{-1}$)	Annual effective dose equivalent ($\mu Sv.y^{-1}$)	Radium equivalent ($Bq.kg^{-1}$)
OKA1	288.06 ± 6.29	353.27 ± 7.72	635.45 ± 13.95
OKA2	232.51 ± 5.86	285.15 ± 7.19	507.70 ± 12.99
OKA3	226.88 ± 5.79	278.26 ± 7.10	498.70 ± 12.95
OKA4	180.81 ± 4.82	221.75 ± 5.91	395.09 ± 10.67
OKA5	212.63 ± 5.55	260.76 ± 6.81	463.55 ± 12.28
OKA6	211.44 ± 5.60	259.31 ± 6.87	462.06 ± 12.45
OKA7	216.44 ± 5.61	265.44 ± 6.87	481.03 ± 12.71
OKA8	227.71 ± 5.85	279.27 ± 7.17	503.38 ± 13.18
OKA9	239.27 ± 6.27	293.44 ± 7.69	519.19 ± 13.77
OKA10	210.65 ± 5.59	258.34 ± 6.86	454.64 ± 12.18
OKA11	200.95 ± 5.34	246.44 ± 6.55	436.22 ± 11.73
OKA12	202.01 ± 5.59	247.75 ± 6.86	440.28 ± 12.36
OKA13	161.91 ±4.61	198.56 ± 5.66	361.80 ± 10.52
OKA14	134.41 ± 4.04	164.84 ± 4.95	295.38 ± 9.01
OKA15	129.15 ± 3.79	158.39 ± 4.65	284.96 ± 8.49
Minimum Maximum	129.15 ± 3.79 288.06 ± 6.29	158.39 ± 4.65 353.27 ± 7.72	284.96 ± 8.49 635.45 ± 13.95
Mean ± s.d.	204.99 ± 40.79	251.40 ± 50.02	449.30 ± 89.15
World mean [16,17]	59	70	<370
% of World mean	347*	359*	121*

*: % of World mean greater than 100%

s.d.: standard deviation

Table 7.15: Radiological hazard indices for radionuclides in ODA.

Sample	Absorbed dose ($nGy.h^{-1}$)	Annual effective dose equivalent ($\mu Sv.y^{-1}$)	Radium equivalent ($Bq.kg^{-1}$)
ODA1	137.62 ± 4.14	168.78 ± 5.07	302.04 ± 9.20
ODA2	178.96 ± 5.07	219.48 ± 6.22	401.69 ± 11.63
ODA3	117.75 ± 3.80	144.41 ± 4.66	262.38 ± 8.62
ODA4	149.13 ± 4.33	182.89 ± 5.31	328.25 ± 9.69
ODA5	138.56 ± 3.90	169.93 ± 4.78	304.91 ± 8.73
ODA6	116.58 ± 3.43	142.97 ± 4.21	255.94 ± 7.65
ODA7	126.32 ± 3.94	154.92 ± 4.83	275.61 ± 8.70
ODA8	93.89 ± 3.18	115.14 ± 3.90	207.32 ± 7.14
ODA9	109.06 ± 3.18	133.76 ± 3.90	240.49 ± 7.12
ODA10	89.49 ± 2.98	109.75 ± 3.65	199.86 ± 6.76
ODA11	102.43 ± 2.88	125.62 ± 3.53	227.45 ± 6.50
ODA12	110.94 ± 3.28	136.05 ± 4.03	249.43 ± 7.51
ODA13	111.63 ± 3.15	136.90 ± 3.87	247.93 ± 7.14
ODA14	114.96 ± 3.23	140.99 ± 3.96	256.57 ± 7.36
ODA15	162.05 ± 4.46	198.74 ± 5.47	359.45 ± 10.08
Minimum Maximum	89.49 ± 2.98 178.96 ± 5.07	109.75 ± 3.65 219.48 ± 6.22	199.86 ± 6.76 401.69 ± 11.63
Mean ± s.d.	123.96 ± 25.05	152.02 ± 30.73	274.62 ± 55.79
World mean [16,17]	59	70	<370
% of World mean	210	217	75

*: % of World mean greater than 100%

s.d.: standard deviation

7.2.2 Synchrotron micro-analysis of uraninite particles

The fate, transport, solubility and associated chemo- and radiotoxicity of U is dependent on its distribution and oxidation state in a matrix. In this section, the uraninite microparticles (P1, P2) earlier identified and extracted from OKA and OMA simulant coal fly ash materials (see chapters four and six) were subjected to synchrotron radiation μ-XRF and μ-XANES analyses to determine U distribution and oxidation state and consequently, the associated hazards.

μ-XRF mapping

Shown in Figures 7.3 and 7.4 are the results of μ-XRF analysis of uranium-bearing microparticles P1 and P2, respectively. The μ-XRF analysis of P1 (Figure 7.3) shows the particle matrix to be composed of a homogenous distribution of U, with no Th detected. However, there exist regions of higher U concentration (brighter regions in Figure 7.3); this is as a result of the botryoidal surface morphology of P1 (earlier reported in Chapter Four, Section 4.2.3). The nonexistence of Th in P1 – which is indicative of the origin of P1, agrees with the literature as Th is usually low or absent in uraninite of purely hydrothermal origin; this is because Th mainly exists in the IV state and does not adopt the distinctive highly-soluble VI state that U can adopt [34]. Similarly, μ-XRF analysis of P2 (Figure 7.4) showed a homogeneous distribution of U (red region), colocalising with low levels of Th (indicated by the yellow region). While Th was detected in P2 using the μ-XRF, it was not detected using energy dispersive spectroscopy (EDS) (earlier reported in Chapter Four, Section 4.2.3) to the lower detection limit of the EDS (≥0.5%) compared to the μ-XRF. These results confirm the results of scanning electron microscopy (SEM) with EDS (Chapter Four, Section 4.2.3); the implications of the homogenous distribution of U in P1 and P2 is the expectedly high leaching rate of surface-bound U (a consequence of decreased reaction time during oxidation and

dissolution in the natural environment due to the high surface area to volume ratio of the micro-scale particles).

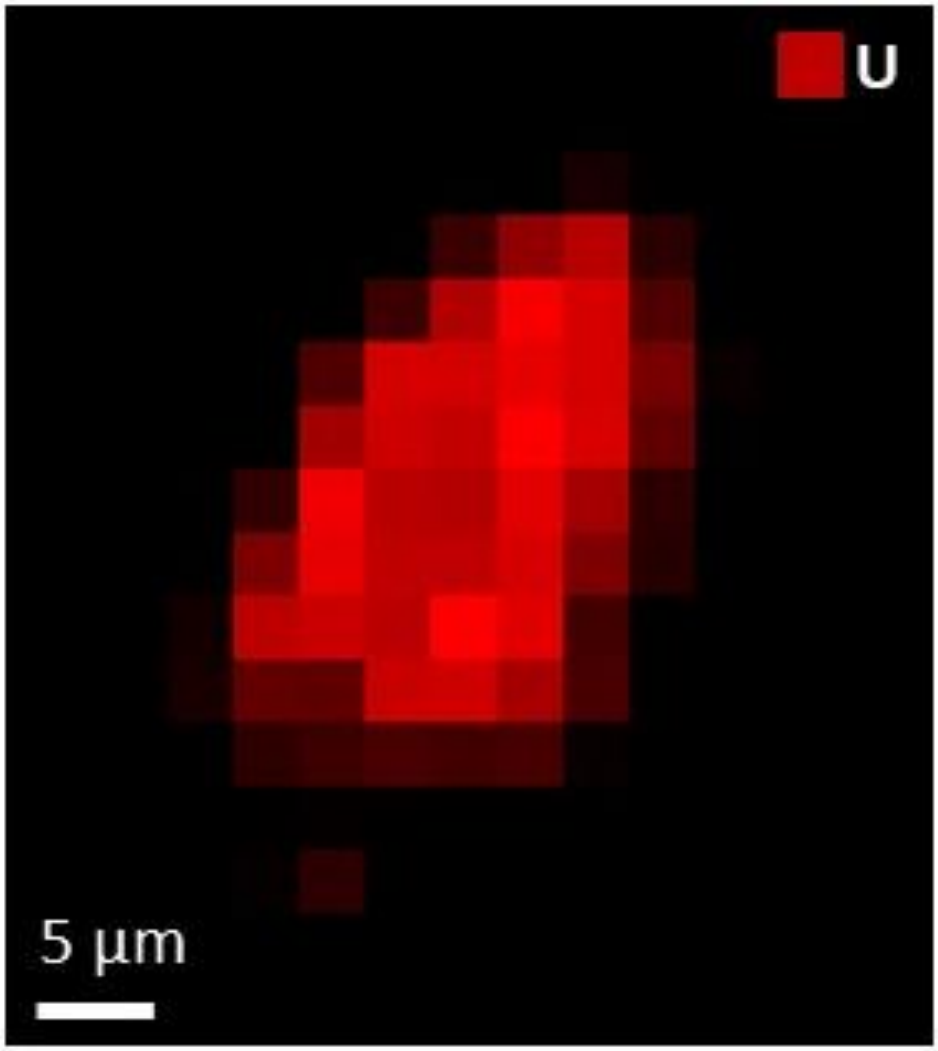

Figure 7.3: µ-XRF plot of P1.

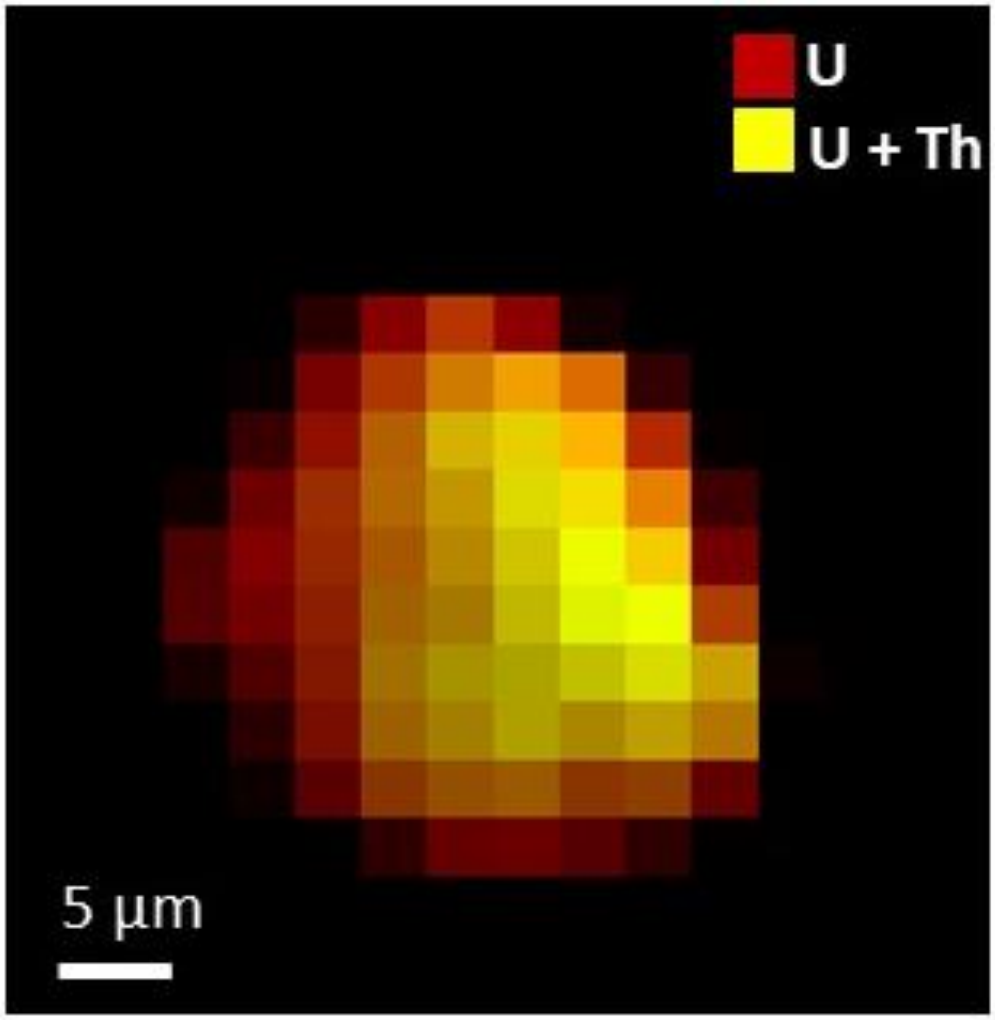

Figure 7.4: µ-XRF plot of P2.

µ-XANES

Figure 7.5 shows µ-XANES spectra of P1 and P2, alongside the spectrum of a UO_2 reference material. The spectra of both P1 and P2 show a main peak at 17,176 eV (labelled as point X), with a subtle peak at 17,216 eV (point Y). These peaks match perfectly with the UO_2 standard spectrum, which shows that U exists in the IV oxidation state in both particles. Uranium oxide in this reduced state is not expected given the temperature experience during combustion which would have driven thermal reduction of any U(VI) [35]. However, studies have shown that natural uraninite when heated recrystallises into UO_2 (IV), U_3O_8 (a mixture of IV and V),

or both [35]. this recrystallisation is dependent on the temperature, the duration of heating and the level of initial oxidation [36].

In studies of bulk UO_2 in the environment, the existence of U in the IV oxidation state typically implies low mobility and solubility of U. However, the fact that UO_2 in the coal fly ash is micro-scale means that when it is exposed to rain, meteoric waters, and oxidising environmental conditions, changes in the oxidation state could quickly result. For example, a previous µ-XANES study on U in coal fly ash [35] reported U in mixed oxidation states (IV and VI) in the untreated coal fly ash studied, but with ~90% in the IV state as determined by $FeSO_{4(aq)}$ treatment giving an indication of uranium reduction, by Fe^{2+}, in the ferrous solution. In another U µ-XANES study on untreated coal fly ash [37], the VI state was reported to dominate, and was oxidation attributable to redox reactions due to factors such as meteoric leaching and generation of acidic waters during open air (uncovered) storage. [37] is an important study when combined with our results as it highlights that these fine uranium-bearing microparticles can easily and rapidly oxidise in the surface environment. Once oxidised to U(VI) then dissolution occurs with relative ease [4].

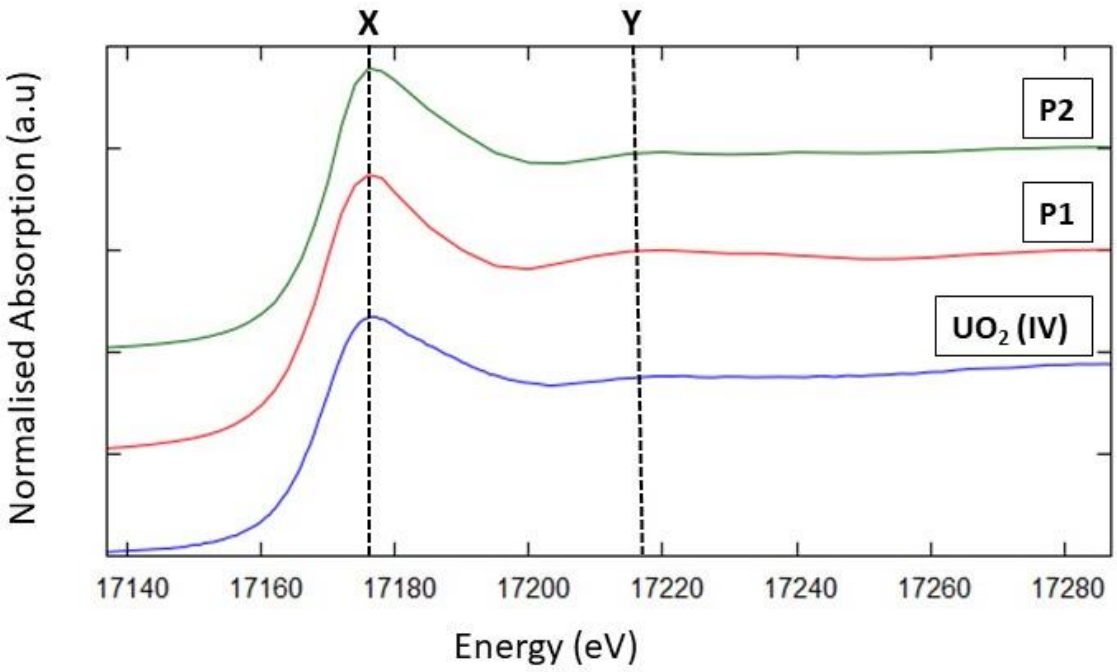

Figure 7.5: XANES plot of P1 and P2 alongside UO_2 reference spectrum.

7.3 Summary

This work has determined the activity concentration and radiological hazard indices of bulk coal (OMC, OKC, ODC) and simulant coal fly ash (OMA, OKA, ODA) samples via gamma spectrometry, alongside the speciation of isolated radioactive particles (P1, P2) by means of μ-XRF and μ-XANES analysis. Using the activity concentration ratios between ^{214}Bi and ^{214}Pb, the assumption of secular equilibrium in the bulk coal and simulant coal fly ash samples during gamma-ray spectrometry was validated. The results of activity concentration and radiological indices (of ^{40}K, ^{232}Th and ^{226}Ra), alongside total Ra for the bulk coal samples (OMC, OKC, ODC), were all significantly below the UNSCEAR 2000 World mean value for soil and considered to be of no significant radiological hazard. Conversely, the results for the simulant coal fly ash samples (OMA, OKA, ODA) were well above the World mean for soil, representing 6% to 10% of the annual natural background effective dose (2.4 mSv), making these fly ash materials unsuitable for reuse in the construction of residential buildings due to the high risk of exposure to radon and gamma radiation. As alluded to in Chapter Five, Section 5.2.4, recovery of rare earth elements, U and Th from the simulant coal fly ash significantly reduces the radioactivity levels, making the resultant ash suitable for use in the construction of residential buildings while also adding extra value. μ-XRF and μ-XANES analyses showed a homogenous distribution of U within P1 and P2, and existing in the IV oxidation state. Though, U in bulk crystals of U(IV) oxide and mineral species is recognised to be relatively immobile due to low solubility, the homogenous distribution of U in microparticles P1 and P2, alongside their high surface area to volume ratios, has the consequence of high risk of localised radiation dose delivery (when inhaled or in contact with the body) and a high leaching rate of surface bound U, polluting drinking waters.

Based on the analysis presented herein, it is strongly recommended the SCFAs derived from burning these Nigerian coal types should be carefully managed to limit meteoric leaching. Care should be taken to shield ash deposits from percolating rainwater or meteoric run offs. This could be achieved by using bonded storage areas using clay, plastic or geopolymers underlay and covering. Failure to manage these wastes could result in acid waste generation that would carry U, Th and other toxic metals into the local groundwater and rivers.

7.4 References

[1] Salbu B., Kashparov V., Lind O.C., Garcia-Tenorio R., Johansen M.P., Child D.P., Roos P., Sancho C. Challenges associated with the behaviour of radioactive particles in the environment. Journal of Environmental Radioactivity, 186 (2018) 101-115.

[2] International Atomic Energy Agency. Radioactive particles in the environment: sources, particle characteristics and analytical techniques. IAEA-TECDOC-1663 Vienna (2011).

[3] McGuire C., Dale P., Copplestone D., Wilson C., Tyler A. Characterising radium-226 particles from legacy contamination to support radiation dose assessments. Journal of Environmental Radioactivity, 212 (2020) 106-127

[4] Salbu B., Lind O.C., Skipperud L. Radionuclide speciation and its relevance in environmental impact assessments. Journal of Environmental Radioactivity, 74 (2004) 233-242.

[5] Gilmore G. Practical gamma-ray spectrometry. Chichester: John Wiley & Sons (1995).

[6] Lépy M.-C. Detection efficiency. IAEA - ALMERA Technical Visit. http://www.nucleide.org/ICRM_GSWG/Training/Efficiency.pdf (2010) (accessed 21 September 2020).

[7] Nancy E.L., Vengosh A., Dai S. Naturally occurring radioactive materials in uranium-rich coals and associated coal combustion residues from China. Environmental Science and Technology, 51 (2017) 13487-13493.

[8] American Society for Testing and Materials. E181-98 standard test: methods for detector calibration and analysis of radionuclides, annual book of ASTM standard vol.12.02: nuclear (II), solar and geothermal energy. ASTM International Standard Worldwide, Philadelphia, U.S.A. (2005).

[9] Eckert and Ziegler. Reference & calibration sources product information. https://www.ezag.com/fileadmin/user_upload/isotopes/isotopes/Isotrak/isotrak-pdf/Product_literature/EZIPL/EZIP_catalogue_reference_and_calibration_sources.pdf (accessed 4 January 2019).

[10] International Atomic Energy Agency. Certified reference material: IAEA-385 radionuclides in Irish sea sediment. https://nucleus.iaea.org/rpst/Documents/rs_iaea_385.pdf (accessed 4 January 2018).

[11] Nancy E.L., James C.H., Heileen H.-K., Ross K., Taggart A.V. Naturally occurring radioactive materials in coals and coal combustion residuals in the United States. Environmental Science and Technology, 49 (2015) 11227-11233.

[12] Isinkaye O.M., Jibiri N.N., Olomide A. Radiological health assessment of natural radioactivity in the vicinity of Obajana cement factory, North Central Nigeria. Journal of Medical Physics 40 (2015) 52-59.

[13] Kolo M.T., Khandaker M.U., Shuaibu H.K. Natural radioactivity in soils around mega coal-fired cement factory in Nigeria and its implications on human health and environment. Arabian Journal of Geosciences, 11 (2018) 755-762.

[14] El-Taher A. Gamma spectroscopic analysis and associated radiation hazards of building materials used in Egypt. Radiation Protection Dosimetry, 138 (2010) 166-173.

[15] National Nuclear Data Center, Brookhaven National Laboratory, USA. http://www.nndc.bnl.gov/ (accessed 19 January 2019).

[16] United Nation Scientific Committee on Effects of Atomic Radiation. Sources and effects of ionizing radiation; report to the General Assembly with scientific annexes; UNSCEAR: New York, NY, USA (2000).

[17] Beretka J., Mathew P.J. Natural radioactivity of Australian building materials, industrial wastes and by-products. Health Physics, 48 (1985) 87-95.

[18] El-Dine N.W. Study of natural radioactivity and the state of radioactive disequilibrium in U-series for rock samples, North Eastern Desert, Egypt. Applied Radiation and Isotopes 66 (2008), 80-85.

[19] Santawamaitre T., Malain D., Al-Sulaiti H.A., Matthews M., Bradley D.A., Regan P.H. (2011), Study of natural radioactivity in riverbank soils along the Chao Phraya river basin in Thailand. Nuclear Instruments and Methods in Physics Research Section A, 652 (2011) 920-924.

[20] Lu X., Jia X., Wang F. Natural radioactivity of coal and its by-products in the Baoji coal-fired power plant, China. Current Science, 91 (2006) 1508-1511.

[21] Mandal A., Sengupta D. Radioelemental study of Kolaghat thermal power plant, West Bengal, India: possible environmental hazards. Environmental Geology, 44 (2003) 180-186.

[22] Kisić D.M., Miletić S.R., Radonjić V.D., Radanović S.B., Filipovic J.Z., Gržetić I.A. Natural radioactivity of coal and fly ash at the Nikola Tesla B TPP. Hemijska Industrija, 67 (2013) 729-738.

[23] Cevik U., Damla N., Nezir S. Radiological characterization of Cayirhan coal-fired power plant in Turkey. Fuel, 86 (2007) 2509-2513.

[24] Mohammed U., Garba U.M., Priscilla E., Azare K.I., Usman S., Onoduku Y., Mohammad S. Characterisation and ash chemistry of selected Nigerian coals for solid fuel combustion. Petroleum and Coal, 58 (2016) 646-654.

[25] Afu D.J., Ifeola E.O., Adesida P.A. Omelewu coal characterization for powering power plant at Dangote cement factory, Obajana, Kogi state, Nigeria. American Journal of Engineering Research, 7 (2018) 143-152.

[26] Labrincha J., Puertas F., Schroeyers W., Kovler K. Naturally occurring radioactive materials in construction. Integrating Radiation Protection in Reuse, (2017) 183-252.

[27] Chen J., Chen P., Yao D., Huang W., Tang S., Wang K., Liu W., Hu Y., Zhang B., Sha J. Abundance, distribution, and modes of occurrence of uranium in Chinese coals. Minerals, 7 (2017) 239p.

[28] United Nation Scientific Committee on Effects of Atomic Radiation. Sources and effects of ionizing radiation; report to the General Assembly with Scientific Annexes; UNSCEAR: New York, NY, USA (1988).

[29] United Nation Scientific Committee on Effects of Atomic Radiation. Sources and effects of ionizing radiation; report to the General Assembly scientific annexes A and B; UNSCEAR: New York, NY, USA (2008).

[30] gnjatović I., Sas Z., Dragaš J., Somlai J., Kovács T. Radiological and material characterization of high volume fly ash concrete. Journal of environmental radioactivity, 168 (2017) 38-45.

[31] Jadambaa Temuujin, Enkhtuul Surenjav, Claus Henning Ruescher, Jan Vahlbruch. Processing and uses of fly ash addressing radioactivity (critical review). Chemosphere, 216 (2019) 866-882.

[32] Leay L., Potts A., Donoclift T. Geopolymers from fly ash and their gamma irradiation. Materials Letters, 227 (2018) 240–242.

[33] Zoorob S.E., Cabrera J.G. Design and construction of a road pavement using fly ash in hot rolled asphalt. Studies in environmental science, 71 (1997) 149–165.

[34] Pohjolainen E. Uranium deposits of Finland. Maier W.D., Lahtinen R., O'Brien H. (eds.), Mineral deposits of Finland, Elsevier, Amsterdam (2015) 659-683.

[35] Sun Y., Wu M., Zheng L., Zheng L., Wang B., Wang Y. Uranium speciation in coal bottom ash investigated via, x-ray absorption fine structure and x-ray photoelectron spectra. Journal of Environmental Sciences, 74 (2018) 88-94.

[36] Brooker E.J., Nuffield E.W. Studies of radioactive compounds: IV—pitchblende from Lake Athabaska, Canada. American Mineralogist, 37 (1952) 363–385.

[37] Rivera N., Hesterberg D., Kaur N., Duckworth O.W. Chemical speciation of potentially toxic trace metals in coal fly ash associated with the Kingston fly ash spill. Energy and Fuels, 31 (2017) 9652-9659.

Chapter 8

Final conclusions and future work

8.1 Final conclusions

To ensure sustained stability in the global market for the supply of in-demand rare earth elements (REEs), and to overcome China's global monopoly on REE production and supply, cheaper and less capital-intensive unconventional sources of REE are being considered for recovery. The work presented in this thesis is a thorough study of Nigerian coal and simulant coal fly ash, which is proven as a promising alternative unconventional source of REEs, utilising a suite of advanced analytical techniques. This study provides enhanced understanding of the distribution, speciation, crystallography and solid-state chemistry of REEs and actinides in Nigerian simulant coal fly ash. This is essential for the development and optimisation of environmentally friendly and cost-effective REE recovery, waste management and environmental protection methodologies, valuable for the Nigerian Government and the global scientific community.

The salient findings and conclusions of each results chapter, alongside implications for REE recovery from coal fly ash in repositories globally are summarised below.

8.1.1 Elemental composition and mineralogical analysis of simulant coal fly ash samples

- The simulant coal fly ashes (SCFAs) were composed of the chemo- and radio-toxic elements Cr, Cd, As, Pb, Th and U in amounts considered to be significant relative to the large volume of fly ash generated by a typical coal-fired power plant.
- Rare earth mineral particles were entrapped in the carbonaceous matter in the coal samples, a disadvantage for direct recovery of REEs from coal as combustion - a process that contributes to global warming - is required to release the rare earth mineral particles.
- SCFAs contain easy to beneficiate gangue minerals, with low amounts of glassy amorphous components - a consequence of the low combustion temperature (1,100 °C) used. This induces little or no encapsulation of rare earth minerals in glassy amorphous phases, thereby avoiding the use of concentrated sulphuric acid for recovery of the rare earth minerals from within the glassy amorphous component. The occurrence of quartz, mullite, haematite and cristobalite as the major mineral phases in SCFAs instead favours cost-effective REE physical beneficiation through gravity or density, magnetic and electrostatic separation.
- The rare earth mineral particles detected in the SCFAs were composed of monazite, xenotime and zircon, with monazite being the most abundant. REEs in the monazite particles were found to be distributed within the particle surfaces; this favours cost-effective and more environmentally-friendly REE leaching from SCFAs using less-aggressive acids, such as ethanoic and oxalic acids.

- Radioactive particles small enough to be inhalable (≤PM20), namely uraninite and thorite, were detected within the SCFAs, a concern for humans and the environment due to the chemo- and radio-toxicity of U, Th and their decay products (e.g. ^{226}Ra and ^{228}Ra). The cracked morphology of these radioactive particles invokes potential fragmentation into the more harmful PM2.5, which could penetrate deep into the lungs and the alveoli.

8.1.2 Bulk characterisation of rare earth elements in simulant coal fly ash

- SCFAs were enriched in both light REEs, LREEs (La to Gd) and critical REEs (Nd, Eu, Tb, Dy, Y, Er), representing a potentially highly valuable source for prized REEs. Compared to conventional rare earth ores, SCFAs were more than three to four times enriched in such critical REEs.
- REE content of Nigerian SCFAs makes them a highly promising future source of revenue for the Nigerian Government, if the coal is utilised as a fuel in power stations.
- REEs in the coal samples were mostly associated with organic matter and mineral components; only a small and insignificant fraction (~1%) of REEs were recovered in the acid-soluble fraction using ethanoic acid.
- From SCFAs, a significant percent (14% to 31%) of the LREEs, heavy REEs (HREEs) and critical REEs were recovered in the acid-soluble fraction using ethanoic acid (or vinegar, ~5% ethanoic acid). This demonstrates that a significant proportion of REEs contained within coal fly ash in repositories globally (sourced from coal-fired power plants burning coal at temperatures ≤1,200 °C) can be potentially recovered in an environmentally friendly manner using cost-effective heap-leaching methods, with cheaply available lixiviants – aqueous media for extraction in hydrometallurgy. Post heap-leaching, the individual REEs in the resultant leachate can be potentially

separated using a cost effective selective extraction method such as the liquid membrane extraction method.

- From coal samples, significant amounts of the toxic heavy metals, As and Cd, were recovered in the acid-soluble fraction; from SCFAs, small but not insignificant amounts of As, Cd, Pb and, to a lesser extent, U, were recovered in the acid-soluble fraction. These results imply easy leaching of these toxic heavy metals when accidentally released into the natural environment, especially in the presence of acidified mine waters. Following heap-leaching and recovery of the REEs, the toxic heavy metal-laden waste water could potentially be evaporated and alongside the residual ash from the heap-leaching process, recycled into concrete and bricks, providing an added value stream for the rare earth recovery process.
- Following from the occurrence of REE-bearing mineral microparticles and the less complex mineralogy of the SCFAs, alongside the significant amount of REEs recovered in the initial acid-soluble phase of the sequential extraction, a potentially cost effective and environmentally friendly procedure for REEs recovery from the simulant coal ash is proposed (Figure 8.1). This procedure proceeds as: 1. High intensity magnetic separation to remove the weakly magnetic haematite and ilmenite; 2. High intensity electrostatic separation to remove rutile; density separation to remove quartz, mullite and cristobalite; 3. The final concentrate (rich in REE-bearing minerals) from step 3 is heap-leached using ethanoic acid/vinegar; 4. Lastly, selective extraction (using liquid membrane extraction) is performed on the REE-laden leachate from the heap-leaching process and compared with other alternative extraction methods.

8.1.3 Synchrotron speciation analysis of rare earth particles in simulant coal fly ash

- Monazite particle isolation prior to synchrotron radiation analysis using a micro-manipulation method, significantly enhanced the resolution and quality of the results obtained.
- Amorphisation of the monazite matrix and oxidation of REEs was observed.
- LREEs in the monazite particles were strongly co-localised and surface-bound, enveloping the actinides in a core-shell pattern distribution pattern.
- The surface distribution of REEs and structural transformation of the monazite matrix are indicative of higher solubility, which translates to more cost-effective REE leaching from monazite.

8.1.4 Bulk and particulate radiological analysis of coal and simulant coal fly ash

- Activity concentrations, radiological indices (of ^{40}K, ^{232}Th and ^{226}Ra) and total Ra for bulk coal samples were all significantly lower than World mean values in soil, thus presenting no significant radiological hazard.
- However, activity concentrations, radiological indices (of ^{40}K, ^{232}Th and ^{226}Ra) and total Ra for SCFAs were all significantly higher than World mean values in soil, making such materials unsafe for the construction of residential buildings.
- Though existing in relatively insoluble IV oxidation state, U in the radioactive particles analysed was homogenously distributed. The small particle sizes and relatively high surface area to volume ratios mean that these particles might still release U into the natural environment at relatively high rates, when leached by meteoric waters.

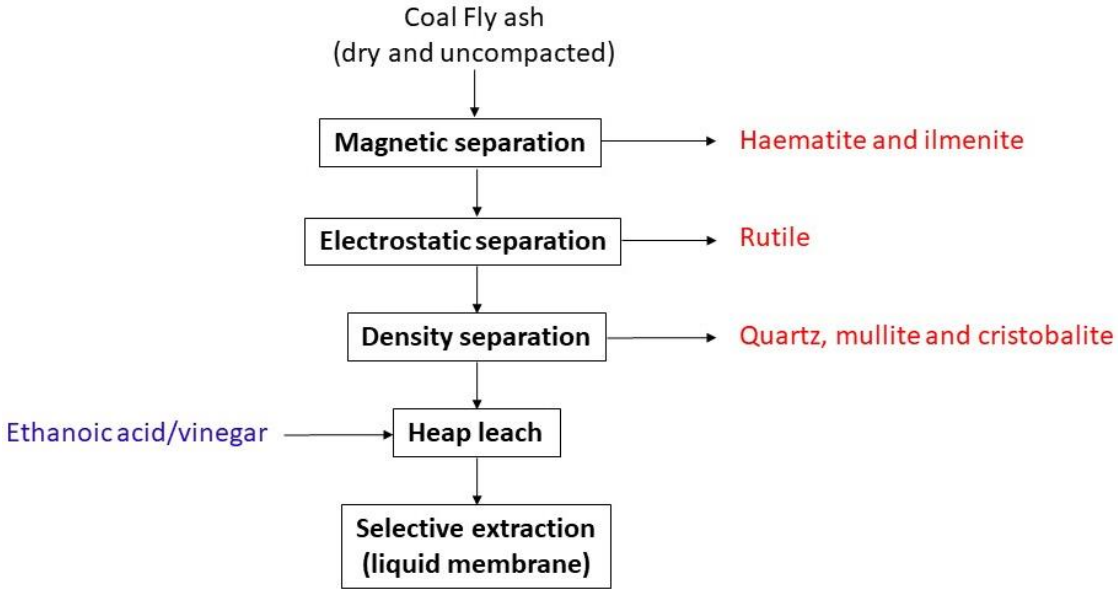

Figure 8.1: Flowsheet for potential REE recovery from simulant coal fly ash.

8.2 Future work

The results of this study have yielded valuable information, essential for the optimisation and development of environmentally friendly and cost-effective REE recovery, waste management and environmental protection methodologies, valuable for both the Nigerian Government and the global scientific community. For the global scientific community, the findings of this thesis are potentially valuable for the coal fly ash accumulations that already exist, as the REEs in coal fly ash could potentially be recovered cheaply using environmentally friendly lixiviants such as ethanoic acid. For the Nigerian Government, the findings on coal fly ash will encourage coal burning thereby contributing to global warming.

However, the following suggested additional work is recommended to provide further reliable data to help the Nigerian Government secure sustainable rare earth resource, and assist the global scientific community in the recovery of REEs from coal fly ash currently held in extensive and polluting repositories:

1. Further synchrotron radiation analysis (principally micro-x-ray fluorescence (μ-XRF) tomography) should be performed on a greater number of monazite and radioactive particles to further validate the results of the three monazite particles and two radioactive particles reported on in this work.
2. To confirm its applicability and efficiency, the proposed procedure for REE recovery - physical beneficiation and heap-leaching (using vinegar/ethanoic acid as lixiviant) should be tested on large volumes (million tonnes) of Nigerian SCFA and coal fly ash sourced from fluidised bed combustion coal-fired power plants operating at temperatures between 750 °C and 1,200 °C.

3. Working with the Nigeria Ministry of Mines and Steel Development, alongside the Nigerian Geological Survey Agency, there is a need to verify the REE resources in Nigerian coal and coal fly ash by identifying and mapping related REE-rich coal deposits in the country. This would help in developing an understanding of the geo-tectonic settings leading to the most REE-abundant coal deposits. Furthermore, coal mine tailings and acid mine drainages should be studied as these could also contain significant amounts of recoverable REEs; this could serve as alternative to coal fly ash generation through burning of coal – a highly detrimental process.
4. Since it is known that significant quantities of rare earth minerals can be recovered as co-products of certain other mineral ores, e.g. iron ore deposits (one example is China's Bayan Obo iron-REE-niobium deposit), and as Nigeria is endowed with over 30 iron ore deposits, there is a need and interest to investigate these iron ore deposits to determine the level of REE-enrichment in them.

Appendix

A1: Activity concentrations of ^{214}Pb and ^{214}Bi (from ^{238}U series), ^{214}Pb/^{214}Bi, and ^{228}Ac and ^{208}Tl (from ^{232}Th series) in OMC.

Sample	Specific activity (Bq.kg^{-1})				
	Uranium series (^{226}Ra)			Thorium series	
	^{214}Pb (352 keV)	^{214}Bi (609 keV)	Ratio (^{214}Pb/^{214}Bi)	^{228}Ra	^{228}Th
				^{228}Ac (911 keV)	^{208}Tl (583 keV)
OMC1	33.85 ± 1.61	30.84 ± 1.69	1.10	27.00 ± 1.67	37.46 ± 1.92
OMC2	32.65 ± 1.55	27.79 ± 1.53	1.18	27.33 ± 1.67	36.56 ± 1.86
OMC3	29.61 ± 1.41	27.51 ± 1.51	1.08	24.92 ± 1.53	32.62 ± 1.68
OMC4	49.54 ± 2.28	44.57 ± 2.35	1.11	37.93 ± 2.21	55.84 ± 2.70
OMC5	46.74 ± 2.16	43.31 ± 2.29	1.08	36.89 ±2.17	52.52 ± 2.57
OMC6	48.93 ± 2.26	44.55 ± 2.35	1.10	36.33 ± 2.13	51.10 ± 2.50
OMC7	48.41 ± 2.23	43.07 ± 2.27	1.12	38.56 ± 2.23	54.18 ± 2.62
OMC8	53.15 ± 2.45	48.83 ± 2.58	1.09	41.54 ± 2.42	54.96 ± 2.69
OMC9	43.08 ± 2.00	37.84 ± 2.02	1.14	31.43 ± 1.88	41.66 ± 2.08
OMC10	61.82 ± 2.81	56.63 ± 2.94	1.09	55.98 ± 3.14	77.14 ± 3.64
OMC11	34.37 ± 1.63	27.53 ± 1.52	1.25	27.55 ± 1.69	38.57 ± 1.96
OMC12	46.00 ± 2.13	41.94 ± 2.23	1.10	35.28 ± 2.08	47.23 ± 2.33
OMC13	46.78 ± 2.17	43.90 ± 2.33	1.07	35.14 ± 2.09	48.56 ± 2.40
OMC14	46.88 ± 2.18	44.01 ± 2.34	1.07	35.47 ± 2.10	48.68 ± 2.41
OMC15	46.96 ± 2.18	44.17 ± 2.35	1.06	35.60 ± 2.11	48.79 ± 2.41
Minimum Maximum	29.61 ± 1.41 61.82 ± 2.81	27.51 ± 1.51 56.63 ± 2.94	1.06 1.25	27.00 ± 1.67 55.98 ± 3.14	32.62 ± 1.68 77.14 ± 3.64
Mean ± s.d.	44.58 ± 8.62	40.43 ± 8.52	1.11 ± 0.05	35.13 ± 7.32	48.39 ± 10.81

s.d.: standard deviation

A2: Activity concentrations of ^{214}Pb and ^{214}Bi (from ^{238}U series), ^{214}Pb/^{214}Bi, and ^{228}Ac and ^{208}Tl (from ^{232}Th series) in OMA.

Sample	Specific activity (Bq.kg^{-1})				
	Uranium series (^{226}Ra)			Thorium series	
	^{214}Pb (352 keV)	^{214}Bi (609 keV)	Ratio (^{214}Pb/^{214}Bi)	^{228}Ra	^{228}Th
				^{228}Ac (911 keV)	^{208}Tl (583 keV)
OMA1	241.15 ± 11.35	204.54 ± 11.13	1.18	124.48 ± 8.02	136.50 ± 7.53
OMA2	235.65 ± 11.33	214.68 ± 11.91	1.10	140.06 ± 9.27	115.10 ± 6.92
OMA3	206.93 ± 9.81	195.94 ± 10.66	1.06	117.32 ± 7.59	127.02 ± 7.04
OMA4	220.59 ± 10.61	210.44 ± 11.64	1.05	111.64 ± 7.64	135.81 ± 7.80
OMA5	228.09 ± 10.98	205.53 ± 11.44	1.11	125.88 ± 8.47	115.18 ± 6.90
OMA6	220.69 ± 10.42	204.86 ± 11.11	1.08	98.39 ± 6.58	125.75 ± 6.99
OMA7	233.95 ± 11.32	227.48 ± 12.64	1.03	121.90 ± 8.41	137.55 ± 8.09
OMA8	264.96 ± 12.64	242.19 ± 13.31	1.09	128.01 ± 8.65	147.67 ± 8.47
OMA9	284.26 ± 13.39	238.77 ± 13.02	1.19	131.69 ± 8.67	180.17 ± 9.77
OMA10	291.85 ± 13.82	275.65 ± 14.98	1.06	141.05 ± 9.36	174.13 ± 9.68
OMA11	283.04 ± 13.21	261.90 ± 14.01	1.08	111.01 ± 7.33	148.80 ± 8.12
OMA12	268.93 ± 12.56	245.44 ± 13.16	1.10	124.83 ± 8.03	156.62 ± 8.43
OMA13	267.82 ± 12.44	248.02 ± 13.20	1.08	118.41 ± 7.56	153.35 ± 8.16
OMA14	255.66 ± 11.86	244.75 ± 12.98	1.04	111.33 ± 7.10	148.47 ± 7.85
OMA15	256.30 ± 11.89	246.53 ± 13.06	1.04	112.78 ± 7.18	136.67 ± 7.32
Minimum Maximum	206.93 ± 9.81 291.85 ± 13.82	195.94 ± 10.66 275.65 ± 14.98	1.03 1.18	98.39 ± 6.58 141.05 ± 9.36	115.10 ± 6.92 180.17 ± 9.77
Mean ± s.d.	250.66 ± 26.16	231.11 ± 23.94	1.09 ± 0.05	121.25 ± 11.13	142.59 ± 18.89

s.d.: standard deviation

A3: Activity concentrations of ^{214}Pb and ^{214}Bi (from ^{238}U series), ^{214}Pb/^{214}Bi, and ^{228}Ac and ^{208}Tl (from ^{232}Th series) in OKC.

Sample	Specific activity (Bq.kg^{-1})				
	Uranium series (^{226}Ra)			Thorium series	
	^{214}Pb (352 keV)	^{214}Bi (609 keV)	Ratio (^{214}Pb/^{214}Bi)	^{228}Ra	^{228}Th
				^{228}Ac (911 keV)	^{208}Tl (583 keV)
OKC1	14.34 ± 0.84	13.34 ± 0.93	1.07	16.83 ± 1.30	20.02 ± 1.30
OKC2	21.84 ± 1.11	17.02 ± 1.03	1.28	13.26 ± 0.98	11.87 ± 0.79
OKC3	12.94 ± 0.81	11.22 ± 0.86	1.15	16.52 ± 1.34	16.66 ± 1.20
OKC4	21.86 ± 1.17	18.38 ± 1.18	1.19	20.89 ± 1.50	23.33 ± 1.44
OKC5	18.10 ± 1.01	14.31 ± 0.98	1.26	19.43 ± 1.45	23.10 ± 1.45
OKC6	22.86 ± 1.21	24.17 ± 1.47	0.95	18.87 ± 1.40	23.32 ± 1.44
OKC7	18.29 ± 1.03	15.42 ± 1.05	1.19	27.68 ± 1.92	26.59 ± 1.63
OKC8	29.47 ± 1.50	25.56 ± 1.53	1.15	21.80 ± 1.53	28.96 ± 1.68
OKC9	12.73 ± 0.77	12.61 ± 0.89	1.01	18.42 ± 1.37	15.51 ± 1.08
OKC10	16.32 ± 0.93	14.82 ± 1.01	1.10	18.05 ± 1.36	17.93 ± 1.20
OKC11	18.65 ± 0.98	17.80 ± 1.09	1.05	14.07 ± 1.04	18.46 ± 1.13
OKC12	16.55 ± 0.98	15.85 ± 1.11	1.04	19.66 ± 1.52	26.42 ± 1.68
OKC13	15.30 ± 0.87	12.59 ± 0.87	1.22	18.55 ± 1.37	20.17 ± 1.28
OKC14	4.95 ± 0.41	5.09 ± 0.50	0.97	5.03 ± 0.61	4.60 ± 0.52
OKC15	12.64 ± 0.75	10.62 ± 0.77	1.19	13.47 ± 1.07	13.52 ± 0.96
Minimum Maximum	4.95 ± 0.41 29.47 ± 1.50	5.09 ± 0.50 25.56 ± 1.53	0.95 1.28	5.03 ± 0.61 27.68 ± 1.92	4.60 ± 0.52 28.96 ± 1.68
Mean ± s.d.	17.12 ± 5.68	15.25 ± 5.11	1.12 ± 0.10	17.50 ± 4.99	19.36 ± 6.40

s.d.: standard deviation

A4: Activity concentrations of ^{214}Pb and ^{214}Bi (from ^{238}U series), ^{214}Pb/^{214}Bi, and ^{228}Ac and ^{208}Tl (from ^{232}Th series) in OKA.

Sample	Specific activity (Bq.kg^{-1})				
	Uranium series (^{226}Ra)			Thorium series	
	^{214}Pb (352 keV)	^{214}Bi (609 keV)	Ratio (^{214}Pb/^{214}Bi)	^{228}Ra	^{228}Th
				^{228}Ac (911 keV)	^{208}Tl (583 keV)
OKA1	192.07 ± 9.50	183.79 ± 10.49	1.05	218.87 ± 11.86	263.70 ± 9.38
OKA2	210.46 ± 10.27	170.38 ± 9.77	1.24	146.84 ± 9.74	173.42 ± 9.71
OKA3	187.45 ± 9.26	173.30 ± 9.92	1.08	140.09 ± 9.31	198.31 ± 10.84
OKA4	154.84 ± 7.85	131.39 ± 7.86	1.18	114.43 ± 7.98	140.95 ± 8.28
OKA5	159.87 ± 8.12	152.81 ± 8.99	1.05	135.92 ± 9.23	168.87 ± 9.65
OKA6	151.08 ± 7.75	130.33 ± 7.88	1.16	141.50 ± 9.57	182.39 ± 10.30
OKA7	176.37 ± 8.67	169.34 ± 9.60	1.04	151.83 ± 9.76	203.90 ± 10.91
OKA8	189.67 ± 9.33	163.91 ± 9.41	1.16	147.79 ± 9.67	213.98 ± 11.49
OKA9	194.89 ± 9.85	158.80 ± 9.51	1.23	158.41 ± 10.77	168.25 ± 9.93
OKA10	163.30 ± 8.38	146.39 ± 8.80	1.12	133.83 ± 9.31	138.98 ± 8.45
OKA11	170.23 ± 8.66	145.63 ± 8.73	1.17	125.18 ± 8.79	141.49 ± 8.52
OKA12	158.82 ± 8.32	132.59 ± 8.27	1.20	138.15 ± 9.79	153.25 ± 9.36
OKA13	120.88 ± 6.31	112.83 ± 6.88	1.07	137.55 ± 9.18	152.68 ± 8.76
OKA14	95.62 ± 5.35	103.13 ± 6.59	0.93	104.09 ± 7.65	103.03 ± 6.73
OKA15	95.91 ± 5.24	107.06 ± 6.64	0.90	81.99 ± 6.21	118.60 ± 7.26
Minimum Maximum	95.62 ± 5.35 210.46 ± 10.27	103.13 ± 6.59 183.79 ± 10.49	0.90 1.24	81.99 ± 6.21 218.87 ± 11.86	103.03 ± 6.73 263.70 ± 9.38
Mean ± s.d.	161.43 ± 8.91	145.45 ± 6.52	1.10 ± 0.10	138.41 ± 7.67	168.12 ± 10.49

s.d.: standard deviation

A5: Activity concentrations of ^{214}Pb and ^{214}Bi (from ^{238}U series), ^{214}Pb/^{214}Bi, and ^{228}Ac and ^{208}Tl (from ^{232}Th series) in ODC.

Sample	Specific activity (Bq.kg^{-1})				
	Uranium series (^{226}Ra)			Thorium series	
	^{214}Pb (352 keV)	^{214}Bi (609 keV)	Ratio (^{214}Pb/^{214}Bi)	^{228}Ra	^{228}Th
				^{228}Ac (911 keV)	^{208}Tl (583 keV)
ODC1	7.88 ± 0.56	8.43 ± 0.69	0.93	12.91 ± 1.10	13.44 ± 1.02
ODC2	11.75 ± 0.72	10.70 ± 0.78	1.10	11.09 ± 0.95	14.69 ± 1.03
ODC3	9.67 ± 0.63	8.91 ± 0.70	1.09	10.95 ± 0.97	13.35 ± 0.99
ODC4	18.50 ± 1.04	15.53 ± 1.05	1.19	23.54 ± 1.70	19.31 ± 1.29
ODC5	5.35 ± 0.44	4.46 ± 0.46	1.20	9.73 ± 0.94	7.80 ± 0.73
ODC6	17.92 ± 1.04	19.03 ± 1.27	0.94	21.49 ± 1.63	27.13 ± 1.71
ODC7	8.80 ± 0.59	7.40 ± 0.61	1.19	13.69 ± 1.14	14.29 ± 1.04
ODC8	12.27 ± 0.78	9.42 ± 0.75	1.30	19.91 ± 1.54	15.96 ± 1.16
ODC9	6.67 ± 0.43	7.09 ± 0.59	0.94	13.52 ± 1.05	15.65 ± 1.00
ODC10	10.90 ± 0.70	10.32 ± 0.79	1.06	14.46 ± 1.19	11.54 ± 0.91
ODC11	3.31 ± 0.31	3.43 ± 0.38	0.97	14.60 ± 1.20	11.90 ± 0.92
ODC12	2.35 ± 0.25	2.14 ± 0.28	1.10	6.29 ± 0.68	7.61 ± 0.68
ODC13	3.48 ± 0.31	3.88 ± 0.40	0.90	11.07 ± 0.96	8.86 ± 0.74
ODC14	4.14 ± 0.35	4.68 ± 0.44	0.88	6.62 ± 0.68	8.51 ± 0.72
ODC15	11.52 ± 0.72	10.67 ± 0.79	1.08	15.73 ± 1.24	13.62 ± 1.00
Minimum Maximum	2.35 ± 0.25 18.50 ± 1.04	2.14 ± 0.28 19.03 ± 1.27	0.88 1.30	6.29 ± 0.68 23.54 ± 1.70	7.80 ± 0.73 27.13 ± 1.71
Mean ± s.d.	8.97 ± 4.99	8.41 ± 4.60	1.06 ± 0.13	13.71 ± 4.96	13.58 ± 5.02

s.d.: standard deviation

A6: Activity concentrations of ^{214}Pb and ^{214}Bi (from ^{238}U series), ^{214}Pb/^{214}Bi, and ^{228}Ac and ^{208}Tl (from ^{232}Th series) in ODA.

Sample	Specific activity (Bq.kg^{-1})				
	Uranium series (^{226}Ra)			Thorium series	
	^{214}Pb (352 keV)	^{214}Bi (609 keV)	Ratio (^{214}Pb/^{214}Bi)	^{228}Ra	^{228}Th
				^{228}Ac (911 keV)	^{208}Tl (583 keV)
ODA1	115.83 ± 6.34	120.96 ± 7.61	0.96	94.72 ± 7.29	99.29 ± 6.70
ODA2	134.98 ± 6.93	122.14 ± 7.34	1.11	166.65 ± 10.73	166.04 ± 9.36
ODA3	82.98 ± 4.81	95.47 ± 6.25	0.87	102.33 ± 7.70	100.06 ± 6.68
ODA4	118.40 ± 6.32	115.25 ± 7.15	1.03	116.42 ± 8.33	110.52 ± 7.03
ODA5	107.03 ± 5.62	91.94 ± 5.72	1.16	102.01 ± 7.17	116.91 ± 6.98
ODA6	104.76 ± 5.55	91.74 ± 5.75	1.14	93.51 ± 6.75	73.29 ± 4.96
ODA7	84.71 ± 4.91	77.09 ± 5.32	1.10	85.65 ± 6.80	107.95 ± 7.09
ODA8	65.95 ± 4.00	71.11 ± 4.94	0.93	81.73 ± 6.48	70.10 ± 5.15
ODA9	99.74 ± 5.26	84.90 ± 5.32	1.17	75.52 ± 5.64	86.78 ± 5.51
ODA10	68.58 ± 4.00	82.70 ± 5.39	0.83	79.35 ± 6.12	69.94 ± 4.94
ODA11	88.89 ± 4.56	90.21 ± 5.32	0.99	80.19 ± 5.51	79.68 ± 4.79
ODA12	98.59 ± 5.15	89.64 ± 5.49	1.10	77.50 ± 5.64	117.98 ± 6.85
ODA13	83.87 ± 4.38	81.23 ± 4.92	1.03	93.25 ± 6.30	95.32 ± 5.60
ODA14	92.19 ± 4.73	89.96 ± 5.34	1.02	96.01 ± 6.42	100.45 ± 5.80
ODA15	128.92 ± 6.64	131.13 ± 7.76	0.98	107.75 ± 7.50	153.52 ± 8.74
Minimum Maximum	65.95 ± 4.00 134.98 ± 6.93	71.11 ± 4.94 131.13 ± 7.76	0.83 1.17	75.52 ± 5.64 166.65 ± 10.73	69.94 ± 4.94 166.04 ± 9.36
Mean ± s.d.	98.36 ± 20.35	95.7 ± 18.03	1.03 ± 0.10	96.84 ± 5.87	103.19 ± 7.23

s.d.: standard deviation